The impact of bile on intestinal permeability of drug substances

Dissertation zur Erlangung des naturwissenschaftlichen Doktorgrades
der Julius-Maximilians-Universität Würzburg

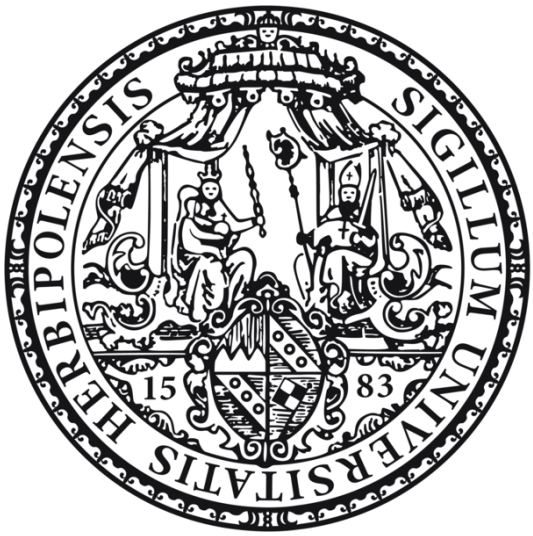

vorgelegt von

Simon Hanio
aus Moers

Würzburg 2023

Eingereicht bei der Fakultät für Chemie und Pharmazie am

_____

Gutachter der schriftlichen Arbeit

1. Gutachter: _____

2. Gutachter: _____

Prüfer des öffentlichen Promotionskolloquiums

1. Prüfer: _____

2. Prüfer: _____

3. Prüfer: _____

Datum des öffentlichen Promotionskolloquiums

_____

Doktorurkunde ausgehändigt am

_____

Die vorliegende Arbeit wurde in der Zeit von Januar 2019 bis Dezember 2022 am Institut für Pharmazie und Lebensmittelchemie der Bayerischen Julius-Maximilians-Universität Würzburg unter der Anleitung von Herrn Prof. Dr. Dr. Lorenz Meinel angefertigt.

To my family.

Table of Contents

Summary

Most medicines are taken orally. To enter the systemic circulation, they dissolve in the intestinal fluid, cross the epithelial barrier, and pass through the liver. Intestinal absorption is driven by the unique features of the gastrointestinal tract, including the bile colloids formed in the lumen and the mucus layer covering the intestinal epithelium. Neglecting this multifaceted environment can lead to poor drug development decisions, especially for poorly water-soluble drugs that interact with bile and mucus. However, there is a lack of a rationale nexus of molecular interactions between oral medicines and gastrointestinal components with drug bioavailability. Against this background, this thesis aims to develop biopharmaceutical strategies to optimize the presentation of oral therapeutics to the intestinal epithelial barrier.

In **Chapter 1**, the dynamics of bile colloids upon solubilization of the poorly-water soluble drug Perphenazine was studied. Perphenazine impacted molecular arrangement, structure, binding thermodynamics, and induced a morphological transition from vesicles to worm-like micelles. Despite these dynamics, the bile colloids ensured stable relative amounts of free drug substance. The chapter was published in Langmuir.

Chapter 2 examined the impact of pharmaceutical polymeric excipients on bile-mediated drug solubilization. Perphenazine and Imatinib were introduced as model compounds interacting with bile, whereas Metoprolol did not. Some polymers altered the arrangement and geometry of bile colloids, thereby affecting the molecularly soluble amount of those drugs interacting with bile. These insights into the bile-drug-excipient interplay provide a blueprint to optimizing formulations leveraging bile solubilization. The chapter was published in Journal of Controlled Release.

Chapter 3 deals with the impact of bile on porcine intestinal mucus. Mucus exposed to bile solution changed transiently, it stiffened, and the overall diffusion rate increased. The bile-induced changes eased the transport of the bile-interacting drug substance Fluphenazine, whereas Metoprolol was unaffected. This dichotomous pattern was linked to bioavailability in rats and generalized based on two previously published data sets. The outcomes point to a bile-mucus interaction relevant to drug delivery. The chapter is submitted.

The **Appendix** provides a guide for biopharmaceutical characterization of drug substances by nuclear magnetic resonance spectroscopy aiming at establishing a predictive algorithm.

In summary, this thesis deciphers bile-driven mechanisms shaping intestinal drug absorption. Based on these molecular insights, pharmaceuticals can be developed along a biopharmaceutical optimization, ultimately leading to better oral drugs of tomorrow.

Zusammenfassung

Die meisten Arzneimittel werden oral eingenommen. Um in den Blutkreislauf zu gelangen, liegen sie in der Darmflüssigkeit gelöst vor, überwinden die Epithelbarriere und passieren die Leber. Die intestinale Absorption wird durch die einzigartigen Eigenschaften des Magen-Darm-Trakts, einschließlich der im Lumen gebildeten Gallenkolloide und der Schleimschicht, die das Darmepithel bedeckt, bestimmt. Die Vernachlässigung dieser facettenreichen Umgebung kann zu schlechten Entscheidungen bei der Arzneimittelentwicklung führen, insbesondere bei schlecht wasserlöslich Wirkstoffen, die mit Galle und Schleim interagieren. Es fehlt jedoch eine rationale Verknüpfung der molekularen Wechselwirkungen zwischen oralen Arzneimitteln und gastrointestinalen Komponenten mit der Bioverfügbarkeit von Arzneimitteln. Vor diesem Hintergrund zielt diese Arbeit darauf ab, biopharmazeutische Strategien zur Optimierung der Präsentation von oralen Therapeutika an der intestinalen Epithelbarriere zu entwickeln.

In **Kapitel 1** wurde die Dynamik von Gallenkolloiden bei der Solubilisierung des schwer wasserlöslichen Wirkstoffes Perphenazin untersucht. Perphenazin beeinflusste die molekulare Anordnung, die Struktur sowie die Bindungsthermodynamik und führte zu einem morphologischen Übergang von Vesikeln hin zu wurmartigen Mizellen. Trotz dieser Dynamik sorgten die Gallenkolloide für stabile relative Mengen an freiem Arzneistoff. Dieses Kapitel wurde in Langmuir veröffentlicht.

In **Kapitel 2** wurde der Einfluss von pharmazeutischen polymeren Hilfsstoffen auf die Solubilisierung von Wirkstoffen durch Galle untersucht. Perphenazin und Imatinib wurden als Modellverbindungen eingeführt, die mit der Galle interagieren, während Metoprolol dies nicht tat. Einige Polymere veränderten die Anordnung und Geometrie der Gallenkolloide und beeinflussten somit die molekular lösliche Menge von solchen Wirkstoffen, die mit der Galle wechselwirken. Diese Einblicke in das Zusammenspiel von Galle und Arzneistoffen bieten einen Ansatz zur Optimierung von Formulierungen, die die Solubilisierung in der Galle nutzen. Dieses Kapitel wurde in Journal of Controlled Release veröffentlicht.

Kapitel 3 befasst sich mit den Auswirkungen von Galle auf den Dünndarmschleim von Schweinen. Schleim, der Gallenlösung ausgesetzt war, veränderte sich vorübergehend, versteifte sich und die Gesamtdiffusionsrate nahm zu. Die durch die Galle hervorgerufenen Veränderungen erleichterten den Transport des mit der Galle interagierenden Wirkstoffs Fluphenazin, während Metoprolol unbeeinflusst blieb. Dieses dichotome Muster konnte mit der Bioverfügbarkeit bei Ratten verknüpft werden und durch zwei zuvor veröffentlichte Datensätze mit insgesamt 50 Verbindungen verallgemeinert werden. Die Ergebnisse deuten

auf eine Wechselwirkung zwischen Galle und Schleim hin, die für die Verabreichung von Medikamenten relevant ist. Dieses Kapitel ist eingereicht.
Der Anhang bietet einen Leitfaden für die biopharmazeutische Charakterisierung von Arzneimittelsubstanzen durch kernmagnetische Resonanzspektroskopie mit dem Ziel des Aufstellens von prädiktiven Algorithmen.
Zusammenfassend entschlüsselt diese Arbeit die von der Galle gesteuerten Mechanismen, die die Aufnahme von Arzneimitteln im Darm beeinflussen. Auf der Grundlage dieser molekularen Erkenntnisse können Arzneimittel entlang einer biopharmazeutischen Optimierung entwickelt werden, was letztendlich zu besseren oralen Arzneimitteln führt.

Introduction

Solubility and permeability

Solubility drives the formulation development

Solubility refers to the maximum amount of a substance that will dissolve in each amount of solvent to form a homogeneous solution at a given temperature and pressure[1]. In general, orally dosed drug compounds must be in the form of a solution to be taken up at the site of absorption[2-4]. As a result, the solubility of a drug in aqueous media is critical to its systemic availability and thus to the clinical outcome[5,6]. Solubility can be limited either by the lipophilicity of the molecule, resulting in insufficient solvation, or by high crystalline forces, which are difficult to break down when in contact with water[7,8]. Drug compounds of these two extreme types are occasionally referred to as "grease balls" or "brick dust". Furthermore, low soluble compounds often suffer from slow dissolution, i.e., the solid drug dissolves only slowly in the gastrointestinal fluid, leaving less drug available for absorption into the bloodstream[10]. In drug development cycles, the solubility profile of a drug is evaluated using a variety of solvents and conditions, including the shake flask method, equilibrium solubility studies, and pH solubility studies[11,12]. These solubility assessments help to identify potential drug delivery challenges, to assess developability risks, and to develop strategies to optimize drug efficacy, e.g., in the selection of adequate excipients and the formulation design.

Holistic assessment of permeability is crucial for rational drug development

Permeability is a measure of a drug's ability to cross biological membranes[13]. Intestinal permeability is essential for orally taken drugs to enter the bloodstream, with passive drug diffusion being the major absorption pathway[14]. An established method to evaluate intestinal drug absorption is the Caco-2 cell permeability assay[15]. The Caco-2 cell line is derived from human colon carcinoma and forms a monolayer when cultured on membranes. Permeability assays measure the rate at which a test compound crosses the barrier, such as a Caco-2 monolayer. The test compound is added to the apical (luminal) side of the monolayer and the amount that crosses to the basolateral (apical) side is measured. The transport rate is expressed as an apparent permeability coefficient, which is a surrogate of the compound's ability to pass the intestinal barrier. Whilst the Caco2 cell model exhibits many features of the intestinal epithelium, it does not fully replicate the complex architecture and functions of the intestine *in vivo*, including the mucus[16,17]. This calls for a combination of the Caco2 model with other *in vitro* and *in vivo* models to obtain a more accurate understanding of

drug permeability and absorption in the intestine. Part of this involves assessing drug transport through the epithelial-covering mucus as well as molecularly dissolved drug, for which there is strong evidence to be the major contributor to membrane permeation[18-20].

Solubility and permeability are interwoven

Solubility and permeability are key parameters for intestinal drug absorption of small, oral therapeutics[21]. In the recent decade, the interplay between the two has come more into focus[21,22]. Furthermore, there are effort to screen virtually for intestinal drug solubility and permeability, which allows to streamline drug discovery programs along drug product developability[23-25]. One system for distinguishing drugs based on the two parameters is the biopharmaceutical classification system (BCS), first proposed in 1995 by Amidon et al. and promulgated by the Food and Drug Administration as an approach to waiving bioavailability studies in 2000[26,27]. Within this regulatory-compliant framework, drugs are classified into four classes according to their solubility and permeability. According to the ICH M9 on biopharmaceutics classification system based biowaivers - Scientific guideline, solubility is high "if the highest single therapeutic dose is completely soluble in 250 ml or less of aqueous media over the pH range of 1.2–6.8 at 37 ± 1 °C"[28]. High permeability is to be shown preferably by *in vivo* studies but can also be proven by a standardized Caco-2 permeability assay outlined in the annex of the guideline. The following classification is the result: BCS class I drugs are high soluble and high permeable; BCS class II are low soluble and high permeable, BCS class III are high soluble and low permeable, and BCS class IV drugs are low soluble and low permeable. The poor solubility and low dissolution rate of poorly water-soluble drugs in the aqueous gastrointestinal fluids often cause insufficient bioavailability resulting in ineffective drug efficacy[29,30]. Especially for BCS class II drugs, the bioavailability may be enhanced by increasing the solubility and dissolution rate of the drug in the gastrointestinal fluids by formulation design[31]. In this vein, this thesis focuses on the pharmaceutical and biopharmaceutical modulation of the oral drug exposure of BCS class II drugs.

Low solubility challenges drug development

There is a trend towards poor soluble drugs in discovery programs

Today's medicinal drug discovery programs are based on combinatorial chemistry and high throughput screening to biological targets[32-34]. This workflow, combined with the targeted search for highly potent compounds, favors the emergence of lipophilic and poorly water-soluble lead compounds. Consequently, the pharmaceutical pipeline is fueled by new

chemical entities (NCEs) with low water solubility (BCS class II and IV drugs). Approximately 40% of today's lead compounds have an aqueous solubility less than 10 μM[35]. As PWSDs are associated with a longer development time and a higher risk of failure, this trend significantly increases the cost of drug development for pharmaceutical companies[36,37]. Yet there is no indication that this shift towards drug candidates with suboptimal physicochemical properties will decline.

Patient and physician prefer oral administration of medicines

From a patient perspective, oral therapeutics are preferred and results in higher patient medication adherence, which is the key for the treatment of chronic illnesses[38]. Oral drug products are also preferred by physicians because they are safe and non-invasive[39]. Patient-centricity is also playing an increasingly important role in regulatory decision-making[40]. This includes optimizing the drug product presentation with the dosage form being key to higher patient adherence to its therapeutics[41]. Consequently, it is to be expected that the convenience of oral administration will continue to propel industrial and academic efforts to improve the clinical performance of orally administered PWSDs.

Pharmaceutical strategies aim to overcome poor solubility

Formulation scientists have a versatile set of tools at their disposal to improve the apparent intraluminal concentration of PWSD. These include chemical modifications, such as prodrug formulations or the inclusion of pH modifier, and physical modifications, such as crystal modification, complexation with artificial surfactants or cyclodextrins, and dispersion of drugs in polymeric carriers[31,42-46]. Over the last 20 years, of these, amorphous solid dispersions have become the most emerging area as manifested by several successful market launches[47]. In an amorphous solid dispersion, the drug substance is largely amorphously embedded into a solid matrix, which allows the dissolution rate and apparent solubility to be increased without the need to break crystals bonds[48]. Against this background, chapter 2 of this thesis focuses on bioavailability-enhancing polymers used as matrices in such solid dispersions.

All these pharmaceutical strategies and physicochemical concepts can be harnessed to tailor the release and absorption profile of an oral medication. To maximize the *in vivo* product performance, though, the fate of the drug in the gastrointestinal tract is critical and must be considered accordingly. In this regard, bile colloids and the mucus layer hold a key role, and these two gastrointestinal players are the focal point of the next section and this thesis.

Biopharmaceutical features on drug absorption

The gastrointestinal tract is a challenging environment for drug delivery

One of the key functions of the gastrointestinal tract is to regulate the absorption of nutrients and water and to prevent the uptake of potentially harmful luminal components into the central circulation[49]. As with nutrients, the small intestine with its large surface area is the main site for drug absorption[50]. The selectivity is ensured by the complex anatomy and physiology of the gastrointestinal tract, which is also faced by a drug after oral intake[51].

Bile colloids are key for natural solubilization system

Bile flows from the common bile duct into the duodenum where two key components for the natural solubilization system, taurocholate and lecithin, form aqueous mixed colloids[52-55]. Thereby, the contraction of the gallbladder is stimulated by the hormone cholecystokinin which prompts bile flow[56]. In the intestine, the colloids resulting from bile solubilize hydrophobic molecules in the GIT, mediating systemic availability of essential fats and fat-soluble vitamins[57-60]. Similarly, poorly water-soluble drugs are uptake into the colloids, which is associated with an improvement in their apparent solubility in the intestine[61-63]. Bile levels are higher in the fed state, which was previously linked to a positive food effect, and efforts are underway to predict this biopharmaceutical lever on bioavailability[64-66]. In the colon, bile acids are mainly reabsorbed by apical sodium-dependent transporter and then returned to the liver via the portal vein[67,68]. This enterohepatic recycling allows conservation of bile acids and maintenance of a constant level of bile acids in the liver. Disturbances in this process, such as a reduction in bile acid absorption, lead to a deficiency of bile acids and subsequently to clinically manifested malabsorption of fats and fat-soluble vitamins[69-71].

To serve as surrogate media for the bile solubilization system, so-called biorelevant dissolution media have been developed[72]. These widely used simulated fluids are standardized media and aim to replicate the complex and dynamic conditions of the human gastrointestinal tract. To this end, their design and composition are based on the physical and chemical properties of gastrointestinal fluids, including pH, buffer capacity, ionic strength, and bile salts levels[66]. In 1998, the first two commercially available biorelevant media were introduced, namely Fasted State Simulated Intestinal Fluid (FaSSIF) and Fed State Simulated Intestinal Fluid (FeSSIF)[73]. In addition to taurocholate and lecithin, digestion products such as fatty acids and monoglycerides were incorporated into FeSSIF media. Biorelevant media have been successfully used to establish *in vitro-in vivo* correlations that streamline pharmaceutical development[72,74]. The colloids formed in biorelevant media are well characterized and indeed show parallels to colloids found in humans[75,76]. However, the dynamic interactions of *in vitro* formed bile colloids with components in oral medicines,

such as polymeric excipients or poorly water-soluble drugs, are poorly understood. In the first two chapters, this thesis deals with this area of research based on molecular-mechanistic case studies.

Mucus layer must be overcome for the drug to be systemically available

Mucus is another feature of the gastrointestinal tract that is increasingly attracting the attention of pharmaceutical scientists, from its significant role in the gut microbiota to the use of purified mucins in biomedical applications and its transport barrier function[77-79]. The mucus layer is a viscoelastic hydrogel network covering every mucosal surface in the body[80]. Small intestinal mucus acts as a selectively permeable barrier at the intestinal mucosa allowing some particles to pass while retaining others, including small-molecule drug substances[81-84]. Besides water and salts, SIM contains lipids, proteins, deoxyribonucleic acids, and the gel forming glycoprotein Mucin-2[85,86]. The various mucosal biomacromolecules can interact with SMDSs in versatile ways affecting intestinal absorption[82,87,88]. Overcoming the intestinal mucosal barrier is imperative for the systemic availability of drug substances orally administered. As a result, the clinical efficacy of drugs may be limited by low mucosal permeability. Since SMDSs are more than an order of magnitude smaller than the mesh size of the mucus network[89,90], their diffusion through mucus is hampered by interaction rather than steric hindrance[81,82]. As an interactive barrier mucus bind to substances, most readily to hydrophobic and positively charged molecules [18,81,82,87,88,91-94]. While attempts are being made to predict mucus permeability of drugs using molecular descriptors, mucus' multifaceted structure and diverse composition make it challenging to evaluate reliably its interaction with drug candidates a priori. To address the challenges posed by mucus in oral drug delivery, researchers have developed several strategies, one of which is colloid based formulations[95,96]. In general, colloidal structures such as micelles, particles, or pathogens respond to the mucin network, which has a pore size of 10-200 nm[97-100]. The diffusion of colloids in mucus is also influenced by surface chemistry and particle coating[101,102]. Along these lines, drug absorption across SIM can be rendered by colloidal delivery systems such as nanoparticles[89], liposomes[103], and microemulsions[104,105]. Another common strategy is the incorporation of mucoadhesive polymers such as chitosan which increases the contact time with the mucus layer[96,106]. In addition, the transient breakdown of mucus' structure has therapeutic applications with mucolytics or for the delivery of transport-impaired peptides[107,108]. Since, especially healthy, human small intestinal mucus is difficult to obtain, various models are used to study the role of mucus in drug delivery[18]. One of these is native gastrointestinal mucus isolated from pigs, which is attracting increasing attention in the pharmaceutical industry because of its similarity to the human digestive tract[86,109,110].

Previous studies demonstrate the utility of this model for studying the diffusion patterns of molecules and colloids[60-63,111]. Using native mucus from pigs as a model system, the extent to which bile and mucus interact in the transport of drug substances to the intestinal epithelium is part of the third chapter of this thesis.

Research gap

The current understanding of how molecular interactions can be leveraged to optimize drug performance is limited

Neglecting the multifaceted environment of the gastrointestinal tract can lead to suboptimal decisions during drug development, particularly for medicines that interact with bile and mucus. Thus, it is important to evaluate the biopharmaceutical features that influence intestinal drug product performance. Although this assessment is often performed thoroughly in the pharmaceutical industry, it often remains descriptive and understanding of the molecular mechanisms underlying the interactions remains limited. Consequently, the nexus between molecular interactions between oral medicines and gastrointestinal compounds with drug bioavailability is poorly understood. For instance, little is known about the interaction of intestinal mucus, bile, and molecules' diffusion. This all complicates a prospective evaluation of the intricate *in vivo* interplay and may hinder informed decision-making. Ultimately, these "traditional" drug developments are based on iterative trial-and-error experiments that lead to empirical optimization of drug formulations and ultimately to innumerable and arbitrary animal experiments with rather unhelpful results.

This thesis aims to decipher the interaction pattern between mucus, bile, polymers, and drug substances and the resulting diffusion dynamics. It details the bile-driven mechanisms in the context of gastrointestinal drug delivery and discusses for their potential to shape intestinal drug absorption. This work focuses on the dynamics of bile colloids with poorly water-soluble drug upon solubilization, the bile-drug-excipient interplay, and the interaction between bile and mucus related to drug diffusion dynamics in chapters 1, 2, and 3 respectively. These mechanistic studies pave the way for generalising these observations with high-throughput datasets and developing strategies to optimize the presentation of oral therapeutics to the intestinal epithelial barrier.

References

1 Savjani, K. T., Gajjar, A. K. & Savjani, J. K. Drug solubility: importance and enhancement techniques. *ISRN Pharm* **2012**, 195727, doi:10.5402/2012/195727 (2012).

2 Viswanathan, P., Muralidaran, Y. & Ragavan, G. in *Nanostructures for Oral Medicine* (eds Ecaterina Andronescu & Alexandru Mihai Grumezescu) 173-201 (Elsevier, 2017).

3 Schittny, A., Huwyler, J. & Puchkov, M. Mechanisms of increased bioavailability through amorphous solid dispersions: a review. *Drug Deliv* **27**, 110-127, doi:10.1080/10717544.2019.1704940 (2020).

4 Fagerberg, J. H. & Bergstrom, C. A. Intestinal solubility and absorption of poorly water soluble compounds: predictions, challenges and solutions. *Ther Deliv* **6**, 935-959, doi:10.4155/tde.15.45 (2015).

5 Williams, H. D. *et al.* Strategies to address low drug solubility in discovery and development. *Pharmacol Rev* **65**, 315-499, doi:10.1124/pr.112.005660 (2013).

6 Kawabata, Y., Wada, K., Nakatani, M., Yamada, S. & Onoue, S. Formulation design for poorly water-soluble drugs based on biopharmaceutics classification system: basic approaches and practical applications. *Int J Pharm* **420**, 1-10, doi:10.1016/j.ijpharm.2011.08.032 (2011).

7 Ditzinger, F. *et al.* Lipophilicity and hydrophobicity considerations in bio-enabling oral formulations approaches - a PEARRL review. *J Pharm Pharmacol* **71**, 464-482, doi:10.1111/jphp.12984 (2019).

8 Bergstrom, C. A., Wassvik, C. M., Johansson, K. & Hubatsch, I. Poorly soluble marketed drugs display solvation limited solubility. *J Med Chem* **50**, 5858-5862, doi:10.1021/jm0706416 (2007).

9 Edueng, K., Mahlin, D. & Bergstrom, C. A. S. The Need for Restructuring the Disordered Science of Amorphous Drug Formulations. *Pharm Res* **34**, 1754-1772, doi:10.1007/s11095-017-2174-7 (2017).

10 Hermans, A. *et al.* Challenges and Strategies for Solubility Measurements and Dissolution Method Development for Amorphous Solid Dispersion Formulations. *AAPS J* **25**, 11, doi:10.1208/s12248-022-00760-8 (2022).

11 Sugano, K. *et al.* Solubility and dissolution profile assessment in drug discovery. *Drug Metab Pharmacokinet* **22**, 225-254, doi:10.2133/dmpk.22.225 (2007).

12 Barrett, J. A., Yang, W., Skolnik, S. M., Belliveau, L. M. & Patros, K. M. Discovery solubility measurement and assessment of small molecules with drug development in mind. *Drug Discov Today* **27**, 1315-1325, doi:10.1016/j.drudis.2022.01.017 (2022).

13 Li, A. P. Preclinical in vitro screening assays for drug-like properties. *Drug Discov Today Technol* **2**, 179-185, doi:10.1016/j.ddtec.2005.05.024 (2005).

14 Di, L. *et al.* The Critical Role of Passive Permeability in Designing Successful Drugs. *ChemMedChem* **15**, 1862-1874, doi:10.1002/cmdc.202000419 (2020).

15 van Breemen, R. B. & Li, Y. Caco-2 cell permeability assays to measure drug absorption. *Expert Opin Drug Metab Toxicol* **1**, 175-185, doi:10.1517/17425255.1.2.175 (2005).

16 Sun, H., Chow, E. C., Liu, S., Du, Y. & Pang, K. S. The Caco-2 cell monolayer: usefulness and limitations. *Expert Opin Drug Metab Toxicol* **4**, 395-411, doi:10.1517/17425255.4.4.395 (2008).

17 Birch, D., Diedrichsen, R. G., Christophersen, P. C., Mu, H. & Nielsen, H. M. Evaluation of drug permeation under fed state conditions using mucus-covered Caco-2 cell epithelium. *Eur J Pharm Sci* **118**, 144-153, doi:10.1016/j.ejps.2018.02.032 (2018).

18 Lock, J. Y., Carlson, T. L. & Carrier, R. L. Mucus models to evaluate the diffusion of drugs and particles. *Adv Drug Deliv Rev* **124**, 34-49, doi:10.1016/j.addr.2017.11.001 (2018).

19 Berben, P. *et al.* Drug permeability profiling using cell-free permeation tools: Overview and applications. *Eur J Pharm Sci* **119**, 219-233, doi:10.1016/j.ejps.2018.04.016 (2018).

20 Indulkar, A. S., Gao, Y., Raina, S. A., Zhang, G. G. & Taylor, L. S. Exploiting the Phenomenon of Liquid-Liquid Phase Separation for Enhanced and Sustained Membrane Transport of a Poorly Water-Soluble Drug. *Mol Pharm* **13**, 2059-2069, doi:10.1021/acs.molpharmaceut.6b00202 (2016).

21 Dahan, A., Beig, A., Lindley, D. & Miller, J. M. The solubility-permeability interplay and oral drug formulation design: Two heads are better than one. *Adv Drug Deliv Rev* **101**, 99-107, doi:10.1016/j.addr.2016.04.018 (2016).

22 Nainwal, N., Singh, R., Jawla, S. & Saharan, V. A. The Solubility-Permeability Interplay for Solubility-Enabling Oral Formulations. *Curr Drug Targets* **20**, 1434-1446, doi:10.2174/1389450120666190717114521 (2019).

23 Stenberg, P., Luthman, K. & Artursson, P. Virtual screening of intestinal drug permeability. *J Control Release* **65**, 231-243, doi:10.1016/s0168-3659(99)00239-4 (2000).

24 Boobier, S., Hose, D. R. J., Blacker, A. J. & Nguyen, B. N. Machine learning with physicochemical relationships: solubility prediction in organic solvents and water. *Nat Commun* **11**, 5753, doi:10.1038/s41467-020-19594-z (2020).

25 Fagerberg, J. H., Karlsson, E., Ulander, J., Hanisch, G. & Bergstrom, C. A. Computational prediction of drug solubility in fasted simulated and aspirated human intestinal fluid. *Pharm Res* **32**, 578-589, doi:10.1007/s11095-014-1487-z (2015).

26 Amidon, G. L., Lennernas, H., Shah, V. P. & Crison, J. R. A theoretical basis for a biopharmaceutic drug classification: the correlation of in vitro drug product dissolution and in vivo bioavailability. *Pharm Res* **12**, 413-420, doi:10.1023/a:1016212804288 (1995).

27 Davit, B. M., Kanfer, I., Tsang, Y. C. & Cardot, J. M. BCS Biowaivers: Similarities and Differences Among EMA, FDA, and WHO Requirements. *AAPS J* **18**, 612-618, doi:10.1208/s12248-016-9877-2 (2016).

28 ICH. *M9: Biopharmaceutics Classification System-Based Biowaivers*. Geneva, Switzerland: Committee for Medicinal Products for Human Use. (2019)

29 Basavaraj, S. & Betageri, G. V. Can formulation and drug delivery reduce attrition during drug discovery and development-review of feasibility, benefits and challenges. *Acta Pharm Sin B* **4**, 3-17, doi:10.1016/j.apsb.2013.12.003 (2014).

30 Kola, I. & Landis, J. Can the pharmaceutical industry reduce attrition rates? *Nat Rev Drug Discov* **3**, 711-715, doi:10.1038/nrd1470 (2004).

31 Singh, A., Worku, Z. A. & Van den Mooter, G. Oral formulation strategies to improve solubility of poorly water-soluble drugs. *Expert Opin Drug Deliv* **8**, 1361-1378, doi:10.1517/17425247.2011.606808 (2011).

32 Benz, M. *et al.* A combined high-throughput and high-content platform for unified on-chip synthesis, characterization and biological screening. *Nat Commun* **11**, 5391, doi:10.1038/s41467-020-19040-0 (2020).

33 Liu, R., Li, X. & Lam, K. S. Combinatorial chemistry in drug discovery. *Curr Opin Chem Biol* **38**, 117-126, doi:10.1016/j.cbpa.2017.03.017 (2017).

34 Di, L., Fish, P. V. & Mano, T. Bridging solubility between drug discovery and development. *Drug Discov Today* **17**, 486-495, doi:10.1016/j.drudis.2011.11.007 (2012).

35 Stegemann, S., Leveiller, F., Franchi, D., de Jong, H. & Linden, H. When poor solubility becomes an issue: from early stage to proof of concept. *Eur J Pharm Sci* **31**, 249-261, doi:10.1016/j.ejps.2007.05.110 (2007).

36 Hann, M. M. Molecular obesity, potency and other addictions in drug discovery. *MedChemComm* **2**, 349-355, doi:10.1039/c1md00017a (2011).

37 Waring, M. J. *et al.* An analysis of the attrition of drug candidates from four major pharmaceutical companies. *Nat Rev Drug Discov* **14**, 475-486, doi:10.1038/nrd4609 (2015).

38 Brown, M. T. & Bussell, J. K. Medication adherence: WHO cares? *Mayo Clin Proc* **86**, 304-314, doi:10.4065/mcp.2010.0575 (2011).

39 Alqahtani, M. S., Kazi, M., Alsenaidy, M. A. & Ahmad, M. Z. Advances in Oral Drug Delivery. *Front Pharmacol* **12**, 618411, doi:10.3389/fphar.2021.618411 (2021).

40 Algorri, M., Cauchon, N. S., Christian, T., O'Connell, C. & Vaidya, P. Patient-Centric Product Development: A Summary of Select Regulatory CMC and Device Considerations. *J Pharm Sci*, doi:10.1016/j.xphs.2023.01.029 (2023).

41 Drumond, N. Future Perspectives for Patient-Centric Pharmaceutical Drug Product Design with Regard to Solid Oral Dosage Forms. *Journal of Pharmaceutical Innovation* **15**, 318-324, doi:10.1007/s12247-019-09407-2 (2019).

42 Jornada, D. H. *et al.* The Prodrug Approach: A Successful Tool for Improving Drug Solubility. *Molecules* **21**, 42, doi:10.3390/molecules21010042 (2015).

43 Almotairy, A. *et al.* Effect of pH Modifiers on the Solubility, Dissolution Rate, and Stability of Telmisartan Solid Dispersions Produced by Hot-melt Extrusion Technology. *J Drug Deliv Sci Technol* **65**, doi:10.1016/j.jddst.2021.102674 (2021).

44 Varshosaz, J., Ghassami, E. & Ahmadipour, S. Crystal Engineering for Enhanced Solubility and Bioavailability of Poorly Soluble Drugs. *Curr Pharm Des* **24**, 2473-2496, doi:10.2174/1381612824666180712104447 (2018).

45 Liu, R. R., Dannenfelser, R.-M. & Li, S. in *Water-insoluble drug formulation*, 269-320, CRC Press (2008).

46 Sareen, S., Mathew, G. & Joseph, L. Improvement in solubility of poor water-soluble drugs by solid dispersion. *Int J Pharm Investig* **2**, 12-17, doi:10.4103/2230-973X.96921 (2012).

47 Pandi, P., Bulusu, R., Kommineni, N., Khan, W. & Singh, M. Amorphous solid dispersions: An update for preparation, characterization, mechanism on bioavailability, stability, regulatory considerations and marketed products. *Int J Pharm* **586**, 119560, doi:10.1016/j.ijpharm.2020.119560 (2020).

48 Huang, Y. & Dai, W. G. Fundamental aspects of solid dispersion technology for poorly soluble drugs. *Acta Pharm Sin B* **4**, 18-25, doi:10.1016/j.apsb.2013.11.001 (2014).

49 Kiela, P. R. & Ghishan, F. K. Physiology of Intestinal Absorption and Secretion. *Best Pract Res Clin Gastroenterol* **30**, 145-159, doi:10.1016/j.bpg.2016.02.007 (2016).

50 Azman, M., Sabri, A. H., Anjani, Q. K., Mustaffa, M. F. & Hamid, K. A. Intestinal Absorption Study: Challenges and Absorption Enhancement Strategies in Improving Oral Drug Delivery. *Pharmaceuticals (Basel)* **15**, doi:10.3390/ph15080975 (2022).

51 Golub, A. L., Frost, R. W., Betlach, C. J. & Gonzalez, M. A. Physiologic considerations in drug absorption from the gastrointestinal tract. *J Allergy Clin Immunol* **78**, 689-694, doi:10.1016/0091-6749(86)90047-3 (1986).

52 Riethorst, D. *et al.* Characterization of Human Duodenal Fluids in Fasted and Fed State Conditions. *J. Pharm. Sci.* **105**, 673-681, doi:10.1002/jps.24603 (2016).

53 Schubiger, G., Stocker, C., Banziger, O., Laubscher, B. & Zimmermann, H. Oral vitamin K1 prophylaxis for newborns with a new mixed-micellar preparation of phylloquinone: 3 years experience in Switzerland. *Eur. J. Pediatr.* **158**, 599-602, doi:10.1007/s004310051155 (1999).

54 Augustijns, P. *et al.* A review of drug solubility in human intestinal fluids: implications for the prediction of oral absorption. *Eur J Pharm Sci* **57**, 322-332, doi:10.1016/j.ejps.2013.08.027 (2014).

55 Dawson, P. A. & Karpen, S. J. Intestinal transport and metabolism of bile acids. *J. Lipid. Res.* **56**, 1085-1099, doi:10.1194/jlr.R054114 (2015).

56 Wiener, I. *et al.* Release of cholecystokinin in man: correlation of blood levels with gallbladder contraction. *Ann Surg* **194**, 321-327, doi:10.1097/00000658-198109000-00010 (1981).

57 Elvang, P. A. *et al.* Co-existing colloidal phases of human duodenal aspirates: Intraindividual fluctuations and interindividual variability in relation to molecular composition. *J. Pharm. Biomed. Anal.* **170**, 22-29, doi:10.1016/j.jpba.2019.03.026 (2019).

58 Russell, D. W. The enzymes, regulation, and genetics of bile acid synthesis. *Annu. Rev. Biochem.* **72**, 137-174, doi:10.1146/annurev.biochem.72.121801.161712 (2003).

59 Malik, N. A. Solubilization and Interaction Studies of Bile Salts with Surfactants and Drugs: a Review. *Appl. Biochem. Biotechnol.* **179**, 179-201, doi:10.1007/s12010-016-1987-x (2016).

60 Hofmann, A. F. The continuing importance of bile acids in liver and intestinal disease. *Arch. Intern. Med.* **159**, 2647-2658, doi:10.1001/archinte.159.22.2647 (1999).

61 Yu, J. N. *et al.* Enhancement of oral bioavailability of the poorly water-soluble drug silybin by sodium cholate/phospholipid-mixed micelles. *Acta. Pharmacol. Sin.* **31**, 759-764, doi:10.1038/aps.2010.55 (2010).

62 Dressman, J. B. & Reppas, C. In vitro-in vivo correlations for lipophilic, poorly water-soluble drugs. *Eur. J. Pharm. Sci.* **11 Suppl 2**, S73-80, doi:10.1016/s0928-0987(00)00181-0 (2000).

63 Bates, T. R., Gibaldi, M. & Kanig, J. L. Rate of dissolution of griseofulvin and hexoestrol in bile salt solutions. *Nature* **210**, 1331-1333, doi:10.1038/2101331a0 (1966).

64 Kawai, Y. *et al.* Profiling and trend analysis of food effects on oral drug absorption considering micelle interaction and solubilization by bile micelles. *Drug Metab Pharmacokinet* **26**, 180-191, doi:10.2133/dmpk.dmpk-10-rg-098 (2011).

65 Schlauersbach, J. *et al.* Predicting Bile and Lipid Interaction for Drug Substances. *Mol Pharm* **19**, 2868-2876, doi:10.1021/acs.molpharmaceut.2c00227 (2022).

66 Dahlgren, D. *et al.* Fasted and fed state human duodenal fluids: Characterization, drug solubility, and comparison to simulated fluids and with human bioavailability. *Eur J Pharm Biopharm* **163**, 240-251, doi:10.1016/j.ejpb.2021.04.005 (2021).

67 Ashby, K. *et al.* Review article: therapeutic bile acids and the risks for hepatotoxicity. *Aliment Pharmacol Ther* **47**, 1623-1638, doi:10.1111/apt.14678 (2018).

68 Small, D. M. The Enterohepatic Circulation of Bile Salts. *Archives of Internal Medicine* **130**, doi:10.1001/archinte.1972.03650040078008 (1972).

69 Westergaard, H. Bile Acid malabsorption. *Curr Treat Options Gastroenterol* **10**, 28-33, doi:10.1007/s11938-007-0054-7 (2007).

70 Shearer, M. J. Vitamin K in parenteral nutrition. *Gastroenterology* **137**, 105-118, doi:10.1053/j.gastro.2009.08.046 (2009).

71 Vanderpas, J. B. *et al.* Malabsorption of liposoluble vitamins in a child with bile acid deficiency. *J Pediatr Gastroenterol Nutr* **6**, 33-41, doi:10.1097/00005176-198701000-00007 (1987).

72 Klein, S. The use of biorelevant dissolution media to forecast the in vivo performance of a drug. *AAPS J* **12**, 397-406, doi:10.1208/s12248-010-9203-3 (2010).

73 Dressman, J. B., Amidon, G. L., Reppas, C. & Shah, V. P. Dissolution testing as a prognostic tool for oral drug absorption: immediate release dosage forms. *Pharm Res* **15**, 11-22, doi:10.1023/a:1011984216775 (1998).

74 Lemos, H. d., Prado, L. D. & Rocha, H. V. A. Use of biorelevant dissolution media in dissolution tests as a predictive method of oral bioavailability. *Brazilian Journal of Pharmaceutical Sciences* **58**, doi:10.1590/s2175-97902022e19759 (2022).

75 Clulow, A. J. *et al.* Characterization of Solubilizing Nanoaggregates Present in Different Versions of Simulated Intestinal Fluid. *J Phys Chem B* **121**, 10869-10881, doi:10.1021/acs.jpcb.7b08622 (2017).

76 Riethorst, D. *et al.* An In-Depth View into Human Intestinal Fluid Colloids: Intersubject Variability in Relation to Composition. *Mol Pharm* **13**, 3484-3493, doi:10.1021/acs.molpharmaceut.6b00496 (2016).

77 Suriano, F., Nystrom, E. E. L., Sergi, D. & Gustafsson, J. K. Diet, microbiota, and the mucus layer: The guardians of our health. *Front Immunol* **13**, 953196, doi:10.3389/fimmu.2022.953196 (2022).

78 Paone, P. & Cani, P. D. Mucus barrier, mucins and gut microbiota: the expected slimy partners? *Gut* **69**, 2232-2243, doi:10.1136/gutjnl-2020-322260 (2020).

79 Winkeljann, B., Boettcher, K., Balzer, B. N. & Lieleg, O. Mucin Coatings Prevent Tissue Damage at the Cornea-Contact Lens Interface. *Advanced Materials Interfaces* **4**, doi:10.1002/admi.201700186 (2017).

80 Bansil, R. & Turner, B. S. Mucin structure, aggregation, physiological functions and biomedical applications. *Current Opinion in Colloid & Interface Science* **11**, 164-170, doi:10.1016/j.cocis.2005.11.001 (2006).

81 Boegh, M. & Nielsen, H. M. Mucus as a barrier to drug delivery - understanding and mimicking the barrier properties. *Basic Clin Pharmacol Toxicol* **116**, 179-186, doi:10.1111/bcpt.12342 (2015).

82 Witten, J., Samad, T. & Ribbeck, K. Selective permeability of mucus barriers. *Curr Opin Biotechnol* **52**, 124-133, doi:10.1016/j.copbio.2018.03.010 (2018).

83 Lieleg, O. & Ribbeck, K. Biological hydrogels as selective diffusion barriers. *Trends Cell Biol* **21**, 543-551, doi:10.1016/j.tcb.2011.06.002 (2011).

84 Johansson, M. E., Sjovall, H. & Hansson, G. C. The gastrointestinal mucus system in health and disease. *Nat Rev Gastroenterol Hepatol* **10**, 352-361, doi:10.1038/nrgastro.2013.35 (2013).

85 Bansil, R. & Turner, B. S. The biology of mucus: Composition, synthesis and organization. *Adv Drug Deliv Rev* **124**, 3-15, doi:10.1016/j.addr.2017.09.023 (2018).

86 Barmpatsalou, V. *et al.* Physiological properties, composition and structural profiling of porcine gastrointestinal mucus. *Eur J Pharm Biopharm* **169**, 156-167, doi:10.1016/j.ejpb.2021.10.008 (2021).

87 Witten, J., Samad, T. & Ribbeck, K. Molecular Characterization of Mucus Binding. *Biomacromolecules* **20**, 1505-1513, doi:10.1021/acs.biomac.8b01467 (2019).

88 Murgia, X., Loretz, B., Hartwig, O., Hittinger, M. & Lehr, C. M. The role of mucus on drug transport and its potential to affect therapeutic outcomes. *Adv Drug Deliv Rev* **124**, 82-97, doi:10.1016/j.addr.2017.10.009 (2018).

89 Lai, S. K., Wang, Y. Y. & Hanes, J. Mucus-penetrating nanoparticles for drug and gene delivery to mucosal tissues. *Adv Drug Deliv Rev* **61**, 158-171, doi:10.1016/j.addr.2008.11.002 (2009).

90 Round, A. N. *et al.* Lamellar structures of MUC2-rich mucin: a potential role in governing the barrier and lubricating functions of intestinal mucus. *Biomacromolecules* **13**, 3253-3261, doi:10.1021/bm301024x (2012).

91 Sigurdsson, H. H., Kirch, J. & Lehr, C. M. Mucus as a barrier to lipophilic drugs. *Int J Pharm* **453**, 56-64, doi:10.1016/j.ijpharm.2013.05.040 (2013).

92 Huang, J. X. *et al.* Mucin Binding Reduces Colistin Antimicrobial Activity. *Antimicrob Agents Chemother* **59**, 5925-5931, doi:10.1128/AAC.00808-15 (2015).

93 Larhed, A. W., Artursson, P., Grasjo, J. & Bjork, E. Diffusion of drugs in native and purified gastrointestinal mucus. *J Pharm Sci* **86**, 660-665, doi:10.1021/js960503w (1997).

94 Larhed, A. W., Artursson, P. & Bjork, E. The influence of intestinal mucus components on the diffusion of drugs. *Pharm Res* **15**, 66-71, doi:10.1023/a:1011948703571 (1998).

95 Bandi, S. P., Bhatnagar, S. & Venuganti, V. V. K. Advanced materials for drug delivery across mucosal barriers. *Acta Biomater* **119**, 13-29, doi:10.1016/j.actbio.2020.10.031 (2021).

96 Shaikh, R., Raj Singh, T. R., Garland, M. J., Woolfson, A. D. & Donnelly, R. F. Mucoadhesive drug delivery systems. *J Pharm Bioallied Sci* **3**, 89-100, doi:10.4103/0975-7406.76478 (2011).

97 Lai, S. K., Wang, Y. Y., Wirtz, D. & Hanes, J. Micro- and macrorheology of mucus. *Adv Drug Deliv Rev* **61**, 86-100, doi:10.1016/j.addr.2008.09.012 (2009).

98 Lai, S. K. *et al.* Rapid transport of large polymeric nanoparticles in fresh undiluted human mucus. *Proc Natl Acad Sci U S A* **104**, 1482-1487, doi:10.1073/pnas.0608611104 (2007).

99 Bajka, B. H., Rigby, N. M., Cross, K. L., Macierzanka, A. & Mackie, A. R. The influence of small intestinal mucus structure on particle transport ex vivo. *Colloids Surf B Biointerfaces* **135**, 73-80, doi:10.1016/j.colsurfb.2015.07.038 (2015).

100 Kirch, J. *et al.* Optical tweezers reveal relationship between microstructure and nanoparticle penetration of pulmonary mucus. *Proc Natl Acad Sci U S A* **109**, 18355-18360, doi:10.1073/pnas.1214066109 (2012).

101 Yildiz, H. M., McKelvey, C. A., Marsac, P. J. & Carrier, R. L. Size selectivity of intestinal mucus to diffusing particulates is dependent on surface chemistry and exposure to lipids. *J Drug Target* **23**, 768-774, doi:10.3109/1061186X.2015.1086359 (2015).

102 Macierzanka, A. *et al.* Adsorption of bile salts to particles allows penetration of intestinal mucus. *Soft Matter* **7**, doi:10.1039/c1sm05888f (2011).

103 Li, X. *et al.* Novel mucus-penetrating liposomes as a potential oral drug delivery system: preparation, in vitro characterization, and enhanced cellular uptake. *Int J Nanomedicine* **6**, 3151-3162, doi:10.2147/IJN.S25741 (2011).

104 Friedl, H. *et al.* Development and evaluation of a novel mucus diffusion test system approved by self-nanoemulsifying drug delivery systems. *J Pharm Sci* **102**, 4406-4413, doi:10.1002/jps.23757 (2013).

105 Zhang, J. *et al.* Influence of microemulsion-mucin interaction on the fate of microemulsions diffusing through pig gastric mucin solutions. *Mol Pharm* **12**, 695-705, doi:10.1021/mp500475y (2015).

106 Sogias, I. A., Williams, A. C. & Khutoryanskiy, V. V. Why is chitosan mucoadhesive? *Biomacromolecules* **9**, 1837-1842, doi:10.1021/bm800276d (2008).

107 Sheffner, A. L. The reduction in vitro in viscosity of mucoprotein solutions by a new mucolytic agent, N-acetyl-L-cysteine. *Ann N Y Acad Sci* **106**, 298-310, doi:10.1111/j.1749-6632.1963.tb16647.x (1963).

108 Srinivasan, S. S. *et al.* RoboCap: Robotic mucus-clearing capsule for enhanced drug delivery in the gastrointestinal tract. *Sci Robot* **7**, eabp9066, doi:10.1126/scirobotics.abp9066 (2022).

109 Bode, G. *et al.* The utility of the minipig as an animal model in regulatory toxicology. *J Pharmacol Toxicol Methods* **62**, 196-220, doi:10.1016/j.vascn.2010.05.009 (2010).

110 van der Laan, J. W. *et al.* Regulatory acceptability of the minipig in the development of pharmaceuticals, chemicals and other products. *J Pharmacol Toxicol Methods* **62**, 184-195, doi:10.1016/j.vascn.2010.05.005 (2010).

111 Krupa, L. *et al.* Comparing the permeability of human and porcine small intestinal mucus for particle transport studies. *Sci Rep* **10**, 20290, doi:10.1038/s41598-020-77129-4 (2020).

Chapter 1: Drug-induced dynamics of bile colloids

Simon Hanio[1,#], Jonas Schlauersbach[1,#], Bettina Lenz[1], Franziska Spiegel[2], Rainer A. Böckmann[2], Ralf Schweins[3], Ivo Nischang[4,5], Ulrich S. Schubert[4,5], Sebastian Endres[6], Ann-Christin Pöppler[6], Ferdinand P. Brandl[7], Theo M. Smit[7], Karl Kolter[7], Lorenz Meinel[1,8]

[1] Institute for Pharmacy and Food Chemistry, University of Wuerzburg, Am Hubland, 97074 Wuerzburg, Germany
[2] Computational Biology, Friedrich Alexander-University Erlangen-Nürnberg, Staudtstrasse 5, 91057 Erlangen, Germany
[3] Institut Laue-Langevin, DS/LSS, 71 Avenue des Martyrs, CS 20 156, 38042 Grenoble CEDEX 9, France
[4] Laboratory of Organic and Macromolecular Chemistry (IOMC), Friedrich Schiller University Jena, Humboldtstrasse 10, 07743 Jena, Germany
[5] Jena Center for Soft Matter (JCSM), Friedrich Schiller University Jena, Philosophenweg 7, 07743 Jena, Germany
[6] Institute of Organic Chemistry, University of Wuerzburg, Am Hubland, 97074 Wuerzburg, Germany
[7] BASF SE, R&D Pharma Ingredients, 67063 Ludwigshafen, Germany
[8] Helmholtz Institute for RNA-based Infection Research (HIRI), Josef-Schneider-Strasse 2, 97080 Wuerzburg, Germany
[#] These authors contributed equally to this work.

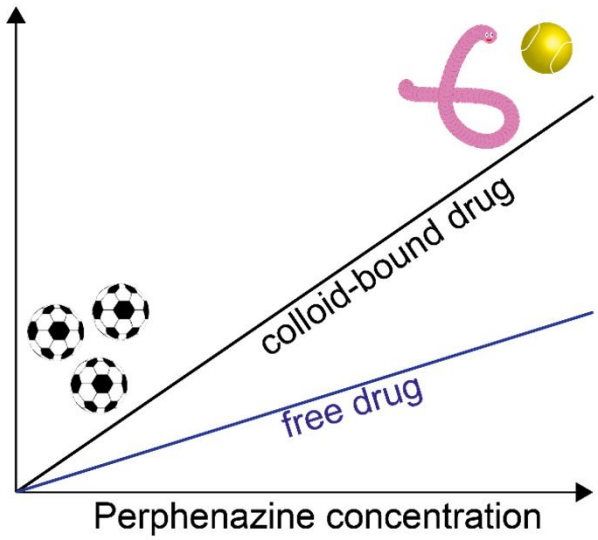

This chapter was originally published in Langmuir. Reprinted with permission from Hanio S., et al. Langmuir, vol. 37, issue 8, pp. 2543-2551, 2021; DOI: 10.1021/acs.langmuir.0c02282.

Abstract

Bile colloids containing taurocholate and lecithin are essential for the solubilization of hydrophobic molecules including poorly water-soluble drugs such as Perphenazine. We detail the impact of Perphenazine concentrations on taurocholate/lecithin colloids using analytical ultracentrifugation, dynamic light scattering, small-angle neutron scattering, nuclear magnetic resonance spectroscopy, coarse-grained molecular dynamics simulations, and isothermal titration calorimetry. Perphenazine impacted colloidal molecular arrangement, structure, and binding thermodynamics in a concentration-dependent manner. At low concentration, Perphenazine was integrated into stable and large taurocholate/lecithin colloids and close to Lecithin. Integration of Perphenazine into these colloids was exothermic. At higher Perphenazine concentration, the taurocholate/lecithin colloids had an approximately five-fold reduction in apparent hydrodynamic size, heat release was less exothermic upon drug integration into the colloids, and Perphenazine interacted with both, lecithin and taurocholate. In addition, Perphenazine induced a morphological transition from vesicles to wormlike micelles as indicated by neutron scattering. Despite these surprising colloidal dynamics, these natural colloids successfully ensured stable relative amounts of free Perphenazine throughout the entire drug concentration range tested here. Future studies are required to further detail these findings both on a molecular structural basis and in terms of in vivo relevance.

Introduction

Bile salts are amphiphilic surfactants stored and released from the gallbladder into the duodenum along with other bile components such as electrolytes, organic anions, cholesterol, and lecithin.[1, 2] During gastrointestinal (GIT) transit, bile salts are reabsorbed up to 95%, particularly in the terminal ileum.[3] Bile resulting colloids solubilize hydrophobic molecules in the GIT[4-6], mediating systemic availability of essential fats and fat-soluble vitamins.[7] Hence, bile colloids solubilize and are important for systemic availability of poorly water-soluble drugs (PWSDs).[8, 9] PWSD solubility and dissolution rate may be impacted by bile colloids affecting intestinal absorption.[10-12] Bile salts are hydroxylated derivatives of cholesterol displaying amphiphilic patterns through planar, polar and hydrophobic surfaces, with the planar design contrasting the polar head - hydrophobic tail design of pharmaceutical surfactants.[13, 14] Bile salts show specific aggregation patterns in water, e.g. by back-to-back dimerization.[15-18]

The impact of bile on solubilization and gastrointestinal absorption of PWSD is frequently approximated by defined artificial media containing taurocholate (TC) and lecithin (L).[19] Previous studies detailed the geometrical and molecular adaptation of bile colloids in general[16, 20-25] but rarely as a function of PWSD concentration.[26, 27] One previous study detailed the drug concentration-dependent formation of two different types of TC/drug mixed micelles next to TC/L colloids.[26] In contrast, concentration-dependent morphological changes of TC/L colloids were observed for the PWSD Imatinib.[27] One yet unaddressed key aspect of these colloidal adaptations to PWSD concentration is the resulting amount of molecularly dissolved or free PWSD which, at least in instances of passive absorption, correlates with the flux across the GIT epithelial barrier.[28] Consequently, the geometrical and molecular interaction of bile colloids at different PWSD concentrations and its impact on the amount of free and colloid-bound drug are of immediate pharmaceutical relevance. In addition, knowledge of drug-induced changes in colloidal structures may further refine predictions of pharmacokinetic profiles[29, 30], in particular for PWSD with bile affected bioavailability.[31] We hypothesize that taking advantage of the dynamics of our endogenous solubilization system will be beneficial to tackle the challenging oral uptake of PWSD.[28, 32-35]

Here, we study the concentration-dependent impact of the PWSD Perphenazine (P) – a first-generation antipsychotic drug[36] – on mixed TC/L colloids formed by the widely used, standardized Fasted State Simulated Intestinal Fluid-V1 (FaSSIF-V1). P was selected from a set of 30 drug substances (data not shown) being one of the candidates with high affinity to the mixed TC/L colloids. Molecular and structural interactions were characterized by ^{1}H Nuclear Magnetic Resonance (^{1}H NMR) spectroscopy and 1D selective Nuclear Overhauser

enhancement spectroscopy (NOESY). Furthermore, colloidal dynamics, drug distribution into TC/L colloids, and resulting free PWSD were studied by analytical ultracentrifugation (AUC), dynamic light scattering (DLS), zeta potential measurements, small-angle neutron scattering (SANS) and further detailed thermodynamically by isothermal titration calorimetry (ITC). The integration of Perphenazine into the mixed TC/L colloids was further studied by coarse-grained molecular dynamics simulations.

Experimental Section

Materials

FaSSIF powder was purchased from Biorelevant.com (London, UK). Deionized, purified water (Millipore water) was generated by a Millipore purification system from Merck (Darmstadt, Germany). Perphenazine (99%), deuterated water (D_2O, 99.9% D) containing 0.05% 3-(trimethylsilyl)propionic-2,2,3,3-d_4 sodium salt (TSP-d_4), 40% sodium deuteroxide in deuterated water (NaOD, 99% D), 35% deuterium chloride in deuterated water (DCl, 99% D), sodium chloride (99%), and monobasic sodium phosphate monohydrate (99%) were purchased from Merck. Hexadeuteriodimethyl sulfoxide (DMSO-d_6, 99.8% D) was purchased from Euriso-top (Saarbrücken, Germany) and deuterated water (D_2O, 99.9% D) from Deutero (Kastellaun, Germany). All other standard chemicals and laboratory consumables, if not otherwise stated, were purchased from either VWR International GmbH (Ismaning, Germany) or Merck.

Media preparation

Modified phosphate buffered saline with a pH value of 6.5 (hereinafter referred to as PBS – identical with FaSSIF-V1 without taurocholate and lecithin) and FaSSIF-V1 (hereinafter referred to as FaSSIF) were prepared according to the protocol of Biorelevant.com. For AUC, DLS, equilibrium solubility determination, ITC, UV-Vis and zeta potential measurements Millipore water, and for NMR and SANS measurements deuterated water, was used. As described before, pD of PBS in deuterated water was adjusted using a previously reported correction factor and DCl and NaOD.[37]

Sample preparation for NMR, zeta potential, AUC, DLS, UV-Vis, and SANS

Amber vials and glassware were used for Perphenazine samples and light protection was ensured by aluminum foil wrapping. DMSO stock solutions of Perphenazine were added to FaSSIF to achieve a nominal drug concentration of up to 0.5 mM, and a maximum of 1.0% (v/v) DMSO. Deuterated DMSO was used for NMR experiments. Samples with respective medium (PBS or FaSSIF) were shaken for 120 min, at a temperature of 298 K, with a shaking

speed of 750 rpm on a Thermomixer F1.5 (Eppendorf, Hamburg, Germany), followed by an equilibration phase for 180 min, at a temperature of 298 K without shaking.

NMR spectroscopy

^{1}H NMR spectra were recorded on a Bruker Avance 400 MHz spectrometer (Karlsruhe, Germany) operating at 400.13 MHz with a BBI BB-H 5 mm probe head and at a temperature of 300 K. For ^{1}H NMR, acquisition parameters were set to 1024 scans with 32 dummy scans, a flip angle of 30°, a spectral width of 20.55 ppm, and a transmitter offset of 6.175 ppm. The acquisition time was 3.985 s followed by a relaxation delay of 1.0 s and collecting 64,000 data points at a sample spinning frequency of 20 Hz. Data was processed with TopSpin 4.0.6 (Bruker BioSpin). An exponential line broadening window function of 0.3 Hz was applied. An automatic baseline correction and manual phasing was performed.

Selective NOESY NMR spectra were recorded at a temperature of 300 K on a Bruker Avance III HD 600 spectrometer operating at 600.13 MHz equipped with a DCH ^{13}C/^{1}H cryoprobe with z gradient, and by using the gradient enhanced pulse sequence "selnogp".[38] For 1D-NOESY spectra, the acquisition parameters were set to a spectral width of 22.04 ppm and a transmitter offset of 7.000 ppm. The acquisition time was 2.477 s followed by a relaxation delay of 0.2 s and collecting 65,536 data points. For the selective inversion a "Gaus1_180r.1000" shape was chosen. Pulse powers and lengths were calculated using the "selau" program. The quality of the selective excitation was confirmed by recording a proton spectrum using the "selgpse" pulse program. For 0.1 mM Perphenazine in FaSSIF, the excitation frequency was set to 7.04 ppm with an excitation range of 456 Hz. For 0.5 mM Perphenazine in FaSSIF, the excitation frequency was set to 6.99 ppm with an excitation range of 399 Hz. The mixing times were chosen at a time of 20 ms, 40 ms, and 60 ms to rule out that spin diffusion interferes with the measurements.

Zeta potential measurements

Zeta potential measurements were performed by electrophoretic light scattering using Delsa Nano HC particle analyzer (Beckman Coulter, Brea, CA) using a pinhole of 50 µm and a scattering angle of 15 ° at a temperature of 298 K. Samples were tested in a flow cell at a fixed voltage of 60 V and a base frequency of 115-140 Hz. All measurements were performed in triplicate. Each measurement consisted of 10 accumulations at five cell positions (0.70, 0.35, 0.00, -0.35, -0.70 mm) and three repetitions each. The zeta potential was calculated by the conversion equation of Smoluchowski using a dynamic viscosity of 0.9227 mPas and a refractive index of 1.333 as measured for FaSSIF and an assumed dielectric constant of 78.5. Density and viscosity were determined using an Automated Microviscometer (Anton Paar, Graz, Austria) at a temperature of 298. The refractive index of FaSSIF was measured by an

Abbe refractometer from Carl Zeiss (Oberkochen, Germany) at a temperature of 298 K. System performance was ensured by using polystyrene latex particles from Otsuka Electronics Co., Ltd. (Osaka, Japan).

Molecular dynamics

Molecular dynamics (MD) simulations were performed using the GROMACS 2020.1 software package[39, 40] and the Martini force field version 2.2.[41] The starting system was a cubic box with side lengths of 25 nm filled with non-polarizable Martini water, to which lecithin (L, i.e. 1-Palmitoyl-2-linoleoylphosphatidylcholine, or PIPC), taurocholate (TC) and Perphenazine (P) were added to randomly chosen positions replacing as many water molecules as needed. Two systems were set up, the first containing 1,250 L and 185 TC molecules. Starting from a random distribution of L and TC at concentrations of ≈ 150 mM and ≈ 23 mM, respectively, the formation of mixed vesicles was followed in ten independent simulations of 10 μs length each in the first system. The concentration and number of L molecules were chosen to allow for the formation of vesicles with a radius of ca. 7-10 nm. The TC:L ratio in the simulation system was reduced with respect to FaSSIF in order to take the increased membrane binding of TC in CG simulations into account. The second system additionally contained 90 randomly distributed P molecules (≈ 11 mM) and was studied conducting twenty simulations of 10 μs length each. Owing to the negative total charge of taurocholate, NA+ particles were added to neutralize the system. Periodic boundary conditions were applied.

For initial energy minimization, 5,000 steps of the steepest descent algorithm were performed, followed by equilibration runs with increasing time steps, starting at 1 fs to 20 fs. Production runs were performed at 320 K and 1 bar for 10 μs with a time step of Δt = 20 fs. Temperature and pressure coupling were achieved using the v-rescale thermostat and the isotropic Parrinello-Rahman pressure coupling scheme with coupling constants τ_T = 1.0 ps and τ_P = 12.0 ps.

The topology of L was taken from the Martini website (PIPC, cgmartini.nl). For TC, a model adapted from the Martini cholesterol topology was used as previously reported[42]: Starting from cholesterol, one SC1 and one SC3 Martini bead were replaced by two SP1 particles to model the effect of the additional hydroxyl groups in TC. An additional Qa particle was introduced to model the taurine group.[42] Here, we additionally changed the CG particle preceding the taurine from C1 to P3 (**Figure S1A**). For the parameterization of P (**Figure S1B**), the CHARMM-GUI Ligand Reader & Modeler[43] was used to obtain initial all-atom coordinates that were mapped to a coarse-grained representation according to the four-to-one mapping rule of heavy atoms in Martini. Bonds, angles, dihedrals and force constants

were manually adapted to generate stable starting structures for the simulations. To prevent excessive self-aggregation of P in the Martini model, the Lennard-Jones potential for the SC4 and SC5 beads within the phenothiazine ring-system was chosen to be semi-repulsive.

Equilibrium solubility determination

The equilibrium solubility of Perphenazine was determined by the shake flask method. 4 to 5 mg of Perphenazine was weighed into a 2.0 mL amber reaction vial, and 1.5 mL of PBS or FaSSIF were added. Samples were shaken with respective medium (PBS or FaSSIF) for 24 h at a temperature of 298 K and a shaking speed of 750 rpm on a Thermomixer F1.5. After shaking, samples were centrifuged at 13,400 rpm for 10 min with a MiniSpin centrifuge (Eppendorf). The pH value was measured. Supernatants were afterward diluted 1:5 with acetonitrile (ACN, 99.9%, v/v) containing 0.1% (v/v) trifluoroacetic acid (TFA). Measurements were performed in triplicate. Samples were analyzed on an Agilent 1260 infinity II HPLC (Waldbronn, Germany) using a Synergi 4 µm Hydro-RP18 80 Å 150 x 4.6 mm LC column (Phenomenex, Aschaffenburg, Germany). The device was equipped with a variable wavelength detector (G7114A, Agilent), an automatic vial sampler (G7129C, Agilent), a pump (G7104C, Agilent), and a multicolumn oven (G7116A, Agilent). Mobile phase A was Millipore water with 0.1% (v/v) TFA. Mobile phase B was ACN (99.9%, v/v) with 0.1% (v v) TFA. The flow was set to 1 mL/min, the injection volume was 50 µL, and the detector was set to a wavelength of λ = 255 nm. The linear gradient started at 20% ACN (v/v) in the mobile phase to 100% within 6 min. 100% ACN was held constant for 4 min, and then the mobile phase composition was adjusted back to 20% ACN in the mobile phase within 1 min. After a 4 min column equilibration time, the next elution experiment was started.

AUC

Sedimentation velocity AUC experiments were performed with an OPTIMA XL-I AUC (Beckman Coulter) utilizing a refractive index and absorbance detector, and an eight-hole rotor (An-50 Ti) operated at a speed of 42,000 rpm. The ultracentrifuge cells contained double-sector epon centerpieces and were equipped with sapphire windows. The optical path length of the solution in the cells for detection was 12 mm. The ultracentrifuge cells were filled with 420 µL of sample solution and with 440 µL of solvent PBS in the reference sector. Pure FaSSIF as well as Perphenazine solutions in FaSSIF were investigated. Next to universal refractive index detection, the wavelength of the absorbance optical detection system was set to λ = 309 nm, being representative of Perphenazine. A different wavelength was used for detection here as in the HPLC experiments based on AUC pilot experiments. These demonstrated that at this wavelength Perphenazine quantification was possible over the entire drug concentration range while in presence of taurocholate and lecithin.

Sedimentation velocity experiments were performed for a typical 24 h with a radial sedimentation profile scan acquired every three minutes. Sedimentation velocity data were analyzed with Sedfit using the ls-g*(s) model, i.e. by least squares boundary modeling by assuming non-diffusing species.[44] Results from this model can be considered representative of the average velocities of sedimentation boundaries, in agreement to more detailed modelling.[45]

DLS

DLS experiments were performed with a DelsaNanoHC particle analyzer from Beckman Coulter with the backscattering monitored at an angle of 165°. The unfiltered samples were measured in disposable 1.5 mL UV-Cuvettes (Brand, Wertheim, Germany) in triplicate with an accumulation of 70 scans. Data was analyzed by the CUMULANT method.[46] The Z-average hydrodynamic size was evaluated with a refractive index of 1.333 for all samples which was determined for FaSSIF using an Abbe refractometer (Carl Zeiss, Oberkochen, Germany). The hydrodynamic diameter was calculated using a dynamic viscosity of 0.9227 mPas for FaSSIF. Density and viscosity were determined using an Automated Microviscometer (Anton Paar, Graz, Austria). Measurements were performed at a temperature of 298 K for all experiments, i.e. identical to the AUC measurements.

UV-Vis measurements

Samples were measured in standard quartz cuvettes with a solution path length of 1 cm. Extinction was measured on an Evolution 201 UV-Visible Spectrophotometer from ThermoFisher Scientific (Waltham, MA) at a wavelength of $\lambda = 499$ nm to detect scattering. The baseline was normalized according to the solvent PBS. Measurements were carried out in triplicate. In addition, a full spectrum of 0.15 mM Perphenazine in PBS was recorded (**Figure S2**).

SANS

SANS experiments were performed with the D11 SANS instrument at the Institut Laue – Langevin (ILL, Grenoble, France).[47] Three instrument configurations were employed at a fixed neutron wavelength of 6 Å and a full width at half maximum of 9%. The sample-detector distances were 1.4 m, 8 m, and 39 m with collimation distances of 8 m, 8 m, and 40.5 m, respectively. Thus, a wide range of momentum transfer q from 0.002 1/Å to 0.4 1/Å was covered, with q being the range of momentum transfer which depends on both the scattering angle 2θ as well as the neutron wavelength λ according to $q = 4*\pi*\sin(\theta)/\lambda$. The neutron beam footprint was 15 mm in diameter, and the samples were confined in Hellma cuvettes of type 120-QS with a path length of 2 mm. Scattered intensities were recorded with

^{3}He MWPC detector (CERCA) with 256 x 256 pixels of 3.75 mm x 3.75 mm pixel size. The data sets were reduced using the facility provided software LAMP, put on absolute scale using a 1 mm H_2O cuvette as secondary calibration standard ($d\Sigma/d\Omega$ = 0.983 1/cm) and azimuthally averaged. The scattering curves of pure FaSSIF and of 0.3 mM Perphenazine in FaSSIF were recorded. The solvent scattering has been measured and subtracted from the sample data. The data were fitted using the SasView software package (www.sasview.org) and the instrumental resolution has been taken into account.

ITC

Thermodynamic signatures were studied using an iTC 200 (GE Healthcare, Buckinghamshire, UK). The cell was filled with 200 µL FaSSIF and 37.7 µL of 2.4 mM Perphenazine in FaSSIF were injected to the measurement cell in steps of 1.5 µL within 3 s time intervals and at intervals of 300 s, all at a temperature of 298 K and stirring in the cell at 300 rpm. The first delivery had a volume of 0.2 µL, with a followed injection after 150 s, by lasting 0.4 s. As good practice, the first injection was excluded from the analysis to minimize cell system equilibration artefacts.[48] As a blank, titration of FaSSIF into FaSSIF was utilized. Another titration was performed. Here, a tenfold concentrated FaSSIF (30 mM TC and 7.5 mM L in PBS) was added to PBS aiming at addressing thermodynamics of colloid dynamics. In addition, a fourth titration was conducted in which 2.4 mM Perphenazine in FaSSIF was added gradually to 0.35 mM Perphenazine in FaSSIF in order to cover the entire concentration range studied here. The ITC data were analyzed using the Microcal Origin 7.0552 software (OriginLab Corporation, Northampton, MA).

Statistics

Differences in Z-average hydrodynamic sizes between measurements and zeta potentials were analyzed by a one-way ANOVA followed by *post hoc* Tukey test. Solubility comparisons were done by Student's *t*-test; *p*-values ≤ 0.05 were considered statistically significant.

Results and Discussion

A ^{1}H NMR reference spectrum of Fasted State Simulating Intestinal Fluid (FaSSIF), consisting of 3.0 mM taurocholate (TC; **Figure 1A**) and 0.75 mM lecithin (L; **Figure 1B**) in phosphate-buffered saline (PBS) at pH 6.5 (**Figure 1C**) was recorded.[27] Perphenazine (P; **Figure 1D**) signals were assigned (**Figure 1E, S3**). P's aryl-proton signals broadened, shifted to lower ppm values (chemical shift is referred to as δ) and decreased in intensity with TC/L colloids present when compared to PBS only, indicating P integration into the TC/L colloids. (**Figure 1F**).

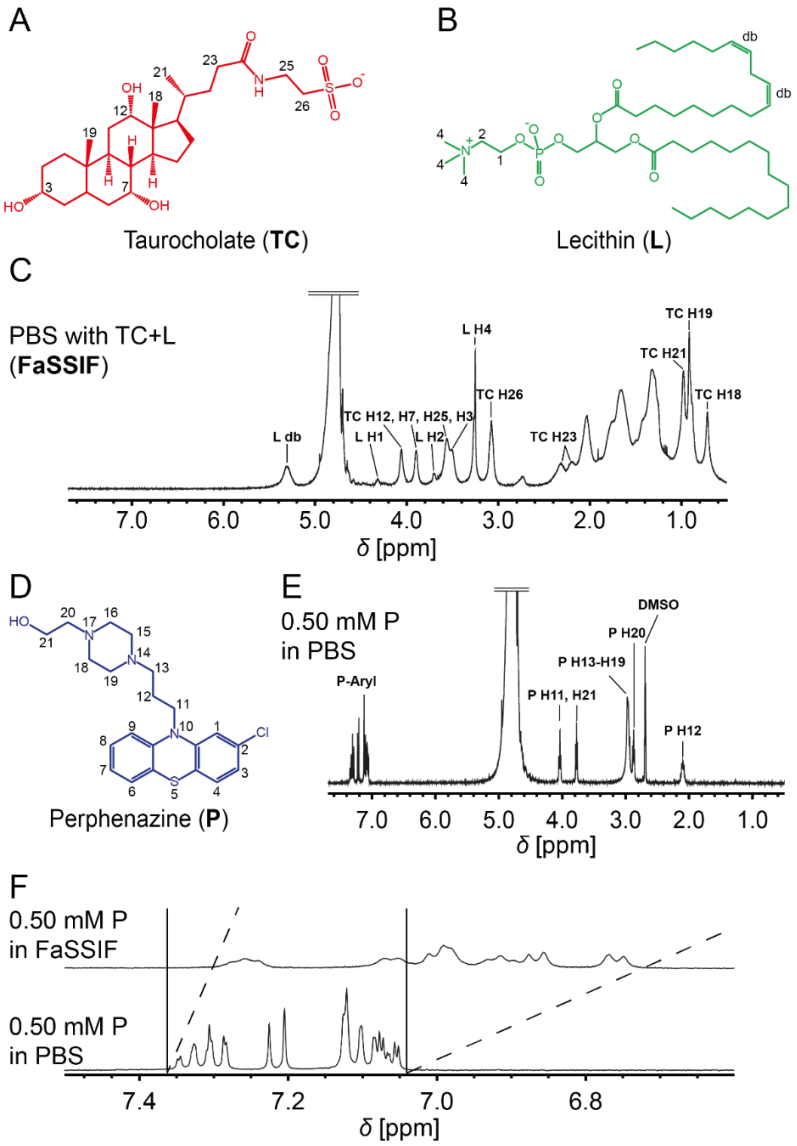

Figure 1: (A) Structure of taurocholate (TC) and (B) lecithin (L). (C) ^{1}H NMR spectrum of FaSSIF with signal assignment as previously reported.[27] (D) Structure of Perphenazine (P). (E) ^{1}H NMR spectrum of 0.5 mM Perphenazine in PBS with signal assignments. (F) Aryl-region of Perphenazine ^{1}H NMR spectra in FaSSIF (top) and PBS (bottom; dotted lines indicate shifts to lower ppm values).

We now studied the molecular interaction of TC/L colloids with increasing P concentration (**Figure 2A, S4**). Phosphatidylcholine (L H1/2) or olefinic proton (L db) signals were not shifted by P. All L signals sharpened particularly L H4. For TC, the methylene signals H23/25/26 sharpened at 0.5 mM P. Shifts to lower ppm values were observed for L H4 and TC H12/7/3 (**Figure S5**, zoom in Figure 2A), and TC H19/18 (**Figure S6**, zoom in Figure 2A). 1D selective NOESY NMR spectra with selective excitation of the P aryl-protons were recorded for 0.5 mM P (top) and 0.1 mM P (center) and are displayed with the FaSSIF assignments from Figure 2A as the reference (bottom; **Figure 2B, S7**). NOE signals arise from protons in close spatial proximity to P aryl-protons. At 0.5 mM P but not 0.1 mM P, we observed interaction of P's aryl-protons with L H4 (3.25 ppm), TC H26 (3.05 ppm), P-P self-interaction at P H13-H_20 (2.7 to 3.0 ppm), TC H23 (2.2 to 2.4 ppm) and TC H21/19/8 (0.6 to 1.0 ppm). Only at 0.1 mM P, broad unassigned NOE signals (2.5 to 3.5 ppm) and a solvent signal from HDO (4.8 ppm) occurred. At both concentrations, 0.1 mM and 0.5 mM, the following interactions were detailed. P's aryl-protons interacted with L db (5.3 ppm) and P-P self-interaction was observed at P H11/21 (3.7 to 4.1 ppm) while P's aryl-protons interacted with other unassigned L protons (1.2 to 1.4 ppm). To rule out effects of spin diffusion, spectra with three different, short mixing times were recorded. Spin diffusion was observed for the P-P interaction at 3.9 ppm only (**Figure S8, S9**).

The zeta potential of the mixed TC/L colloids formed in FaSSIF was -27.6 ± 0.8 mV (**Figure S10**) and in line with previous reports.[49] P loading up to 0.5 mM did not impact surface charge of the colloidal structures, possibly reflecting P integration into the colloids and away from their outer surface. In order to detail these finding, we performed coarse-grained (CG) molecular dynamics (MD) simulations. Resulting models suggested preferential binding of the bulky TC to the outer surface of the TC/L vesicles, which were formed after a simulation time of 1400 ns (**Figure S11**). P supplementation to these TC/L systems resulted in similar colloid shapes as compared to the drug-free systems. However, in contrast to TC, P preferentially bound to the inner vesicle leaflet, while L and TC orientation was virtually unchanged as compared to drug-free conditions. P was incorporated in the hydrophobic bilayer core with its polar piperacyl part pointing towards the lipid head groups while the phenothiazine ring was surrounded by the lipids' hydrocarbon chains (**Figure S12**). That said, P adopted the conformation of an inverted cone within the membrane, accomodating to the convex curvature of the inner leaflet. These modeling insights were experimentally supported by a stable zeta potential with increasing P (**Figure S10**). Furthermore, simulated positions were congruent with spectroscopic findings detailing the incorporation of P into the membrane of the mixed TC/L colloids and P's affinity to L (**Figure 1, 2, S12**).

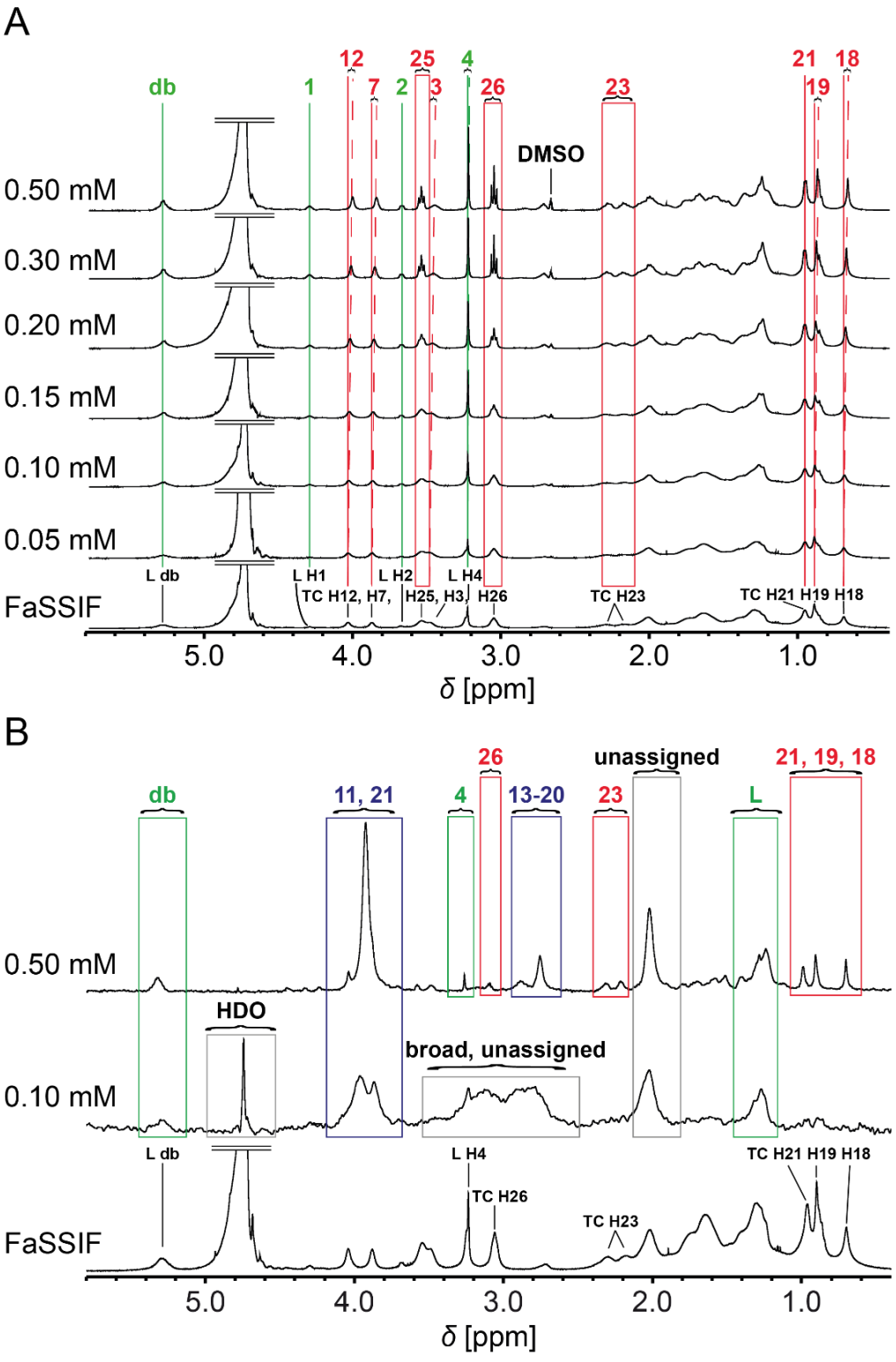

Figure 2: (A) Extracts from ^{1}H NMR spectra of TC/L colloids as a function of Perphenazine concentration. Red boxes (TC) and green lines (L) highlight signal sharpening for TC H25/26/23 and for L db, L H1/2/ 4, respectively. Red (TC) and green (L) dotted lines represent shifts to lower ppm values for TC H12/7/3/19/18 and L H4, respectively. (B) Extracts from 1D NOESY spectra of 0.1 mM and 0.5 mM Perphenazine concentration with TC/L with selective excitation at ca. 7 ppm and a mixing time of 60 ms colloids (^{1}H NMR spectrum of FaSSIF is from Figure 1C and used for reference; red, green, blue, and grey boxes indicate NOE signals for TC, L, P, and unassigned signals respectively).

Equilibrium solubility of P was 0.86 ± 0.19 mM in PBS and significantly increased to 2.46 ± 0.42 mM in FaSSIF. The pH value increased very slightly from 6.51 ± 0.01 to 6.54 ± 0.02 in PBS, and 6.72 ± 0.01 in FaSSIF, respectively. Previous studies linked PWSD solubilization into TC/L colloids to reduced passive transcellular permeation across the intestinal epithelial membrane.[28, 50]

We further studied the colloidal dynamics by AUC and DLS. Sedimentation velocity profiles were numerically approximated using SEDFIT and the least-squares boundary model without considering diffusion effects (ls-g*(s)).[44] Detection was performed by either the refractive index in terms of interference fringes or absorbance detector in terms of optical density (OD), also allowing colocalization of components in colloidal species.[51] The relative species concentrations were estimated by integration of differential distributions of sedimentation coefficients or, alternatively, by comparing the plateau intensities of sedimentation velocity scans among colloidal species. One example illustrating this approach was a two-step sedimentation profile reflecting two colloidal species as recorded for 0.2 mM P in FaSSIF (**Figure S13**). Either read-out - refractive index or absorbance detection – resulted in comparable outcome for the species sedimentation coefficient (**Figure S14**). We also confirmed that results were independent of the used cell (**Figure S15**), and confirmed the overall mass balance in the AUC cells as observed for P (**Figure S16**). One fraction of colloidal structures was observed in pure FaSSIF at about 25 S (**Figure 3A**), in line with previous reported analysis by flow field-flow fractionation.[52] At 0.05 mM P, one colloid species was identified at about 33 S. Further increase in P concentration to 0.20 mM resulted in larger colloidal structures (at about 49 S) coexisting with small colloids (at about 6 S). At 0.5 mM P, the larger colloidal structures disappeared and only small colloids were observed at about 4 S.

At ≤ 0.05 mM P, relatively large colloids were observed with apparent sedimentation coefficients between ca. 23 to 33 S (**Figure 3B**). At 0.05-0.25 mM P, large colloids were observed with ca. 30 to 47 S alongside with a small colloid fraction having sedimentation coefficients located at ca. 3-5 S. At ≥ 0.25 mM P, the large colloidal structures were entirely replaced by small colloidal structures with sedimentation coefficients of ca. 4–7 S. These geometrical adaptations were also studied by dynamic light scattering (DLS). Corroborating the AUC findings, the Z-average hydrodynamic diameter initially increased from 54.6 ± 3.3 nm (mean ± standard deviation of three independent measurements; PDI 0.022 ± 0.023) observed in FaSSIF to 70.0 ± 1.4 nm (PDI 0.103 ± 0.028) at 0.20 mM P (**Figure 3C**). At 0.30 mM P, a high polydispersity was recorded (PDI 0.246 ± 0.027, Figure **S17**) along with an up to approx. five-fold reduction in apparent hydrodynamic size at higher P concentrations.

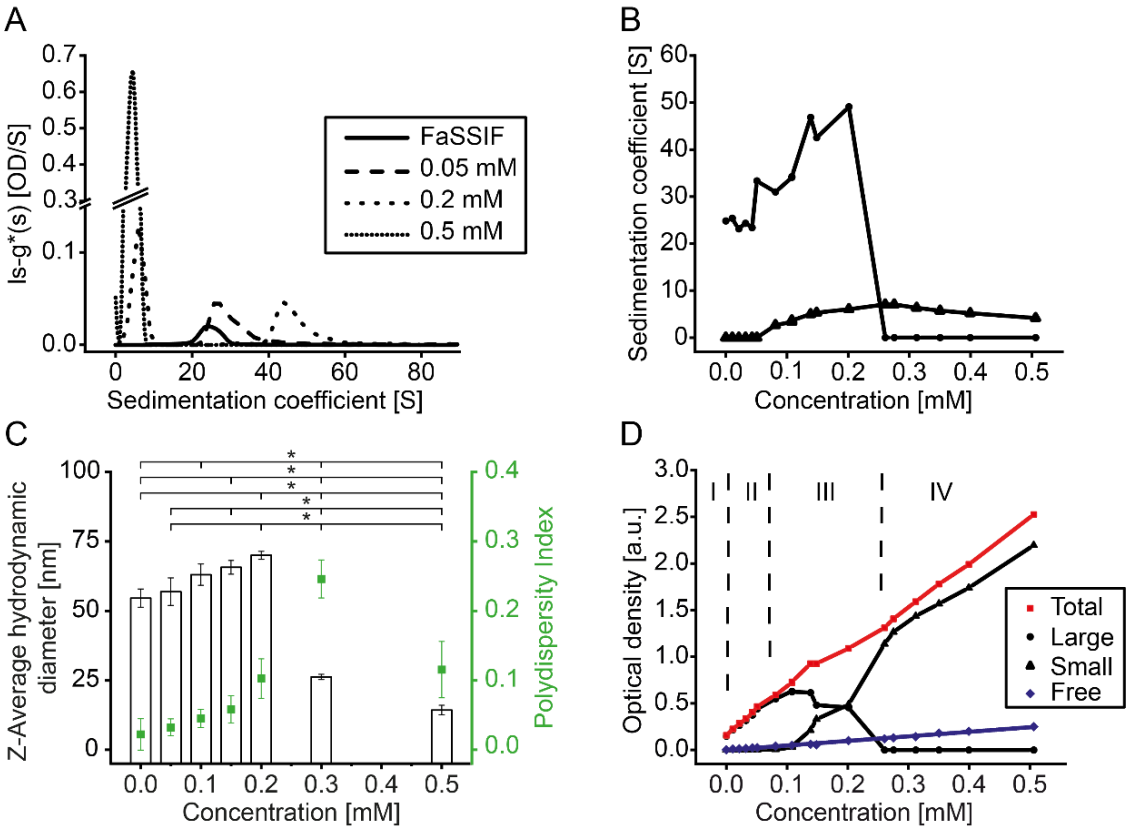

Figure 3: (A) Differential distribution of sedimentation coefficients, ls-g*(s), in FaSSIF at selected Perphenazine concentrations and (B) sedimentation coefficients of species throughout the overall Perphenazine concentration range as determined by analytical ultracentrifugation utilizing a wavelength of λ = 309 nm. (C) Z-Average hydrodynamic diameter from DLS with polydispersity index (PDI) in FaSSIF at different Perphenazine concentrations (mean ± SD, ANOVA followed by Tukey post-hoc pairwise comparison compared Z-average hydrodynamic diameters). (D) Apparent optical density (OD) at a wavelength of λ = 309 nm of different Perphenazine concentrations in the species mixtures determined by AUC and derived from the areas under the curve of differential distributions of sedimentation coefficients together with apparent total ODs (sum of all species). Total OD (red) and OD of free Perphenazine (blue) increased with the Perphenazine concentration.

The P concentration dependent decrease in colloidal size was also reflected by decreased light scattering probed at λ = 499 nm (**Figure S18**).

The amount of P was analyzed at λ = 309 nm in the various population fractions (**Figure 3D**). Initially, P did not impact the colloid size found in pure FaSSIF and distributed into these relatively large colloidal structures. Within the transition zone, characterized by coexistence of small and large colloids (0.05 mM-0.25 mM P), the location of P branched out into the small and large colloidal structures with about equal apparent concentration at 0.2 mM P, respectively (**Figure S13**).

We further detailed these AUC findings by SANS experiments, selecting two characteristic P concentrations, absence of P and 0.3 mM as of the high polydispersity seen in DLS experiments for the latter. For pure FaSSIF, the scattering curve fitted to a vesicle form factor

model with a core radius of 28.4 nm and a shell thickness of 2.75 nm (**Figure 4, Table 1**), corroborating previous reports.[22, 42] The core radius but not shell thickness – fitted to a lognormal distribution – was polydisperse. At 0.3 mM P, the scattering curve did not fit to a one-form model. The first minimum and maximum – although smeared – were located at a scattering vector q of ca. 0.01 1/Å and ca. 0.014 1/Å, respectively. Exceeding q values of ca. 0.02 1/Å changed the intensity decay and indicating elongated particles. The low q parts of the scattering curves were similar for pure FaSSIF and FaSSIF with 0.3 mM P, suggesting two distinct populations existing at 0.3 mM P, a vesicular one and an elongated one. The data was fitted using a sum of two form factor models, namely of vesicles and of elongated structures. For the latter we assumed a wormlike micellar structure (referred to as flexible cylinder in SasView). Such structures were previously reported for comparable systems.[22-25]

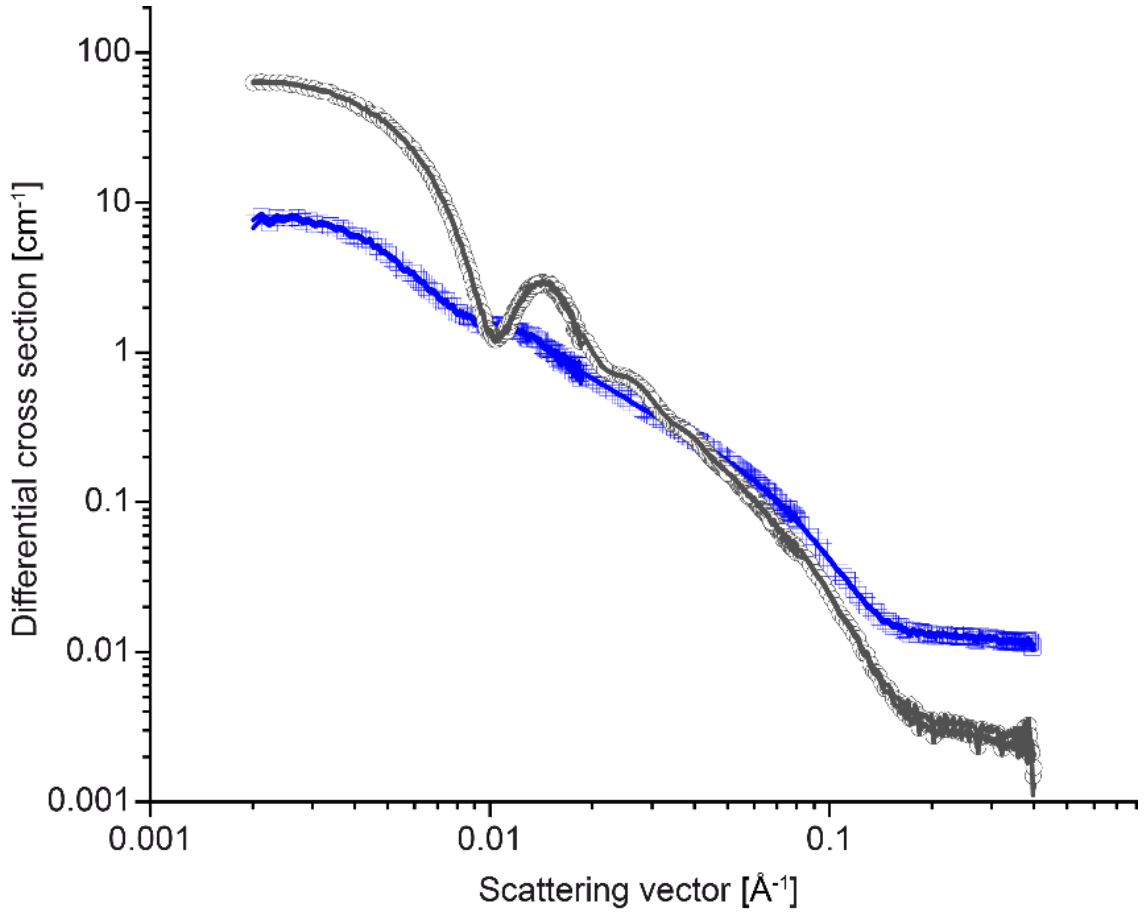

Figure 4: Experimental SANS profiles of pure FaSSIF (grey circles) and 0.3 mM Perphenazine in FaSSIF (blue circles). The resulting model fits are shown by full lines.

Taken together, supplementation of 0.3 mM P shrank vesicles as compared to pure FaSSIF resulting in an apparent core radius of 14.3 nm and a shell thicknesses of 3.6 nm. The flexible cylinder of the wormlike structures had a radius of 2.3 nm and a total cylinder length of 357

nm. The outcome for cylinder length is preliminarily, as it is calculated from the mid and low q part of the scattering curve, a region dominated by the vesicle form factor confounding the cylinder scattering contribution and, therefore, the readout for cylinder lengths. The calculated Kuhn length of the wormlike structures was 16.8 nm. These wormlike structures were not observed by AUC. Future experiments with varying P concentration are planned to further detail these morphological transition from vesicles into wormlike micelles. In addition, these future experiments may allow to revisit the fitting procedure based on more scattering curves spanning a wider P concentration range. Taken together, DLS, AUC, and SANS outcome suggested P induced morphological changes form larger vesicles in pure FaSSIF to smaller vesicles and co-existing wormlike structures.

Table 1: SANS fitting parameters. A vesicular structure was fitted to the SANS profile for pure FaSSIF, in case of 0.3 mM Perphenazine in FaSSIF both vesicles as well as elongated micellar structures were assumed for the fitting procedure. Error bars refer to the uncertainty in the fitting procedure.

Fitting parameters	**Pure FaSSIF**	**0.3 mM Perphenazine in FaSSIF**
vesicle radius [nm]	28.4 ± 0.013	14.4 ± 0.5
polydispersity of radius	0.128 ± 0.00037	0.28
vesicle shell thickness [nm]	2.75 ± 0.007	3.6 ± 0.9
cylinder length [nm]		357 ± 5
Kuhn length [nm]		16.8 ± 0.2
cylinder radius [nm]		2.3 ± 0.02
χ^2 fitting curve	11.7	95

Based on these experiments, we defined four regions for further studies. Region I is pure FaSSIF, region II the region in which only larger colloidal structures were found, region III in which large and small colloidal structures identified concomitantly, and region IV with only small colloidal structures. In spite of these quite substantial morphological changes, the concentration of free P found in the supernatant increased linearly with the P supplementation (**Figure 3D**), suggesting that the colloid-water partition coefficient of P was independent on colloidal morphologies. Initially, we hypothesized differences in the ratio of bound P to free P as a function of changing morphologies, for example reflecting supersaturation with decreasing vesicular radii[53] or effects of a larger surface area .

The interaction of P and FaSSIF was further characterized by isothermal titration calorimetry (ITC; **Figure 5**). Throughout all regions I to IV, increasing P reduced the initial exothermic signal from -0.73 to -0.23 µcal/s (**Figure 5, top**). Furthermore, we observed second negative spikes following the initial spikes in region III (0.05 to 0.25 mM P). Arguably, we hypothesize that the initial heat signal reflected interactions of P meeting the colloidal surfaces and the

second signal reflecting the resulting morphological adaptation. Although speculative at this point, the appearance of second spikes in phase III would coincide the morphological transition as seen by DLS, AUC, and SANS. Regarding enthalpy change, region II changed from -9.80 µcal to -9.95 µcal at 0.02 and 0.04 mM P, respectively (**Figure 5, bottom**). In region III, the exothermic signal changed from -10.22 through -14.60 to -5.03 µcal at 0.06, 0.15, and 0.24 mM P, respectively. In region IV, the decrease of the exothermic signals continued, leading to -2.92 µcal at 0.38 mM P and did not change substantially, thereafter (**Figure S19**).

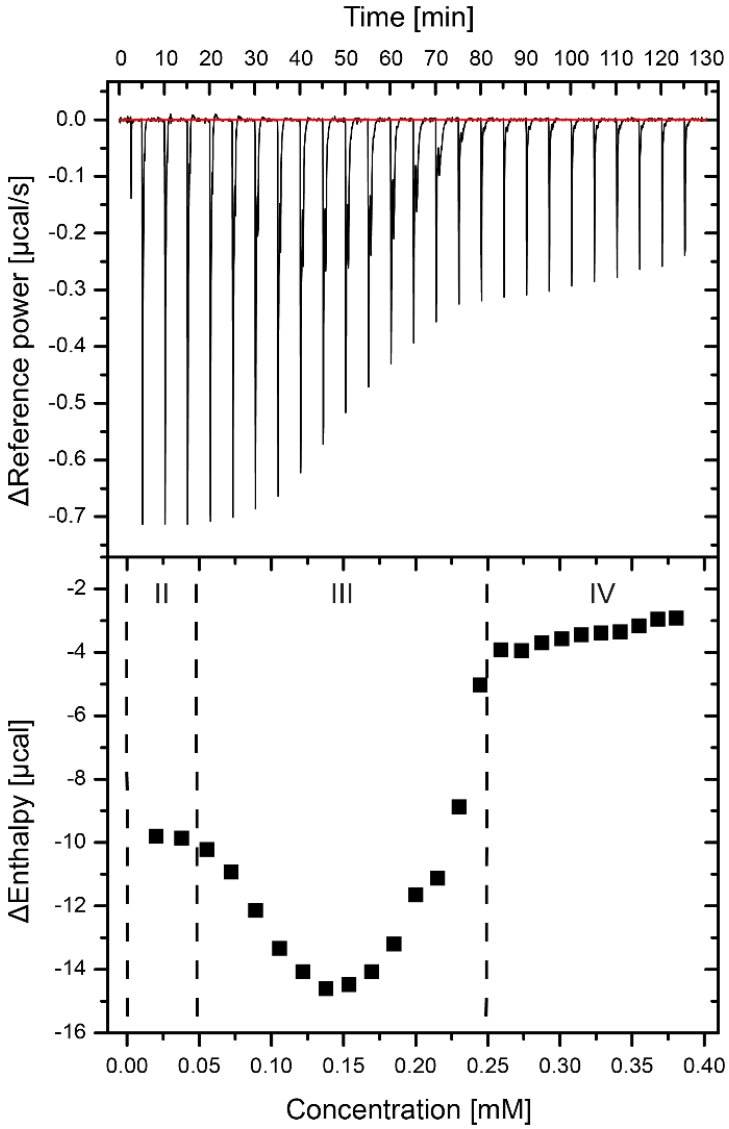

Figure 5: ITC data resulting from titration of a Perphenazine stock solution in FaSSIF to FaSSIF. The top graph shows the raw data of the reference power and the bottom graph shows the calculated enthalpy data, which was divided into four regions in accordance with Figure 3D.

Our interpretation of the enthalpy curve is qualitative for two reasons, firstly because the TC/L colloids were not saturated with P and secondly as the heat reflecting colloidal dynamics confounded heat signals resulting from immediate interactions of P. Nevertheless, the exothermic signals in region II as compared to region IV pointed to stronger intermolecular interaction between P and TC/L, a finding corroborated by NMR detailing P-L interaction (**Figure 2B**) and coarse-grained modeling of P loaded vesicles (**Figure S12**). Control titrations of FaSSIF to FaSSIF marginally impacted averaged enthalpy changes for each injection (-0.11 ± 0.02 µcal; **Figure S20**). In additional control experiments, a 10 fold concentrated FaSSIF was titrated into PBS with an exothermic signal (**Figure S21**), experiments which were previously linked to a vesicular size reduction.[22, 54]

In summary, P impacted the molecular arrangement, mobility, structure, and binding thermodynamics of TC/L colloids (**Figure 2-5**), effects which we separated into four regions. In absence of P (region I) we observed one fraction of pure TC/L vesicles (**Figure 3A, 4**) with a Z-average hydrodynamic diameter of 54.6 ± 3.3 nm from DLS (**Figure 3C**) and in line with previously reported small-angle X-ray scattering data.[42] At low P concentration (0.05 mM; region II), P inclusion did not impact colloidal structure (**Figure 2A**), but we observed an increase in sedimentation coefficients as compared to lower concentration (**Figure 3A, 3B**). In region III (0.05 to 0.25 mM), large and small colloidal species coexisted (**Figure 3B, 3D**) with P being integrated into stable structures mainly being associated with L (**Figure 2B**). Lastly, within region IV (0.25 mM and higher P), P was integrated into smaller TC/L colloids consisting of coexisting vesicles and elongated structures within which P was more mobile and associated with both, TC and L (**Figure 3A, 4, 2B**). These patterns observed for the natural TC/L colloidal systems (**Figure 6**) are contrasting to colloids from synthetic pharmaceutical polymers (e.g. sodium dodecyl sulfate or Pluronic F127), which either show no or very limited drug-concentration dependent dynamics.[55, 56]

So far, the *in vivo* relevance of our findings remains unclear. Future experiments in aspirated intestinal fluids along with flux studies across excised intestinal biopsies will further push the outcome on the structural and geometrical colloidal dynamics reported here.

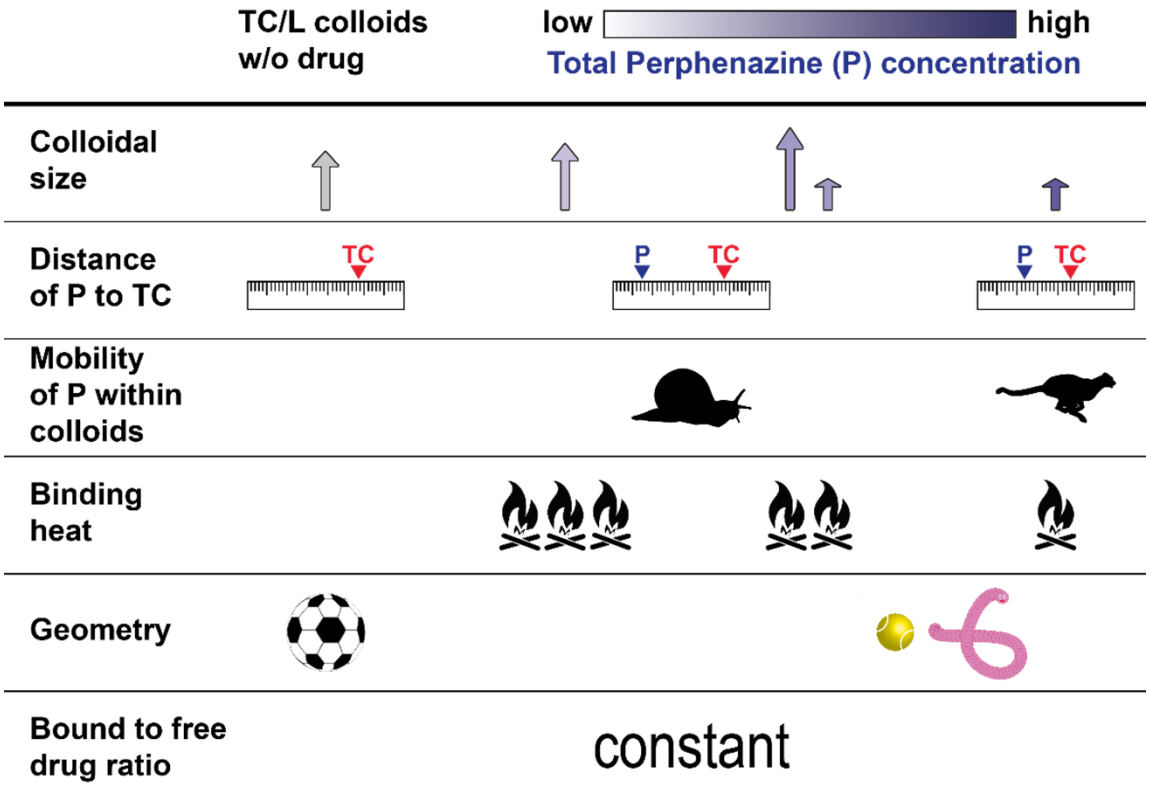

Figure 6: Schematic representation of colloidal dynamics as a function of Perphenazine concentration.

Conclusion

The supplementation of Perphenazine to taurocholate/lecithin colloids changed hydrodynamic size, geometry, enthalpy, molecular interaction, and molecular mobility. Despite these dynamics, the relative amount of free Perphenazine remained constant. These findings point to a remarkable structural adaptability of the natural colloids toward solubilization challenges providing an intriguing mechanism to keep a key parameter constant – the relative free concentration of poorly water-soluble drugs.

Acknowledgement

We gratefully acknowledge funding from BASF SE for SH and by the German Ministry of Education and Research (grant number 13XP5049B). IN acknowledges support of his work through the Collaborative Research Center PolyTarget (SFB 1278 – project number 316213987, project Z01), funded by the Deutsche Forschungsgemeinschaft (DFG) as well as the "Thüringer Aufbaubank (TAB)" and the "Europäischer Fonds für regionale Entwicklung (EFRE)" (2018FGI0025) through funding analytical ultracentrifugation facilities at the Jena Center for Soft Matter (JCSM). The authors thank the Institut Laue – Langevin for supplying beam-time under the proposal number EASY-643 (https://doi.ill.fr/10.5291/ILL-DATA.EASY-643). This work benefited from the use of the SasView application, originally developed under NSF award DMR-0520547. SasView contains codes developed with funding from the European Union's Horizon 2020 research and innovation program, under the SINE2020 project, grant agreement No 654000. We would like to thank Christopher Heidenreich for his highly appreciated technical assistance.

Conflict of interest

FPB, TMS, KK are full time employees of BASF SE and state a potential conflict of interest.

References

1. Boyer, J. L., Bile formation and secretion. Compr. Physiol. **2013**, 3 (3), 1035-78.
2. Perez de la Cruz Moreno, M.; Oth, M.; Deferme, S.; Lammert, F.; Tack, J.; Dressman, J.; Augustijns, P., Characterization of fasted-state human intestinal fluids collected from duodenum and jejunum. J. Pharm. Pharmacol. **2006**, 58 (8), 1079-89.
3. Dawson, P. A.; Karpen, S. J., Intestinal transport and metabolism of bile acids. *J. Lipid. Res.* **2015,** *56* (6), 1085-99.
4. Elvang, P. A.; Bohsen, M. S.; Stein, P. C.; Bauer-Brandl, A.; Riethorst, D.; Brouwers, J.; Augustijns, P.; Brandl, M., Co-existing colloidal phases of human duodenal aspirates: Intraindividual fluctuations and interindividual variability in relation to molecular composition. *J. Pharm. Biomed. Anal.* **2019,** *170*, 22-29.
5. Russell, D. W., The enzymes, regulation, and genetics of bile acid synthesis. *Annu. Rev. Biochem.* **2003,** *72*, 137-74.
6. Malik, N. A., Solubilization and Interaction Studies of Bile Salts with Surfactants and Drugs: a Review. *Appl. Biochem. Biotechnol.* **2016,** *179* (2), 179-201.
7. Hofmann, A. F., The continuing importance of bile acids in liver and intestinal disease. *Arch. Intern. Med.* **1999,** *159* (22), 2647-58.
8. Pavlovic, N.; Golocorbin-Kon, S.; Danic, M.; Stanimirov, B.; Al-Salami, H.; Stankov, K.; Mikov, M., Bile Acids and Their Derivatives as Potential Modifiers of Drug Release and Pharmacokinetic Profiles. *Front. Pharamcol.* **2018,** *9*.
9. Enhsen, A.; Kramer, W.; Wess, G., Bile acids in drug discovery. *Drug Discovery Today* **1998,** *3* (9), 409-418.
10. Yu, J. N.; Zhu, Y.; Wang, L.; Peng, M.; Tong, S. S.; Cao, X.; Qiu, H.; Xu, X. M., Enhancement of oral bioavailability of the poorly water-soluble drug silybin by sodium cholate/phospholipid-mixed micelles. *Acta. Pharmacol. Sin.* **2010,** *31* (6), 759-64.
11. Dressman, J. B.; Reppas, C., In vitro-in vivo correlations for lipophilic, poorly water-soluble drugs. *Eur. J. Pharm. Sci.* **2000,** *11 Suppl 2*, S73-80.
12. Bates, T. R.; Gibaldi, M.; Kanig, J. L., Rate of dissolution of griseofulvin and hexoestrol in bile salt solutions. *Nature* **1966,** *210* (5043), 1331-3.
13. Monte, M. J.; Marin, J. J.; Antelo, A.; Vazquez-Tato, J., Bile acids: chemistry, physiology, and pathophysiology. *World J. Gastroenterol.* **2009,** *15* (7), 804-16.
14. Mukhopadhyay, S.; Maitra, U., Chemistry and biology of bile acids. *Curr. Sci.* **2004,** *87*, 1666-1683.
15. Mukerjee, P.; Moroi, Y.; Murata, M.; Yang, A. Y., Bile salts as atypical surfactants and solubilizers. *Hepatology (Hoboken, NJ, U. S.)* **1984,** *4* (5 Suppl), 61S-65S.
16. Carey, M. C., Micelle Formation by Bile Salts. *Arch. Intern. Med.* **1972,** *130* (4).
17. Gouin, S.; Zhu, X. X., Fluorescence and NMR Studies of the Effect of a Bile Acid Dimer on the Micellization of Bile Salts. *Langmuir* **1998,** *14* (15), 4025-4029.

18. Madenci, D.; Egelhaaf, S. U., Self-assembly in aqueous bile salt solutions. *Curr. Opin. Colloid Interface Sci.* **2010,** *15* (1-2), 109-115.
19. Klein, S., The Use of Biorelevant Dissolution Media to Forecast the In Vivo Performance of a Drug. *AAPS J.* **2010,** *12* (3), 397-406.
20. Long, M. A.; Kaler, E. W.; Lee, S. P., Structural characterization of the micelle-vesicle transition in lecithin-bile salt solutions. *Biophys. J.* **1994,** *67* (4), 1733-42.
21. Nichols, J. W.; Ozarowski, J., Sizing of lecithin-bile salt mixed micelles by size-exclusion high-performance liquid chromatography. *Biochemistry* **1990,** *29* (19), 4600-6.
22. Nawroth, T.; Buch, P.; Buch, K.; Langguth, P.; Schweins, R., Liposome formation from bile salt-lipid micelles in the digestion and drug delivery model FaSSIF(mod) estimated by combined time-resolved neutron and dynamic light scattering. *Mol. Pharmaceutics* **2011,** *8* (6), 2162-72.
23. Schurtenberger, P.; Mazer, N.; Kaenzig, W., Micelle to vesicle transition in aqueous solutions of bile salt and lecithin. *J. Phys. Chem.* **1985,** *89* (6), 1042-1049.
24. Egelhaaf, S. U.; Schurtenberger, P., Shape Transformations in the Lecithin-Bile Salt System: From Cylinders to Vesicles. *J. Phys. Chem.* **1994,** *98* (34), 8560-8573.
25. Madenci, D.; Salonen, A.; Schurtenberger, P.; Pedersen, J. S.; Egelhaaf, S. U., Simple model for the growth behaviour of mixed lecithin-bile salt micelles. *Phys. Chem. Chem. Phys.* **2011,** *13* (8), 3171-8.
26. Vogtherr, M.; Marx, A.; Mieden, A. C.; Saal, C., Investigation of solubilising effects of bile salts on an active pharmaceutical ingredient with unusual pH dependent solubility by NMR spectroscopy. *Eur. J. Pharm. Biopharm.* **2015,** *92*, 32-41.
27. Wiest, J.; Saedtler, M.; Boucher, B.; Grune, M.; Reggane, M.; Galli, B.; Holzgrabe, U.; Meinel, L., Geometrical and Structural Dynamics of Imatinib within Biorelevant Colloids. *Mol. Pharmaceutics* **2018,** *15* (10), 4470-4480.
28. Sugano, K.; Kataoka, M.; Mathews Cda, C.; Yamashita, S., Prediction of food effect by bile micelles on oral drug absorption considering free fraction in intestinal fluid. *Eur. J. Pharm. Sci.* **2010,** *40* (2), 118-24.
29. Parrott, N.; Lavé, T., Prediction of intestinal absorption: comparative assessment of gastroplus™ and idea™. *Eur. J. Pharm. Sci.* **2002,** *17* (1-2), 51-61.
30. Kleberg, K.; Jacobsen, J.; Mullertz, A., Characterising the behaviour of poorly water soluble drugs in the intestine: application of biorelevant media for solubility, dissolution and transport studies. *J. Pharm. Pharmacol.* **2010,** *62* (11), 1656-68.
31. Holm, R.; Mullertz, A.; Mu, H., Bile salts and their importance for drug absorption. *Int. J. Pharm. (Amsterdam, Neth.)* **2013,** *453* (1), 44-55.
32. Singh, A.; Worku, Z. A.; Van den Mooter, G., Oral formulation strategies to improve solubility of poorly water-soluble drugs. *Expert Opin. Drug Delivery* **2011,** *8* (10), 1361-78.

33. Schlauersbach, J.; Hanio, S.; Lenz, B.; Vemulapalli, S. P. B.; Griesinger, C.; Poppler, A. C.; Harlacher, C.; Galli, B.; Meinel, L., Leveraging bile solubilization of poorly water-soluble drugs by rational polymer selection. *J. Controlled Release* **2020,** *330*, 36-48.
34. Goke, K.; Lorenz, T.; Repanas, A.; Schneider, F.; Steiner, D.; Baumann, K.; Bunjes, H.; Dietzel, A.; Finke, J. H.; Glasmacher, B.; Kwade, A., Novel strategies for the formulation and processing of poorly water-soluble drugs. *Eur. J. Pharm. Biopharm.* **2018,** *126*, 40-56.
35. Balk, A.; Holzgrabe, U.; Meinel, L., 'Pro et contra' ionic liquid drugs - Challenges and opportunities for pharmaceutical translation. *Eur. J. Pharm. Biopharm.* **2015,** *94*, 291-304.
36. Rees, L., Chlorpromazine and allied phenothiazine derivatives. *BMJ* **1960,** *2* (5197), 522-5.
37. Baucke, F. G. K., Further insight into the dissociation mechanism of glass electrodes. The response in heavy water. *J. Phys. Chem. B* **1998,** *102* (24), 4835-4841.
38. Kessler, H.; Oschkinat, H.; Griesinger, C.; Bermel, W., Transformation of homonuclear two-dimensional NMR techniques into one-dimensional techniques using Gaussian pulses. *J. Magn. Reson. (1969-1992)* **1986,** *70* (1), 106-133.
39. Van Der Spoel, D.; Lindahl, E.; Hess, B.; Groenhof, G.; Mark, A. E.; Berendsen, H. J., GROMACS: fast, flexible, and free. *J. Comput. Chem.* **2005,** *26* (16), 1701-18.
40. Abraham, M. J.; Murtola, T.; Schulz, R.; Páll, S.; Smith, J. C.; Hess, B.; Lindahl, E., GROMACS: High performance molecular simulations through multi-level parallelism from laptops to supercomputers. *SoftwareX* **2015,** *1-2*, 19-25.
41. Marrink, S. J.; Risselada, H. J.; Yefimov, S.; Tieleman, D. P.; de Vries, A. H., The MARTINI force field: coarse grained model for biomolecular simulations. *J. Phys. Chem. B* **2007,** *111* (27), 7812-24.
42. Clulow, A. J.; Parrow, A.; Hawley, A.; Khan, J.; Pham, A. C.; Larsson, P.; Bergstrom, C. A. S.; Boyd, B. J., Characterization of Solubilizing Nanoaggregates Present in Different Versions of Simulated Intestinal Fluid. *J. Phys. Chem. B* **2017,** *121* (48), 10869-10881.
43. Kim, S.; Lee, J.; Jo, S.; Brooks, C. L., 3rd; Lee, H. S.; Im, W., CHARMM-GUI ligand reader and modeler for CHARMM force field generation of small molecules. *J. Comput. Chem.* **2017,** *38* (21), 1879-1886.
44. Schuck, P.; Rossmanith, P., Determination of the sedimentation coefficient distribution by least-squares boundary modeling. *Biopolymers* **2000,** *54* (5), 328-41.
45. Grube, M.; Perevyazko, I.; Heinze, T.; Schubert, U. S.; Nischang, I., Revisiting very disperse macromolecule populations in hydrodynamic and light scattering studies of sodium carboxymethyl celluloses. *Carbohydr. Polym.* **2020,** *229*, 115452.
46. Koppel, D. E., Analysis of Macromolecular Polydispersity in Intensity Correlation Spectroscopy: The Method of Cumulants. *J. Chem. Phys.* **1972,** *57* (11), 4814-4820.
47. Lindner, P.; Schweins, R., The D11 Small-Angle Scattering Instrument: A New Benchmark for SANS. *Neutron News* **2010,** *21* (2), 15-18.
48. Malvern, Routine ITC data analysis. In *MicroCal iTC200 system User Manual MAN0560*, Malvern: Worcestershire, UK, 2014; pp 118-252.

49. Wickham, M.; Garrood, M.; Leney, J.; Wilson, P. D.; Fillery-Travis, A., Modification of a phospholipid stabilized emulsion interface by bile salt: effect on pancreatic lipase activity. *Journal of Lipid Research* **1998,** *39* (3), 623-632.
50. Kawai, Y.; Fujii, Y.; Tabata, F.; Ito, J.; Metsugi, Y.; Kameda, A.; Akimoto, K.; Takahashi, M., Profiling and trend analysis of food effects on oral drug absorption considering micelle interaction and solubilization by bile micelles. *Drug Metab. Pharmacokinet.* **2011,** *26* (2), 180-91.
51. Cinar, G.; Englert, C.; Lehmann, M.; Nischang, I., In Situ, Quantitative Assessment of Multifunctional Nanoscale Drug Delivery Systems in Human Serum. *Anal. Chem. (Washington, DC, U. S.)* **2020,** *92* (11), 7932-7939.
52. Elvang, P. A.; Hinna, A. H.; Brouwers, J.; Hens, B.; Augustijns, P.; Brandl, M., Bile Salt Micelles and Phospholipid Vesicles Present in Simulated and Human Intestinal Fluids: Structural Analysis by Flow Field-Flow Fractionation/Multiangle Laser Light Scattering. *J. Pharm. Sci.* **2016,** *105* (9), 2832-2839.
53. Mukerjee, P., Solubilization in Aqueous Micellar Systems. In *Solution Chemistry of Surfactants*, Mittal, K. L., Ed. Springer New York: Boston, MA, 1979; Vol. 1, pp 153-174.
54. Sugano, K.; Okazaki, A.; Sugimoto, S.; Tavornvipas, S.; Omura, A.; Mano, T., Solubility and dissolution profile assessment in drug discovery. *Drug Metab. Pharmacokinet.* **2007,** *22* (4), 225-54.
55. Waters, L. J.; Hussain, T.; Parkes, G. M. B., Titration calorimetry of surfactant–drug interactions: Micelle formation and saturation studies. *J. Chem. Thermodyn.* **2012,** *53*, 36-41.
56. Sharma, P. K.; Reilly, M. J.; Jones, D. N.; Robinson, P. M.; Bhatia, S. R., The effect of pharmaceuticals on the nanoscale structure of PEO-PPO-PEO micelles. *Colloids Surf., B* **2008,** *61* (1), 53-60.

Supporting information

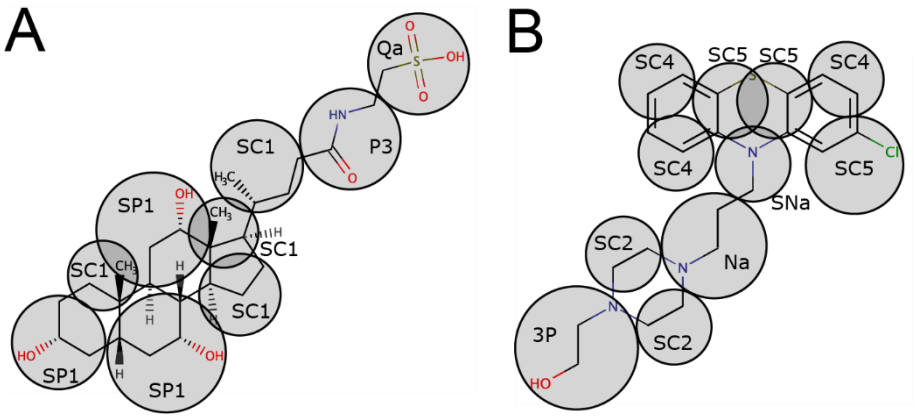

Figure S1: Coarse-grained mapping of taurocholate (A) and Perphenazine (B) with assigned Martini bead types.

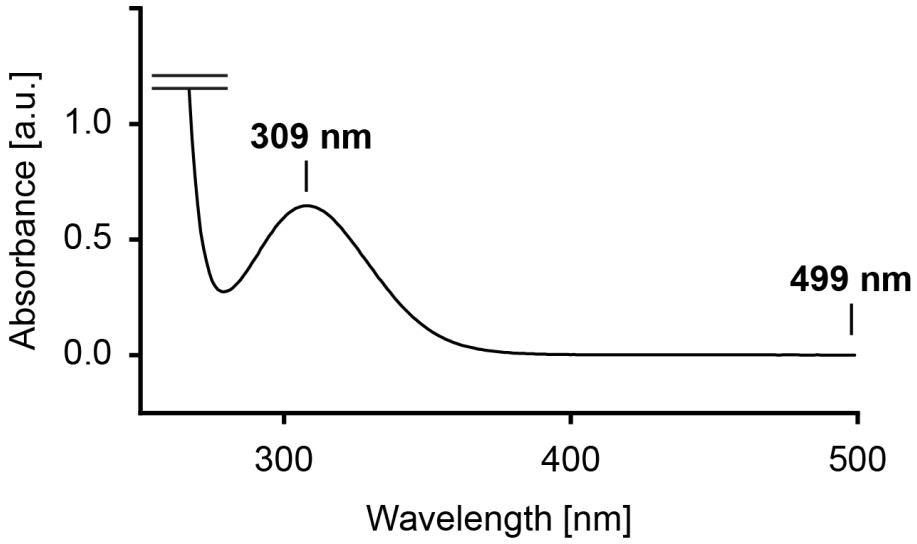

Figure S2: UV-Vis spectrum of 0.15 mM Perphenazine in PBS.

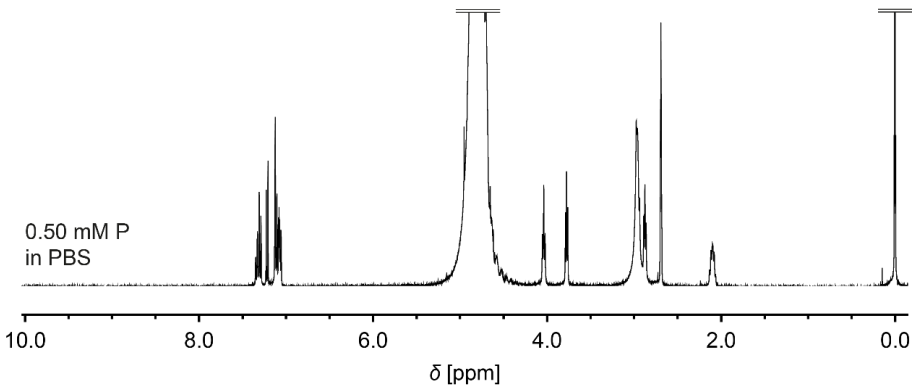

Figure S3: ^{1}H NMR spectrum of 0.5 mM Perphenazine (P) in PBS. Chemical shift is referred to as δ.

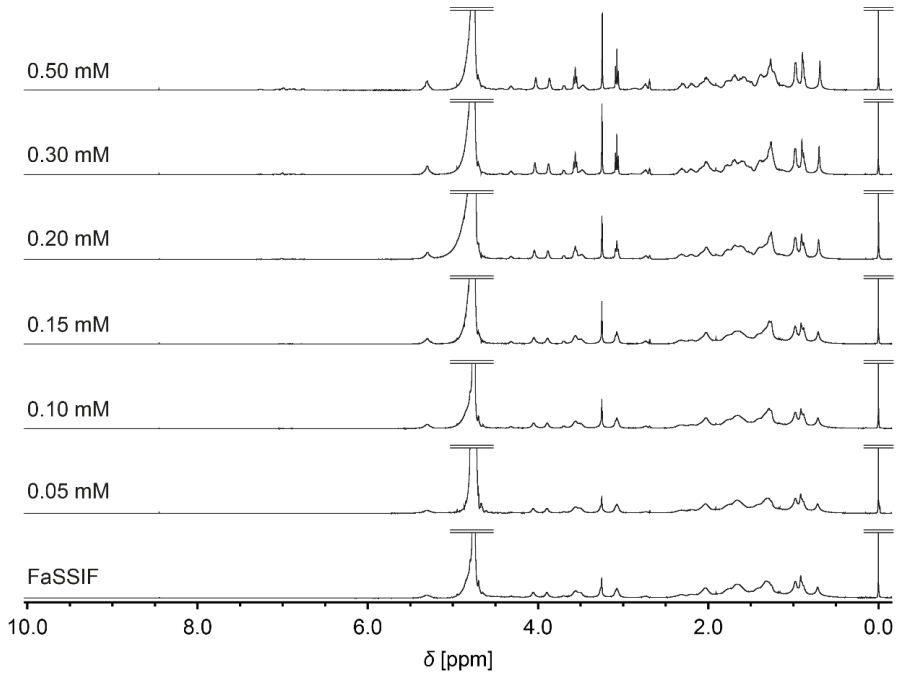

Figure S4: ^{1}H NMR spectra of TC/L colloids as a function of Perphenazine concentration.

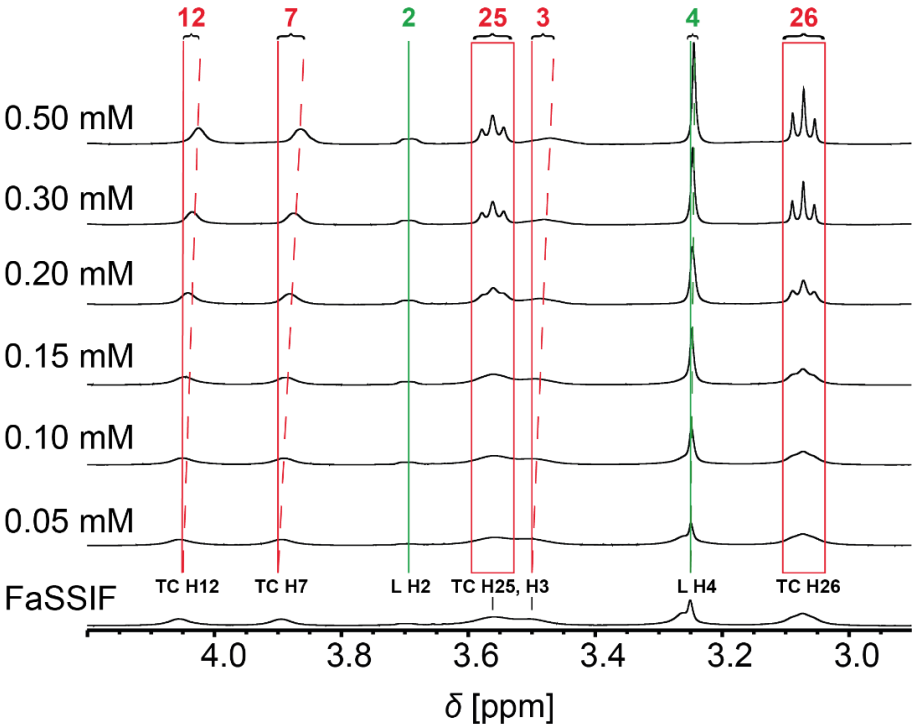

Figure S5: Zoom in Figure 2 at 2.9 to 4.2 ppm detailing the chemical shifts of TC and L as a function of Perphenazine concentration. Red boxes (TC) highlight signal sharpening for TC H25/26. Red (TC) and green (L) dotted lines represent shifts to lower ppm values for TC H12/7/3 and L H4, respectively.

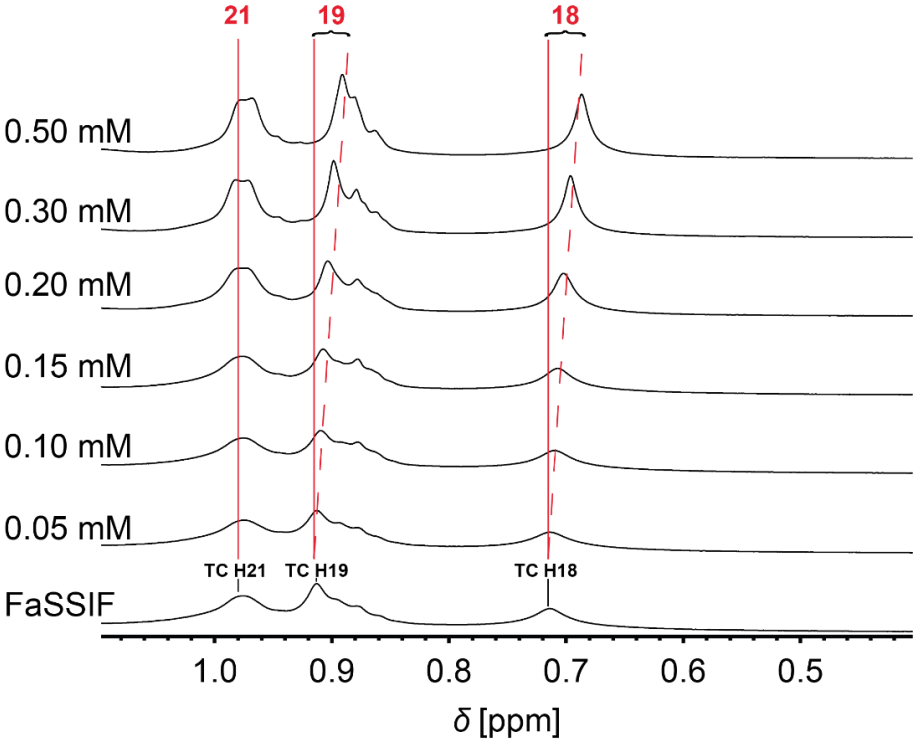

Figure S6: Zoom in Figure 2 at 0.4 to 1.1 ppm detailing the chemical shifts of TC as a function of Perphenazine concentration. Red (TC) dotted lines represent shifts to lower ppm values for TC H19/18.

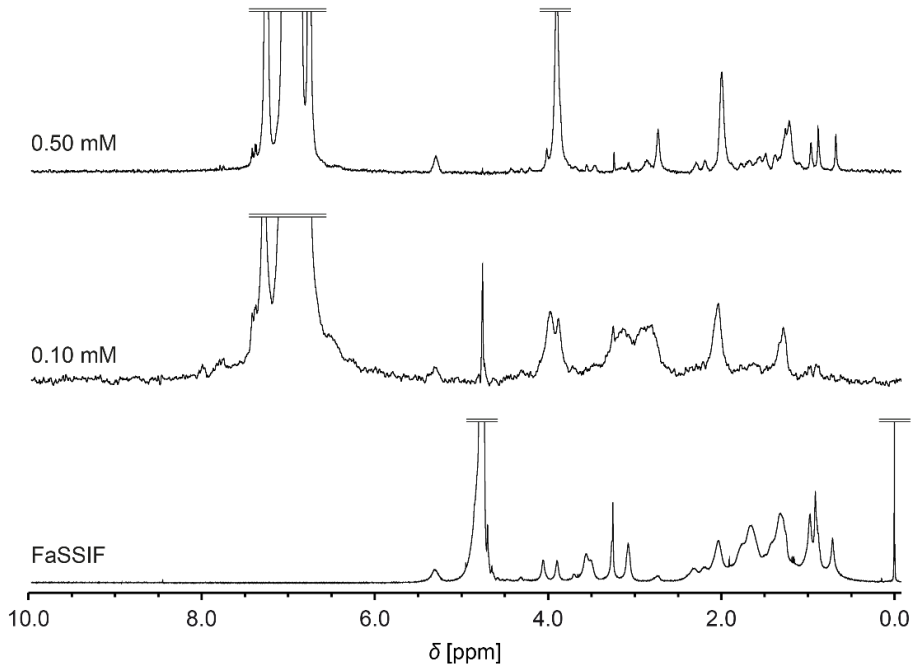

Figure S7: 1D NOESY spectra of 0.1 mM and 0.5 mM Perphenazine with TC/L colloids recorded with selective excitation at ca. 7 ppm and a mixing time of 60 ms (^{1}H NMR spectrum of FaSSIF is from Figure 1C and used for reference).

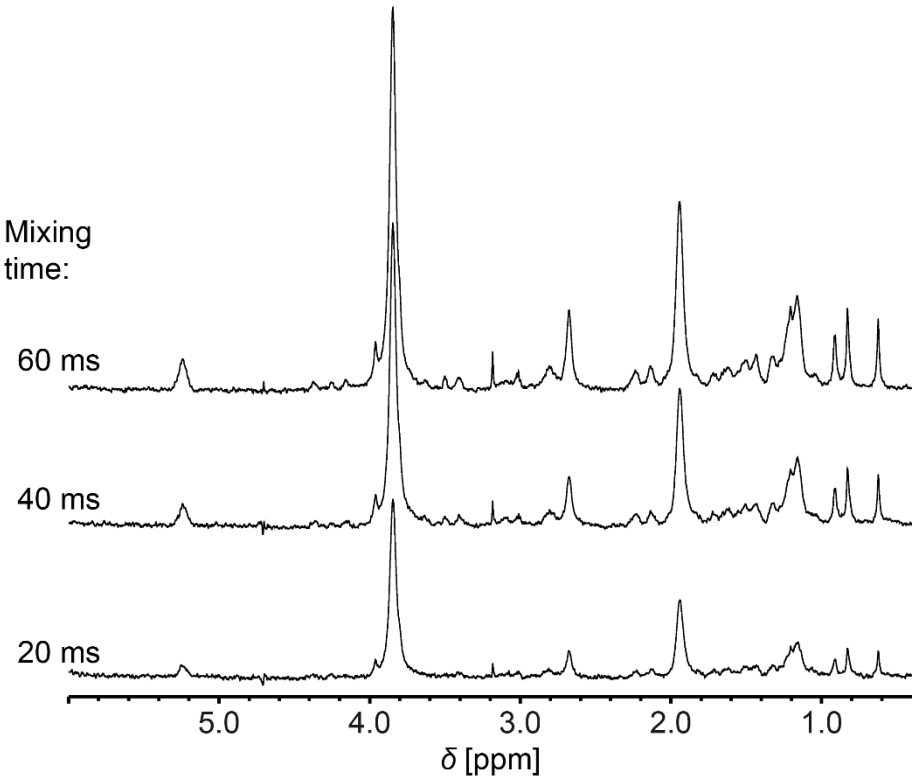

Figure S8: Extracts from 1D NOESY spectra of 0.5 mM Perphenazine in FaSSIF with selective excitation at ca. 7 ppm for different mixing times. *Non*-linear increase in signal intensity with mixing times at 3.9 ppm was caused by spin diffusion. Other signal intensities increased linearly with mixing times ruling out spin diffusion.

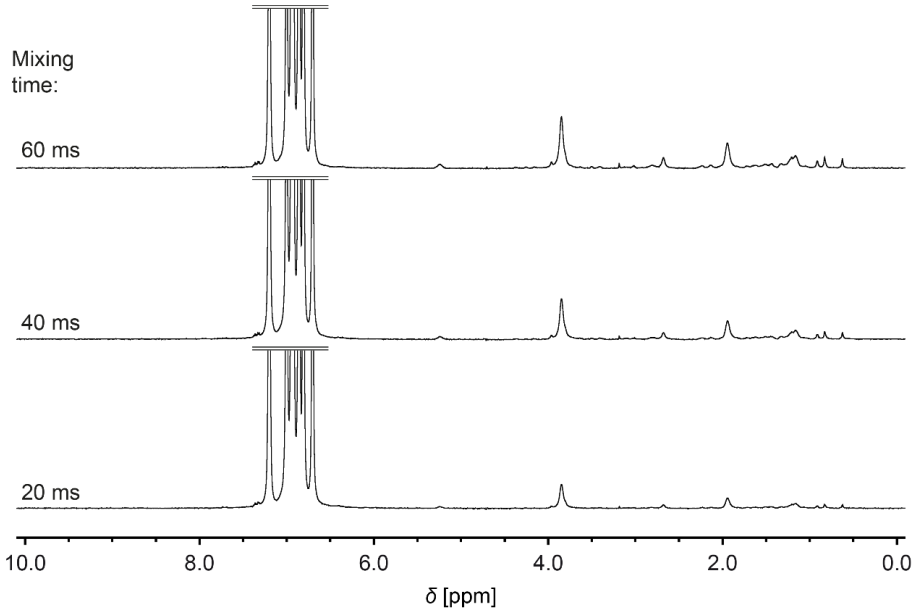

Figure S9: 1D NOESY spectra of 0.5 mM Perphenazine in FaSSIF with selective excitation at ca. 7 ppm using different mixing times.

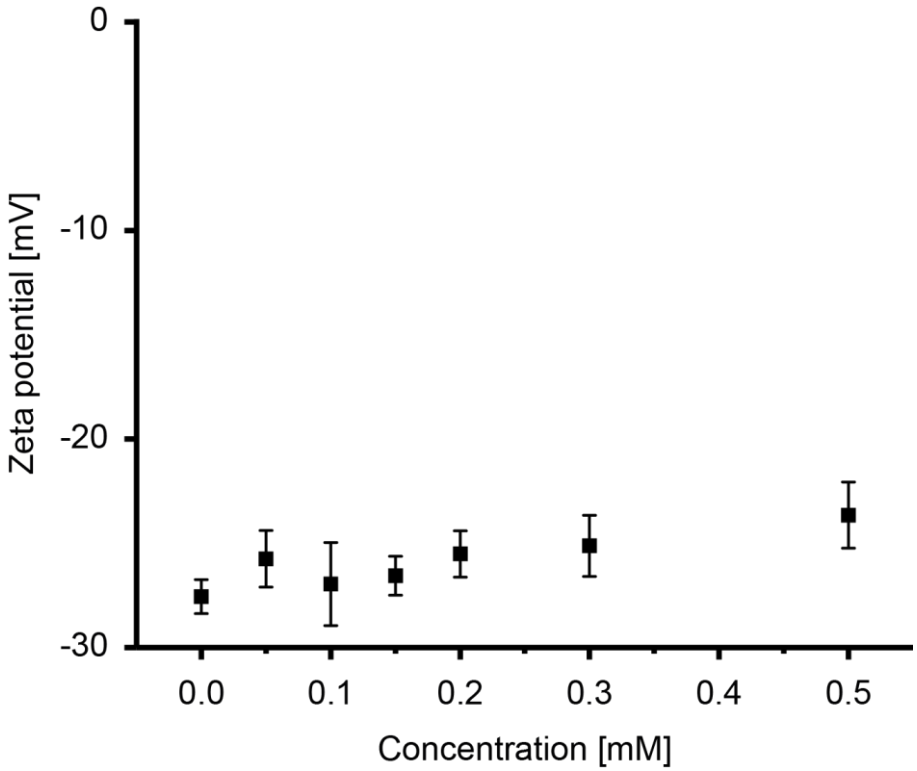

Figure S10: Zeta potential in FaSSIF at different Perphenazine concentrations (mean ± SD), the means were not significantly different as tested by one-way ANOVA ($p \leq 0.05$).

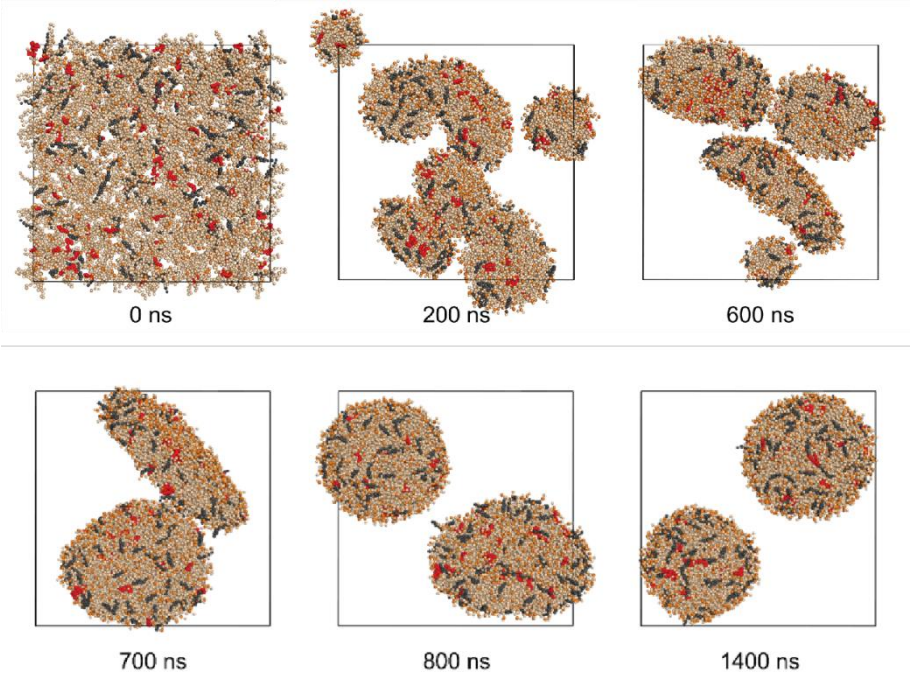

Figure S11: Time-resolved formation of TC/L vesicles. From the initial random configuration of the TC/L system, small bilayer patches and micellar structures were formed. Fusion of these small aggregates resulted in larger bicelle intermediates which – when sufficiently large – curled up and formed vesicles.

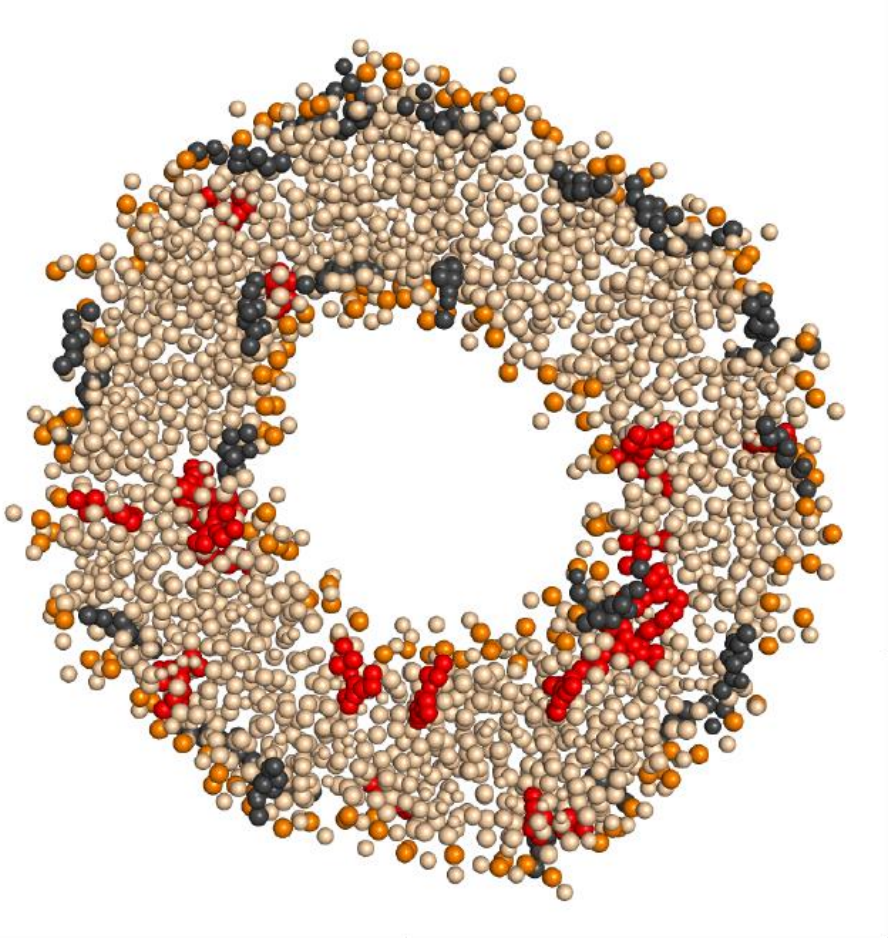

Figure S12: Cross-sectional view of a spontaneously assembled vesicle composed of phospholipids (beige/orange), taurocholate (dark gray), and Perphenazine molecules (red).

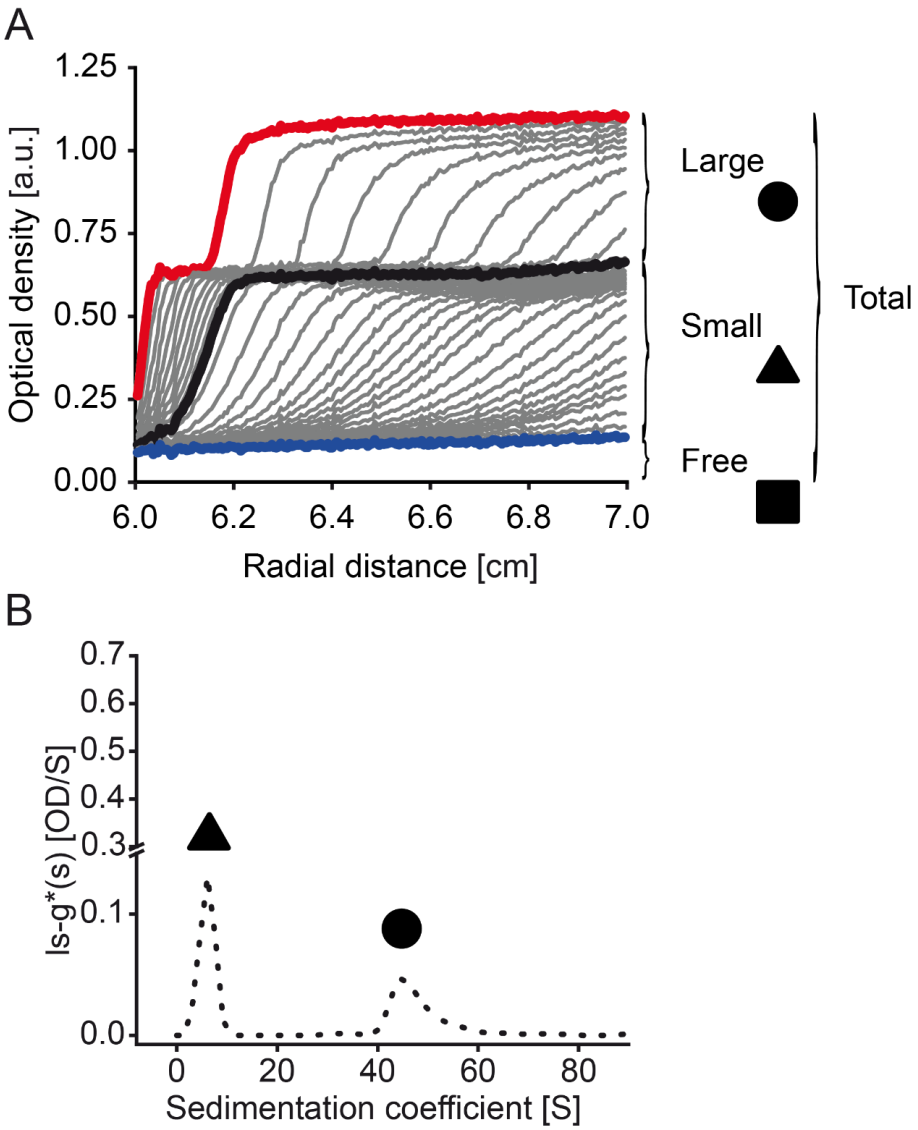

Figure S13: (A) Selected sedimentation velocity profiles of 0.2 mM Perphenazine in FaSSIF with highlighted profiles close to beginning of the experiment (red), at an intermediate timescale (black) and close to the end (blue) monitored at a wavelength of λ = 309 nm in terms of optical density (OD). (B) Corresponding differential distributions of sedimentation coefficients, ls-g*(s), resolving the two apparent species from A.

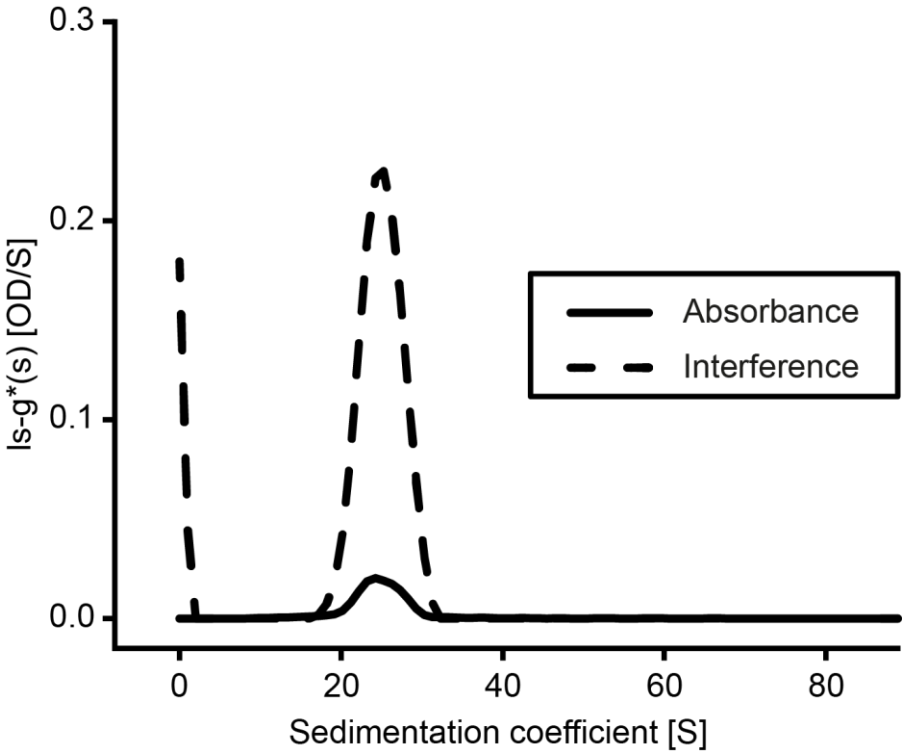

Figure S14: Differential distribution of sedimentation coefficient, ls-g*(s), utilizing universal refractive index detection (RI) and absorbance detection (at a wavelength of λ = 309 nm) in terms of OD for FaSSIF. The unresolved signal at infinitely small sedimentation coefficients from RI data is considered as a modelling artefact from rather unspecified refractive index changes.

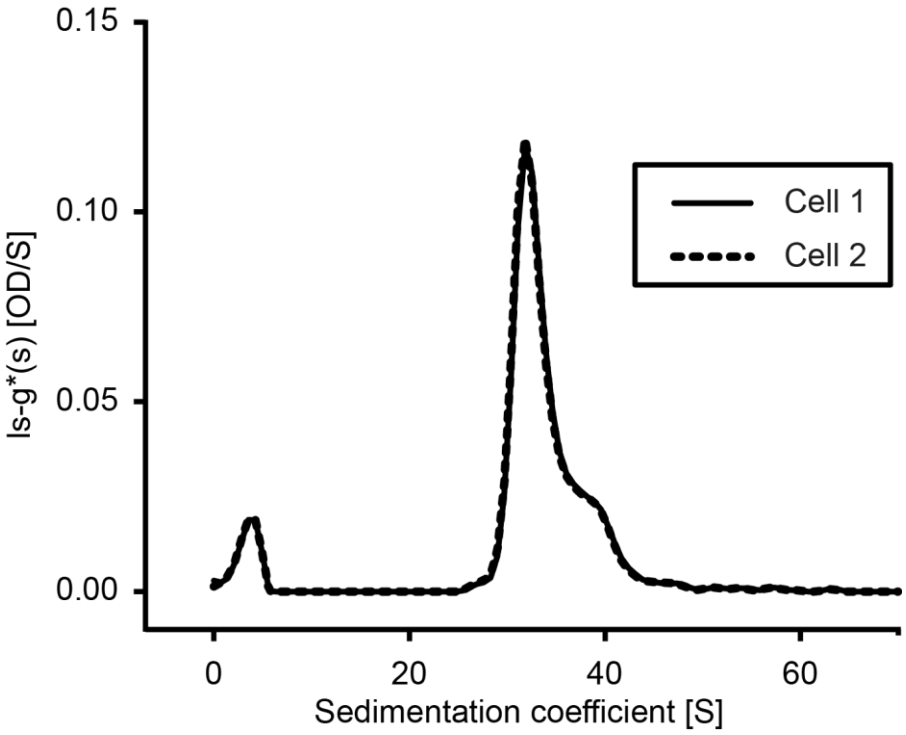

Figure S15: Repeatability test of measurement and data analysis accuracy of AUC. Differential distributions of sedimentation coefficients, ls-g*(s), acquired at a wavelength of λ = 309 nm in terms of OD, of 0.11 mM Perphenazine in FaSSIF performed in two different cells (solid and dotted lines).

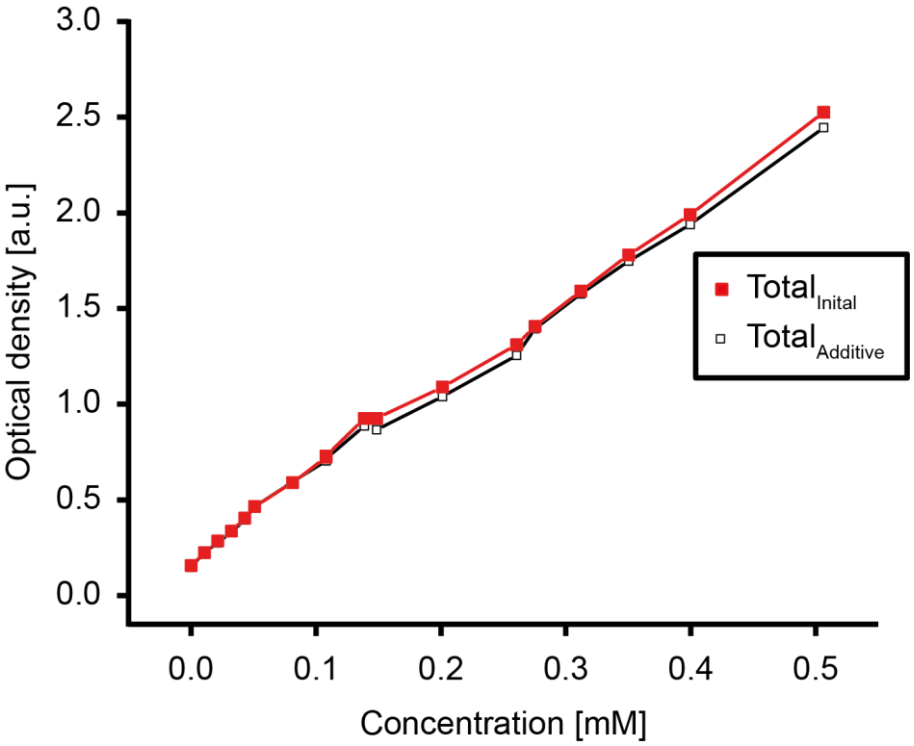

Figure S16: Comparison of initial total ODs as determined from the first sedimentation velocity scan and additive ODs consisting of individually resolved species from integration of differential distributions of sedimentation coefficients (supernatant, large colloids, small colloids) monitored at a wavelength of λ = 309 nm in terms of OD.

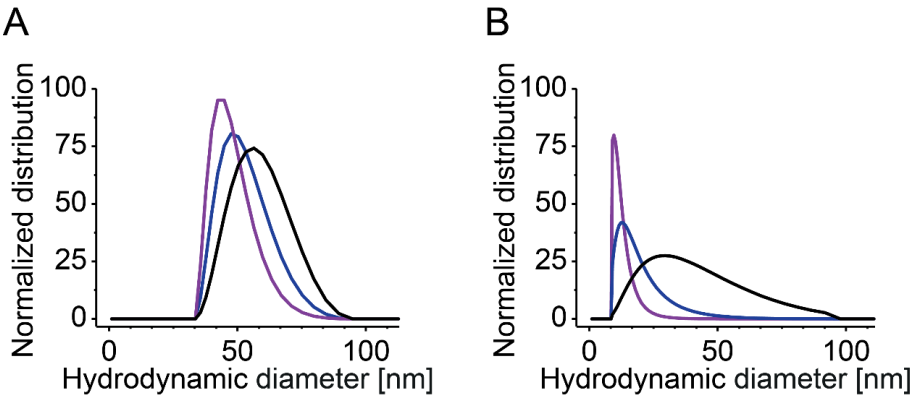

Figure S17: Representative intensity (black), volume (blue), and number (purple) weighted hydrodynamic diameter distributions for (A) pure FaSSIF and (B) 0.3 mM Perphenazine in FaSSIF as determined by dynamic light scattering. The intensity size distributions were converted into volume and number distributions applying Mie theory.

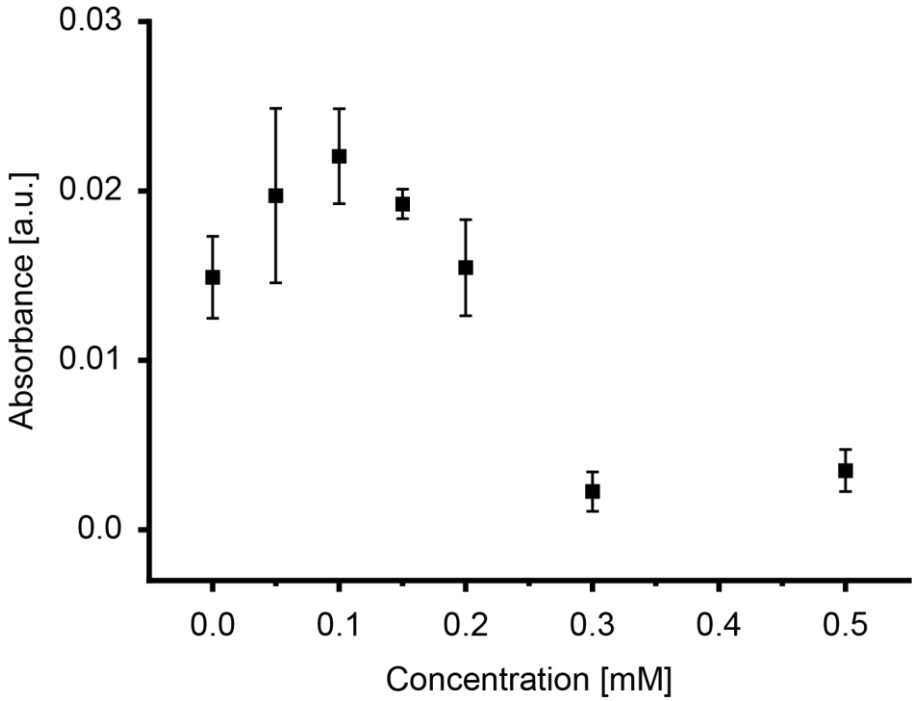

Figure S18: Absorbance at a wavelength λ = 499 nm in FaSSIF at different Perphenazine concentrations (mean ± SD).

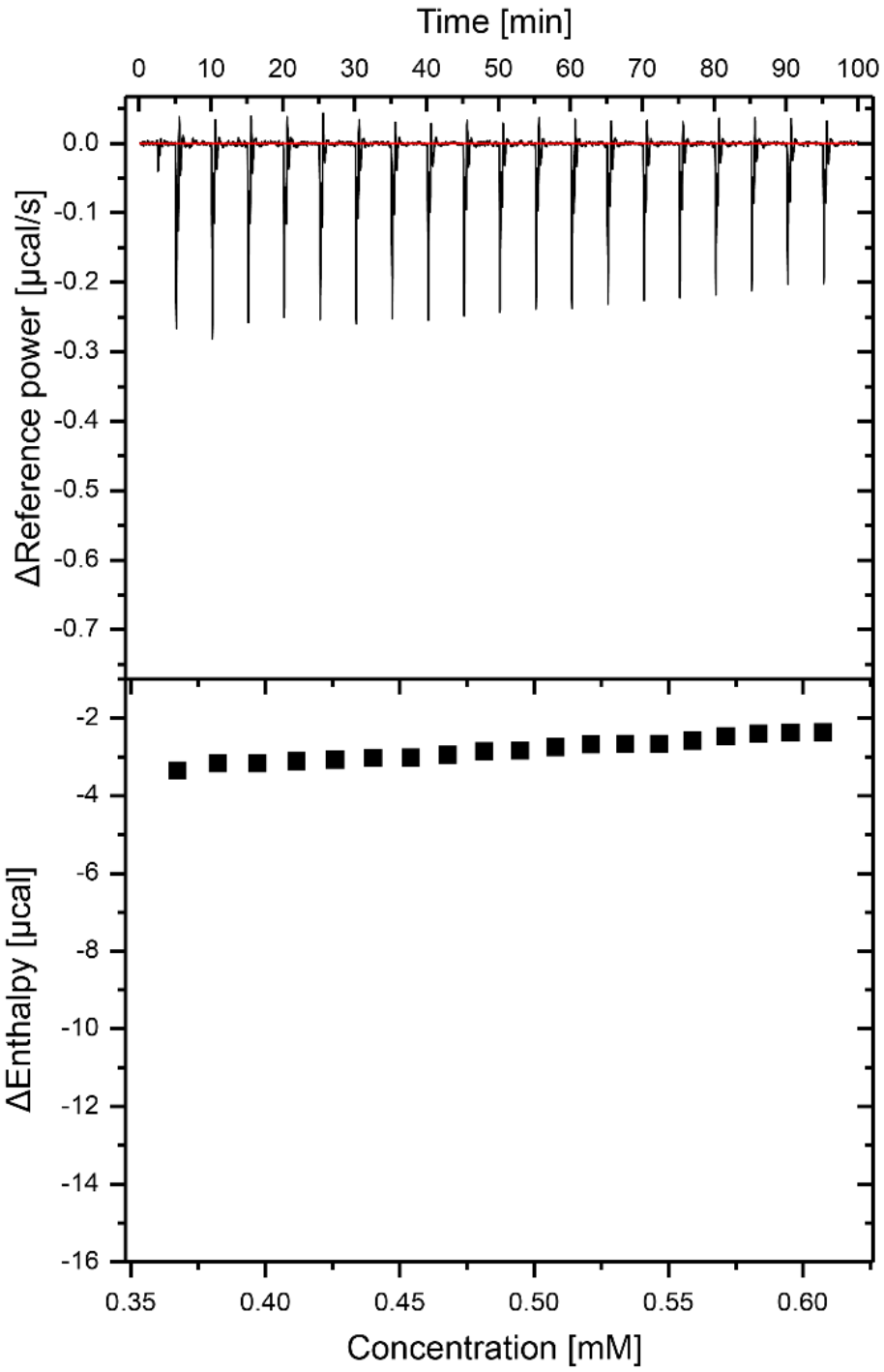

Figure S19: ITC data resulting from titration of a Perphenazine stock solution in FaSSIF to FaSSIF with 0.35 mM Perphenazine. The top graph shows the raw data of the reference power and the bottom graph shows the calculated enthalpy data.

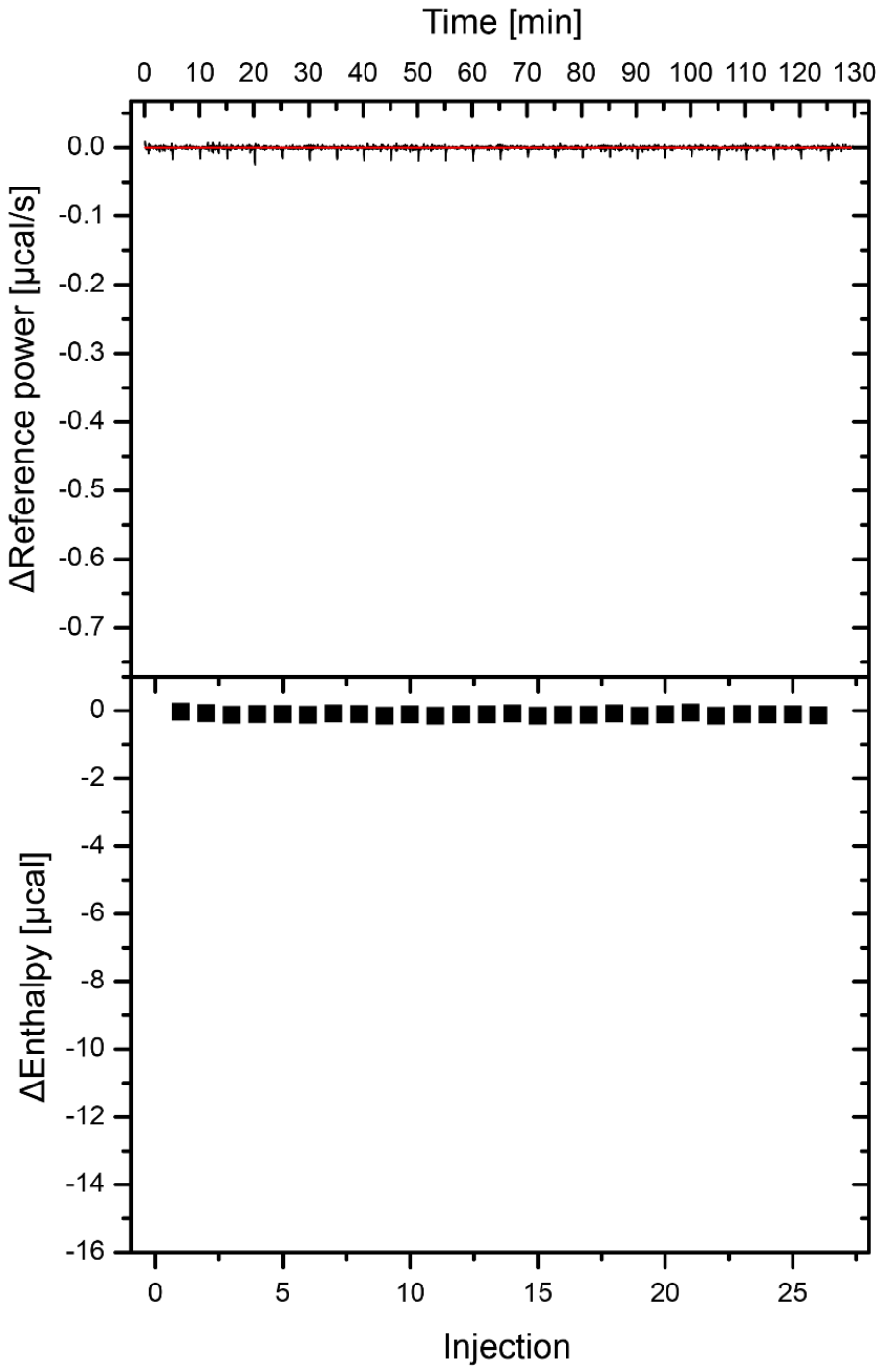

Figure S20: ITC data resulting from titration of FaSSIF w/o Perphenazine to FaSSIF w/o Perphenazine. The top graph shows the raw data of the reference power and the bottom graph shows the calculated enthalpy data. Enthalpy change was low.

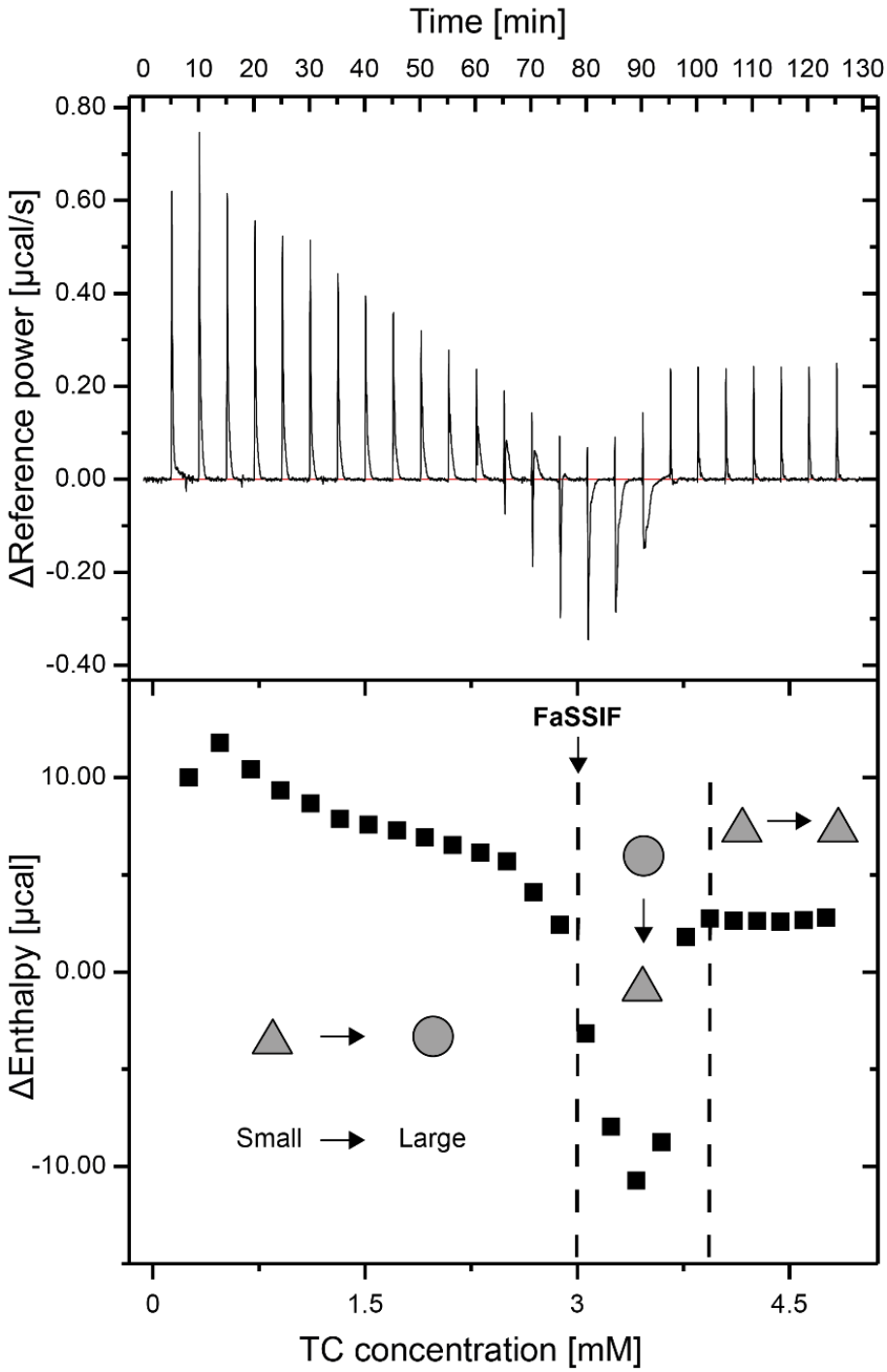

Figure S21: ITC data resulting from titration of tenfold concentrated FaSSIF (30 mM TC and 7.5 mM L in PBS) to PBS. The top graph shows the raw data of the reference power and the bottom graph shows the calculated enthalpy data. Reduction in colloidal size was exothermic and vice versa.

Chapter 2: Leveraging bile solubilization of poorly water-soluble drugs by rational polymer selection

Jonas Schlauersbach[1,#], Simon Hanio[1,#], Bettina Lenz[1], Sahithya P. B. Vemulapalli[2], Christian Griesinger[2], Ann-Christin Pöppler[3], Cornelius Harlacher[4], Bruno Galli[4], Lorenz Meinel[1,5]

[1] Institute for Pharmacy and Food Chemistry, University of Wuerzburg, Am Hubland, DE-97074 Wuerzburg, Germany
[2] Max Planck Institute for Biophysical Chemistry, Am Faßberg 11, DE-37077 Goettingen, Germany
[3] Institute of Organic Chemistry, University of Wuerzburg, Am Hubland, DE-97074 Wuerzburg, Germany
[4] Novartis Pharma AG, Lichtstrasse 35, CH-4056 Basel, Switzerland
[5] Helmholtz Institute for RNA-based Infection Biology (HIRI), Josef-Schneider-Straße 2/D15, DE-97080 Wuerzburg, Germany
[#] These authors contributed equally to this work.

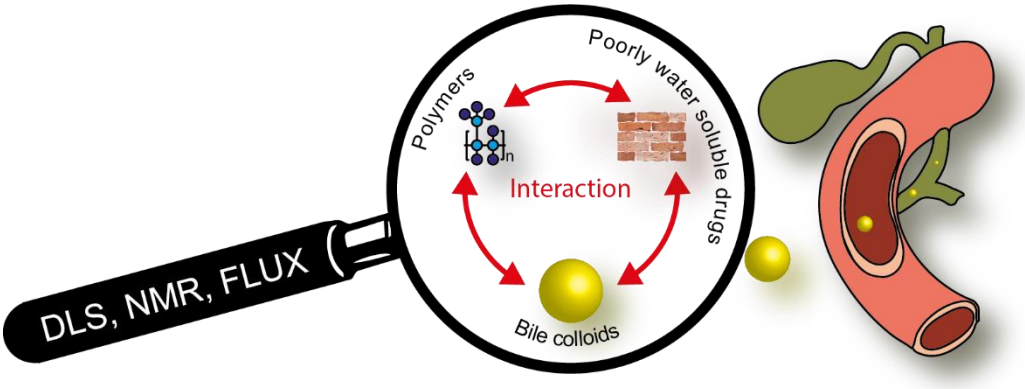

This chapter was originally published in Journal of Controlled Release. Reprinted with permission from Schlauersbach J., et al. Journal of controlled release, "Leveraging bile solubilization of poorly water-soluble drugs by rational polymer selection", vol. 330, pp. 36-48, 2021;
DOI: 10.1016/j.jconrel.2020.12.016.

Abstract

Poorly water-soluble drugs frequently solubilize into bile colloids and this natural mechanism is key for efficient bioavailability. We tested the impact of pharmaceutical polymers on this solubilization interplay using proton nuclear magnetic resonance spectroscopy, dynamic light scattering, and by assessing the flux across model membranes. Eudragit E, Soluplus, and a therapeutically used model polymer, Colesevelam, impacted the bile-colloidal geometry and molecular interaction. These polymer-induced changes reduced the flux of poorly water-soluble and bile interacting drugs (Perphenazine, Imatinib) but did not impact the flux of bile non-interacting Metoprolol. Non-bile interacting polymers (Kollidon VA 64, HPMC-AS) neither impacted the flux of colloid-interacting nor colloid-non-interacting drugs. These insights into the drug substance/polymer/bile colloid interplay potentially point toward a practical optimization parameter steering formulations to efficient bile-solubilization by rational polymer selection.

Introduction

Long-lasting supersaturating systems and/or strategies increasing dissolution rates address pharmaceutical challenges of **p**oorly **w**ater-**s**oluble **d**rugs (**PWSD**),[1] including salt design,[2-7] nanoparticles[8, 9] and, **a**morphous **s**olid **d**ispersions (**ASD**)[10, 11] among other approaches[12-17] to obtain reproducible and adequate **p**harmaco**k**inetics (**PK**). Polymer excipients used for drug formulation were traditionally referred to as "inert"[18-20] in spite of a role in e.g. drug transporter inhibition,[21] allergic reactions,[22] or physicochemical interactions.[23] Other reports highlighted the impact of these excipients on the natural solubilization systems[24, 25] and the current manuscript is within this context. Bile salts (including **t**auro**c**holate – **TC**), phospholipids (including **l**ecithin – **L**), cholesterol, and lipids pour out of the common bile duct into the duodenum and are largely reabsorbed in the ileum.[26] The resulting aqueous **t**auro**c**holate and **l**ecithin **mi**xed **mi**celles (denoted **TC/L MIM**) form the natural solubilization systems for poorly water-soluble vitamins and PWSDs.[27-30] For example, MIM solubilization is key for vitamin K absorption,[31] e.g. reflected by the fact that healthy neonates readily absorb orally given vitamin K,[29] while absorption occurs to a lesser extent in neonates with an obstructed bile duct/cholestasis.[32] For the most part, the focus of publications on pharmaceutical polymers detail aspects of drug dissolution and the impact on drug permeation across the gut epithelial barrier.[33-35] Selected examples along these lines are the use of **H**ydroxy**p**ropyl **m**ethyl**c**ellulose **a**cetate **s**uccinate (**HPMC-AS**) increasing the bioavailability of a PWSD,[36] while the amino methacrylate copolymer Eudragit E, though increasing the apparent drug solubility *in vitro*, resulted in delayed and reduced systemic availability as compared to control without polymer.[37] We hypothesize that reduced bioavailability for PWSDs in the presence of polymer excipients such as Eudragit E is in part due to polymer induced changes in the MIM colloidal structure, thereby impacting MIM solubilization of drugs. We used **Fa**sted **S**tate **S**imulated **I**ntestinal **F**luid (**FaSSIF**) as a model biological fluid containing TC/L MIM as seen in bile.[24, 27, 38] We characterized the impact of polymers (modified polyallylamine (Colesevelam), Eudragit E, polyvinyl caprolactam–polyvinyl acetate–polyethylene glycol graft copolymer (Soluplus), vinylpyrrolidone-vinyl acetate copolymer (Kollidon VA 64), and HPMC-AS) on the molecular interaction within TC/L MIM by **^{1}H n**uclear **m**agnetic **r**esonance (**^{1}H NMR**) and on changes on colloidal geometries by **d**ynamic **l**ight **s**cattering (**DLS**). Both methods combined provided the necessary granularity to assess geometries by hydrodynamic radii and molecular interaction by ^{1}H NMR analysis. Throughout the manuscript we are using the terms "MIM interacting polymers" or "MIM *non*-interacting polymers" to indicate the interaction of *polymers* with TC/L MIM. Colesevelam was selected as a model polymer used therapeutically due to its bile

acid/TC binding ability.[39] Eudragit E is a glazing agent used for taste masking in many pharmaceutical formulations[40, 41] and in ASD formulations.[42] Soluplus has also been used for ASDs.[43, 44] Kollidon VA 64 is a dry binder, granulating agent, and film forming agent,[45] HPMC-AS an enteric coating material,[46] and both polymers are used as solid dispersion carrier, or precipitation inhibitor.[47] Furthermore, we compared the polymer impact on the solubilization and flux across an artificial membrane for the poorly water soluble drugs Perphenazine and Imatinib with the water soluble and well permeable drug Metoprolol.[48] Throughout the manuscript we are using the terms "MIM interacting drugs" or "MIM *non*-interacting drugs" to indicate the interaction of *drugs* with TC/L MIM. The flux across these artifical membranes has been previously correlated to bioavailability.[49-51] The outcome of our experiments led to a preliminary decision tree by which drug substances are firstly categorized in those for which interaction with bile colloids is critical or not. Depending on this initial classification, secondly classes of pharmaceutical polymers are proposed for TC/L MIM solubilizing drug substances or for drug substance, which do not or marginally interact with TC/L MIM.

Materials and Methods

Materials

Hydroxypropyl methylcellulose acetate succinate (HPMC-AS, grade LF) was obtained from Shin-Etsu Chemical Co Ltd. (Tokyo, Japan). Eudragit E PO was kindly provided by Evonik Nutrition and Care GmbH (Essen, Germany). Kollidon VA 64 and Soluplus were kindly provided by BASF SE (Ludwigshafen, Germany). Colesevelam was purchased from BOCSCI Inc. (New York, USA). Deionized, purified water (Millipore water) was generated by in-house Millipore purification system from Merck KGaA (Darmstadt, Germany). Hexadeuteriodimethyl sulfoxide (DMSO-d_6, 99.8% D) was purchased from Euriso-top (Saarbrücken, Germany) and deuterated water (D_2O, 99.9% D) from Deutero GmbH (Kastellaun, Germany). Deuterated water (D_2O, 99.9% D) containing 0.05% 3-(trimethylsilyl)propionic-2,2,3,3-d_4 sodium salt (TSP-d_4), 40% sodium deuteroxide in deuterated water (NaOD, 99% D), 35% deuterium chloride in deuterated water (DCl, 99% D), sodium chloride (99%), monobasic sodium phosphate monohydrate (99%), D-α-Tocopherol polyethylene glycol 1000 succinate (Vitamin E TPGS), Perphenazine (99%), Metoprolol (99%) were purchased from Sigma-Aldrich (Schnelldorf, Germany). Imatinib free base was kindly provided by Novartis Pharma AG (Basel, Switzerland). Coaxial insert tubes and NMR tubes (5 mm, clear and amber glass) were purchased from Norell, Inc. (Landisville, PA USA). FaSSIF (FeSSIF/FaSSGF) powder was purchased from

biorelevant.com Ltd. (London, UK). All other standard chemicals and laboratory consumables, if not stated otherwise, were purchased from either VWR International GmbH (Ismaning, Germany) or Sigma-Aldrich.

Methods

Dynamic Light Scattering

DLS was assessed by a DelsaNanoHC particle analyzer (Beckman Coulter Inc., Brea, California) with a backscattering angle of 165°. Modified **p**hosphate **b**uffered **s**aline pH 6.5 (**PBS**) and FaSSIF-V1 (hereinafter referred to as TC/L in PBS) with a concentration of 3 mmol/l TC and 0.75 mmol/l L were prepared according to the manufacturer's protocol (biorelevant.com). The respective polymer amount in medium (PBS or TC/L in PBS) was shaken for 2 h at 25 °C, 750 rpm on a Thermomixer F1.5 (Eppendorf AG, Hamburg, Germany). Unfiltered samples were measured in disposable 1.5 ml UV-Cuvettes (Brand GmbH & Co. KG, Wertheim, Germany) in triplicate with an accumulation of 70 scans in each run. Data was analyzed using the CUMULANT method. The Z-Average particle size was evaluated with a refractive index of 1.333 as determined for TC/L in PBS by an Abbe refractometer (Carl Zeiss AG, Oberkochen, Germany). The hydrodynamic diameter was adjusted by the dynamic viscosities of the respective solutions as read with a rolling-ball viscometer LOVIS 2000 M using capillary LOVIS 1.8 equipped with a steel ball at an inclination angle of 70° (diameter 1.5 mm, steel 1.4125, density 7.66 g/cm^3, Anton Paar GmbH, Graz, Austria). The temperature was set to 298 K for all experiments. Density was determined using an Anton Paar Density Meter DMA 4100 M. Samples with visible particles were excluded from statistical analysis.

^{1}H Nuclear Magnetic Resonance Spectroscopy

For ^{1}H NMR measurements a 0.1 mol/l DMSO-d_6 drug stock solution was prepared. Deuterated water was used for media preparation. Briefly, for pH adjustment in deuterated water a correction factor was used adjusting pD to 6.91 using DCl and NaOD.[52] Perphenazine experiments were carried out under light protection. 1 mmol/l drug solutions were prepared by adding stock solution to the deuterated medium or polymer/medium mixtures, subsequently shaking for 2 h, 25 °C, and 750 rpm on a Thermomixer. ^{1}H NMR spectra were recorded on a Bruker Avance 400 MHz spectrometer (Bruker BioSpin GmbH, Karlsruhe, Germany) operating at 400.13 MHz with a BBI BB-H 5 mm probe head and at a temperature of 300 K. For ^{1}H NMR experiments the acquisition parameters were set to 256 scans with 56 dummy scans for sample equilibration, flip angle of 30°, a broad spectral width of 20.55 ppm to record all possible signals, and transmitter offset of 6.175 ppm. The acquisition time was 3.985 seconds followed by a relaxation delay of 1.0 second with

collection of 64 000 data points at a sample spinning frequency of 20 Hz to ensure proper signal resolution (no spinning side bands were observed). The data were processed using TopSpin 4.0.6 (Bruker BioSpin). An exponential line broadening window function of 0.3 Hz was used (no difference in noise was seen at 0.5 Hz, data not shown). Automatic baseline correction and manual phasing were applied. The chemical shifts were referenced to the external standard of 0.05% TSP-d_4 in D_2O filled in a coaxial insert tube. Proton peaks from deuterated solvents such as DMSO-d_6 are denoted DMSO-d_5 which comprises all isotopomers of DMSO with at least one detectable proton. For ^{1}H **d**iffusion-**o**rdered **s**pectroscop**y** (DOSY) polymers and media compounds were dried (60 °C, 24 h) in a vacuum drier (Heraeus GmbH, Hanau, Germany). Samples in deuterated TC/L in PBS and PBS were prepared in a constantly nitrogen flushed sekuroka glove box (Carl Roth GmbH & Co. KG, Karlsruhe, Germany). Signal assignment was done using ^{13}C, ^{1}H-^{1}H **co**rrelated **s**pectroscop**y** (COSY), and edited ^{1}H-^{13}C **h**eteronuclear **s**ingle **q**uantum **c**oherence (**HSQC**) spectra as described before [24]. DOSY spectra were recorded at 298 K on Bruker Avance Neo 600 MHz spectrometer (Bruker BioSpin) operating at 600.25 MHz for ^{1}H, equipped with a 5 mm TCI cryo probe containing a z-axis gradient coil with a maximum gradient strength of 58.305 G cm^{-1}. A pulse sequence for diffusion measurement using double stimulated echo for convection compensation and longitudinal eddy current delay sequence with bipolar gradient pulses for diffusion and 3 spoil gradients was used (dstebpgp3s).[53, 54] A series of 16 spectra with a linear gradient ramp from 25 to 70% of the maximum gradient strength were recorded with an eddy current delay of 5 ms and a recycle delay of 5 s. The water (HDO) diffusion coefficients were obtained after data processing by fitting signal intensity at 4.703 ppm using dynamics center 2.6 (Bruker BioSpin) as a function of gradient strength (Eq. 1).

$$I(G) = I_0 \cdot e^{-\gamma^2 \cdot G^2 \cdot \delta^2 \cdot (\Delta - \frac{\delta}{3}) \cdot D} \quad \text{(Eq.1)}$$

Where $I(G)$ is the gradient strength dependent signal intensity, I_0 initial signal intensity, γ gyromagnetic ratio of protons (4258 Hz/Gauss), G gradient strength, δ gradient length (2 ms), Δ diffusion time (50 ms), and D diffusion coefficient. The HDO signal decayed to below 5% of the initial signal intensity.

Flux

A side-by-side diffusion cell (PermeGear Inc., Hellertown, USA) was used (for assay workflow refer to **Figure S1**). The donor and receiver compartments (each with a filling volume of 10 ml) were separated by a regenerated cellulose membrane with an average pore size of 33 nm according to the manufacturer (innoME GmbH, Espelkamp, Germany). The orifice had a diameter of 15 mm resulting in a surface area of 1.77 cm^2. The five polymers were tested either in TC/L in PBS or in PBS (0.05% and 1%; % means weight per weight

unless stated otherwise) and shaken on an orbital shaker Reax 20 for 2 h (Heidolph GmbH, Schwabach, Germany), and then transferred to the donor chamber. Eudragit E was additionally tested at a concentration of 0.01%. The receiver compartment was filled with PBS containing 0.2% Vitamin E TPGS. In all experiments, the maximum concentration in the receiver cell was less than one tenth of the amount added to the donor (sink condition). The temperature was held at 298 K using a Haake Fisons C1 water circulator (Thermo Fisher Scientific Inc., Karlsruhe, Germany) with a DLK 1002 cooling unit (FRYKA GmbH, Esslingen, Germany). The fluids in the cells were stirred continuously at 500 rpm on a H9-CB-02 stirring apparatus (SES GmbH, Bechenheim, Germany). At the beginning of the diffusion experiment, a 0.1 mol/l drug stock solution in DMSO was added to achieve a nominal starting concentration of 1 mmol/l. The total amount of DMSO never exceeded 1% (v/v). Perphenazine experiments were carried out under light protection. After 5, 15, 30, 60, 120, 180, and 240 minutes aliquots of 100 µl were taken from the receiver medium and replaced with fresh PBS containing 0.2% Vitamin E TPGS. Subsequently, the samples were diluted with 25 µl of **ac**eto**n**itrile (**ACN**) containing 0.1% **t**rif**l**uoro**a**cetic acid (**TFA**), vortexed for at least 30 seconds (VTX-3000L, LMSCO. LTD., Tokyo, Japan), and centrifuged with a MiniSpin centrifuge (Eppendorf) at 13000 rpm for 10 minutes.

High Pressure Liquid Chromatography Analysis

High **P**ressure **L**iquid **C**hromatography (**HPLC**) was used to determine the receiver compartment concentration change over time. The flux in nmol/min·cm² was obtained from the slope of the resulting concentration versus time profile using linear regression per permeated area. The amount of drug in the acceptor increased linearly showing a high coefficient of correlation ($R^2 > 0.996$). Experiments were carried out in triplicate. Samples were analyzed with an Agilent 1260 infinity II HPLC (Agilent Technologies Inc., Waldbronn, Germany) using a Synergi™ 4 µm Hydro-RP18 80 Å 150 x 4.6 mm LC column (Phenomenex LTD, Aschaffenburg, Germany). The device was equipped with a variable wavelength detector (G7114A, Agilent), an automatic vialsampler (G7129C, Agilent), flexible Pump (G7104C, Agilent), and multicolumn oven (G7116A, Agilent). Mobile phase A was 0.1% TFA in Millipore water. Mobile phase B was ACN with 0.1% TFA, flow was set to 1 ml/min, injection volume was 50 µl, and the wavelength of the detector was set to λ = 255 nm for Perphenazine, λ = 267 nm for Imatinib, and λ = 275 nm for Metoprolol. The gradient started at 20% B increasing to 100% within 6 minutes, held for 4 minutes, then back to 20% B within 1 minute, and held for 4 minutes. Quantification was done by calibration curves (**Figure S2**).

Statistical Analysis

DLS and Metoprolol flux were statistically evaluated by one-way ANOVA followed by *post hoc* Dunnett's test for pairwise comparison with the control group. For flux, pairwise comparisons of all groups were done by *post hoc* Tukey test. Homogeneity of variance was tested by a Levene-test. A double-sided Grubb's test was used for outlier testing and excluded data points are always mentioned in the respective figure legend. Data was considered statistically significant at $p \leq 0.05$. OriginPro 2017 (OriginLab Corporation, Northampton, MA, USA) was used for statistical analysis.

Results

Drug interaction with taurocholate/lecithin mixed micelles

We analyzed the interaction of Perphenazine and Metoprolol with TC/L MIM by ^{1}H NMR spectroscopy. In the ^{1}H NMR spectrum, the TC/L signals appeared in the range 0.7 to 5.3 ppm which is in agreement with the previously reported measurement (**Figure 1A, S3, S4**).[24] TC H12, H7, H3, H21, H19, H18, and L H4 proton signals shifted to lower ppm in the presence of Perphenazine thereby indicating interaction of the drug substance with TC/L MIM. This was also reflected by Perphenazine's aryl-proton signals shifting to lower ppm in the presence of TC/L MIM (**Figure 1B, S4, S7**). In contrast, no chemical shift of TC/L signals were observed in the presence of Metoprolol including Metoprolol's aryl-proton resonances (**Figure 1A, 1C**), orthogonally confirming previous reports.[55] We refer to analogous studies for Imatinib, which is integrated into the assessment of drug substance/polymer/TC/L MIM interactions (*vide infra*).[24] Complete ^{1}H NMR spectra, chemical structures, and the approach of aryl-proton spectra interpretation is outlined in the supplementary information (**Figure S3-8**).

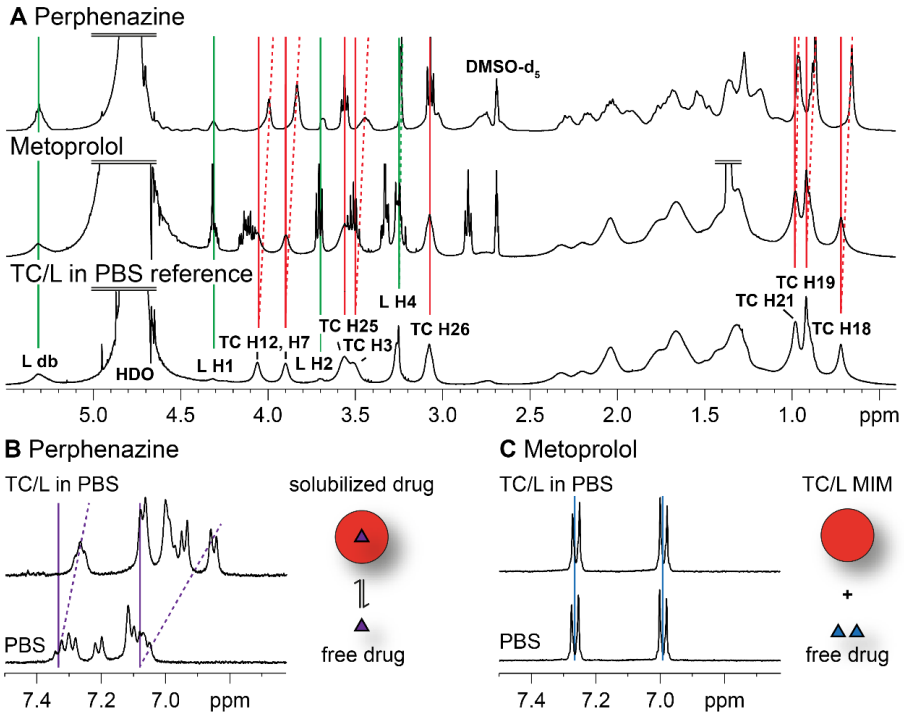

Figure 1: ^{1}H NMR spectra of Perphenazine – interacting with TC/L MIM - and Metoprolol - not interacting with TC/L MIM. (A) ^{1}H NMR spectra of TC/L in PBS as reference (bottom; green and red lines for L and TC signals, respectively), TC/L in PBS with Metoprolol (center), and TC/L in PBS with Perphenazine (top). ^{1}H NMR aryl-proton excerpt of (B) Perphenazine, and (C) Metoprolol in TC/L in PBS (top), and in PBS (bottom) including cartoons abstracting findings for the TC/L MIM interaction with (B) Perphenazine (purple triangle) and absence of interaction of (C) Metoprolol (blue triangles). Signal shifts are indicated by dotted lines.

Polymer interaction with taurocholate/lecithin mixed micelles

We characterized the polymers in PBS and their impact on TC/L in PBS concerning colloidal size change and molecular interaction by DLS and ^{1}H NMR spectroscopy, respectively. The hydrodynamic diameter of TC/L MIM was 73.0 ± 0.9 nm (**Figure 2A**). Colesevelam at 0.5 and 1% resulted in visually turbid samples (**Figure 2A**). Eudragit E - insoluble at 0.01% in TC/L in PBS – was visually turbid (**Figure 2B**). At ≥ 0.05% Eudragit E, particles were formed with 15 to 30 nm in diameter. Soluplus did not impact the size of the TC/L MIM other than at 1% (**Figure 2C**) nor did Kollidon VA 64 (**Figure 2D**), or HPMC-AS (**Figure 2E**). DLS results of the polymers in PBS are detailed in the supplementary information (**Figure S9, Table S1-3**).

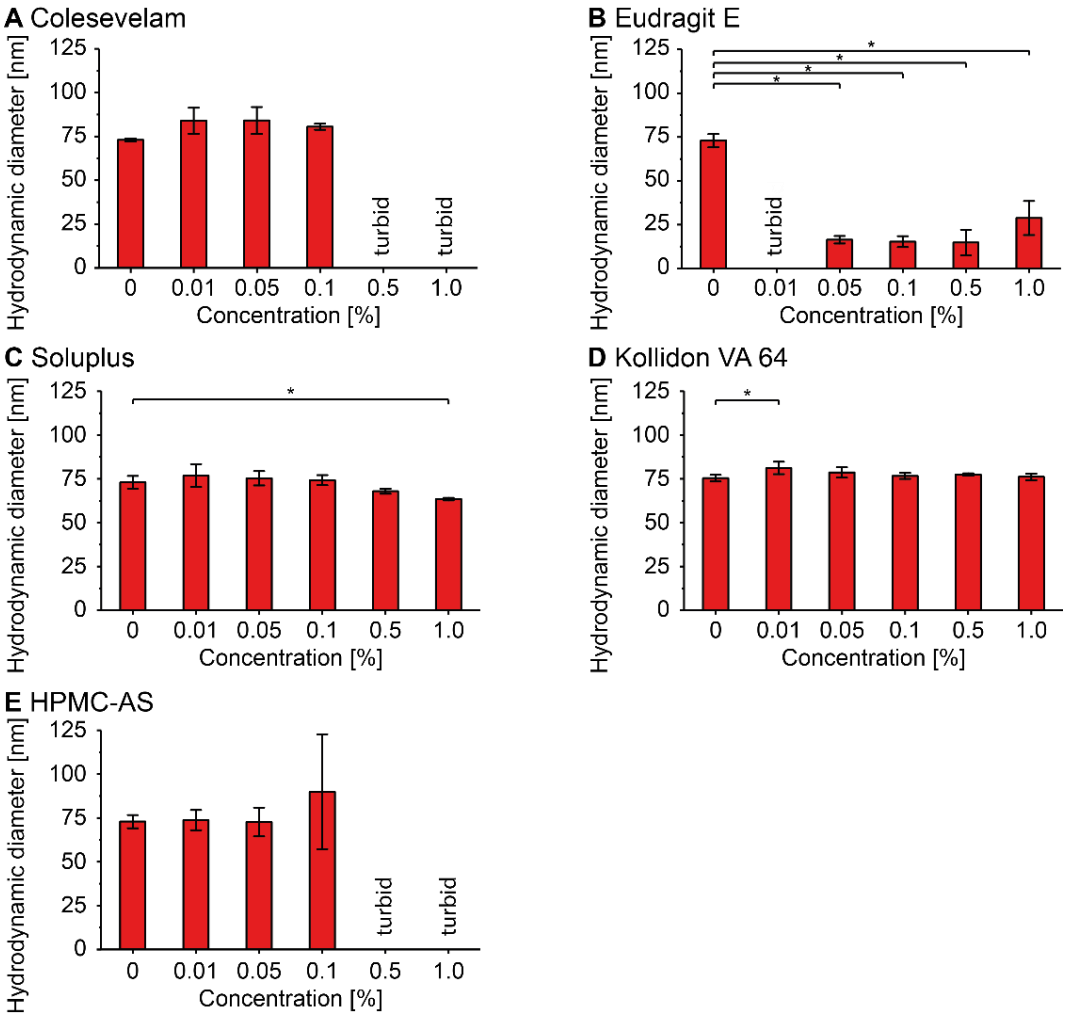

Figure 2: Hydrodynamic diameter of colloids in TC/L in PBS with (A) Colesevelam, (B) Eudragit E, (C) Soluplus, (D) Kollidon VA 64, and (E) HPMC-AS at concentrations as indicated measured by DLS. DLS outcome from turbid samples is qualitatively reported. Data shown as mean ± **s**tandard **d**eviation (**SD**), ANOVA considering $p \leq 0.05$ as statistically significant followed by Dunnett's *post-hoc* for pairwise comparison to the 0% polymer group (significant differences are shown by asterisks).

Furthermore, we analyzed polymers in TC/L in PBS and in PBS by ^{1}H NMR spectroscopy. No Colesevelam signals were seen in PBS and the TC/L signal intensities decreased in presence of this TC binding polymer (**Figure 3A**). Eudragit E reduced the intensity of the TC/L signals with signal broadening observed for TC protons in the range 0.5 to 1.2 ppm (**Figure 3B**).

TC signals from 3.8 to 4.2 ppm were no longer observed, while L H4 at 3.25 ppm and TC H26 at 3.1 ppm remained detectable. Soluplus effects in TC/L in PBS were comparable to Eudragit E (**Figure 3C**). In contrast, neither the presence of Kollidon VA 64 (**Figure 3D**) nor HPMC-AS (**Figure 3E**) shifted TC/L signals. Concentration dependent polymer effects on TC/L signals, polymer signals in PBS, chemical structures, and complete ^{1}H NMR spectra are detailed in the supplementary information (**Figure S10-S22**).

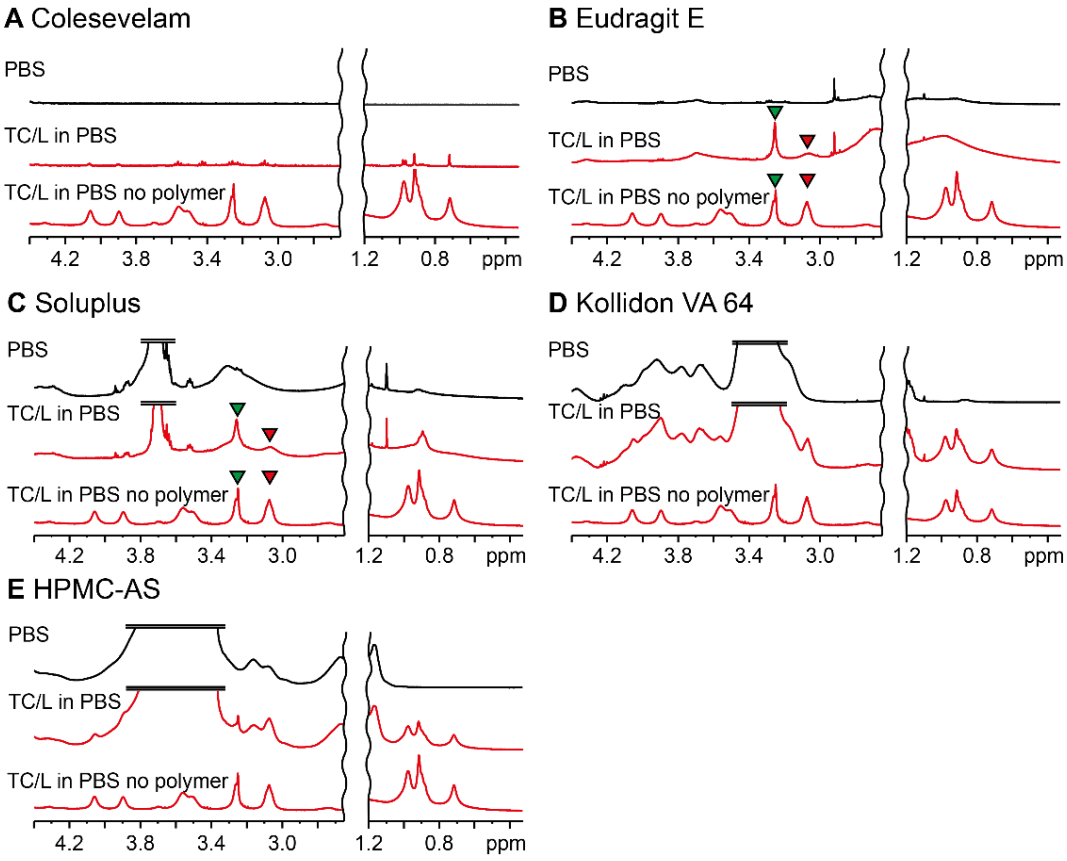

Figure 3: Extracts from ^{1}H NMR spectra of 1% (A) Colesevelam, (B) Eudragit E, (C) Soluplus, (D) Kollidon VA 64, and (E) HPMC-AS in PBS (top, black), in TC/L in PBS (center, red), and for comparison and identical across panels in TC/L in PBS without polymer as reference (bottom, red). L H4 (green triangle pointing at 3.25 ppm) and TC H26 (red triangle pointing at 3.1 ppm) are highlighted for the assessment of polymer/TC/L MIM interaction, which was seen for (A) Colesevelam, (B) Eudragit E, and (C) Soluplus but not (D) Kollidon VA 64, nor (E) HPMC-AS.

Impact of polymers on Perphenazine flux across and aryl-proton signals in presence and in absence of taurocholate/lecithin mixed micelles

Subsequently, we focused on the impact of the polymers on Perphenazine's flux in TC/L in PBS and in PBS across regenerated cellulose membranes, which were previously used in correlation studies of flux and bioavailability.[49-51] DLS studies indicated that aggregates did not permeate across the cellulose membrane (nominal pore size 33 nm according to the manufacturer), including aggregates bellow 33 nm as seen for Eudragit E (data not shown). Perphenazine's flux was reduced by 82% when solubilized into TC/L MIM as compared to PBS (**Figure 4**). Colesevelam increased the Perphenazine flux in TC/L in PBS in a concentration dependent manner contrasting observations in PBS (**Figure 4A**). Increased Perphenazine flux was recorded at low Eudragit E concentrations (0.01 and 0.05%) in TC/L in PBS but was reduced at 1% Eudragit E in TC/L in PBS and at all Eudragit E concentrations in PBS (**Figure 4B**). Soluplus resulted in a concentration dependent flux decrease in both TC/L in PBS and in PBS (**Figure 4C**). The flux did not change in TC/L in PBS when Kollidon VA 64 was added but decreased in PBS at 1% Kollidon VA 64 (**Figure 4D**). Similarly, HPMC-AS did not reduce the flux in TC/L in PBS, contrasting findings in PBS (**Figure 4E**). The lag time of Perphenazine increased at 1% Eudragit E in TC/L in PBS and in PBS as compared to without polymer (**Figure 4F**). Colesevelam reduced the lag time as a function of the polymer concentration in TC/L in PBS. 1% HPMC-AS increased the lag time in TC/L in PBS and in PBS (**Figure S44**). In addition to flux experiments, we analyzed Perphenazine's aryl-proton signals in TC/L in PBS in the presence of the polymers detailing the molecular interactions likely driving the flux effects.

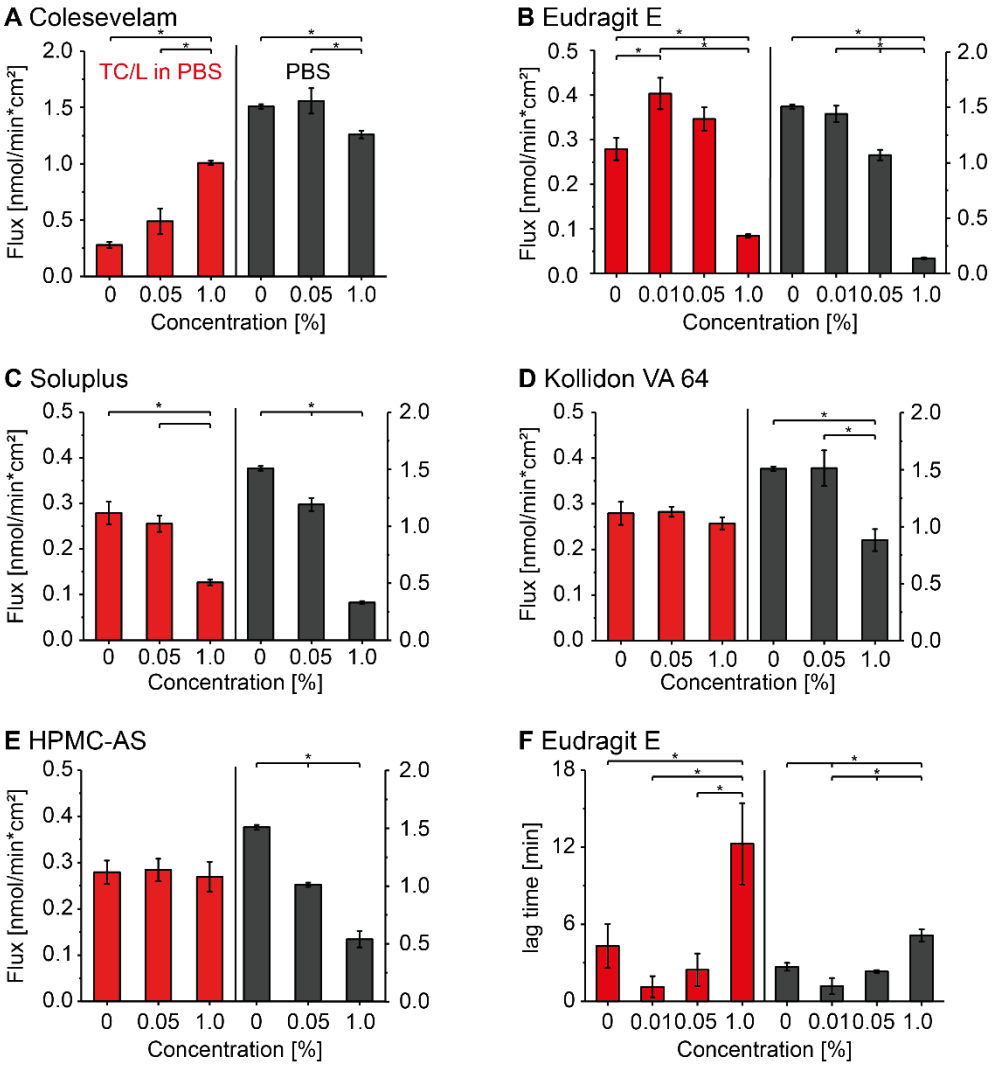

Figure 4: Perphenazine flux with (A) Colesevelam, (B) Eudragit E, (C) Soluplus, (D) Kollidon VA 64, and (E) HPMC-AS in TC/L in PBS (red) and in PBS (black) at concentrations as indicated. (F) Lag time with Eudragit E in TC/L in PBS (red) and in PBS (black) at concentrations as indicated. The left ordinate refers to data recorded in TC/L in PBS (red bars), the right ordinate to in PBS (black bars). Data at 0% polymer concentration are identical for all flux panels and given for comparison. Data shown as mean ± SD, ANOVA considering $p \leq 0.05$ as statistically significant followed by Tukey *post-hoc* test for pairwise comparison (significant differences are shown by asterisks).

Signals broadened and shifted to higher ppm at 1% Colesevelam as compared to Perphenazine in TC/L in PBS, while in PBS signal intensity decreased and signals broadened (**Figure 5A**). The aryl-proton signals shifted to higher ppm with increasing Eudragit E concentration, decreased in intensity, and disappeared at 1% Eudragit E in TC/L in PBS (**Figure 5B**). In PBS, aryl-proton signals shifted with increasing Eudragit E concentration to lower ppm and broadened along with intensity decrease. Soluplus decreased Perphenazine's signal intensity with increasing polymer concentration in TC/L in PBS and in PBS (**Figure 5C**). Additionally, broadening of the signals was observed.

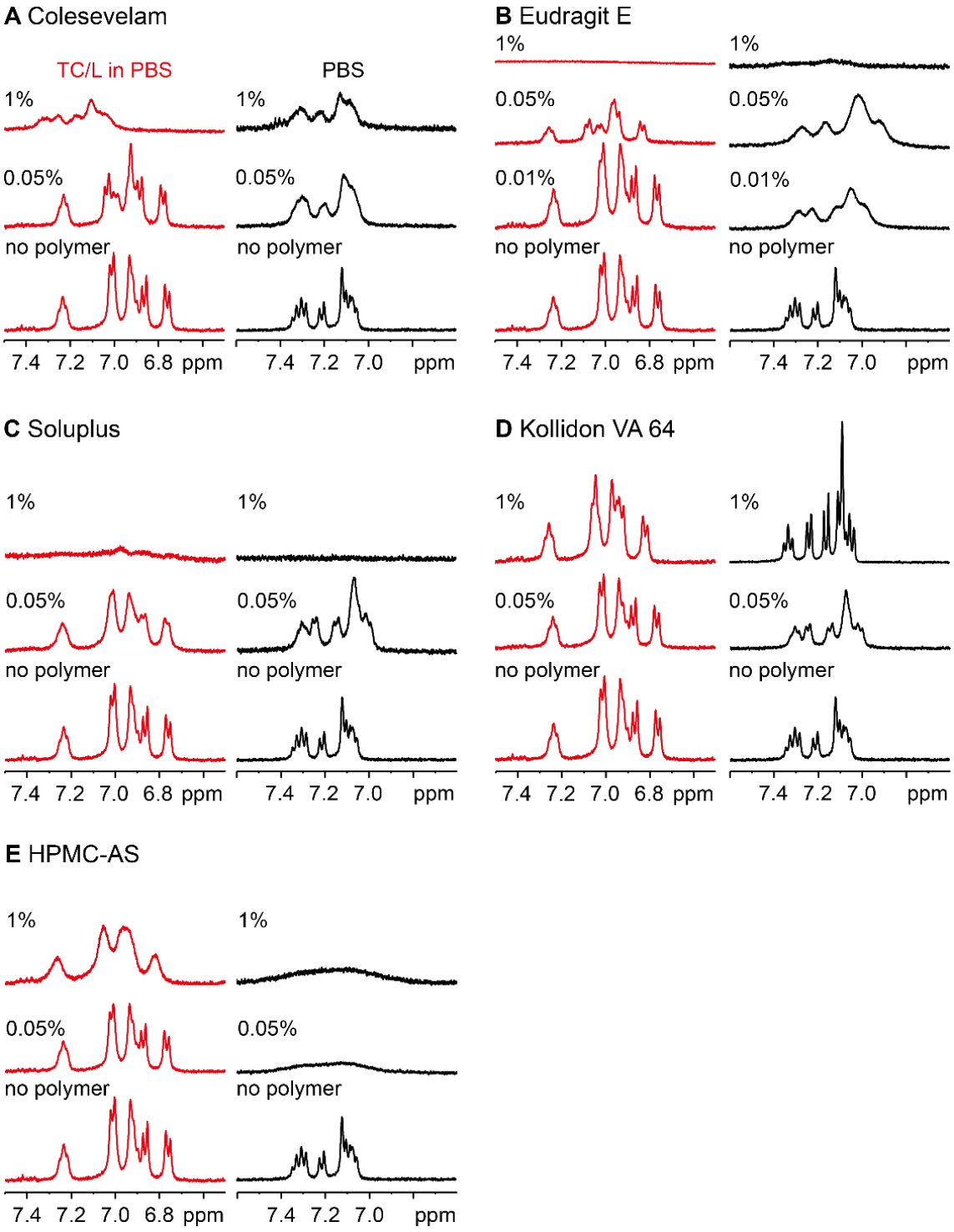

Figure 5: ^{1}H NMR excerpt of Perphenazine aryl-protons in TC/L in PBS (red) and in PBS (black) with (A) Colesevelam, (B) Eudragit E, (C) Soluplus, (D) Kollidon VA 64, and (E) HPMC-AS at concentrations as indicated. The reference spectrum of Perphenazine recorded in TC/L in PBS (red) and in PBS (black) is identical across panels and for comparison (no polymer).

Kollidon VA 64 had no impact on the aryl-proton signals and only a slight shift to higher ppm was observed in TC/L in PBS (**Figure 5D**). In PBS signals sharpened and intensity increased as compared to Perphenazine in PBS. Perphenazine's aryl-proton signals broadened and shifted to higher ppm at 1% HPMC-AS with unchanged signal intensity in TC/L in PBS (**Figure 5E**). In PBS signals broadened and intensity decreased as a function of HPMC-AS concentration. Our interpretation of the aryl-proton spectra is outlined (**Figure S8**) and complete ^{1}H NMR spectra are provided in the supplementary information (**Figure S23-S27**).

Impact of polymers on Imatinib flux across and aryl-proton signals in presence and in absence of taurocholate/lecithin mixed micelles

In addition to Perphenazine, we analyzed the impact of the polymers on Imatinib's flux in TC/L in PBS and in PBS (**Figure 6**).

Imatinib's interaction with TC/L MIM was previously described.[24] Imatinib's flux was reduced in TC/L in PBS as compared to in PBS. Adding Colesevelam to TC/L in PBS increased the flux as a function of Colesevelam concentration (**Figure 6A**). At 1% Colesevelam, the flux in TC/L in PBS was within the range of flux in PBS. At 0.05% Eudragit E, the flux increased in TC/L in PBS and decreased at 1% Eudragit E in TC/L in PBS and in PBS (**Figure 6B**). Soluplus reduced the flux in a concentration dependent manner in both, in TC/L in PBS and in PBS (**Figure 6C**). Kollidon VA 64 reduced Imatinib flux at 1% in TC/L in PBS (**Figure 6D**), as well as in PBS throughout the entire concentration range (**Figure 6D**). HPMC-AS also reduced the Imatinib flux at 1% in TC/L in PBS and in PBS (**Figure 6E**). The lag time was significantly increased in presence of 1% Eudragit E in TC/L in PBS but not in PBS (**Figure 6F**) and the other polymers had no impact on the lag time (**Figure S45**).

We also analyzed Imatinib's aryl-proton signals in the presence of the polymers in TC/L in PBS and in PBS. Imatinib aryl-proton signals in TC/L in PBS sharpened and shifted at 1% Colesevelam as compared to Imatinib without polymer (**Figure 7A**). At 1% Colesevelam in PBS, Imatinib aryl-proton signals shifted to higher ppm as compared to without polymer. Eudragit E caused signal shifts and at 1% the signals broadened and their intensity decreased in TC/L in PBS and in PBS (**Figure 7B**). Broad signals were recorded at 1% Eudragit E in TC/L in PBS.

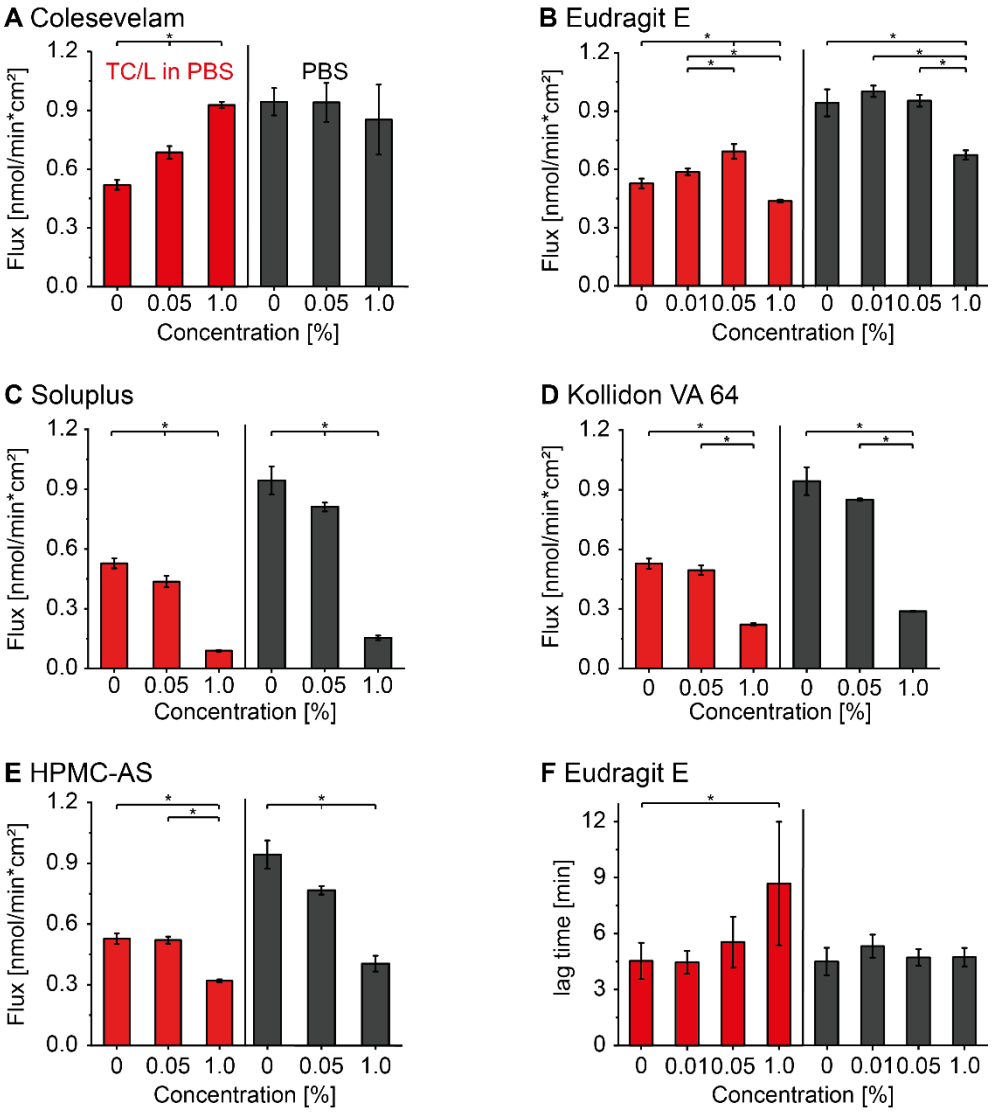

Figure 6: Imatinib flux with (A) Colesevelam, (B) Eudragit E, (C) Soluplus, (D) Kollidon VA 64, and (E) HPMC-AS in TC/L in PBS (red) and in PBS (black) at concentrations as indicated. (F) Lag time with Eudragit E in TC/L in PBS (red) and in PBS (black) at concentrations as indicated. The left ordinate refers to data recorded in TC/L in PBS (red bars), the right ordinate to in PBS (black bars). Data at 0% polymer concentration are identical for all panels and given for comparison. Data shown as mean ± SD, ANOVA considering $p \leq 0.05$ as statistically significant followed by Tukey *post-hoc* test for pairwise comparison (significant differences are shown by asterisks).

With increasing Soluplus concentration the signal intensity decreased continuously and shifting to higher ppm. At 1% Soluplus all signals disappeared in TC/L in PBS and in PBS (**Figure 7C**). In the presence of Kollidon VA 64 signals shifted to higher ppm values as a function of concentration in TC/L in PBS and in PBS (**Figure 7D**). Increasing HPMC-AS concentration resulted in signal broadening along with intensity decrease in TC/L in PBS and in PBS (**Figure 7E**). Broad signals were recorded at 1% HPMC-AS in PBS. All complete ^{1}H NMR spectra are detailed in the supplementary information (**Figure S28-S32**).

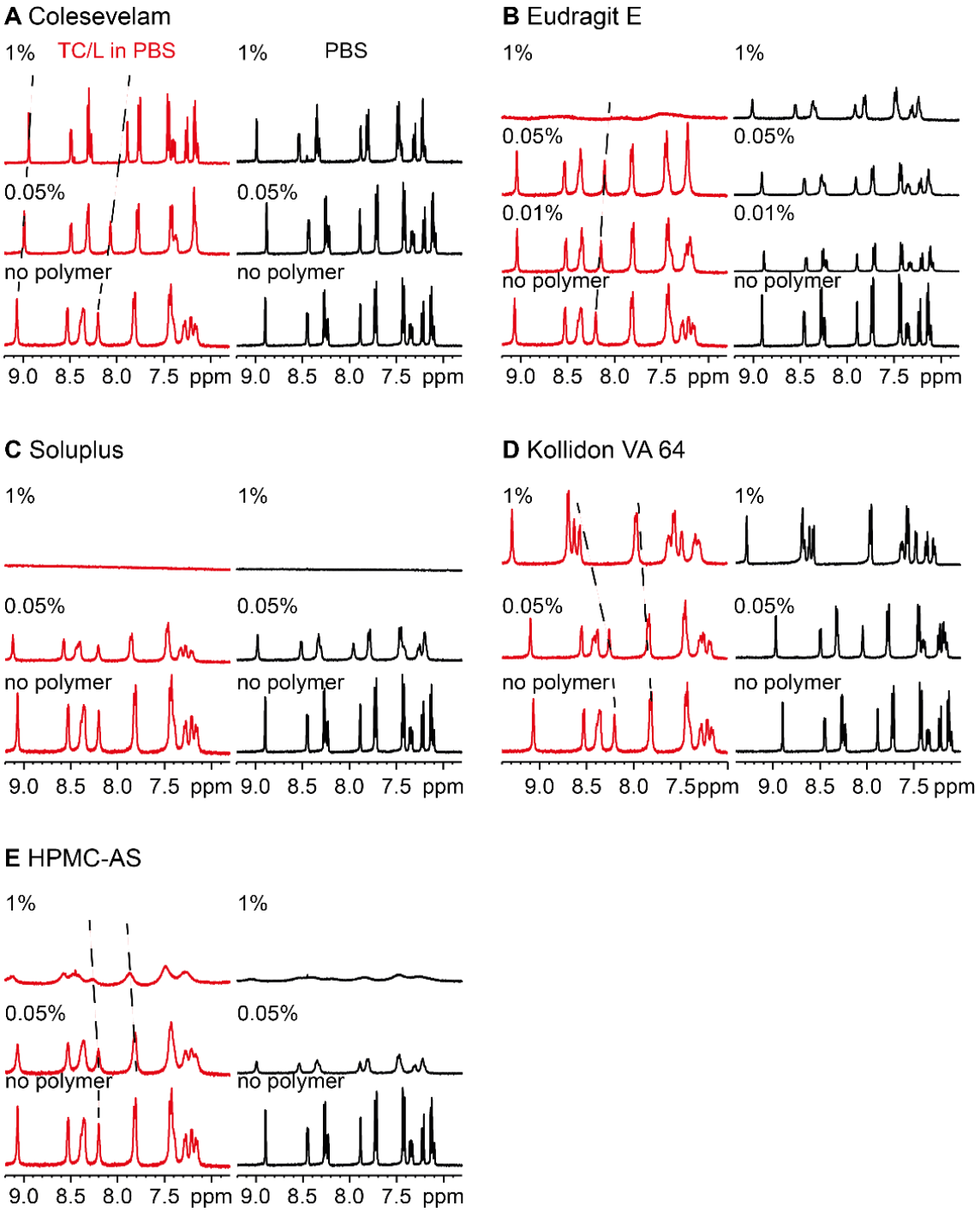

Figure 7: ^{1}H NMR excerpt of Imatinib aryl-protons in TC/L in PBS (red) and in PBS (black) with (A) Colesevelam, (B) Eudragit E, (C) Soluplus, (D) Kollidon VA 64, and (E) HPMC-AS at concentrations as indicated. The reference spectrum of Imatinib recorded in TC/L in PBS (red) and in PBS (black) is identical across panels and for comparison (no polymer). Signal shifts are indicated by dotted lines.

Impact of polymers on Metoprolol flux across and aryl-proton signals in presence and in absence of taurocholate/lecithin mixed micelles

The last studied drug was Metoprolol. The flux was reduced in TC/L in PBS as compared to in PBS (**Figure 8**). None of the polymers had an impact on Metoprolol flux in TC/L in PBS. Significant flux reduction was observed for 1% HPMC-AS in PBS as compared to in PBS. Except for Soluplus, Metoprolol aryl-proton signals were not impacted by the polymers in TC/L in PBS and in PBS (**Figure S33, S34**).

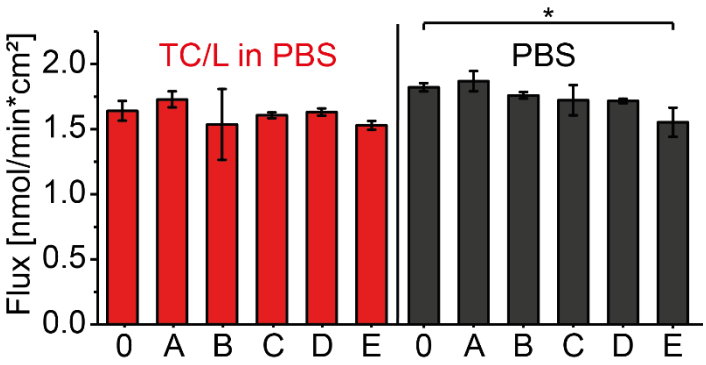

Figure 8: Metoprolol flux (0) in absence of polymer, with 1% (A) Colesevelam, (B) Eudragit E, (C) Soluplus, (D) Kollidon VA 64, and (E) HPMC-AS in TC/L in PBS (red) and in PBS (black). Data shown as mean ± SD, ANOVA considering $p \leq 0.05$ as statistically significant followed by Dunnett's *post-hoc* for pairwise comparison with the 0% polymer group (significant differences are shown by asterisks).

Diffusion coefficient of water in taurocholate/lecithin in PBS and the impact of polymer supplementation

At last, we determined diffusion coefficients of HDO in the presence of the polymers to assess the impact of diffusion on flux. The HDO diffusivity - in TC/L in PBS with Perphenazine - was $2.79 \cdot 10^{-9}$ m^2/s (**Figure S35**) and was not impacted by the presence of any of the polymers at any concentration (**Table S4**).

Discussion

Colesevelam, Eudragit E, and Soluplus impacted TC/L MIM structure (referred to as "MIM interacting polymers") and Kollidon VA 64 or HPMC-AS did not ("MIM *non*-interacting polymers"; **Figure 2, 3**). These MIM *non*-interacting polymers formed supramolecular aggregates existing next to the TC/L MIM (**Figure S9**). Perphenazine was effectively solubilized into TC/L MIM (**Figure 1**). Similarly, Imatinib was integrated into TC/L MIM as previously described.[24] In the presence of MIM interacting polymers the molecular interaction of these drugs within the MIM and the resulting free drug fraction were

significantly impacted as compared to polymer-free conditions (**Figure 4, 6**). Perphenazine shifts observed in presence of Colesevelam – used as a positive control among our polymers - were particularly striking, arguably reflecting the therapeutic use of this polymer in contrast to the other polymers which are used as excipients. In contrast, water soluble and well permeable Metoprolol did not interact with TC/L MIM (**Figure 1**) and its flux across membranes was barely or not affected by the MIM interacting polymers (**Figure 8**).

We hypothesized that MIM interacting polymers impact the molecular dynamics of TC/L MIM differently, as compared to MIM *non*-interacting polymers, and that these differences impact the flux of PWSDs across membranes. To address this hypothesis, we screened polymer concentrations from 0.01 to 1% - concentrations with possible clinical significance (**Section S6**).[41, 56-59] We started analyzing the impact of Colesevelam- an ion exchanging polymer used for bile salt binding[39] – on MIM structure and MIM molecular assembly hypothesizing and confirming that the polymer particularly impacted negatively charged TC (**Figure S3, S10, S12**). Colesevelam reduced the ^{1}H NMR signal intensity of TC and L in a Colesevelam-concentration dependent manner (**Figure 3, S12**), indicating that Colesevelam pushes TC/L from MIM into insoluble TC/L/Colesevelam particles and further reflected by the presence of aggregates (**Figure 2**). Consequently, we expected less TC/L MIM in presence of Colesevelam, hence reduced effects on crystallization inhibition, solubility, or dissolution rate of PWSDs, respectively, and as previously suggested.[60-62] Similarly, Eudragit E – frequently used in numerous formulations[41] - impacted the TC/L micellar system in a concentration dependent manner. Low Eudragit E concentrations resulted in *insoluble* aggregates containing TC/L with non-detectable ^{1}H NMR signals for L but still detectable TC signals suggesting efficient entrapment of L and to a lesser extent TC within these Eudragit E aggregates (**Figure 2, S14**). Furthermore, the lag time was significantly increased at 1% Eudragit E for both, Perphenazine and Imatinib (**Figure 4, 6**), whereas the other polymers had marginal lag time effects (**Figures S44, S45**). This may point to slower exchange kinetics of drug substance from Eudragit E structures as compared to the other polymers. Hence, Eudragit E's ability of integrating TC and L into its aggregates may critically jeopardize the solubilization of PWSD, findings which have previously suggested by others[63-65] and possibly causal to previously observed reductions in bioavailability of PWSD in presence of Eudragit E.[37, 66-68] At higher concentrations, these Eudragit E aggregates were not observed and *soluble* Eudragit E/TC/L MIM were formed. The ^{1}H NMR TC/L signals broadened and decreased in signal intensity indicating aggregates with high molecular density and the colloids were smaller for the Eudragit E/TC/L MIM as compared to TC/L MIM (**Figure 2, 3, S8, S9**). This data confirmed previous studies reporting Eudragit E dynamics leading to either insoluble or soluble supramolecular aggregates as a function of

polymer concentration.[27, 58] Similar to Eudragit E, Soluplus - an excipient enhancing the bioavailability of some PWSDs[68, 69] – interacted with TC/L MIM but in contrast to Eudragit E did not show polymer concentration effects on the formation of insoluble aggregates and soluble colloids (**Figure 3**). In alignment with previous reports, Soluplus impacted the size of TC/L MIM (**Figure 2, S8, S9**).[70, 71] Temperature effects in this range are particularly pronounced for Soluplus with a cloud point between 25 - 37 °C.[72] Kollidon VA 64 and similarly HMPC-AS at a concentration of up to 0.1% had no impact on TC/L MIM molecular structure or colloidal hydrodynamic diameters and our data indicated that pure polymer aggregates existed separate of the TC/L MIM (**Figure 2, 3**). HPMC-AS at a concentration of 0.5% and 1% generated insoluble aggregates in TC/L in PBS and in PBS resulting in turbid solutions (**Figure 2, S9**). Based on ^{1}H NMR we observed a coexistence of TC/L MIM and HPMC-AS supramolecular aggregates (**Figure 3, S20**). Soluplus had a minor impact on hydrodynamic diameters in DLS (**Figure 2**) but interacted with TC/L MIM (^{1}H NMR; **Figure 3, S25**). Future studies may further detail the resulting colloidal structures, particularly whether these structures are supramolecular or ionic. In summary, we categorized our polymers as MIM interacting (Colesevelam, Eudragit E, and Soluplus) or MIM *non*-interacting polymers (Kollidon VA 64, HPMC-AS).

We then proceeded to study the impact of either polymer category on the solubilization of drugs into TC/L MIM, and detailed the resulting supramolecular interaction of polymer, TC/L MIM, and flux. In analogy to the polymers (*vide supra*), we categorized drugs into those which interact with TC/L MIM and others that do not. Perphenazine and Imatinib interacted with TC/L MIM[24] whereas Metoprolol did not (**Figure 1**). Drug integration into the TC/L MIM - as observed for Perphenazine and Imatinib - reduced the flux across cellulose membranes (**Figure 4, 6**). These effects depended on the TC/L concentration with higher TC/L concentrations (simulating fed state) further reducing the flux (**Figure S36-S38**) and as described before.[73] Furthermore, flux depended on drug substance solubility which is why we selected a concentration (1 mmol/l) resulting in kinetically stable solutions throughout all experimental durations (**Figure S38-S43**). The flux was tested across cellulose membranes, which had previously been correlated to drug substance bioavailability.[49-51] This has been also shown for lipophilic membranes[74, 75] but we selected cellulose membranes here to focus mostly on size exclusion. We confirmed efficient size exclusion by the absence of visible particles or DLS determined structures (data not shown). Thereby, the rate limiting step in our experiments were the events in the donor chamber and not in the diffusion layer (membrane and aqueous boundary layers) for all polymers as seen with Metoprolol (**Figure 8**). In addition, we excluded possible obstruction effects by the polymers in the donor compartment as demonstrated by comparable water (HDO) diffusion in solution among the

experimental conditions (**Figure S35**).[76, 77] In conclusion, the absence of polymer obstruction effects on diffusion (**Figure S35**), absence of polymer impact on the diffusion across the diffusion layer as concluded from unaltered flux and lag time for Metoprolol (**Figure 8, S46**), we assigned the differences in flux as discussed below (**Figure 4, 6**) and lag times observed for Perphenazine and Imatinib (**Figure S44, S45**) directly to drug release phenomena from supramolecular structures including colloids being present in the donor chamber.

Starting off these findings, we studied the impact of MIM interacting polymers and MIM *non*-interacting polymers on these drugs in presence of TC/L MIM. This resulted in the differentiation of three distinct patterns. One pattern was seen with (i) Colesevelam or Eudragit E (at low concentrations) reducing the available TC/L for solubilization and consequently increasing the free drug fraction (^{1}H NMR signal shift) and flux of the MIM interacting drugs Perphenazine and Imatinib (**Figure 4-7**). An increase in free drug fraction of Perphenazine in presence of Colesevelam – as seen by higher flux (**Figure 4A**) – might also be reflected by the increased diffusion coefficient (**Table S5**). In contrast, the MIM *non*-interacting drug Metoprolol was not impacted by the presence of these polymers (**Figure 8, S33, and S34**). Metaphorically, both polymers push the drugs out of the TC/L MIM and into solution – obviously, a finding only relevant for drugs integrating into TC/L MIM. This might reduce bioavailability of drugs and fat-soluble vitamins relying on bile related solubilization.[32, 60-62] A contrasting pattern (ii) was observed for Eudragit E at higher concentration and Soluplus at any concentration. Both reduced the free drug fraction (^{1}H NMR signals shifted and decreased in intensity) and consequently the flux of MIM interacting but not MIM *non*-interacting drugs, respectively. This was in line with the formation of new colloidal structures combining all components, the polymer, the drug, and the TC/L MIM (**Figure 4-8**). Signals for Perphenazine (**Figure 5**) and Imatinib (**Figure 7**) shifted to higher ppm or lower ppm as compared to without polymer, phenomena detailed for guest-host cyclodextrin complexes before linking shifts to higher and lower ppm to hydrophilic and hydrophobic interaction, respectively.[78-80] Lastly, a third (iii) pattern was observed for the polymers which did not substantially interact with TC/L MIM but formed separate aggregates (Kollidon VA 64 and HPMC-AS; **Figure 3**). These polymers did not (Perphenazine) or marginally (Imatinib) impact the flux of MIM interacting (**Figure 4, 6, Section S8**) or MIM *non*-interacting drugs (Metoprolol; **Figure 8**). For example, in spite of unaltered flux - hence unaltered free drug fraction - aryl-proton signal broadening of Perphenazine was observed at 1% as compared to 0.05% HPMC-AS (**Figure 5**). Because of concurrent Perphenazine flux reduction with HPMC-AS in PBS but not in TC/L in PBS, we attribute this signal broadening to drug-polymer but not MIM-polymer interaction, respectively, assuming that the MIM *non*-interacting character of the polymers does not

change in presence of drug. This interpretation would also link to previous reports, reporting improved drug bioavailability with these MIM *non*-interacting polymers.[50, 81, 82] The three polymer patterns are summarized below (**Figure 9**) and potentially introduce a further optimization parameter in formulation design.

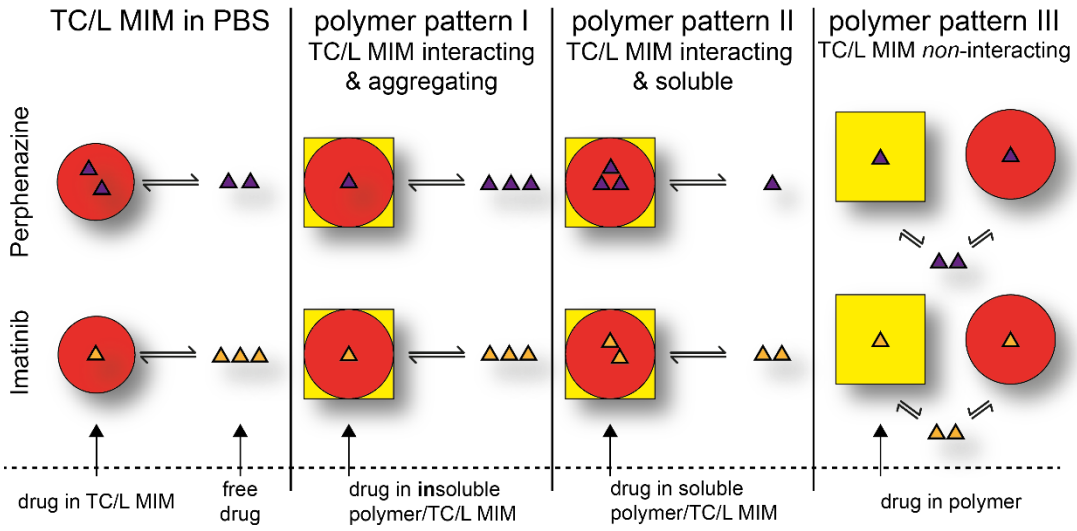

Figure 9: Illustration of interaction patterns seen for polymers (yellow squares) with TC/L MIM (red circle) with respective drugs. The cartoon abstracts Perphenazine's (purple triangle) and Imatinib's (orange triangle) relative partition into different structures formed by polymer and TC/L MIM as seen from the flux experiments.

Conclusion

Efficient solubilization by bile colloids is important for the bioavailability of many PWSD, hydrophobic vitamins or other essential components.[25, 32, 50] Hence, supporting this mechanism with properly selected polymers for formulation might offer advantages and lead to better performing medication. Along these lines, we identified three patterns by which polymers impacted the molecular assembly and geometry of bile colloids and we linked these patterns to different flux rates of PWSD. Flux rates were previously correlated to bioavailability.[49-51] For those who wish to translate these findings into pharmaceutical application, we propose starting with the assessment whether a PWSD is solubilized by bile or not. If not (as for Metoprolol), polymer selection is rather uncritical even if the polymers affect TC/L molecular assembly and structure. However, if the PWSD interacts with the TC/L (as for Perphenazine and Imatinib), polymer selection is critical. Hence, this strategy integrates into polymer selection for maximizing the molecularly dissolved drug substance at resorption sites and extends these known strategies by taking polymer effects on bile

solubilization into account. This and other exciting formulation strategies may unfold at this point. We summarize this approach in a preliminary decision tree (**Figure 10**).
Possibly, future algorithms may allow prediction including performances in other fluids, e.g. fed state simulating gastrointestinal fluids and potentially biological aspirates.

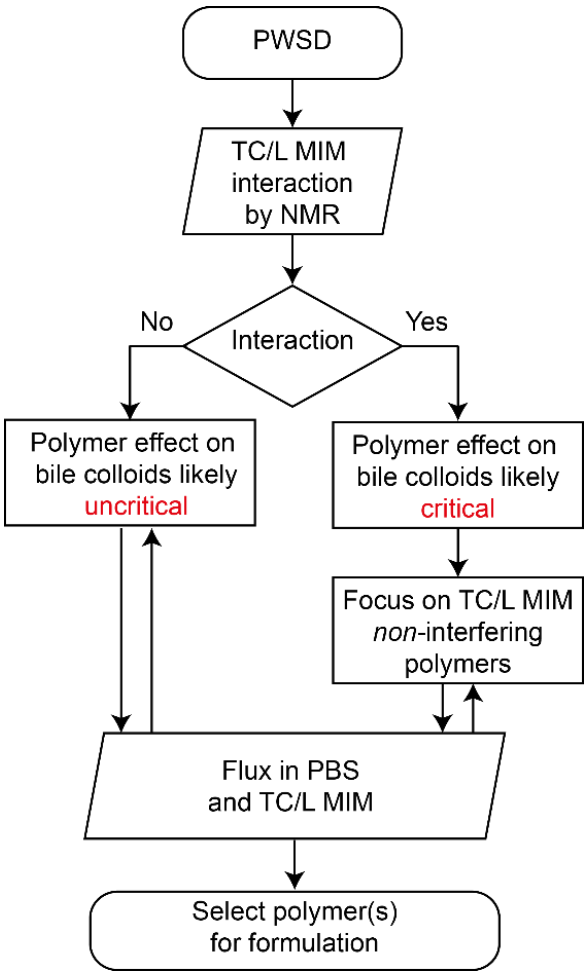

Figure 10: Preliminary decision tree for polymer selection. We classify Colesevelam, Eudragit E, and Soluplus as critical polymers in terms of TC/L MIM interaction, in contrast to uncritical polymers Kollidon VA 64 and HPMC-AS.

Acknowledgements

We gratefully acknowledge the financial support by Novartis Pharma AG for JS. BG and CH are full time associated of Novartis and declare a possible conflict of interest. We also acknowledge the kind support by the Max Planck Gesellschaft. We would like to thank Christopher Heidenreich and Alexandra Mony for their great technical assistance.

References

1. Jiang, T.; Han, N.; Zhao, B.; Xie, Y.; Wang, S., Enhanced dissolution rate and oral bioavailability of simvastatin nanocrystal prepared by sonoprecipitation. *Drug Dev. Ind. Pharm.* **2012,** *38* (10), 1230-9.
2. Reggane, M.; Wiest, J.; Saedtler, M.; Harlacher, C.; Gutmann, M.; Zottnick, S. H.; Piechon, P.; Dix, I.; Muller-Buschbaum, K.; Holzgrabe, U.; Meinel, L.; Galli, B., Bioinspired co-crystals of Imatinib providing enhanced kinetic solubility. *Eur. J. Pharm. Biopharm.* **2018,** *128*, 290-299.
3. Balk, A.; Holzgrabe, U.; Meinel, L., 'Pro et contra' ionic liquid drugs - Challenges and opportunities for pharmaceutical translation. *Eur. J. Pharm. Biopharm.* **2015,** *94*, 291-304.
4. Balk, A.; Wiest, J.; Widmer, T.; Galli, B.; Holzgrabe, U.; Meinel, L., Transformation of acidic poorly water soluble drugs into ionic liquids. *Eur. J. Pharm. Biopharm.* **2015,** *94*, 73-82.
5. Balk, A.; Widmer, T.; Wiest, J.; Bruhn, H.; Rybak, J. C.; Matthes, P.; Muller-Buschbaum, K.; Sakalis, A.; Luhmann, T.; Berghausen, J.; Holzgrabe, U.; Galli, B.; Meinel, L., Ionic liquid versus prodrug strategy to address formulation challenges. *Pharm. Res.* **2015,** *32* (6), 2154-67.
6. Wiest, J.; Saedtler, M.; Balk, A.; Merget, B.; Widmer, T.; Bruhn, H.; Raccuglia, M.; Walid, E.; Picard, F.; Stopper, H.; Dekant, W.; Luhmann, T.; Sotriffer, C.; Galli, B.; Holzgrabe, U.; Meinel, L., Mapping the pharmaceutical design space by amorphous ionic liquid strategies. *J. Control. Release.* **2017,** *268*, 314-322.
7. Güntzel, P.; Schilling, K.; Hanio, S.; Schlauersbach, J.; Schollmayer, C.; Meinel, L.; Holzgrabe, U., Bioinspired Ion Pairs Transforming Papaverine into a Protic Ionic Liquid and Salts. *ACS Omega* **2020,** *5* (30), 19202-19209.
8. Horn, D.; Rieger, J., Organic Nanoparticles in the Aqueous Phase—Theory, Experiment, and Use. *Angew. Chem. Int. Ed.* **2001,** *40* (23), 4330-4361.
9. Merisko-Liversidge, E. M.; Liversidge, G. G., Drug nanoparticles: formulating poorly water-soluble compounds. *Toxicol. Pathol.* **2008,** *36* (1), 43-8.
10. Six, K.; Daems, T.; de Hoon, J.; Van Hecken, A.; Depre, M.; Bouche, M. P.; Prinsen, P.; Verreck, G.; Peeters, J.; Brewster, M. E.; Van den Mooter, G., Clinical study of solid dispersions of itraconazole prepared by hot-stage extrusion. *Eur. J. Pharm. Sci.* **2005,** *24* (2-3), 179-86.
11. Pöppler, A. C.; Lübtow, M. M.; Schlauersbach, J.; Wiest, J.; Meinel, L.; Luxenhofer, R., Loading-Dependent Structural Model of Polymeric Micelles Encapsulating Curcumin by Solid-State NMR Spectroscopy. *Angew. Chem. Int. Ed. Engl.* **2019,** *58* (51), 18540-18546.
12. Porter, C. J.; Pouton, C. W.; Cuine, J. F.; Charman, W. N., Enhancing intestinal drug solubilisation using lipid-based delivery systems. *Adv. Drug Deliv. Rev.* **2008,** *60* (6), 673-91.
13. Singh, D.; Bedi, N.; Tiwary, A. K., Enhancing solubility of poorly aqueous soluble drugs: critical appraisal of techniques. *J. Pharm. Investig.* **2017,** *48* (5), 509-526.

14. Bevernage, J.; Brouwers, J.; Brewster, M. E.; Augustijns, P., Evaluation of gastrointestinal drug supersaturation and precipitation: strategies and issues. *Int. J. Pharm.* **2013,** *453* (1), 25-35.
15. Rodriguez-Aller, M.; Guillarme, D.; Veuthey, J. L.; Gurny, R., Strategies for formulating and delivering poorly water-soluble drugs. *J. Drug Deliv. Sci. Technol.* **2015,** *30*, 342-351.
16. Wiest, J.; Kehrein, J.; Saedtler, M.; Schilling, K.; Cataldi, E.; Sotriffer, C. A.; Holzgrabe, U.; Rasmussen, T.; Bottcher, B.; Cronin-Golomb, M.; Lehmann, M.; Jung, N.; Windbergs, M.; Meinel, L., Controlling Supramolecular Structures of Drugs by Light. *Mol Pharm* **2020,** *17* (12), 4704-4708.
17. Gamboa, A.; Schussler, N.; Soto-Bustamante, E.; Romero-Hasler, P.; Meinel, L.; Morales, J. O., Delivery of ionizable hydrophilic drugs based on pharmaceutical formulation of ion pairs and ionic liquids. *Eur. J. Pharm. Biopharm.* **2020,** *156*, 203-218.
18. Crowley, P.; Martini, L. G., Drug-excipient interactions. *Pharm. Technol.* **2001,** *4*, 7-12.
19. Pottel, J.; Armstrong, D.; Zou, L.; Fekete, A.; Huang, X. P.; Torosyan, H.; Bednarczyk, D.; Whitebread, S.; Bhhatarai, B.; Liang, G.; Jin, H.; Ghaemi, S. N.; Slocum, S.; Lukacs, K. V.; Irwin, J. J.; Berg, E. L.; Giacomini, K. M.; Roth, B. L.; Shoichet, B. K.; Urban, L., The activities of drug inactive ingredients on biological targets. *Science* **2020,** *369* (6502), 403-413.
20. Golightly, L.; Smolinske, S.; Bennett, M.; Sutherland, E. r.; Rumack, B., Pharmaceutical excipients. Adverse effects associated with inactive ingredients in drug products (Part I). *Med. Toxicol. Adv. Drug.* **1988 Mar-Apr,** *3(2)*, 128-65.
21. Werle, M., Natural and synthetic polymers as inhibitors of drug efflux pumps. *Pharm. Res.* **2008,** *25* (3), 500-511.
22. Reker, D.; Blum, S. M.; Steiger, C.; Anger, K. E.; Sommer, J. M.; Fanikos, J.; Traverso, G., "Inactive" ingredients in oral medications. *Sci. Transl. Med.* **2019,** *11* (483).
23. Borbas, E.; Tozser, P.; Tsinman, K.; Tsinman, O.; Takacs-Novak, K.; Volgyi, G.; Sinko, B.; Nagy, Z. K., Effect of Formulation Additives on Drug Transport through Size-Exclusion Membranes. *Mol. Pharm.* **2018,** *15* (8), 3308-3317.
24. Wiest, J.; Saedtler, M.; Böttcher, B.; Grüne, M.; Reggane, M.; Galli, B.; Holzgrabe, U.; Meinel, L., Geometrical and Structural Dynamics of Imatinib within Biorelevant Colloids. *Mol. Pharmaceutics* **2018,** *15* (10), 4470-4480.
25. Sugano, K.; Kataoka, M.; Mathews Cda, C.; Yamashita, S., Prediction of food effect by bile micelles on oral drug absorption considering free fraction in intestinal fluid. *Eur. J. Pharm. Sci.* **2010,** *40* (2), 118-24.
26. Hofmann, A. F., The enterohepatic circulation of bile acids in mammals: form and functions. *Front. Biosci.* **2009,** *14*, 2584-98.
27. Riethorst, D.; Baatsen, P.; Remijn, C.; Mitra, A.; Tack, J.; Brouwers, J.; Augustijns, P., An In-Depth View into Human Intestinal Fluid Colloids: Intersubject Variability in Relation to Composition. *Mol. Pharm.* **2016,** *13* (10), 3484-3493.

28. Riethorst, D.; Mols, R.; Duchateau, G.; Tack, J.; Brouwers, J.; Augustijns, P., Characterization of Human Duodenal Fluids in Fasted and Fed State Conditions. *J. Pharm. Sci.* **2016,** *105* (2), 673-681.
29. Schubiger, G.; Stocker, C.; Banziger, O.; Laubscher, B.; Zimmermann, H., Oral vitamin K1 prophylaxis for newborns with a new mixed-micellar preparation of phylloquinone: 3 years experience in Switzerland. *Eur. J. Pediatr.* **1999,** *158* (7), 599-602.
30. Augustijns, P.; Wuyts, B.; Hens, B.; Annaert, P.; Butler, J.; Brouwers, J., A review of drug solubility in human intestinal fluids: implications for the prediction of oral absorption. *Eur. J. Pharm. Sci.* **2014,** *57*, 322-32.
31. Shearer, M. J., Vitamin K in parenteral nutrition. *Gastroenterology* **2009,** *137* (5 Suppl), S105-18.
32. Sun, F.; Jaspers, T. C.; van Hasselt, P. M.; Hennink, W. E.; van Nostrum, C. F., A Mixed Micelle Formulation for Oral Delivery of Vitamin K. *Pharm. Res.* **2016,** *33* (9), 2168-79.
33. Schittny, A.; Huwyler, J.; Puchkov, M., Mechanisms of increased bioavailability through amorphous solid dispersions: a review. *Drug Deliv.* **2020,** *27* (1), 110-127.
34. Karolewicz, B., A review of polymers as multifunctional excipients in drug dosage form technology. *Saudi Pharm. J.* **2016,** *24* (5), 525-536.
35. Liu, H.; Taylor, L. S.; Edgar, K. J., The role of polymers in oral bioavailability enhancement; a review. *Polymer* **2015,** *77*, 399-415.
36. Stewart, A. M.; Grass, M. E.; Brodeur, T. J.; Goodwin, A. K.; Morgen, M. M.; Friesen, D. T.; Vodak, D. T., Impact of Drug-Rich Colloids of Itraconazole and HPMCAS on Membrane Flux in Vitro and Oral Bioavailability in Rats. *Mol. Pharm.* **2017,** *14* (7), 2437-2449.
37. Saal, W.; Wyttenbach, N.; Alsenz, J.; Kuentz, M., Interactions of dimethylaminoethyl methacrylate copolymer with non-acidic drugs demonstrated high solubilization in vitro and pronounced sustained release in vivo. *Eur. J. Pharm. Biopharm.* **2018,** *125*, 68-75.
38. Vogtherr, M.; Marx, A.; Mieden, A. C.; Saal, C., Investigation of solubilising effects of bile salts on an active pharmaceutical ingredient with unusual pH dependent solubility by NMR spectroscopy. *Eur. J. Pharm. Biopharm.* **2015,** *92*, 32-41.
39. Davidson, M. H.; Dillon, M. A.; Gordon, B.; Jones, P.; Samuels, J.; Weiss, S.; Isaacsohn, J.; Toth, P.; Burke, S. K., Colesevelam hydrochloride (cholestagel): a new, potent bile acid sequestrant associated with a low incidence of gastrointestinal side effects. *Arch. Intern. Med.* **1999,** *159* (16), 1893-900.
40. Evonik Nutrition and Care GmbH, Eudragit Polymers for immediate release. https://healthcare.evonik.com/product/health-care/en/products/pharmaceutical-excipients/immediate-release/, 2020 (accessed 01 April 2020).
41. Medizinische Medien Informations GmbH, Gelbe Liste. https://www.gelbe-liste.de/, 2021 (accessed 15 December 2021).
42. Onoue, S.; Kojo, Y.; Aoki, Y.; Kawabata, Y.; Yamauchi, Y.; Yamada, S., Physicochemical and pharmacokinetic characterization of amorphous solid dispersion of tranilast with enhanced

solubility in gastric fluid and improved oral bioavailability. *Drug Metab. Pharmacokinet.* **2012,** *27* (4), 379-87.

43. BASF SE, Technical information soluplus. https://documents.basf.com/d4806db3b7c1fd04c2fb8d78c37595a170986618?response-content-disposition=inline, 2019 (accessed 01 April 2020).
44. Linn, M.; Collnot, E. M.; Djuric, D.; Hempel, K.; Fabian, E.; Kolter, K.; Lehr, C. M., Soluplus(R) as an effective absorption enhancer of poorly soluble drugs in vitro and in vivo. *Eur. J. Pharm. Sci.* **2012,** *45* (3), 336-43.
45. BASF SE, Technical information Kollidon VA 64. https://documents.basf.com/54e50e670d2ea311a27b33287436dadc3d8373c1?response-content-disposition=inline, 2019 (accessed 01 April 2020).
46. Shin-Etsu Chemical Co. Ltd, information about Shin-Etsu AQOAT. https://www.shinetsupharmausa.com/en/pharma_excipients/Shin_etsu_aquoat/index.pmode, 2020 (accessed 01 April 2020).
47. Tanno, F.; Nishiyama, Y.; Kokubo, H.; Obara, S., Evaluation of hypromellose acetate succinate (HPMCAS) as a carrier in solid dispersions. *Drug Dev. Ind. Pharm.* **2004,** *30* (1), 9-17.
48. Yang, Y.; Faustino, P. J.; Volpe, D. A.; Ellison, C. D.; Lyon, R. C.; Yu, L. X., Biopharmaceutics Classification of Selected β-Blockers: Solubility and Permeability Class Membership. *Mol. Pharm.* **2007,** *4* (4), 608-14.
49. Berben, P.; Bauer-Brandl, A.; Brandl, M.; Faller, B.; Flaten, G. E.; Jacobsen, A. C.; Brouwers, J.; Augustijns, P., Drug permeability profiling using cell-free permeation tools: Overview and applications. *Eur. J. Pharm. Sci.* **2018,** *119*, 219-233.
50. Kawai, Y.; Fujii, Y.; Tabata, F.; Ito, J.; Metsugi, Y.; Kameda, A.; Akimoto, K.; Takahashi, M., Profiling and Trend Analysis of Food Effects on Oral Drug Absorption Considering Micelle Interaction and Solubilization by Bile Micelles. *Drug Metab. Pharmacokinet.* **2011,** *26* (2), 180-191.
51. Berben, P.; Brouwers, J.; Augustijns, P., The artificial membrane insert system as predictive tool for formulation performance evaluation. *Int. J. Pharm.* **2018,** *537* (1-2), 22-29.
52. Baucke, F. G. K., Further Insight into the Dissociation Mechanism of Glass Electrodes. The Response in Heavy Water. *J. Phys. Chem. B* **1998,** *102* (24), 4835-4841.
53. Jerschow, A.; Müller, N., 3D Diffusion-Ordered TOCSY for Slowly Diffusing Molecules. *J. Magn. Reson.* **1996,** *123* (2), 222-225.
54. Jerschow, A.; Müller, N., Suppression of Convection Artifacts in Stimulated-Echo Diffusion Experiments. Double-Stimulated-Echo Experiments. *J. Magn. Reson.* **1997,** *125* (2), 372-375.
55. Grosvenor, M. P.; Lofroth, J. E., Interaction between bile salts and beta-adrenoceptor antagonists. *Pharm. Res.* **1995,** *12* (5), 682-6.

56. Guthrie, B.; Makubate, B.; Hernandez-Santiago, V.; Dreischulte, T., The rising tide of polypharmacy and drug-drug interactions: population database analysis 1995-2010. *BMC Med.* **2015,** *13*, 74.
57. Charlesworth, C. J.; Smit, E.; Lee, D. S.; Alramadhan, F.; Odden, M. C., Polypharmacy Among Adults Aged 65 Years and Older in the United States: 1988-2010. *J. Gerontol. A Biol. Sci. Med. Sci.* **2015,** *70* (8), 989-95.
58. Schiller, C.; Fröhlich, C. P.; Giessmann, T.; Siegmund, W.; Monnikes, H.; Hosten, N.; Weitschies, W., Intestinal fluid volumes and transit of dosage forms as assessed by magnetic resonance imaging. *Aliment. Pharmacol. Ther.* **2005,** *22* (10), 971-9.
59. Koziolek, M.; Grimm, M.; Schneider, F.; Jedamzik, P.; Sager, M.; Kuhn, J. P.; Siegmund, W.; Weitschies, W., Navigating the human gastrointestinal tract for oral drug delivery: Uncharted waters and new frontiers. *Adv. Drug Deliv. Rev.* **2016,** *101*, 75-88.
60. Bakatselou, V.; Oppenheim, R. C.; Dressman, J. B., Solubilization and wetting effects of bile salts on the dissolution of steroids. *Pharm. Res.* **1991,** *8* (12), 1461-9.
61. Mithani, S. D.; Bakatselou, V.; TenHoor, C. N.; Dressman, J. B., Estimation of the increase in solubility of drugs as a function of bile salt concentration. *Pharm. Res.* **1996,** *13* (1), 163-7.
62. Chen, J.; Mosquera-Giraldo, L. I.; Ormes, J. D.; Higgins, J. D.; Taylor, L. S., Bile Salts as Crystallization Inhibitors of Supersaturated Solutions of Poorly Water-Soluble Compounds. *Cryst. Growth Des.* **2015,** *15* (6), 2593-2597.
63. Serajuddin, A. T.; Sheen, P. C.; Mufson, D.; Bernstein, D. F.; Augustine, M. A., Physicochemical basis of increased bioavailability of a poorly water-soluble drug following oral administration as organic solutions. *J. Pharm. Sci.* **1988,** *77* (4), 325-9.
64. Hu, K.; Cao, S.; Hu, F.; Feng, J., Enhanced oral bioavailability of docetaxel by lecithin nanoparticles: preparation, in vitro, and in vivo evaluation. *Int. J. Nanomed.* **2012,** *7*, 3537-45.
65. Kumar, B. S.; Saraswathi, R.; Kumar, K. V.; Jha, S. K.; Venkates, D. P.; Dhanaraj, S. A., Development and characterization of lecithin stabilized glibenclamide nanocrystals for enhanced solubility and drug delivery. *Drug Deliv.* **2014,** *21* (3), 173-84.
66. Sinha, V. R.; Kumria, R., Binders for colon specific drug delivery: an in vitro evaluation. *Int. J. Pharm.* **2002,** *249* (1-2), 23-31.
67. Moustafine, R. I.; Salachova, A. R.; Frolova, E. S.; Kemenova, V. A.; Van den Mooter, G., Interpolyelectrolyte complexes of Eudragit E PO with sodium alginate as potential carriers for colonic drug delivery: monitoring of structural transformation and composition changes during swellability and release evaluating. *Drug Dev. Ind. Pharm.* **2009,** *35* (12), 1439-51.
68. Yoshida, T.; Kurimoto, I.; Umejima, H.; Watanabe, S.; Sako, K.; Kikuchi, A., Effects of dissolved state of aminoalkyl methacrylate copolymer E/HCl on solubility enhancement effect for poorly water-soluble drugs. *Colloid Polym. Sci.* **2012,** *291* (5), 1191-1199.
69. Pignatello, R.; Corsaro, R., Polymeric Nanomicelles of Soluplus® as a Strategy for Enhancing the Solubility, Bioavailability and Efficacy of Poorly Soluble Active Compounds. *Curr. Nanomed.* **2019,** *9* (3), 184-197.

70. Pinto, J. M. O.; Rengifo, A. F. C.; Mendes, C.; Leao, A. F.; Parize, A. L.; Stulzer, H. K., Understanding the interaction between Soluplus(R) and biorelevant media components. *Colloids Surf. B* **2020,** *187*, 110673.
71. Thiry, J.; Broze, G.; Pestieau, A.; Tatton, A. S.; Baumans, F.; Damblon, C.; Krier, F.; Evrard, B., Investigation of a suitable in vitro dissolution test for itraconazole-based solid dispersions. *Eur. J. Pharm. Sci.* **2016,** *85*, 94-105.
72. Hughey, J. R.; Keen, J. M.; Miller, D. A.; Kolter, K.; Langley, N.; McGinity, J. W., The use of inorganic salts to improve the dissolution characteristics of tablets containing Soluplus(R)-based solid dispersions. *Eur. J. Pharm. Sci.* **2013,** *48* (4-5), 758-66.
73. Yano, K.; Masaoka, Y.; Kataoka, M.; Sakuma, S.; Yamashita, S., Mechanisms of membrane transport of poorly soluble drugs: role of micelles in oral absorption processes. *J. Pharm. Sci.* **2010,** *99* (3), 1336-45.
74. Dahan, A.; Miller, J. M., The solubility-permeability interplay and its implications in formulation design and development for poorly soluble drugs. *AAPS. J.* **2012,** *14* (2), 244-51.
75. Abdiche, Y. N.; Myszka, D. G., Probing the mechanism of drug/lipid membrane interactions using Biacore. *Anal. Biochem.* **2004,** *328* (2), 233-43.
76. Cvijic, S.; Parojcic, J.; Langguth, P., Viscosity-mediated negative food effect on oral absorption of poorly-permeable drugs with an absorption window in the proximal intestine: In vitro experimental simulation and computational verification. *Eur. J. Pharm. Sci.* **2014,** *61*, 40-53.
77. Gao, P.; Fagerness, P. E., Diffusion in HPMC gels. I. Determination of drug and water diffusivity by pulsed-field-gradient spin-echo NMR. *Pharm. Res.* **1995,** *12* (7), 955-64.
78. Eckenroad, K. W.; Manley, G. A.; Yehl, J. B.; Pirnie, R. T.; Strein, T. G.; Rovnyak, D., An Edge Selection Mechanism for Chirally Selective Solubilization of Binaphthyl Atropisomeric Guests by Cholate and Deoxycholate Micelles. *Chirality* **2016,** *28* (7), 525-33.
79. O'Farrell, C. M.; Hagan, K. A.; Wenzel, T. J., Water-Soluble Calix[4]Resorcinarenes as Chiral NMR Solvating Agents for Bicyclic Aromatic Compounds. *Chirality* **2009,** *21* (10), 911-921.
80. Smith, K. J.; Wilcox, J. D.; Mirick, G. E.; Wacker, L. S.; Ryan, N. S.; Vensel, D. A.; Readling, R.; Domush, H. L.; Amonoo, E. P.; Shariff, S. S.; Wenzel, T. J., Calix[4]arene, calix[4]resorcarene, and cyclodextrin derivatives and their lanthanide complexes as chiral NMR shift reagents. *Chirality* **2003,** *15 Suppl*, S150-8.
81. Pinto, J. M. O.; Leao, A. F.; Riekes, M. K.; Franca, M. T.; Stulzer, H. K., HPMCAS as an effective precipitation inhibitor in amorphous solid dispersions of the poorly soluble drug candesartan cilexetil. *Carbohydr. Polym.* **2018,** *184*, 199-206.
82. Chmiel, K.; Knapik-Kowalczuk, J.; Jurkiewicz, K.; Sawicki, W.; Jachowicz, R.; Paluch, M., A New Method To Identify Physically Stable Concentration of Amorphous Solid Dispersions (I): Case of Flutamide + Kollidon VA64. *Mol. Pharm.* **2017,** *14* (10), 3370-3380.

Supporting Information

S1 Methods

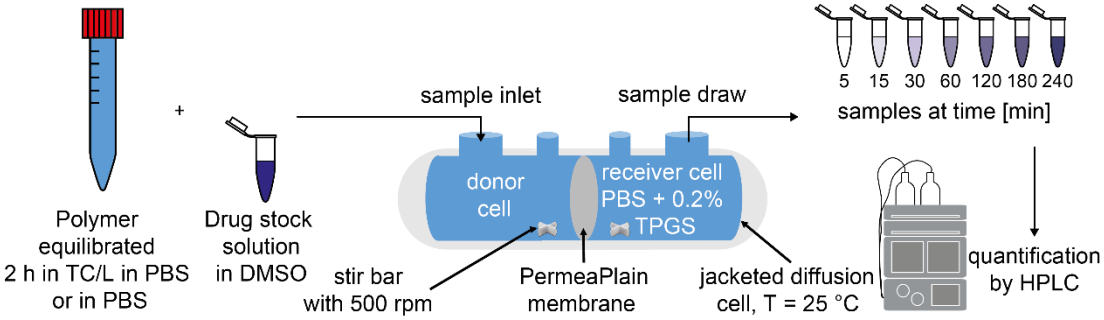

Figure S1: Flux assay as described in 2.2.3

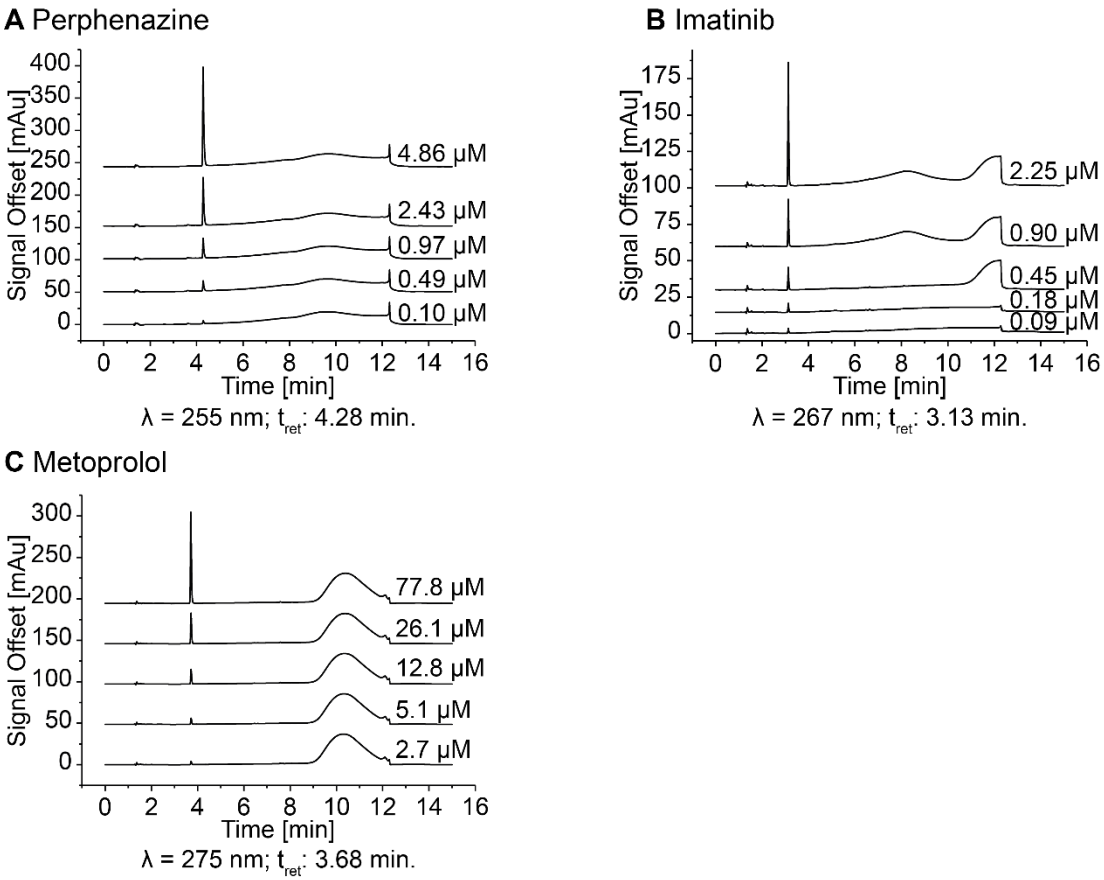

Figure S2: HPLC calibration spectra for (A) Perphenazine, (B) Imatinib, and (C) Metoprolol. Signal area under the curve (AUC) increased linearly with concentration. Respective nominal drug concentrations are shown on the right side of each spectrum. λ represents wavelength of detector and t_{ret} retention time of respective drug peak.

S2 ^{1}H nuclear magnetic resonance (NMR) data interpretation

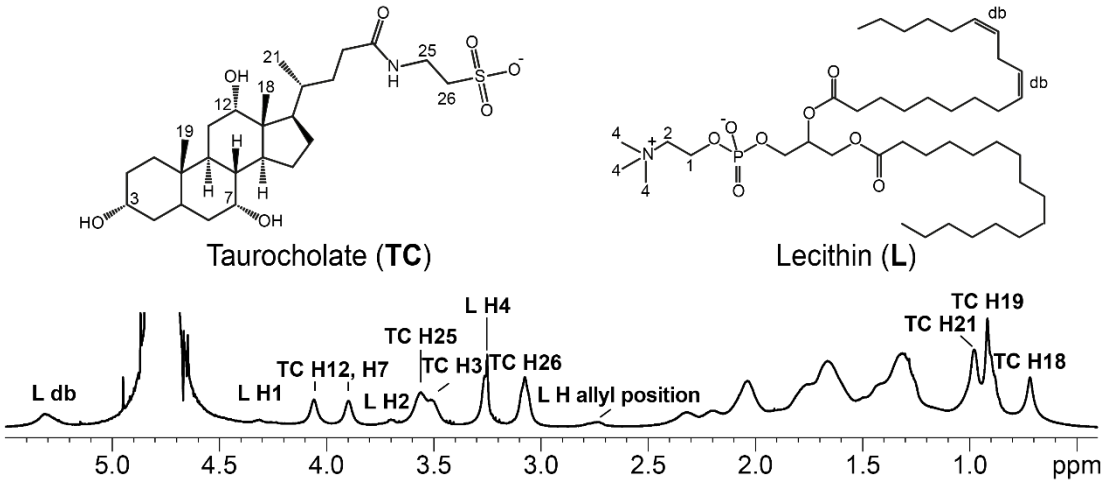

Figure S3: ^{1}H NMR signal assignment of **t**auro**c**holate (**TC**) and lecithin (**L**) based on.[1]

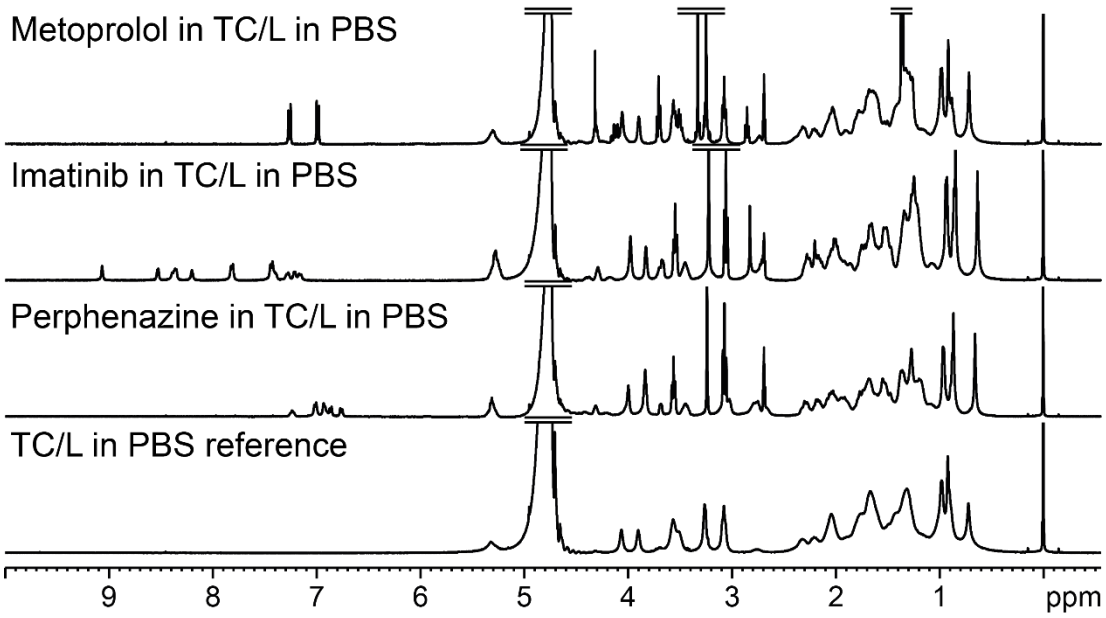

Figure S4: Complete ^{1}H NMR spectra of Metoprolol, Imatinib, and Perphenazine with TC/L. Bottom shows TC/L reference spectrum.

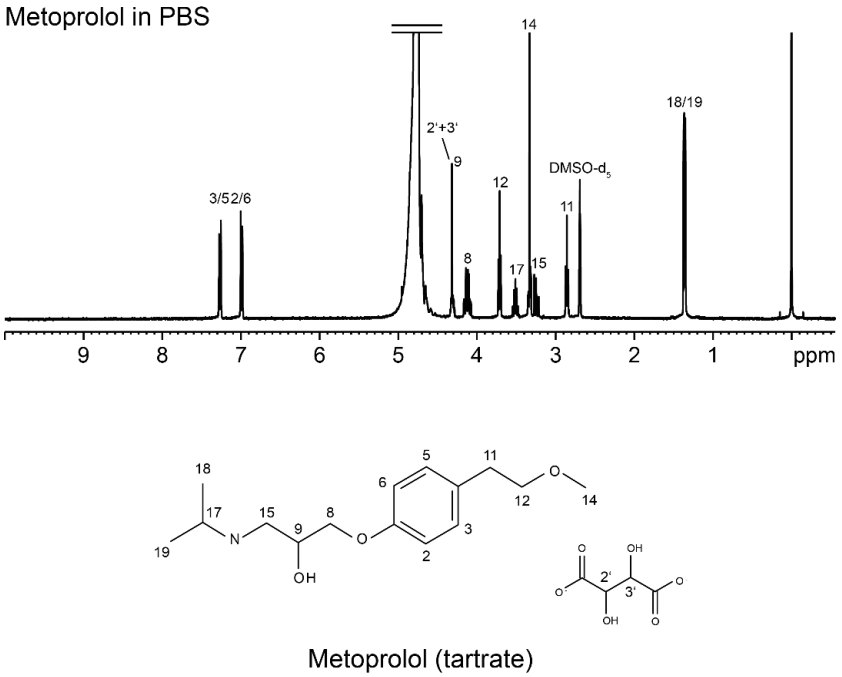

Figure S5: Complete ^{1}H NMR spectrum with signal assignment and respective molecular structure of Metoprolol in PBS. Standard 1D and 2D NMR techniques were applied for signal assignment.

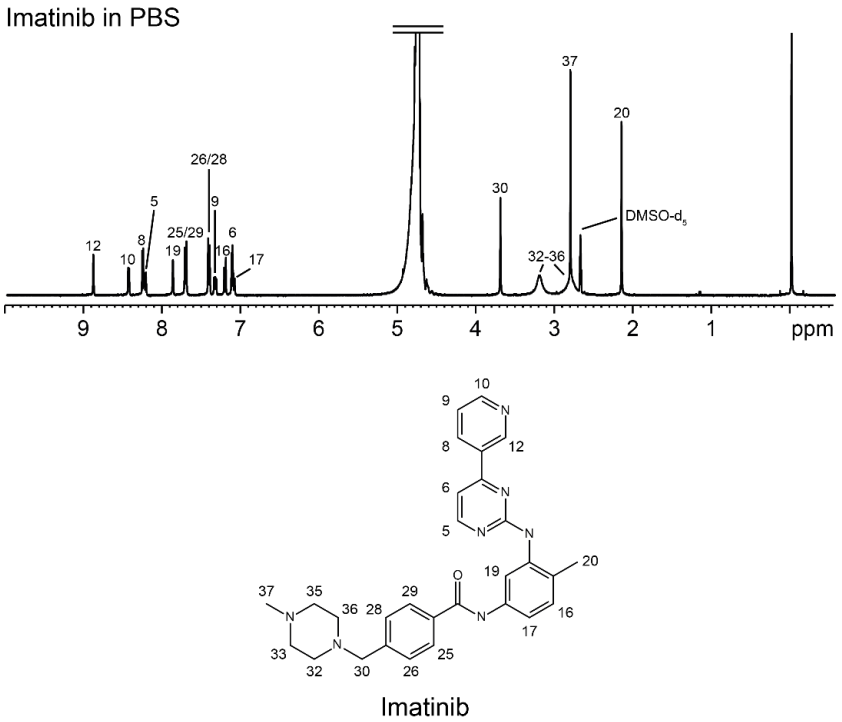

Figure S6: Complete ^{1}H NMR spectrum with signal assignment and respective molecular structure of Imatinib in PBS. Standard 1D and 2D NMR techniques were applied for signal assignment.

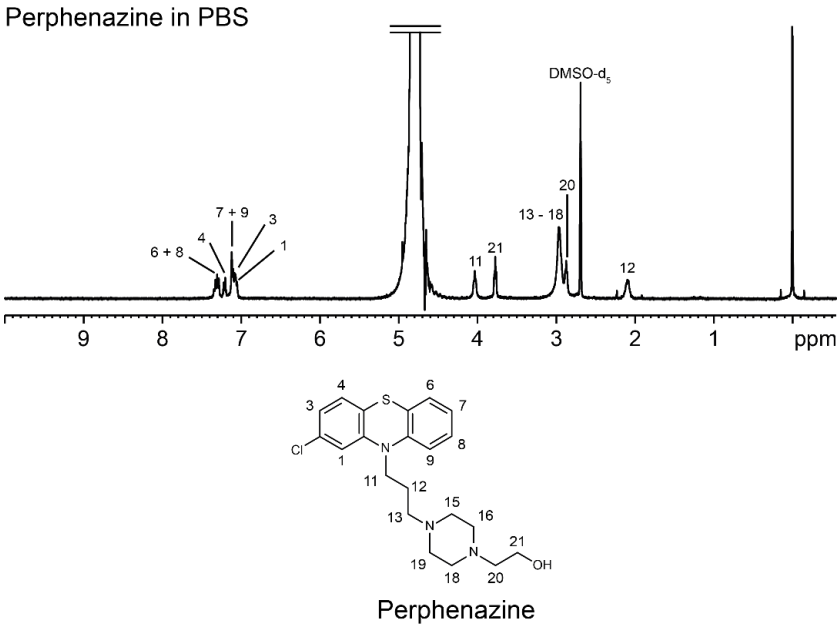

Figure S7: Complete ^{1}H NMR spectrum with signal assignment and respective molecular structure of Perphenazine in PBS. Standard 1D and 2D NMR techniques were applied for signal assignment.

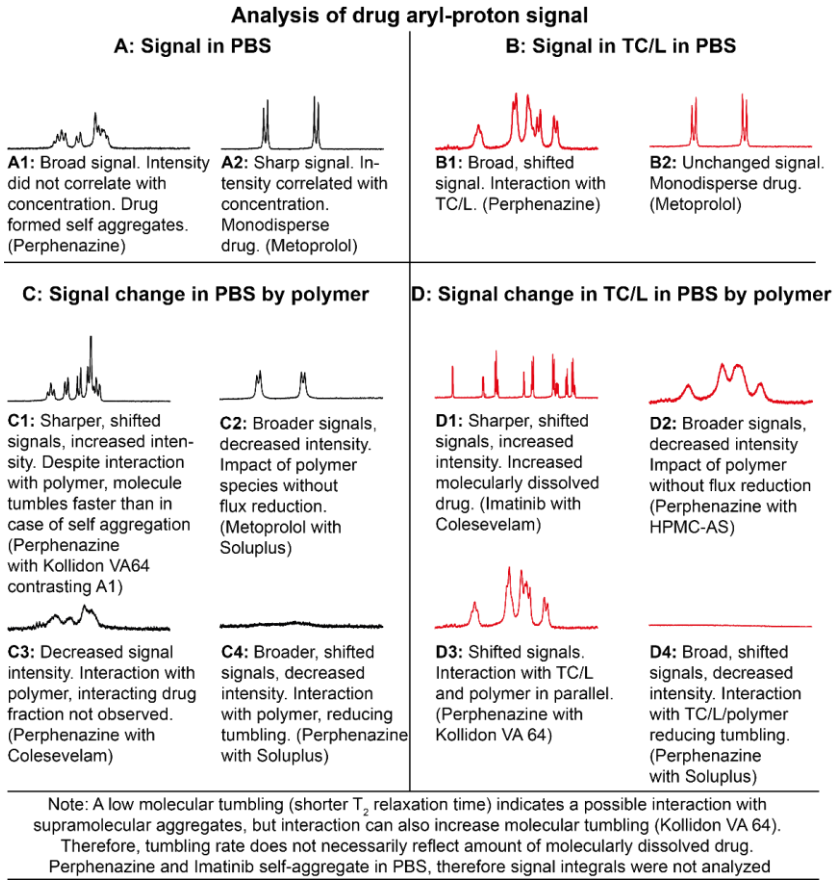

Figure S8: Interpretation of the NMR spectral patterns of the aryl-proton signals of drug molecules without polymer in PBS (A) and in TC/L in PBS (B) and with polymer in PBS (C) and in TC/L in PBS (D).

S3 Polymer characterization in TC/L in PBS and in PBS

S3.1 Particle size analysis in PBS by dynamic light scattering (DLS)

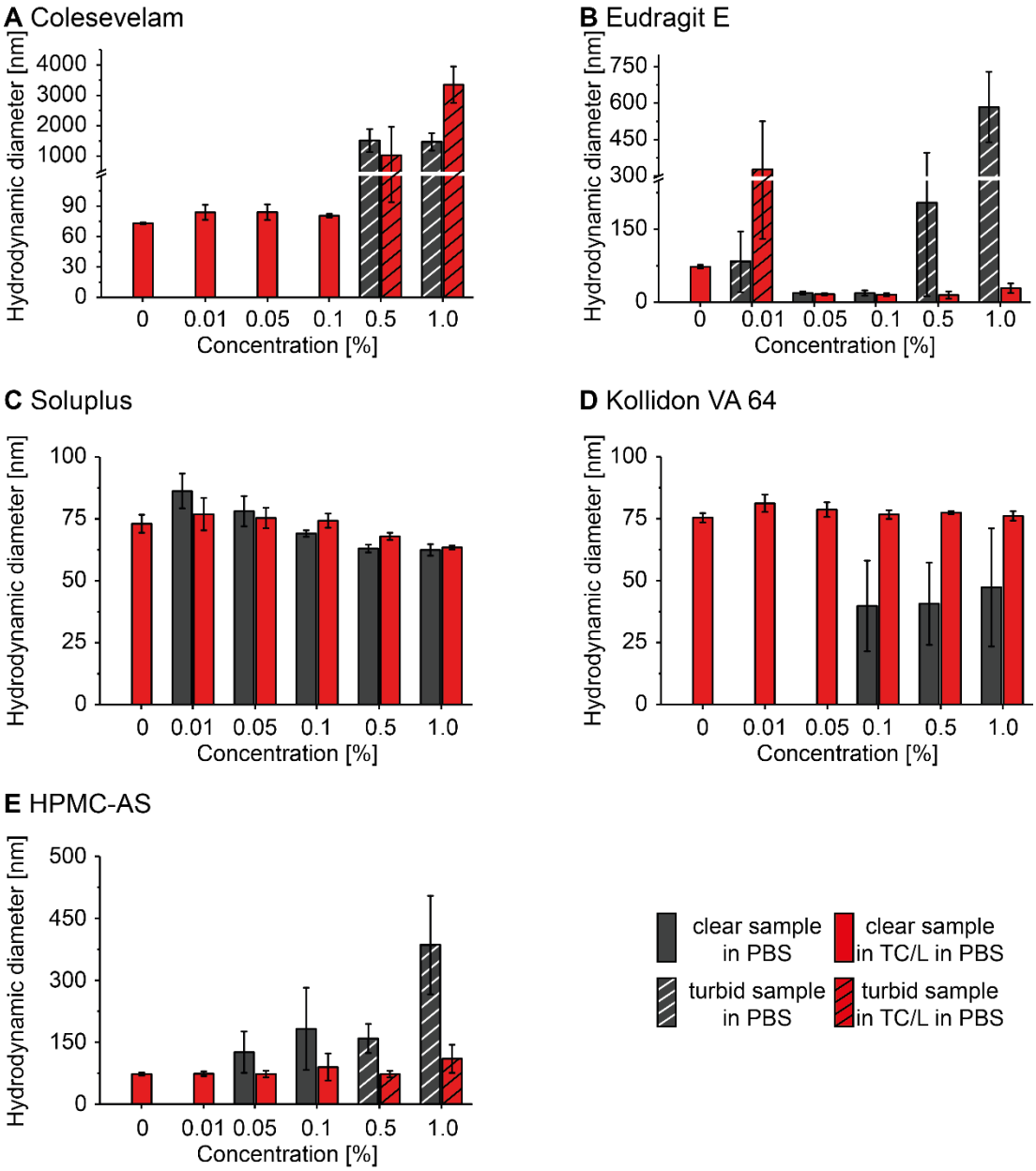

Figure S9: Mean hydrodynamic diameters of colloids in PBS (grey) and in TC/L in PBS (red) with (A) Colesevelam, (B) Eudragit E, (C) Soluplus, (D) Kollidon VA 64, and (E) HPMC-AS at different concentrations by DLS (mean ± SD). At ≥0.5% Colesevelam particles were detected (A grey). Turbidity was also observed for Eudragit E at 0.01, 0.5, and 1% (B, grey). At 0.05 and 0.1% Eudragit E formed colloids around 20 nm. Conversely, Eudragit E in TC/L in PBS formed colloids at ≥0.05% (B, red). Soluplus formed 60-90 nm particles in PBS (C, grey). At ≥0.1% Kollidon VA 64 particles around 40 nm were observed (D, grey). Hydrodynamic diameters of HPMC-AS ranged from 70 to 250 nm at 0.05 and 0.1% (E, grey). At ≥0.5% particle size up to 500 nm were observed along with turbidity.

Table S1: Polymer dynamic viscosities in TC/L in PBS and in PBS at 25 °C used for DLS data adjustment [mPa*s].

Concentration [%]	Colesevelam		Eudragit E		Soluplus		Kollidon VA 64		HPMC-AS	
	PBS	TC/L in PBS	PBS	TC/L in PBS	PBS	TC/L in PBS	PBS	TC/L in PBS	PBS	TC/L in PBS
0.01			0.9410	0.9457	0.9431	0.9312	N/A	0.9339	N/A	0.9488
0.05			0.9300	0.9258	0.9255	0.9400	N/A	0.9398	0.9540	0.9767
0.1	N/A	N/A	0.9337	0.9275	0.9269	0.9450	0.9527	0.9503	1.0014	1.0251
0.5			0.9689	0.9422	0.9572	0.9805	0.9866	1.0116	1.3985	1.3942
1			0.9366	0.9602	1.0014	1.0376	1.0685	1.0945	1.8190	1.4707
PBS	0.9104									
TC/L reference	0.9258									

Table S2: Mean polydispersity index (PDI) with standard deviation of colloids in TC/L in PBS.

Concentration [%]	Colesevelam		Eudragit E		Soluplus		Kollidon VA 64		HPMC-AS	
	PDI mean	PDI SD	PDI mean	PDI SD	PDI mean	PDI SD	PDI mean	PDI SD	PDI mean	PDI SD
0.01	0.075	0.036	0.23	0.12	0.108	0.007	0.143	0.032	0.083	0.049
0.05	0.050	0.030	0.180	0.088	0.099	0.018	0.086	0.020	0.060	0.015
0.1	0.095	0.015	0.19	0.10	0.077	0.033	0.097	0.012	0.107	0.078
0.5	0.40	0.24	0.13	0.13	0.066	0.024	0.104	0.032	0.126	0.044
1	0.933	0.070	0.249	0.029	0.062	0.013	0.127	0.025	0.173	0.014
TC/L reference	0.144	0.057	0.06	0.030	0.056	0.041	0.069	0.019	0.06	0.030

Table S3: Mean polydispersity index (PDI) with standard deviation of colloids in PBS.

Concentration [%]	Colesevelam		Eudragit E		Soluplus		Kollidon VA 64		HPMC-AS	
	PDI mean	PDI SD	PDI mean	PDI SD	PDI mean	PDI SD	PDI mean	PDI SD	PDI mean	PDI SD
0.01	N/A	N/A	0.32	0.26	0.14	0.02	N/A	N/A	N/A	N/A
0.05	N/A	N/A	0.20	0.13	0.088	0.023	N/A	N/A	0.30	0.09
0.1	N/A	N/A	0.27	0.01	0.059	0.013	0.40	0.03	0.21	0.07
0.5	0.52	0.15	0.23	0.08	0.051	0.018	0.24	0.04	0.23	0.03
1	0.37	0.09	0.30	0.04	0.053	0.024	0.23	0.02	0.36	0.03

S3.2 ^{1}H nuclear magnetic resonance (1H NMR) analysis of polymers

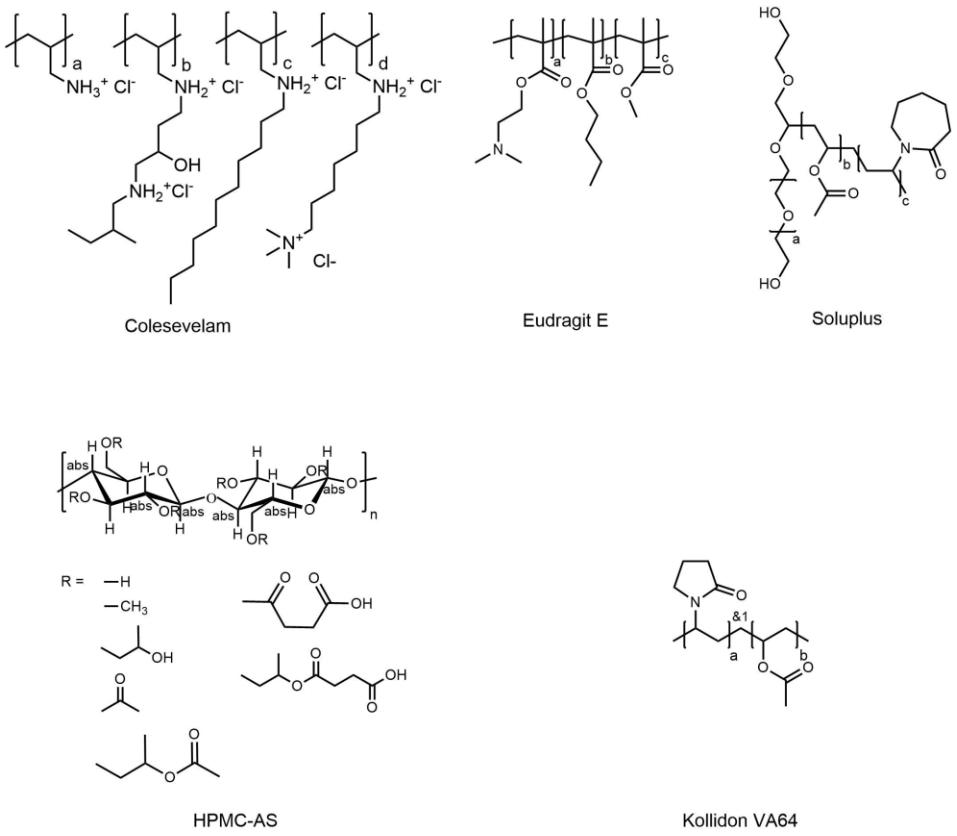

Figure S10: Chemical structures of used polymers.

S3.2.1 Colesevelam in PBS

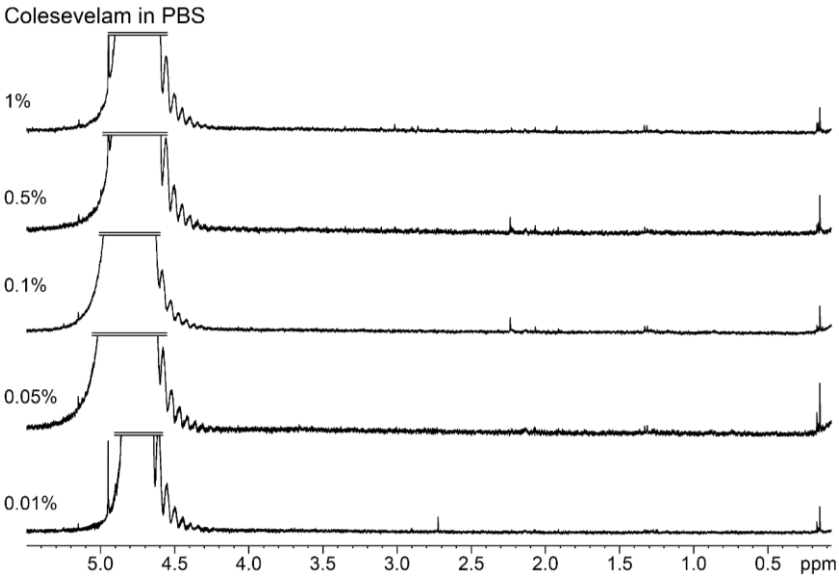

Figure S11: [1]H NMR spectra of Colesevelam at 0.01, 0.05, 0.1, 0.5, and 1% in PBS. No Colesevelam signals were detected.

S3.2.2 Colesevelam in TC/L in PBS

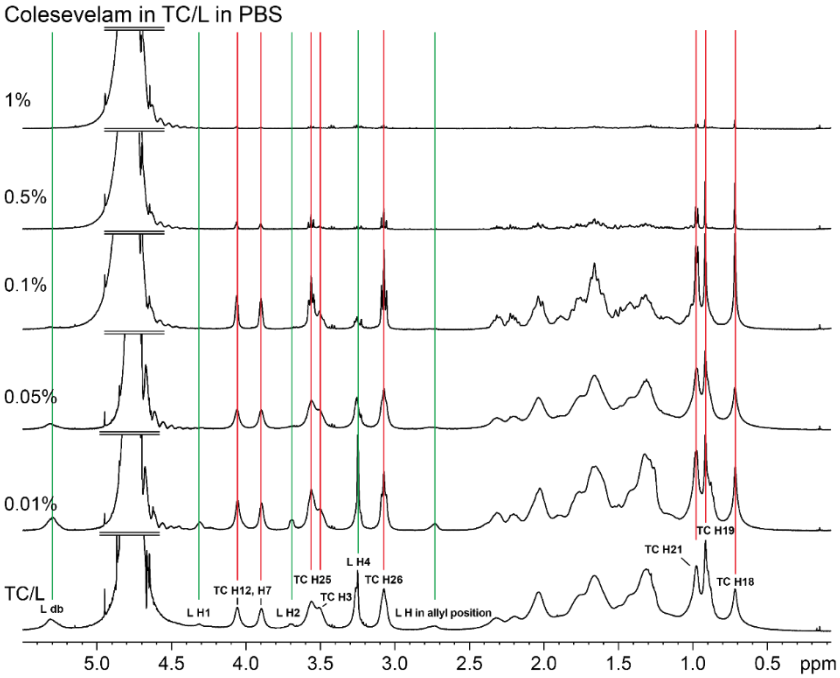

Figure S12: [1]H NMR spectra of Colesevelam at 0.01, 0.05, 0.1, 0.5, and 1% in TC/L in PBS indicated as (L) green lines and (TC) red lines. TC/L reference spectrum is shown (bottom). TC/L signal intensities decreased as a function of Colesevelam concentration. At ≥0.1% signals sharpened (e.g. TC H25 and H26). At ≥0.5 sharp TC signals with low intensity were found indicating precipitation of TC/L. Few TC remains in solution, but does not aggregate.

S3.2.3 Eudragit E in PBS

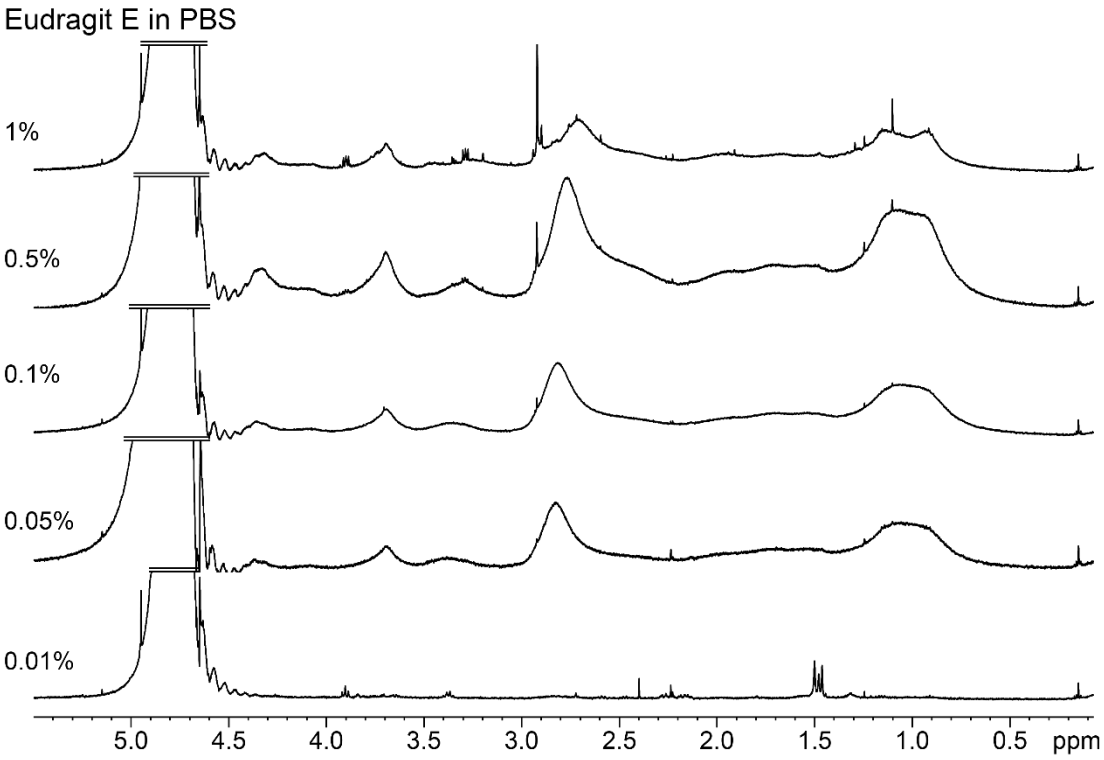

Figure S13: ^{1}H NMR spectra of Eudragit E at 0.01, 0.05, 0.1, 0.5, and 1% in PBS. Sharp signals with low intensity were detected at 0.01%. At ≥0.05%, broad Eudragit E signals were observed. Some sharp signals shifted to lower ppm dependent on concentration (e.g. at 2.8 ppm).

S3.2.4 Eudragit E in TC/L in PBS

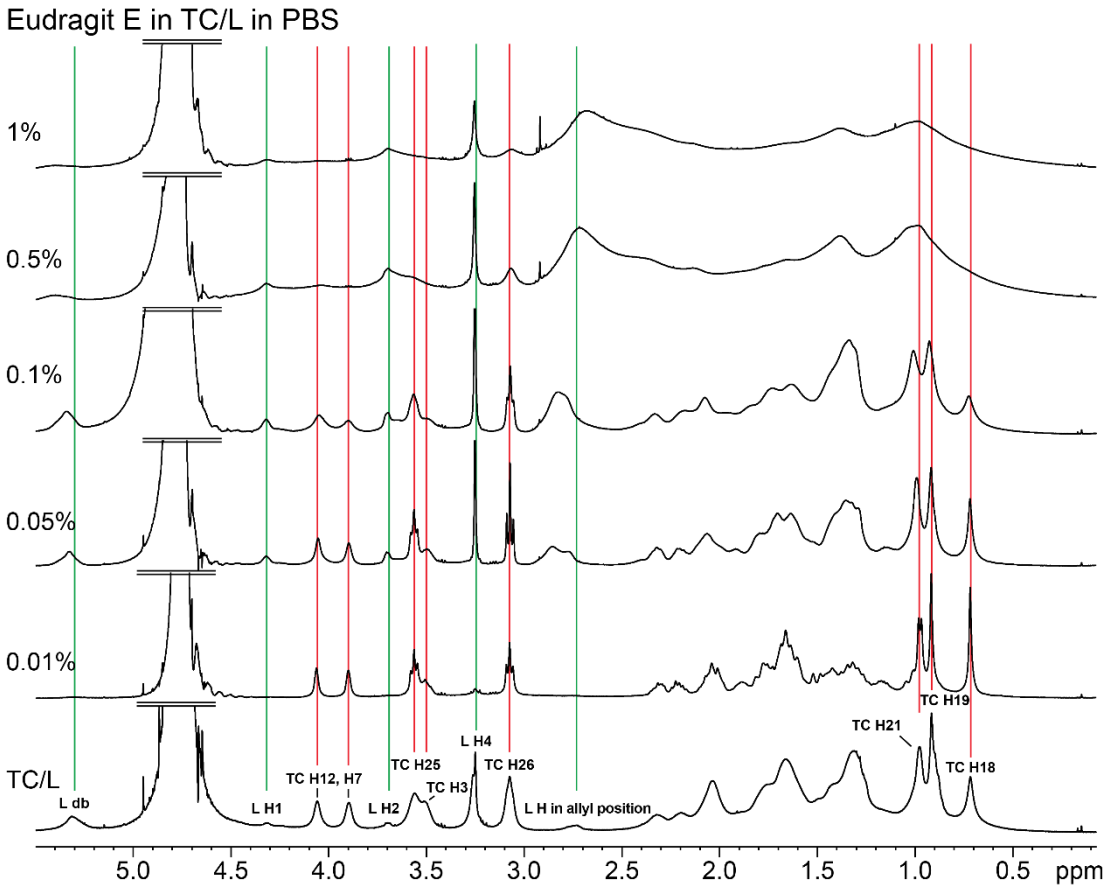

Figure S14: ^{1}H NMR spectra of Eudragit E at 0.01, 0.05, 0.1, 0.5, and 1% in TC/L in PBS indicated as (L) green lines and (TC) red lines. TC/L reference spectrum is shown (bottom). At 0.01% L signals disappeared, while TC signals sharpened. At ≥0.05% L signals reappeared. At ≥0.1% some TC/L signals shifted and at ≥0.5% disappeared (e.g. TC H21, H19, and 18). Other signals did not disappear, but intensity decreased along with signal broadening (e.g. L H4, TC H26).

S3.2.5 Soluplus in PBS

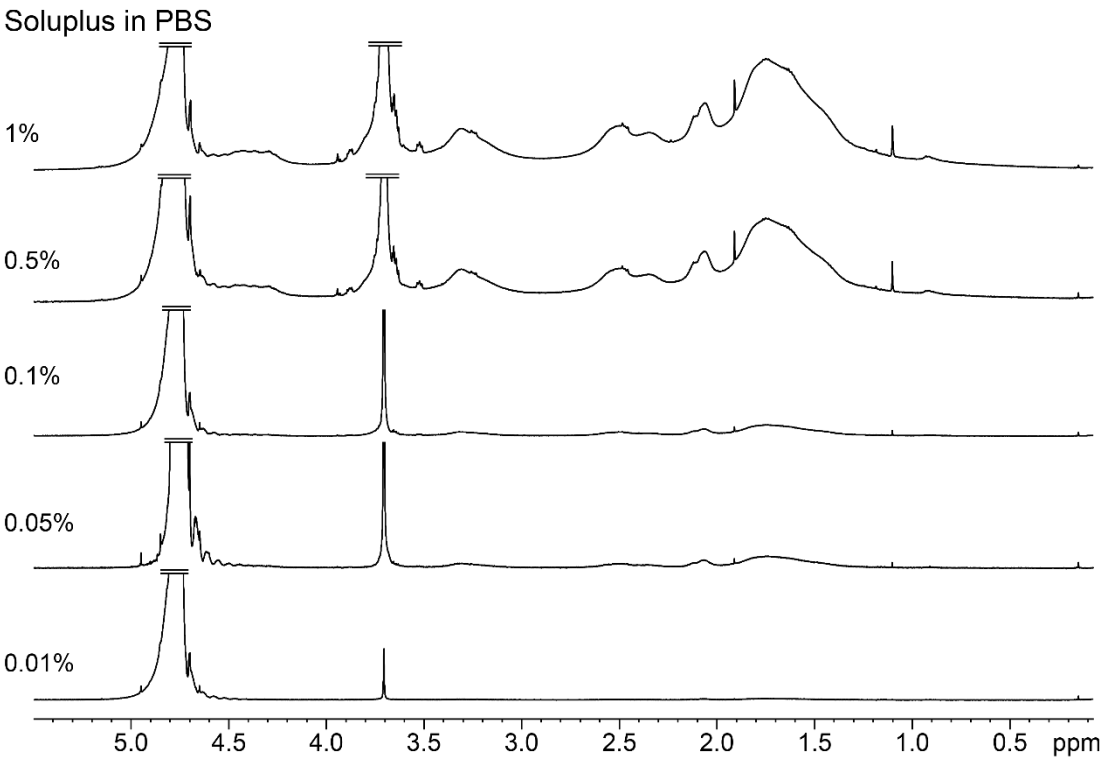

Figure S15: ^{1}H NMR spectra of Soluplus at 0.01, 0.05, 0.1, 0.5 and 1% in PBS. Signal intensity increased as a function of concentration. Broad signals (e.g. at 1.3-2.6 ppm) and sharp signals (e.g. at 1.1 and 1.9 ppm) were detected in parallel.

S3.2.6 Soluplus in TC/L in PBS

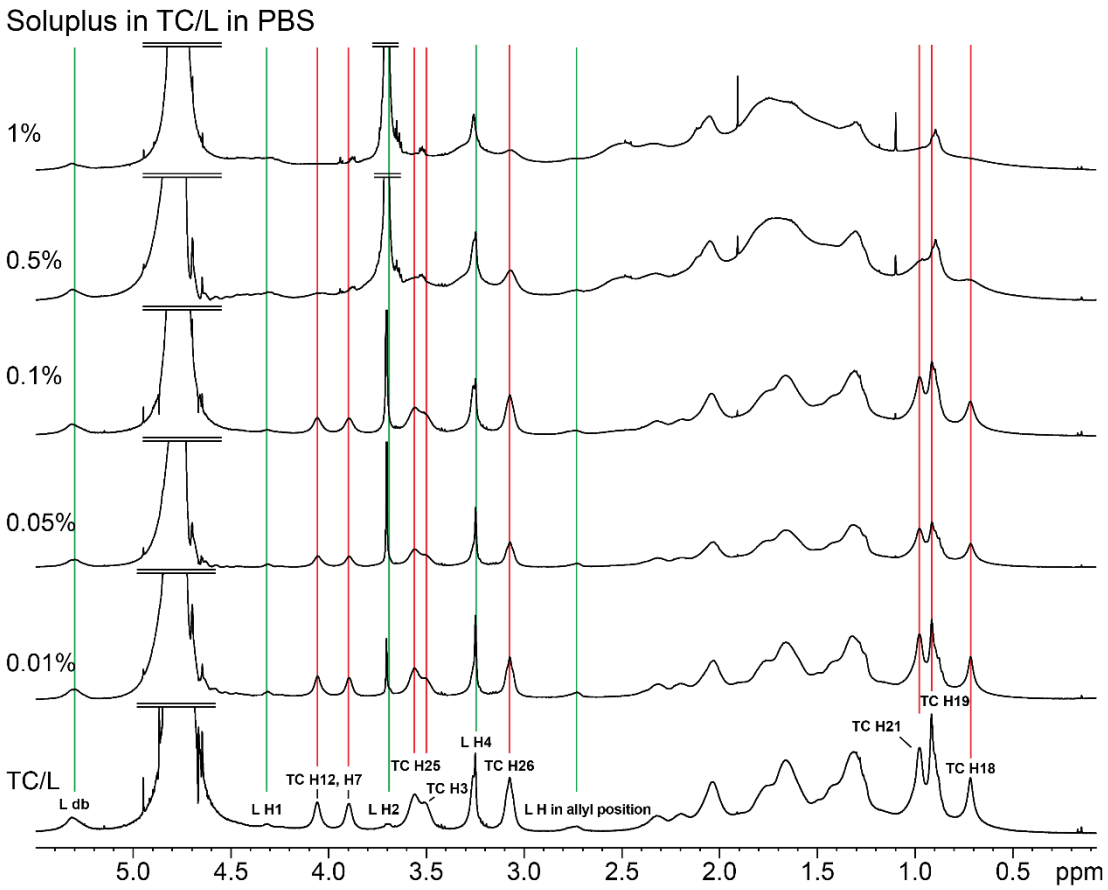

Figure S16: ^{1}H NMR spectra of Soluplus at 0.01, 0.05, 0.1, 0.5 and 1% in TC/L in PBS indicated as (L) green lines and (TC) red lines. TC/L reference spectrum is shown (bottom). At 1% some TC signals appeared very broad (e.g. TC H12, H7, H25, H3, H21, H19, and H18). Other signals were still observed (e.g. all L and TC H26).

S3.2.7 Kollidon VA 64 in PBS

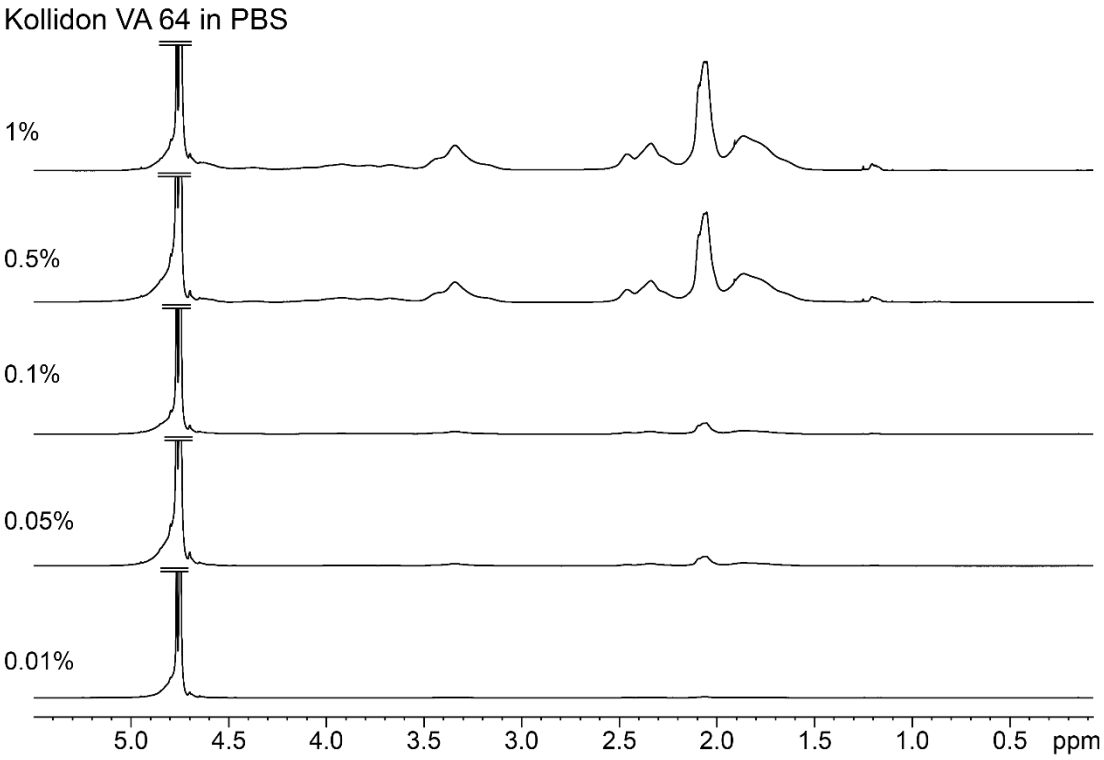

Figure S17: ^{1}H NMR spectra of Kollidon VA 64 at 0.01, 0.05, 0.1, 0.5 and 1% in PBS. Signal intensity increased as a function of concentration. Broad signals (e.g. at 1.6-2.5 ppm) were detected.

S3.2.8 Kollidon VA 64 in TC/L in PBS

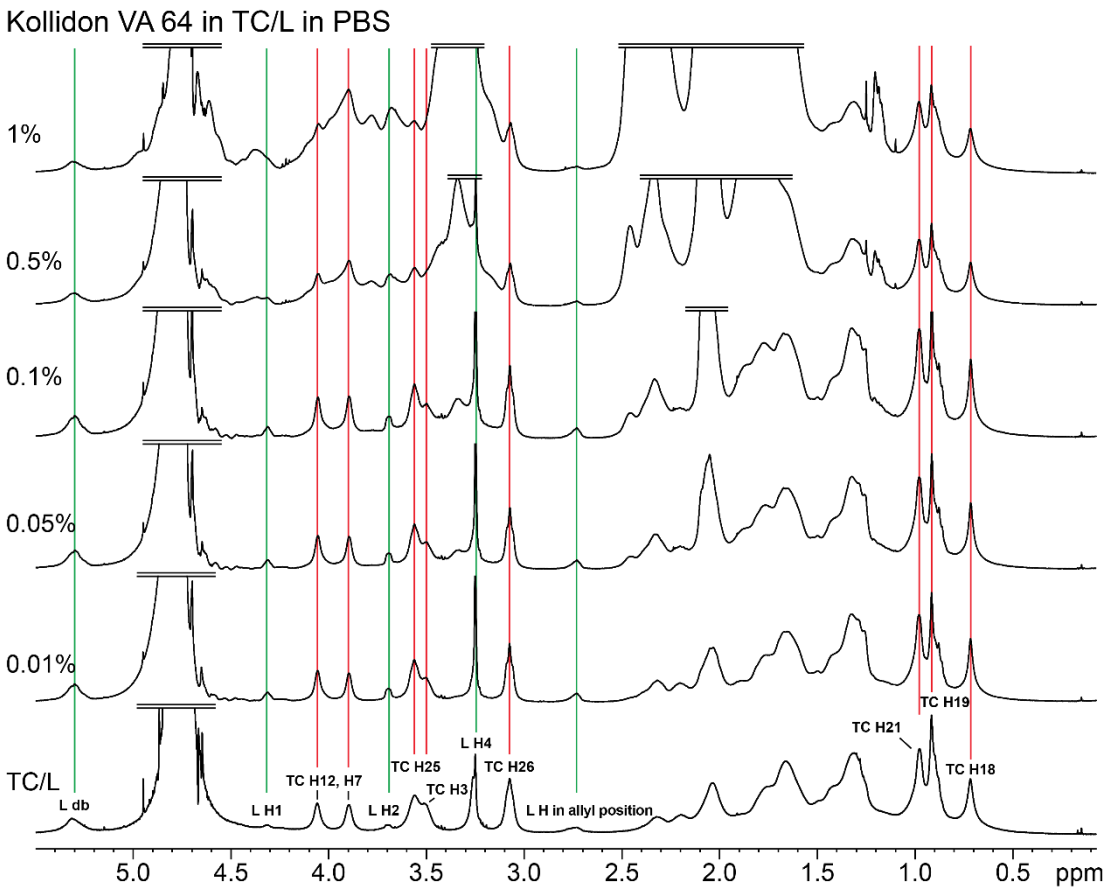

Figure S18: ^{1}H NMR spectra of Kollidon VA 64 at 0.01, 0.05, 0.1, 0.5 and 1% in TC/L in PBS indicated as (L) green lines and (TC) red lines. TC/L reference spectrum is shown (bottom). TC/L signals did not change. Kollidon VA 64 signals increased as a function of concentration overlapping with TC/L signals.

S3.2.9 HPMC-AS in PBS

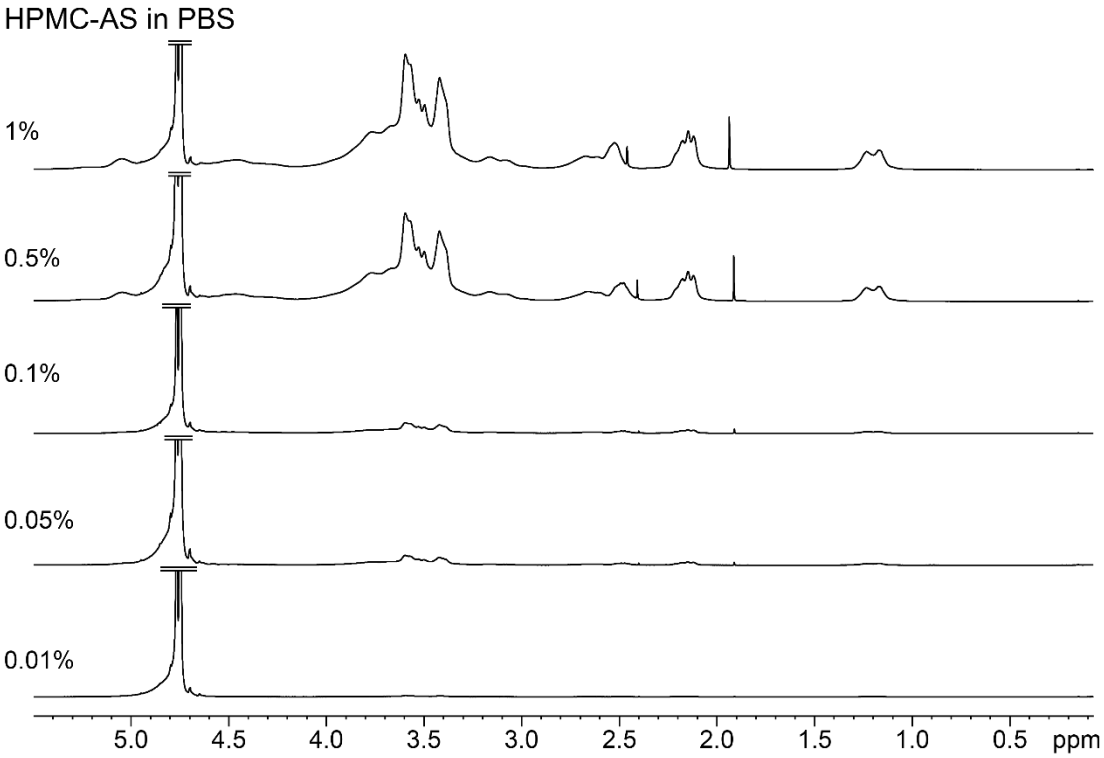

Figure S19: ^{1}H NMR spectra of HPMC-AS at 0.01, 0.05, 0.1, 0.5 and 1% in PBS. Signal intensity increased as a function of concentration. Broad signals (e.g. at 3.0-4.0 ppm) were detected along with sharp signals (e.g. at 1.9 and 2.4 ppm).

S3.2.10 HPMC-AS in TC/L in PBS

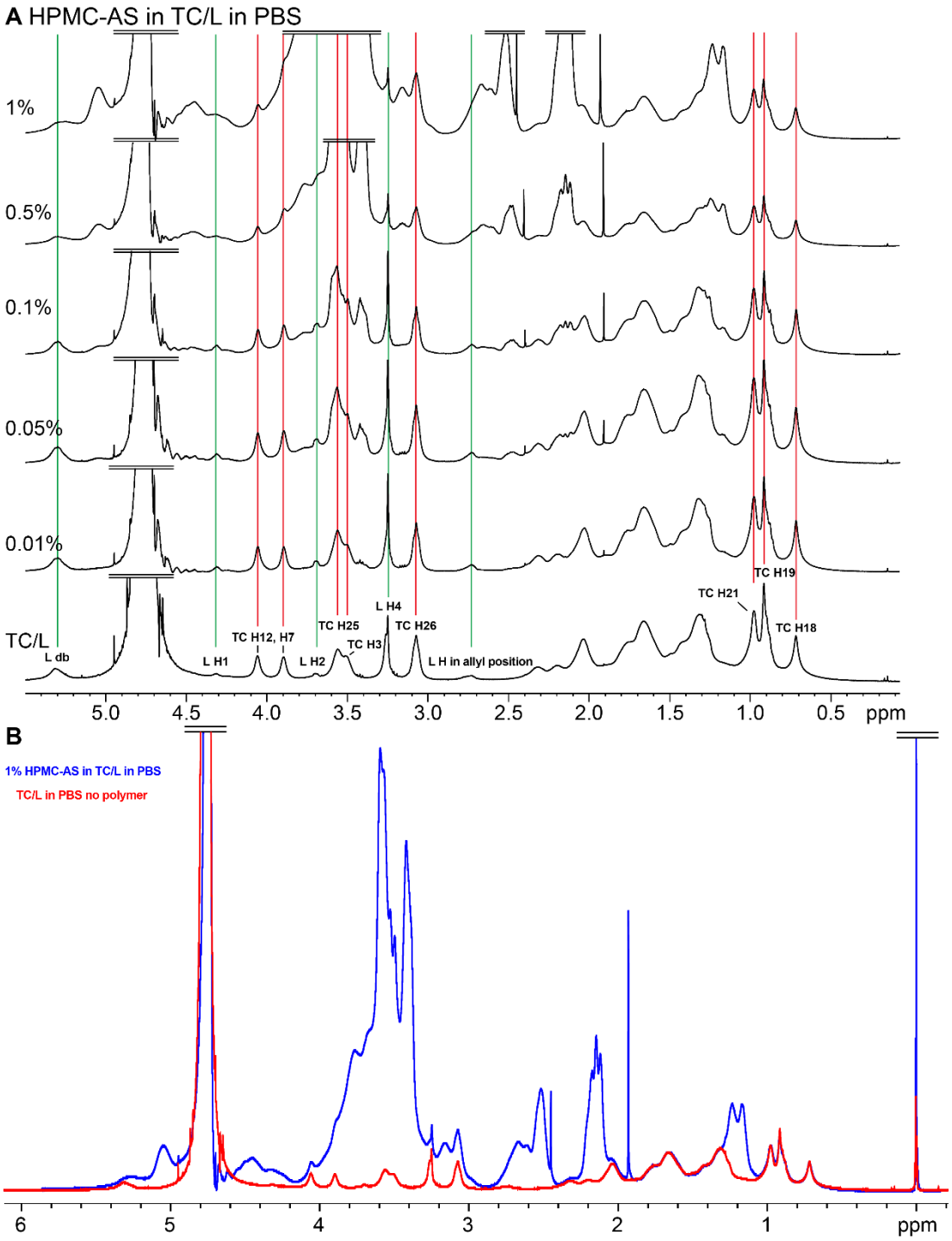

Figure S20: (A) ^{1}H NMR spectra of HPMC-AS at 0.01, 0.05, 0.1, 0.5 and 1% in TC/L in PBS indicated as (L) green lines and (TC) red lines. TC/L reference spectrum is shown (bottom). (B) Overlay of 1% HPMC-AS with TC/L and TC/L reference spectrum (B). TC/L signals did not change. HPMC-AS signals increased as a function of concentration and overlapped TC/L signals.

S3.2.11 Complete ^{1}H NMR spectra

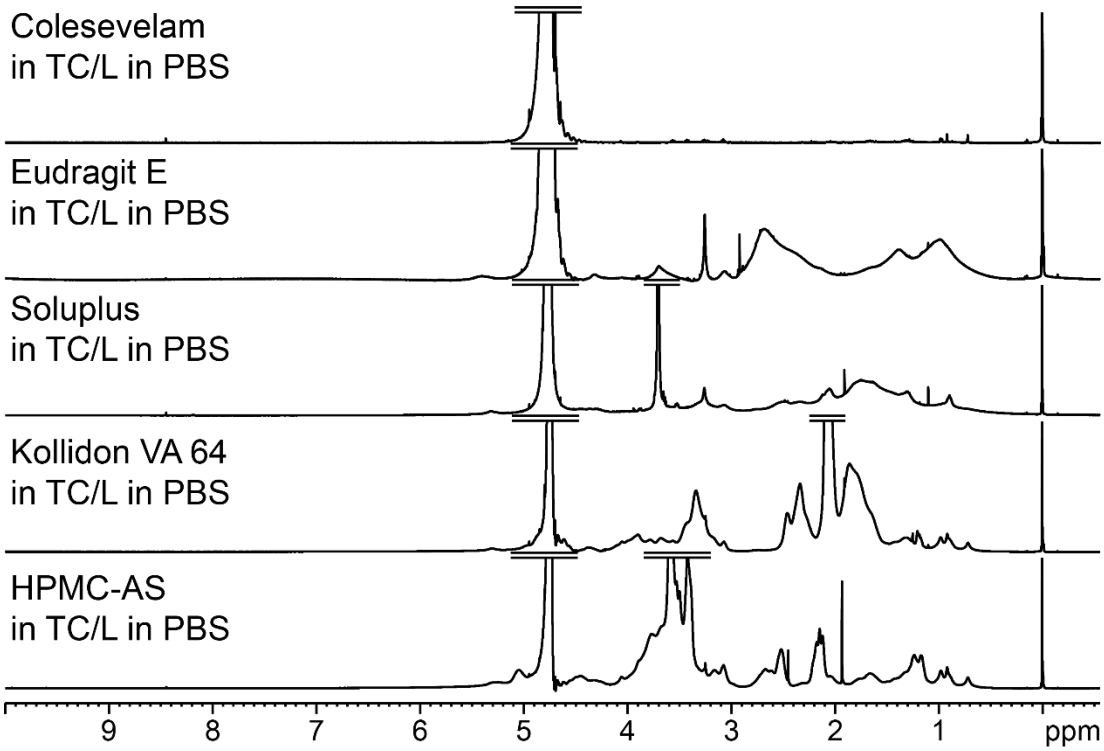

Figure S21: ^{1}H NMR spectra of 1% Colesevelam, Eudragit E, Soluplus, Kollidon VA 64, and HPMC-AS in TC/L in PBS.

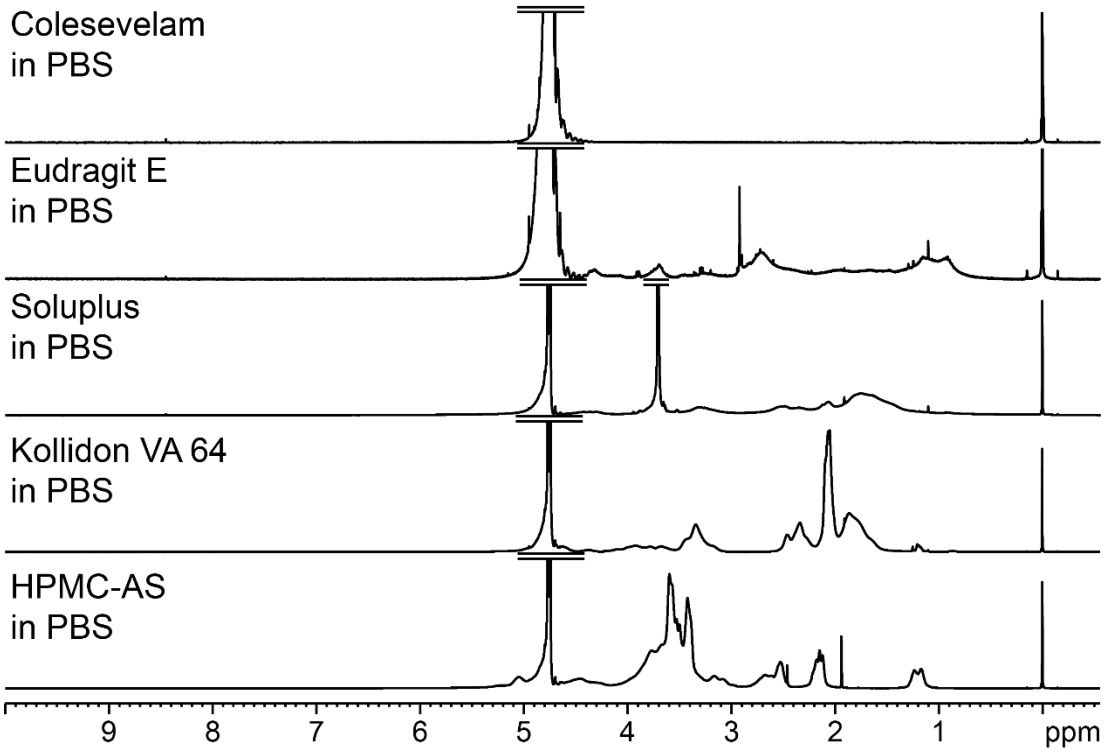

Figure S22: Complete ^{1}H NMR spectra of 1% Colesevelam, Eudragit E, Soluplus, Kollidon VA 64, and HPMC-AS in PBS.

S4 Polymer impact on free drug

S4.1 Perphenazine ^{1}H nuclear magnetic resonance (^{1}H NMR) analysis

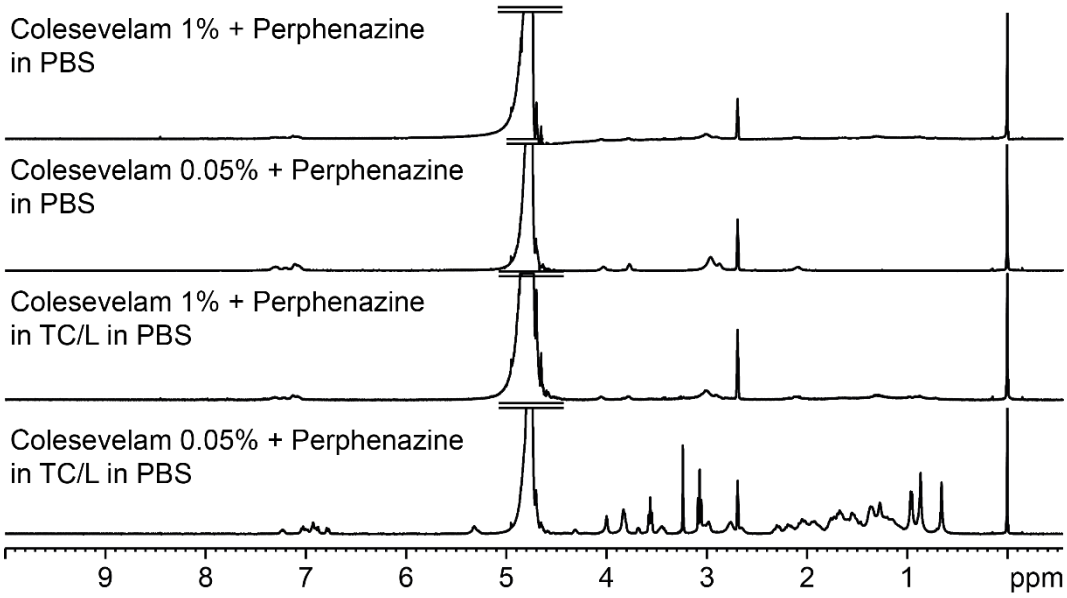

Figure S23: Complete ^{1}H NMR spectra of Colesevelam with Perphenazine in TC/L in PBS and in PBS.

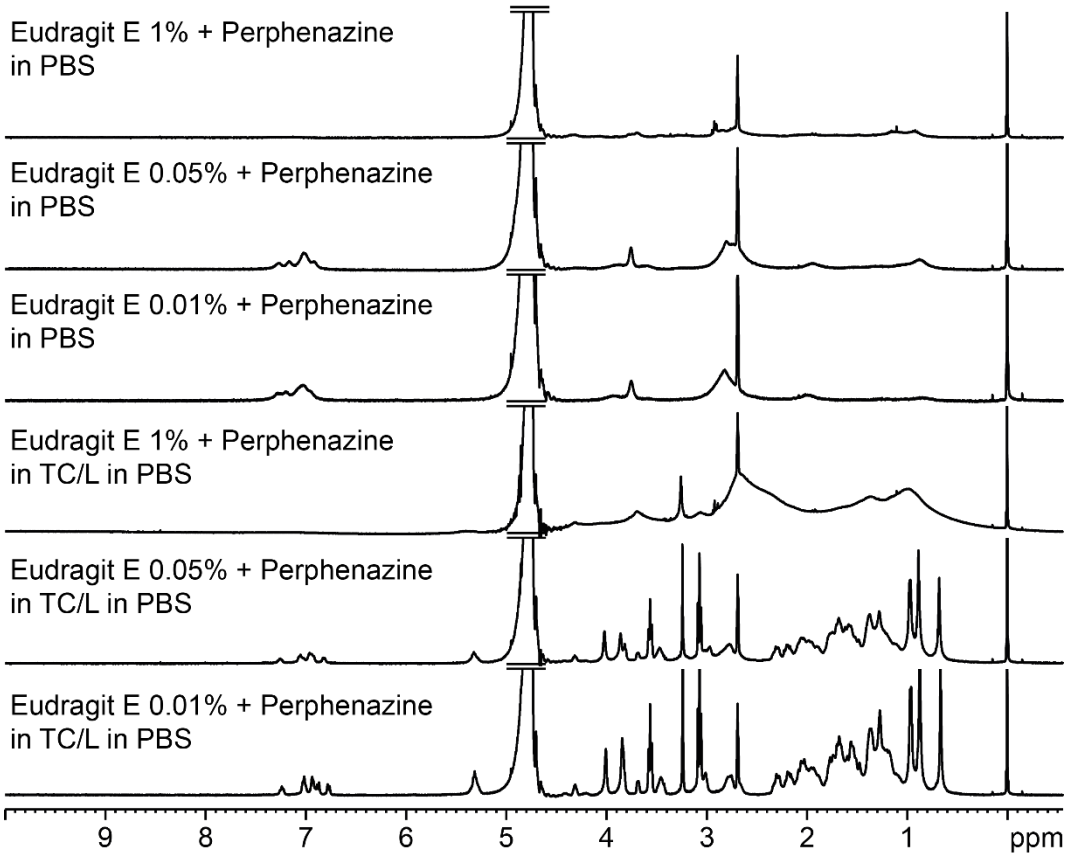

Figure S24: Complete ^{1}H NMR spectra of Eudragit E with Perphenazine in PBS in TC/L and in PBS

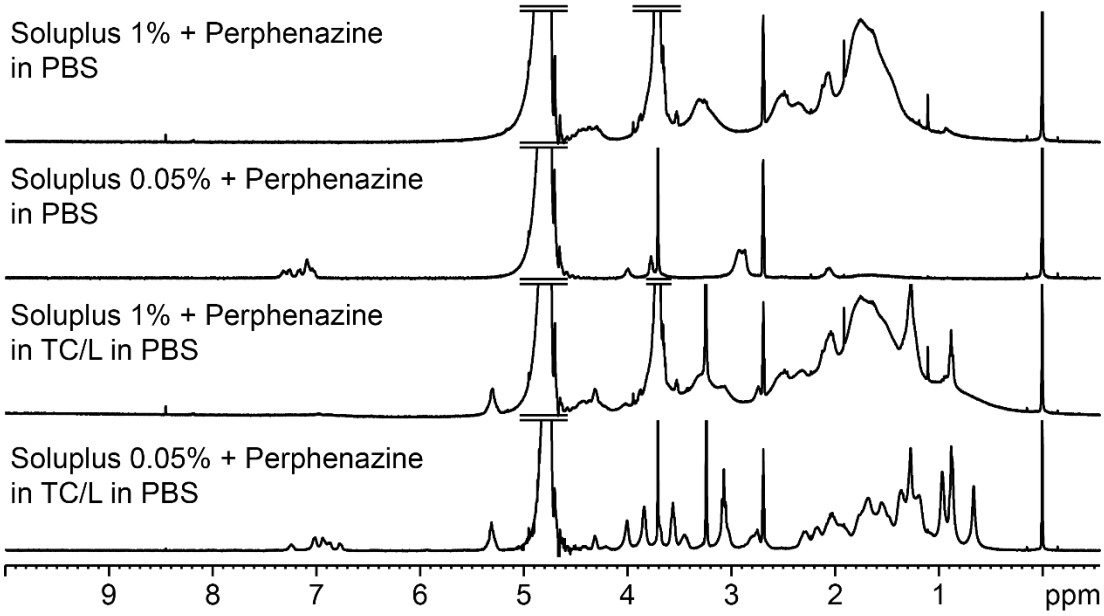

Figure S25: Complete ^{1}H NMR spectra of Soluplus with Perphenazine in PBS in TC/L and in PBS.

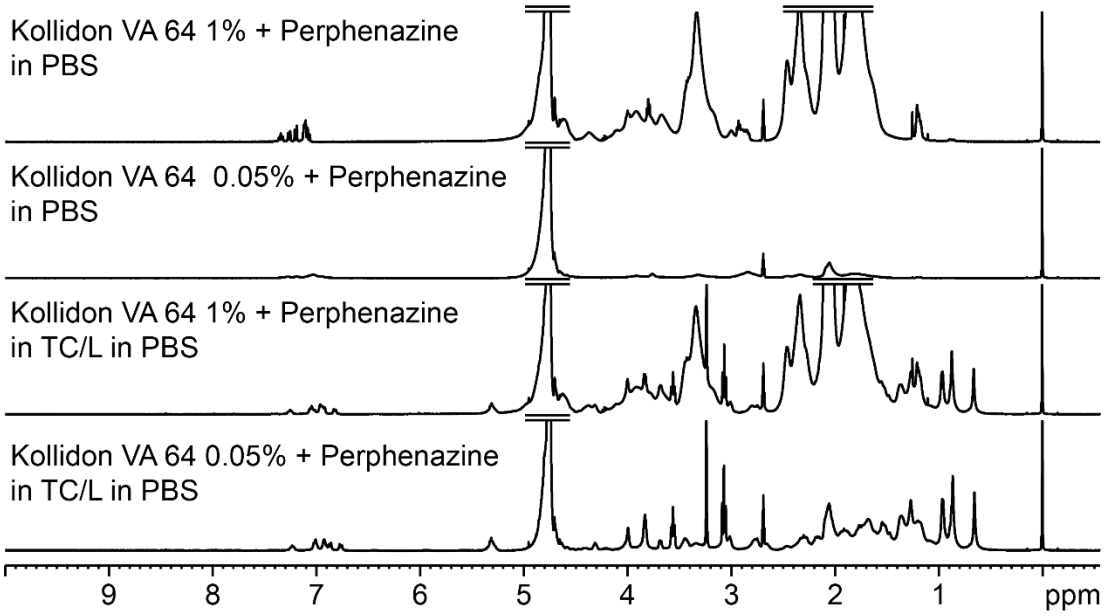

Figure S26: Complete ^{1}H NMR spectra of Kollidon VA 64 with Perphenazine in PBS in TC/L and in PBS.

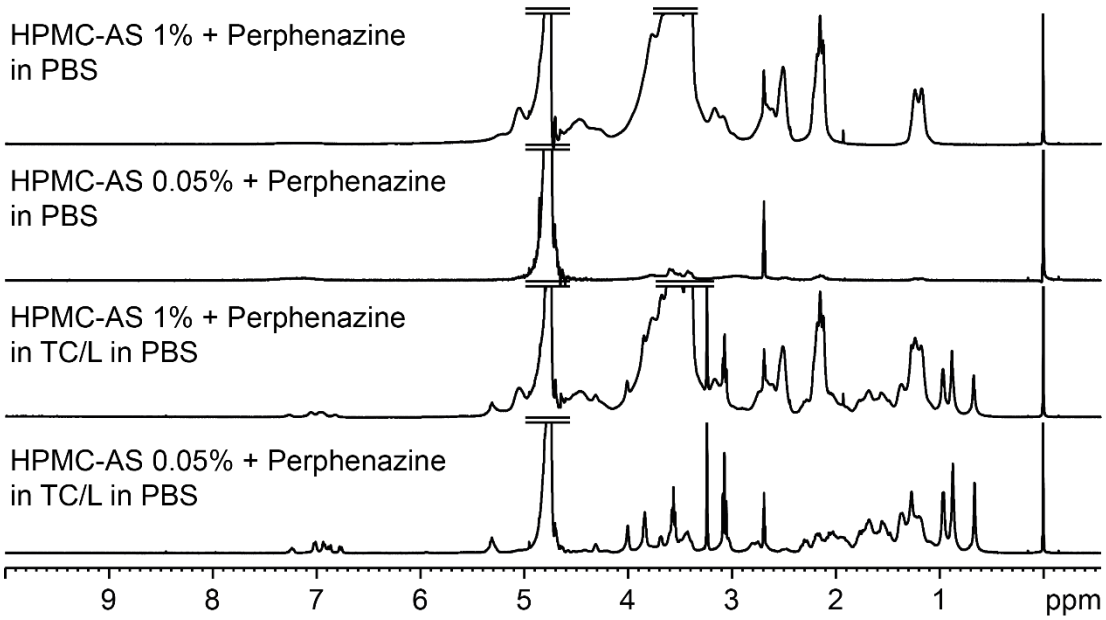

Figure S27: Complete ^{1}H NMR spectra of HPMC-AS with Perphenazine in PBS in TC/L and in PBS.

S4.2 Imatinib ^{1}H nuclear magnetic resonance (^{1}H NMR) analysis

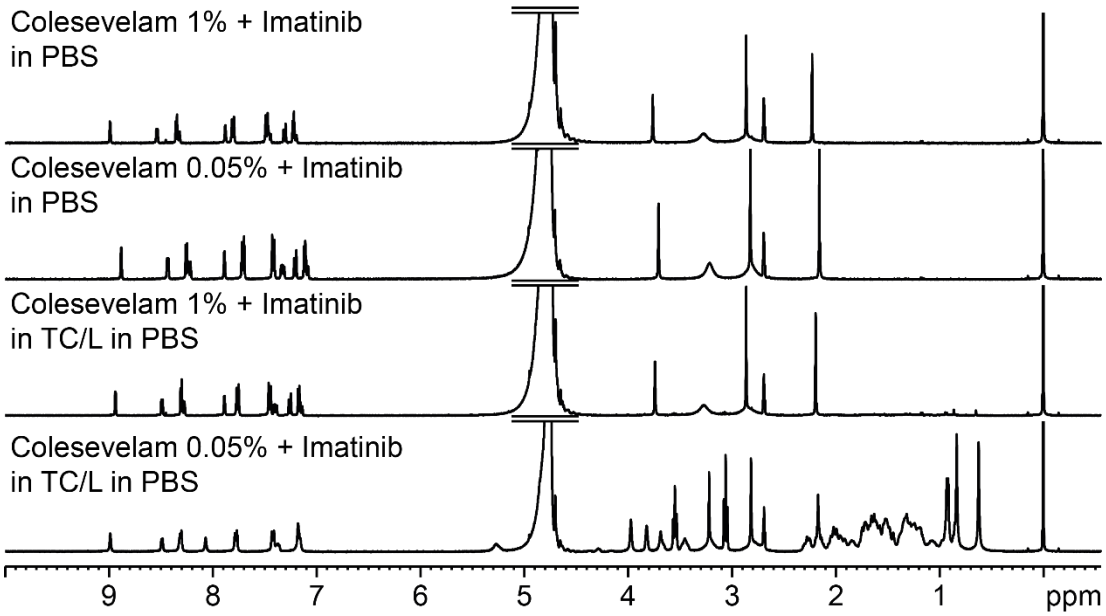

Figure S28: Complete ^{1}H NMR spectra of Colesevelam with Imatinib in PBS in TC/L and in PBS.

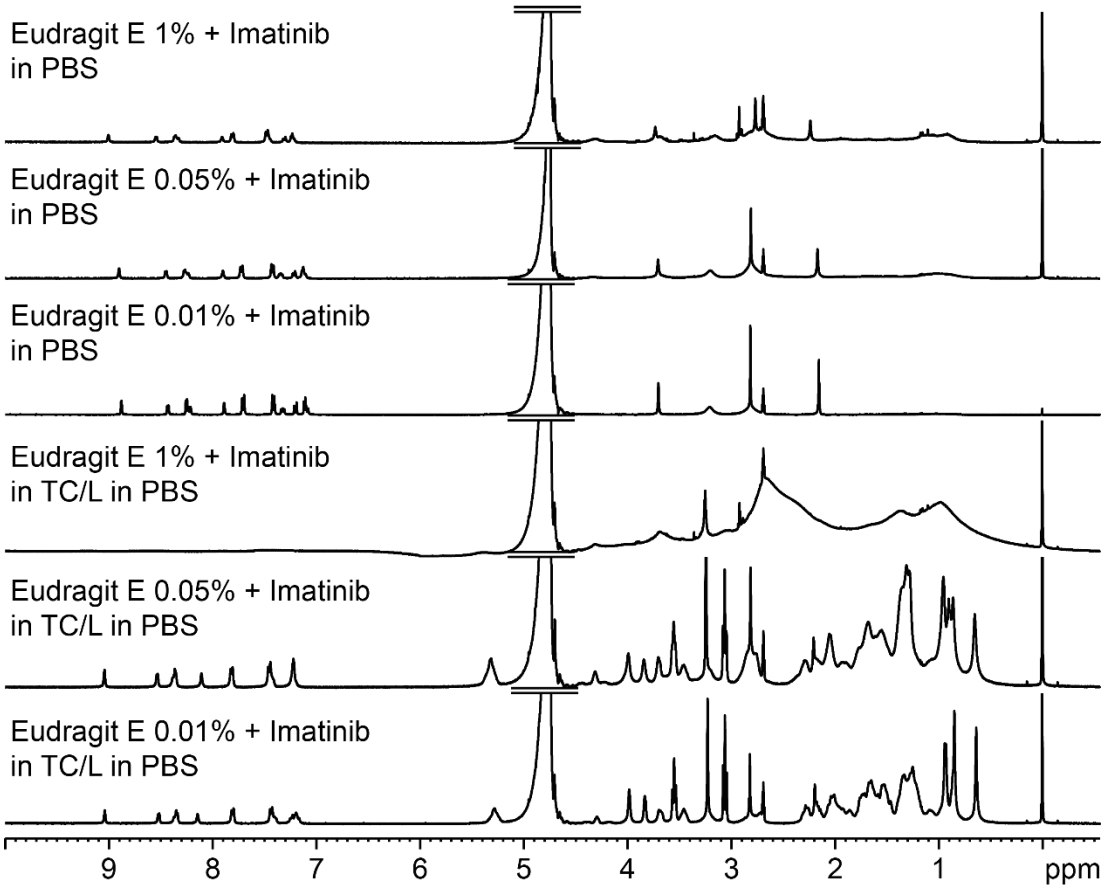

Figure S29: Complete ^{1}H NMR spectra of Eudragit E with Imatinib in PBS in TC/L and in PBS.

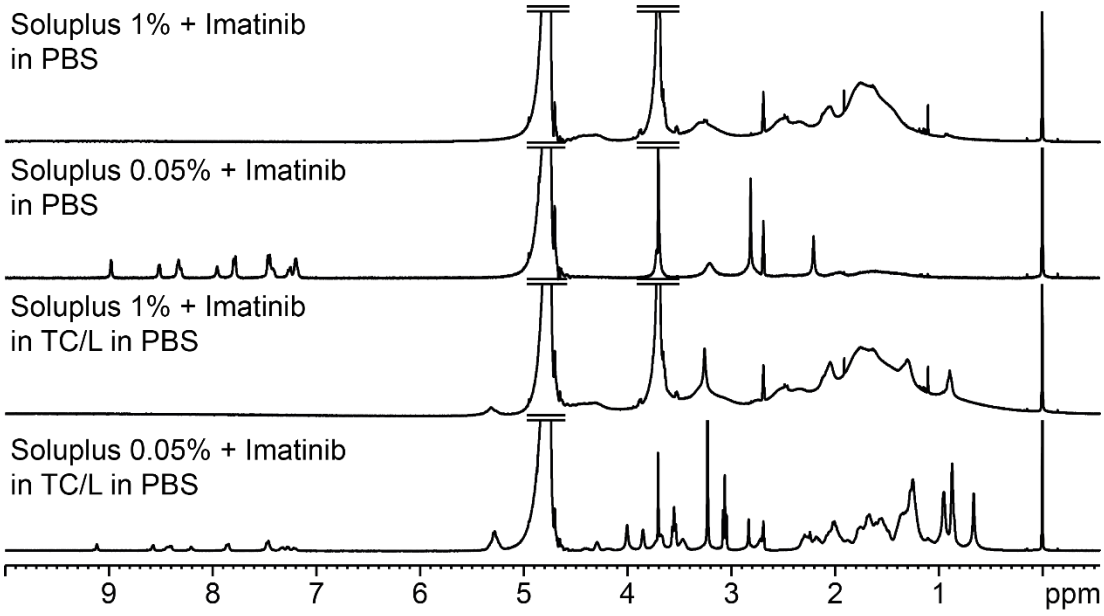

Figure S30: Complete ^{1}H NMR spectra of Soluplus with Imatinib in PBS in TC/L and in PBS.

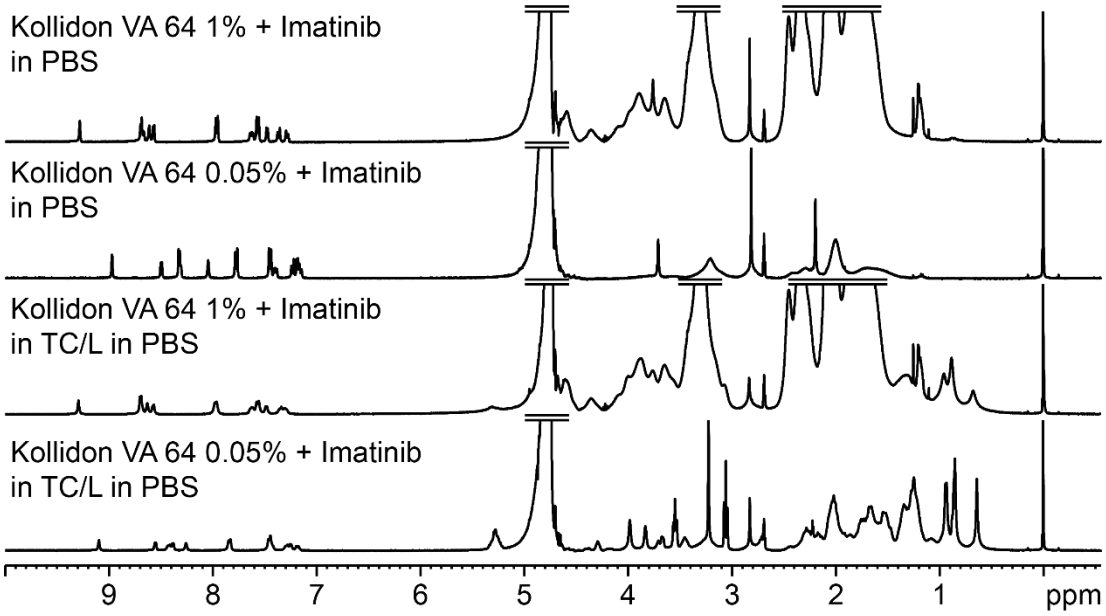

Figure S31: Complete ^{1}H NMR spectra of Kollidon VA 64 with Imatinib in PBS in TC/L and in PBS.

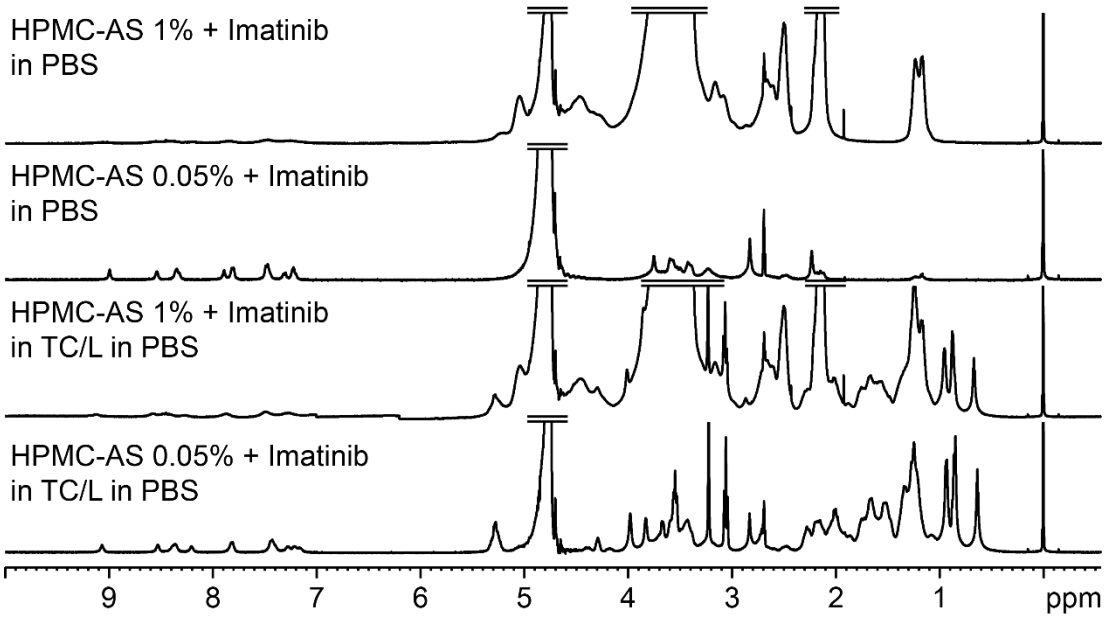

Figure S32: Complete ^{1}H NMR spectra of HPMC-AS with Imatinib in PBS in TC/L and in PBS.

S4.3 Metoprolol ^{1}H nuclear magnetic resonance (^{1}H NMR) analysis

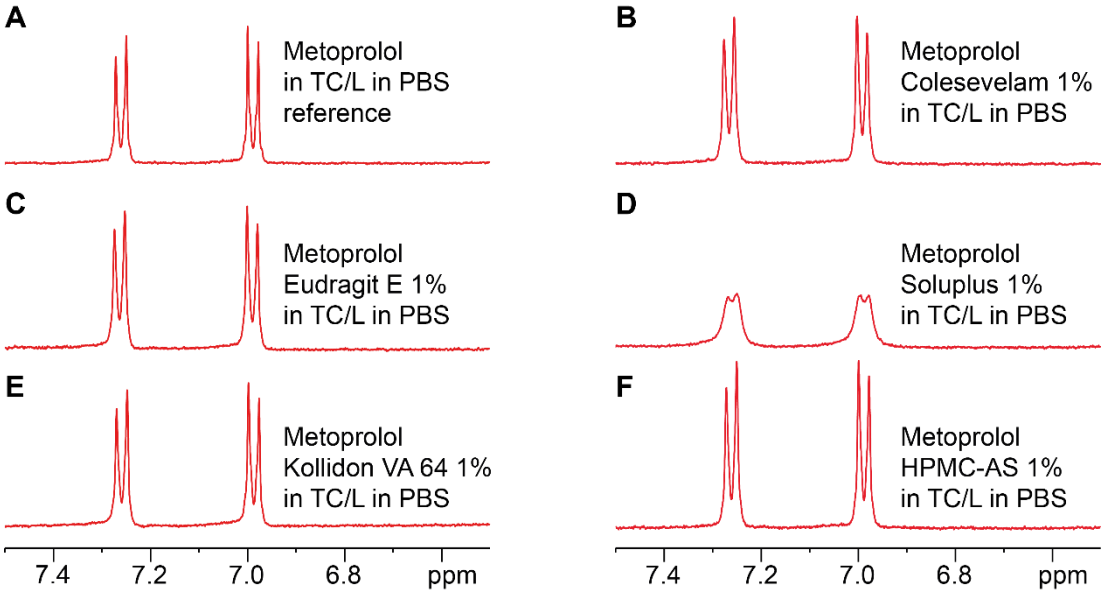

Figure S33: Metoprolol ^{1}H NMR aryl-proton spectra (A) in TC/L in PBS and with 1% respective polymer in TC/L in PBS (B-F). Metoprolol aryl-proton signals were not impacted by (B) Colesevelam, (C) Eudragit E, (E) Kollidon VA 64, and (F) HPMC-AS at 1% in TC/L in PBS. (D) Signal decreased in intensity and broadened by Soluplus.

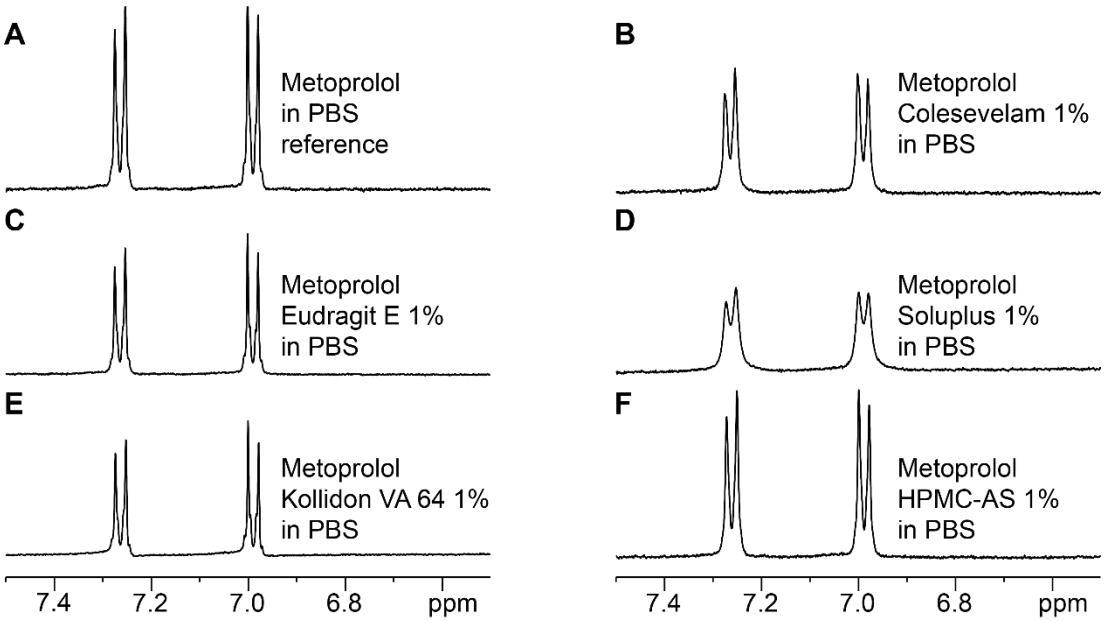

Figure S34: Metoprolol ^{1}H NMR aryl-proton spectra (A) in PBS and with 1% respective polymer in PBS (B-F). (B) Colesevelam, (C) Eudragit E, (D) Soluplus and (E) Kollidon VA 64 decreased signal intensity in PBS. (D) Soluplus broadened signals. (F) Signals were not impacted by 1% HPMC-AS in PBS.

S5 Polymer impact on HDO diffusivity

Table S4: HDO diffusion coefficients (D in m^2/s) for polymers in TC/L in PBS with Perphenazine at 4.703 ppm.

Concentration [%]	Colesevelam		Eudragit E		Soluplus		Kollidon VA 64		HPMC-AS	
	D $*10^{-9}$	Error by fit $*10^{-11}$	D $*10^{-9}$	Error by fit $*10^{-11}$	D $*10^{-9}$	Error by fit $*10^{-11}$	D $*10^{-9}$	Error by fit $*10^{-11}$	D $*10^{-9}$	Error by fit $*10^{-11}$
0.01	N/A	N/A	2.60	0.597	N/A	N/A	N/A	N/A	N/A	N/A
0.05	2.61	9.9	2.56	1.74	2.57	0.745	2.60	0.948	2.60	0.626
1	2.62	0.624	2.58	0.864	2.55	0.318	2.47	3.19	2.52	0.717
0	$2.60*10^{-9}$ Error by fit: $2.70*10^{-12}$									

Table S5: Perphenazine aryl-proton diffusion coefficients (D in m^2/s) for polymers (0.05%) in TC/L in PBS at 7.2 and 6.7 ppm. Preliminary data set as signal decay did not reach < 10 % of initial intensity.

Concentration, signal	Colesevelam		Eudragit E		Soluplus		Kollidon VA 64		HPMC-AS	
	D $*10^{-10}$	Error by fit $*10^{-11}$	D $*10^{-10}$	Error by fit $*10^{-11}$	D $*10^{-10}$	Error by fit $*10^{-11}$	D $*10^{-10}$	Error by fit $*10^{-11}$	D $*10^{-10}$	Error by fit $*10^{-11}$
0.05% 7.2ppm	1.55	2.92	1.12	6.00	0.782	4.46	1.23	2.49	1.22	2.40
0.05% 6.7ppm	1.62	3.09	1.12	4.94	0.538	4.72	1.31	3.04	1.02	2.37
0% 7.2ppm	$1.16*10^{-10}$ Error by fit: $2.10*10^{-11}$									
0% 6.7ppm	$1.35*10^{-10}$ Error by fit: $2.57*10^{-11}$									

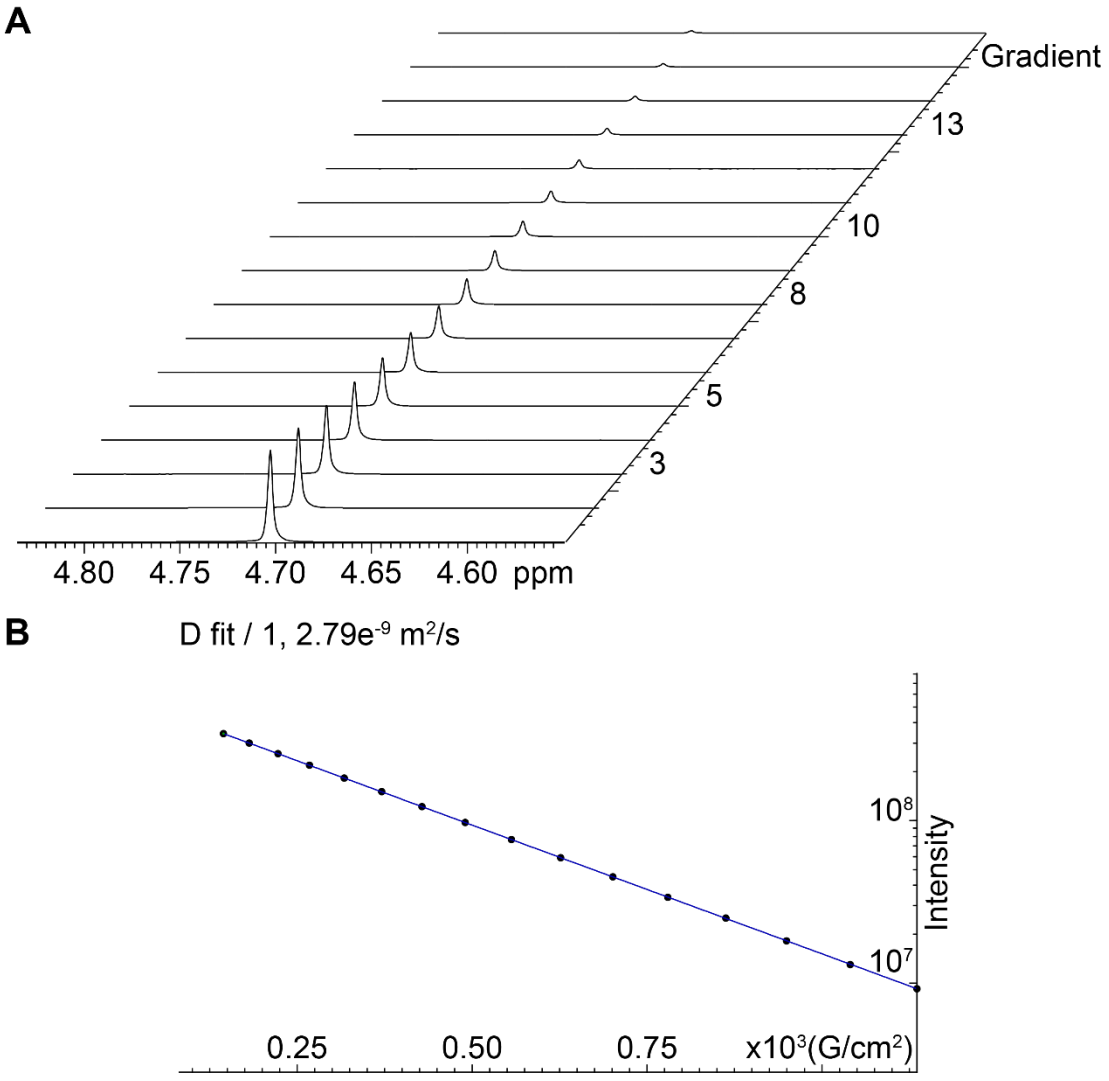

Figure S35: DOSY analysis: (A) HDO (4.703 ppm) signal attenuation with increased gradient strength and (B) fitted curve of experimental intensity decay as a function of the gradient strength for Perphenazine in TC/L in PBS (without polymer).

S6 Excipient concentration under physiological conditions

The fluid volume in the fasted small intestine varies between 45 and 319 ml (mean: 107 ± 72 ml), unevenly distributed in roughly four fluid pockets with a median volume of 12 ml.[2] An average oral dosage form contains 280 mg excipients.[3] Hence, dissolving 280 mg excipient in a fluid pocket with a volume of 12 ml results in a mass concentration of 2.33%. For tablet coating, few milligrams of glazing agent are required.[4] Assuming 2 mg coating mass results in a concentration of 0.017%. A tablet is usually composed of more than one excipient, consequently the concentration for one respective excipient is <2.33%. Therefore, our tested polymer concentrations ranging from 0.01-1% reflects the physiological situation.

S7 Flux evaluation

S7.1 Flux at different TC/L concentrations

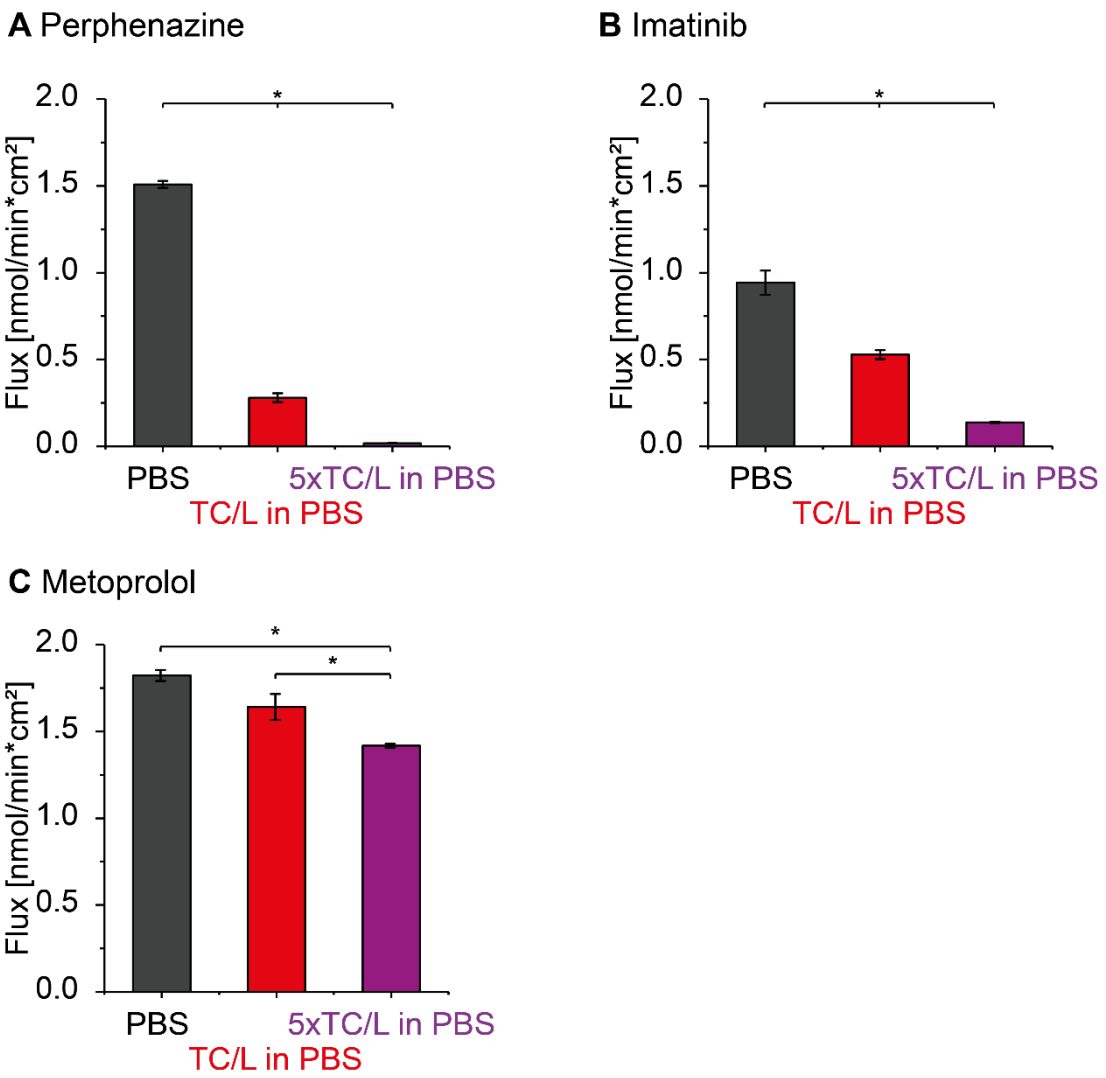

Figure S36: Flux of (A) Perphenazine, (B) Imatinib, and (C) Metoprolol (each at 1000 µmol/l) in PBS (black), in TC/L in PBS (red; simulating a fasted state and known as FaSSIF V1),[5] and in TC/L at fivefold concentration in PBS as compared to FaSSIF V1 (purple; simulating a fed state and known as FeSSIF V1).[5] Flux was significantly reduced for Perphenazine and Imatinib in TC/L in PBS and in 5xTC/L in PBS. Metoprolol flux was not significantly reduced in TC/L in PBS compared to PBS, but in 5xTC/L in PBS. Data shown as mean ± SD, ANOVA considering $p \leq 0.05$ as statistically significant followed by Games-howell *post-hoc* test for pairwise comparison as the criteria of variance homogeneity was not fulfilled (significant differences are shown by asterisks).

S7.2 Flux at different drug starting concentrations

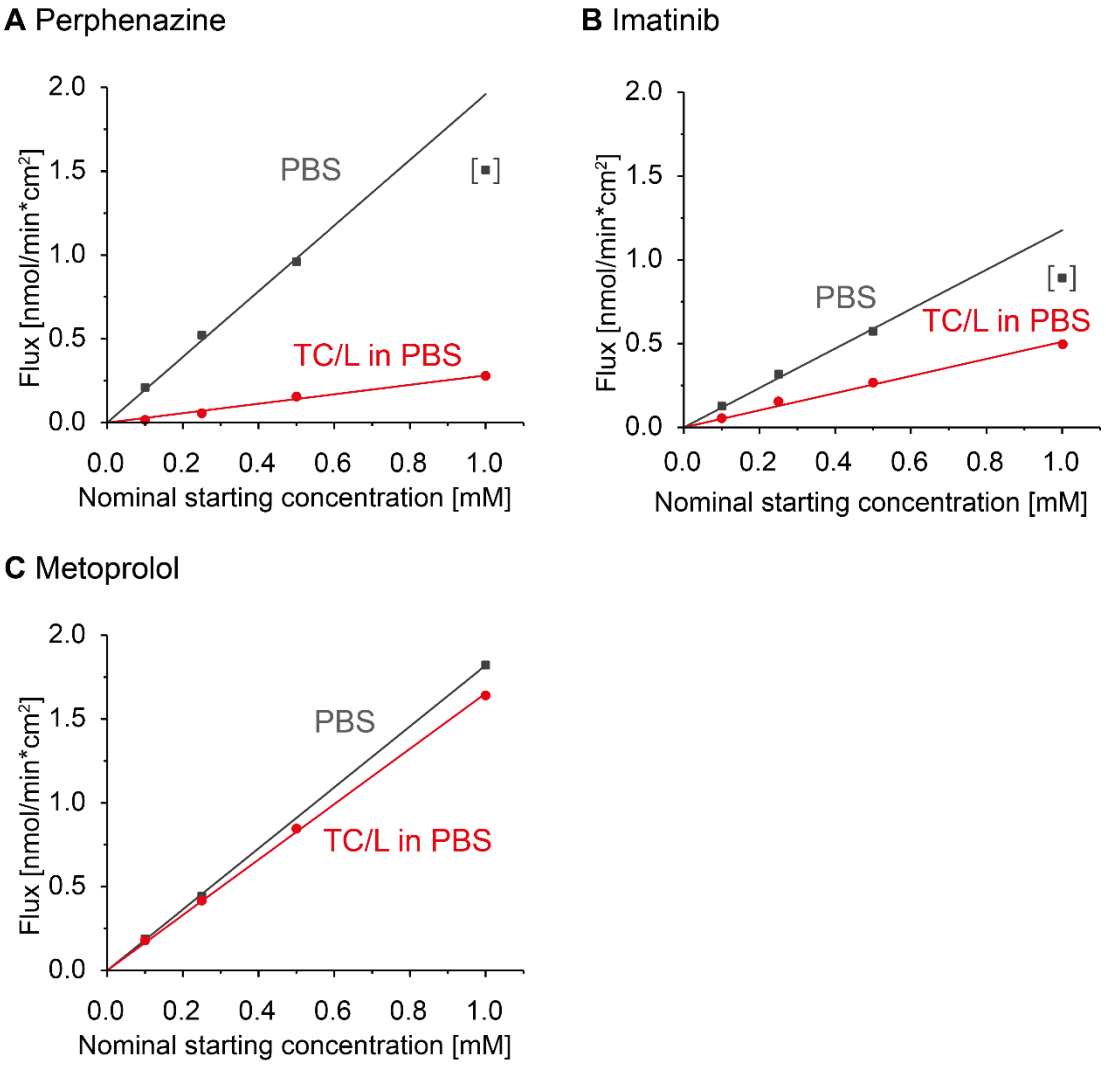

Figure S37: Flux of (A) Perphenazine, (B) Imatinib, and (C) Metoprolol at different starting concentrations (100, 250, 500, and 1000 µmol/l) in PBS (black) and in TC/L in PBS (red). Flux increased linearly over concentration in all cases in TC/L in PBS. In PBS at 1000 µM flux for (A) Perphenazine and (B) Imatinib did not follow the linear trend of measurements at low concentrations (data point in brackets). Nevertheless, flux was stable over time for this concentration (**Figure S37**). Data shown as a single point measurement.

S7.3 Drug concentration over time

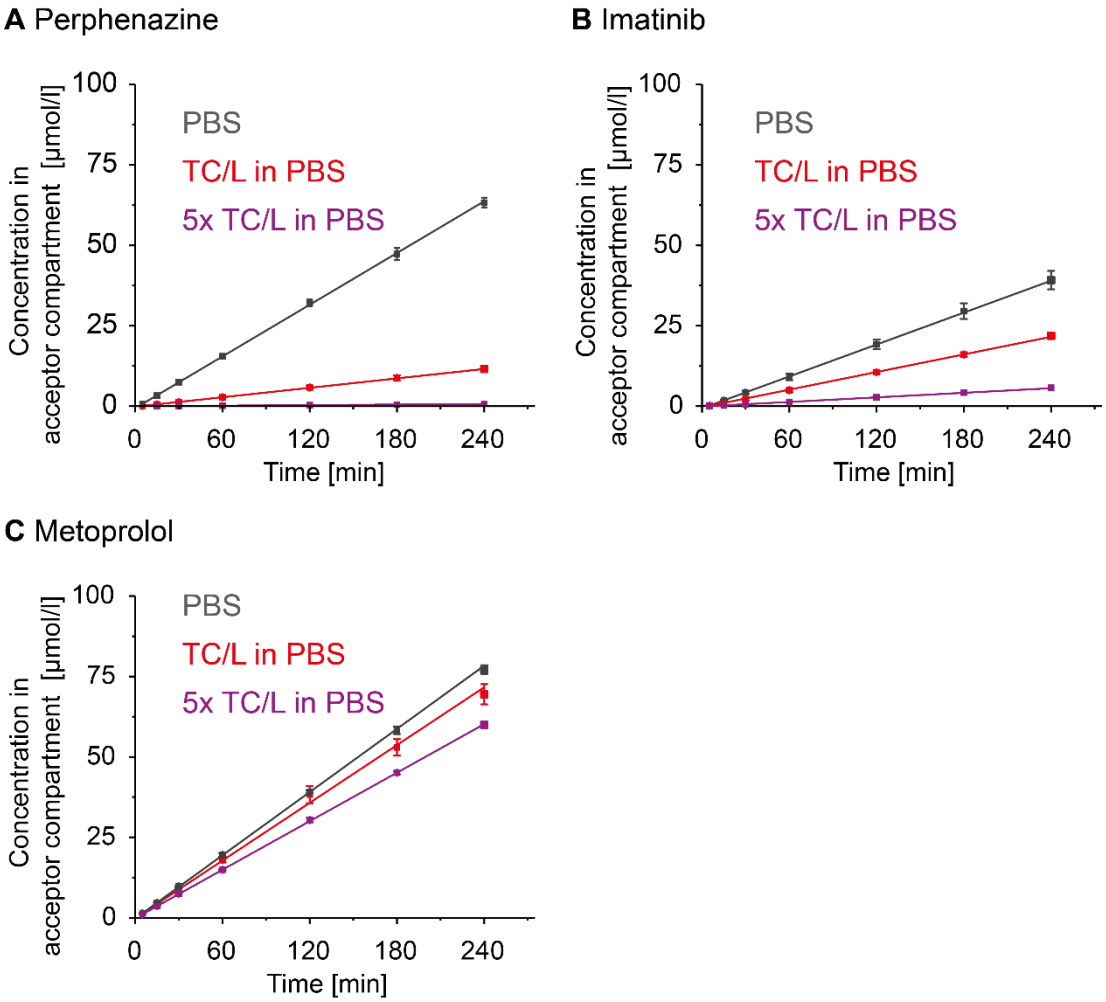

Figure S38: (A) Perphenazine, (B) Imatinib, and (C) Metoprolol concentration [µmol/l] in the flux acceptor compartment in PBS (black), in TC/L in PBS (simulating fasted state/FaSSIF V1; red), and with TC/L at fivefold concentration in PBS as compared to FaSSIF V1 (simulating fed state; FeSSIF V1; purple) over time at a starting concentration of 1000 µmol/l in the donor compartment. Concentration increased linearly over time in all cases indicating stable experimental conditions. Data shown as mean ± SD.

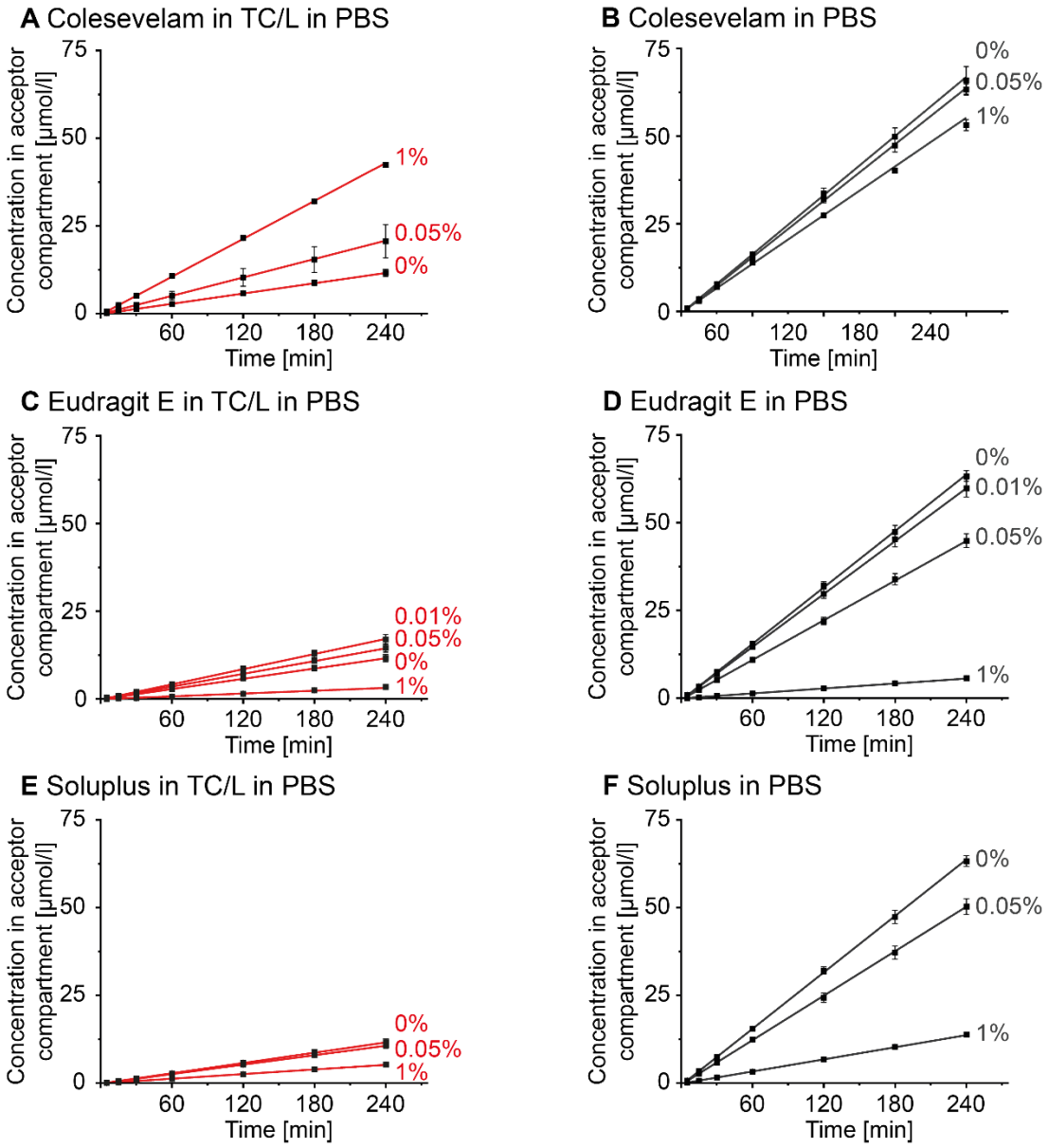

Figure S39: Perphenazine concentration [µmol/l] in the flux acceptor compartment over time with (A, B) Colesevelam, (C, D) Eudragit E, (E, F) Soluplus in TC/L in PBS (respective left panel) and in PBS (respective right panel) at concentrations as indicated. Data at 0% polymer concentration are identical for all panels and given for comparison.

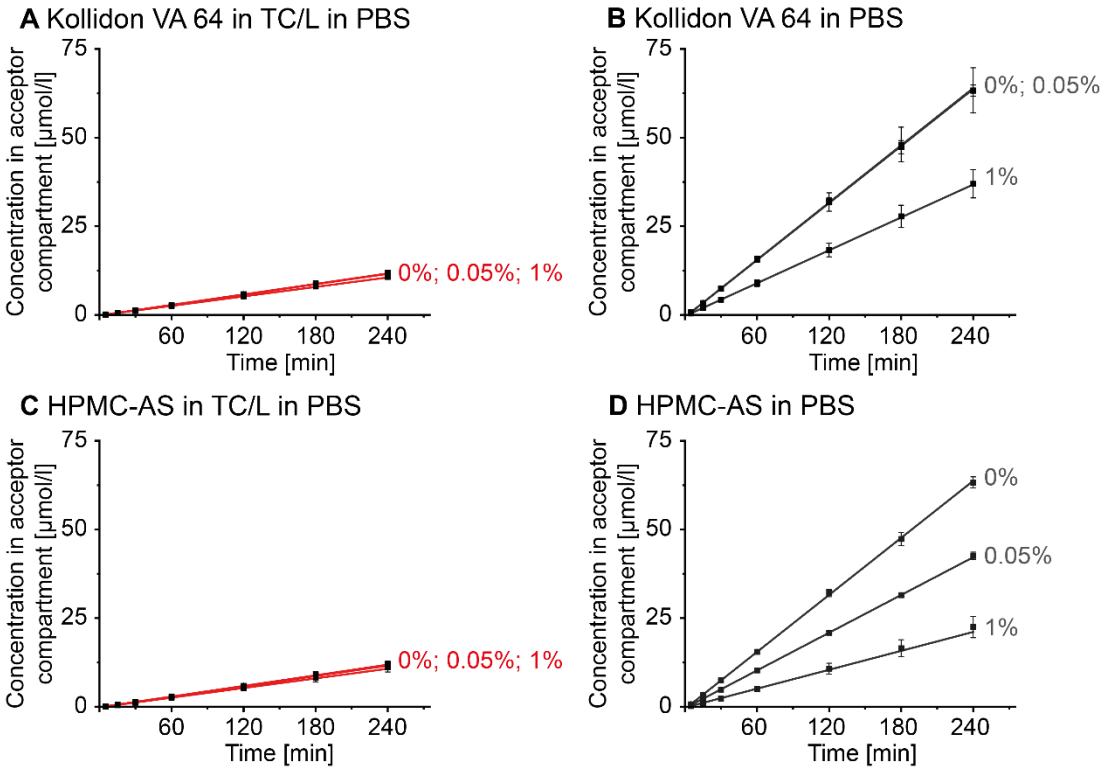

Figure S40: Perphenazine concentration [µmol/l] in the flux acceptor compartment over time with (A, B) Kollidon VA 64, (C, D) HPMCAS in TC/L in PBS (respective left panel) and in PBS (respective right panel) at concentrations as indicated. Data at 0% polymer concentration are identical for all panels and given for comparison.

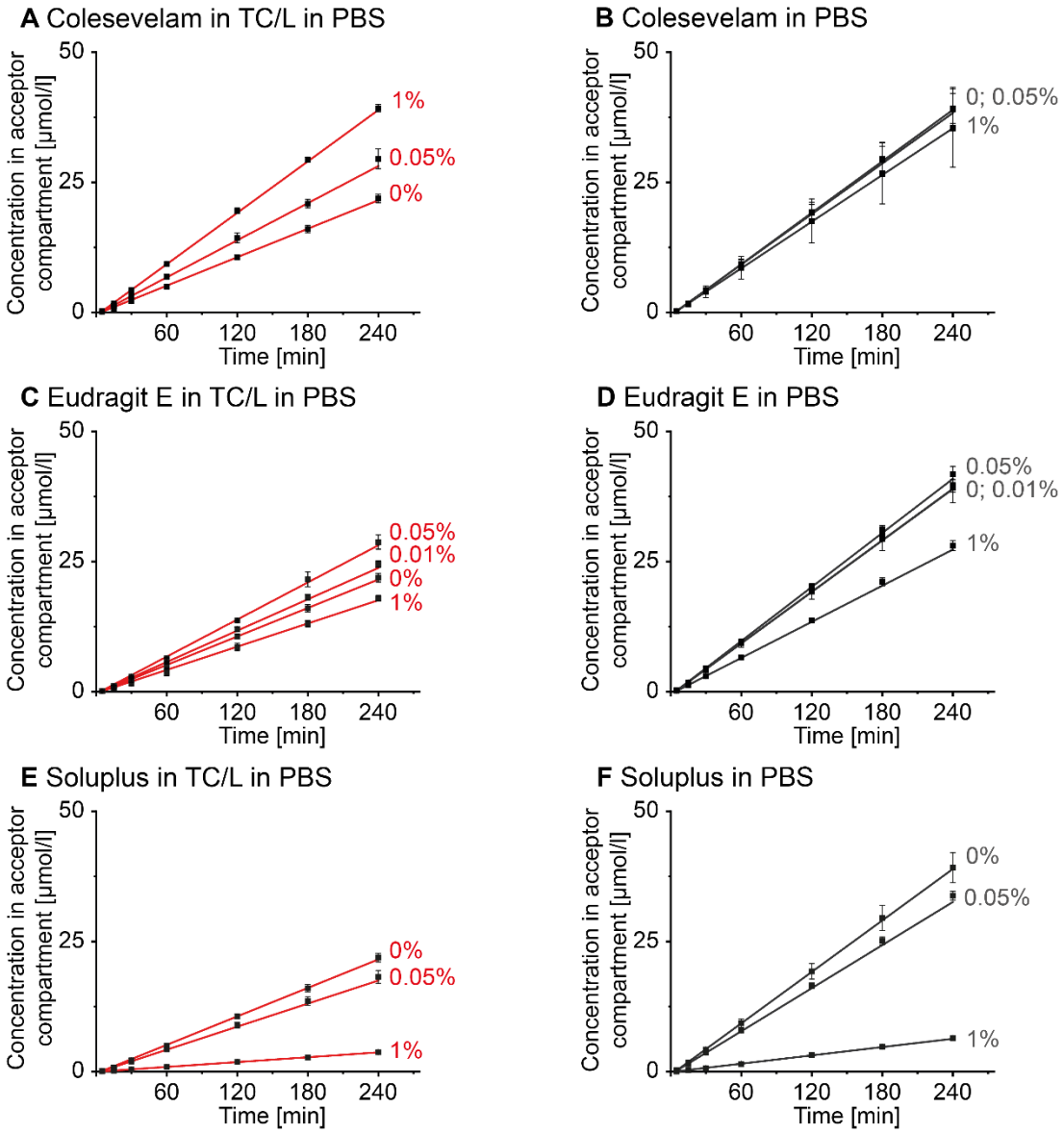

Figure S41: Imatinib concentration [µmol/l] in the flux acceptor compartment over time with (A, B) Colesevelam, (C, D) Eudragit E, (E, F) Soluplus in TC/L in PBS (respective left panel) and in PBS (respective right panel) at concentrations as indicated. Data at 0% polymer concentration are identical for all panels and given for comparison.

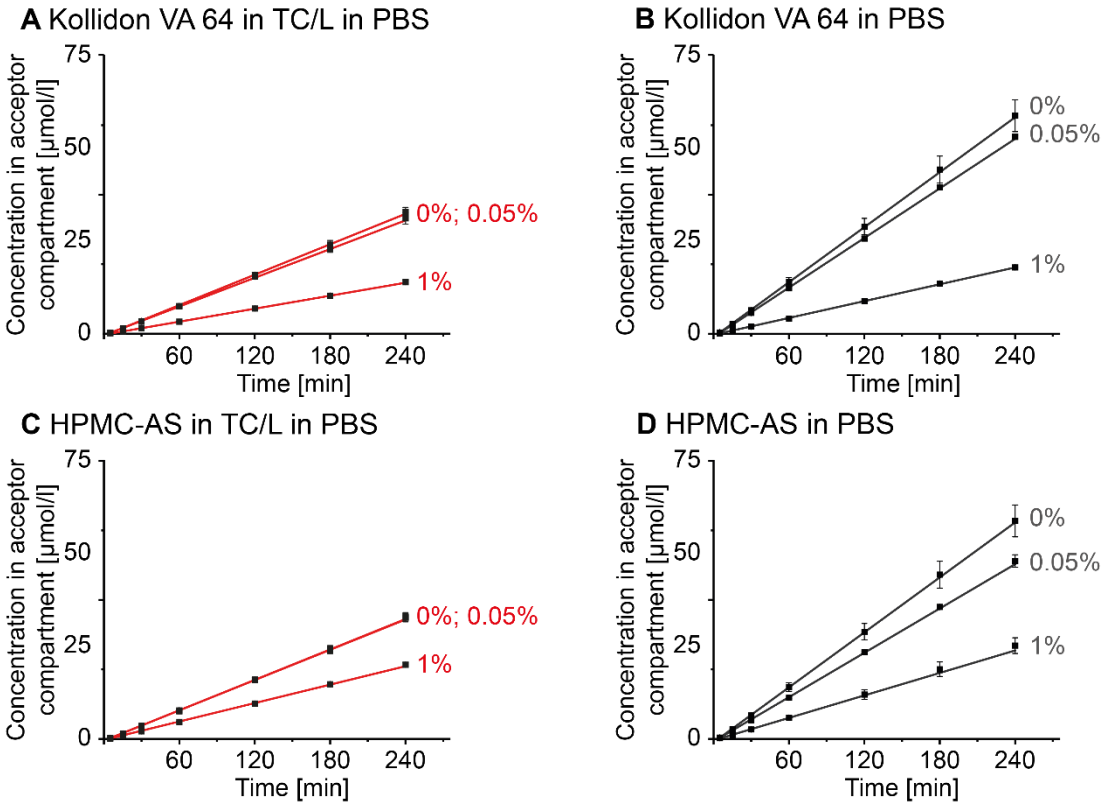

Figure S42: Imatinib concentration [µmol/l] in the flux acceptor compartment over time with (A, B) Kollidon VA 64, (C, D) HPMCAS in TC/L in PBS (respective left panel) and in PBS (respective right panel) at concentrations as indicated. Data at 0% polymer concentration are identical for all panels and given for comparison.

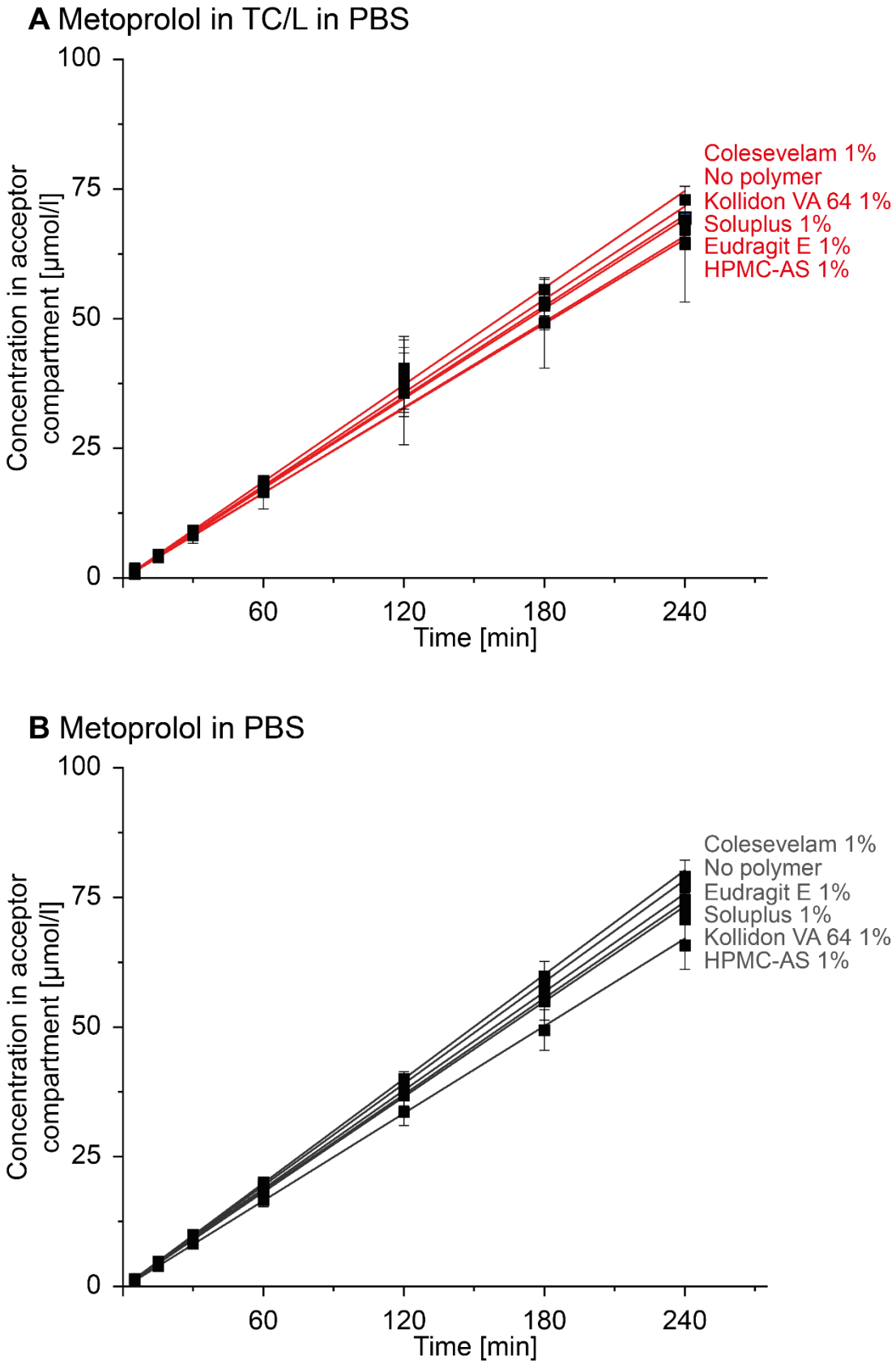

Figure S43: Metoprolol concentration [µmol/l] in the flux acceptor compartment over time with polymers as indicated (A) in TC/L in PBS and (B) in PBS at 1% polymer concentration. Data at 0% polymer concentration are provided in each panel.

S7.4 Flux lag time

S7.4.1 Lag time Perphenazine

Initial experiments were conducted at n = 3, thereby not allowing reasonable outlier testing. For the four groups with larger standard deviation as outlined in the table below, three additional experiments were conducted and outlier tests were performed. Subsequently, the lag time of these groups were evaluated (**Table S6**). One lag time observation for Perphenazine in PBS was categorized as an outlier based on a double-sided Grubb's outlier test and consequently excluded from the statistical analysis (**Figure S44**).

Table S6: Double-sided Grubb's outlier test for lag time of Perphenazine in PBS, in TC/L in PBS, in TC/L in PBS with 1% Eudragit E, and in TC/L in PBS with 1% HPMC-AS with a significance level of 0.05. One outcome was excluded as highlighted in bold/italic numbers.

Number	**Lag time Perphenazine in PBS [min]**	**Lag time Perphenazine in TC/L in PBS [min]**	**Lag time Perphenazine in TC/L in PBS with 1% Eudragit E [min]**	**Lag time Perphenazine in TC/L in PBS with 1% HPMC-AS [min]**
1	3,05	3,75	13,98	5,63
2	2,70	3,06	13,49	9,90
3	*-0,13*	1,81	16,66	5,50
4	2,84	5,93	8,57	7,76
5	2,24	5,62	12,21	7,29
6	2,60	5,77	8,73	7,52
Result from Grubb's-test	Outlier (-0,13)	No Outlier	No Outlier	No Outlier

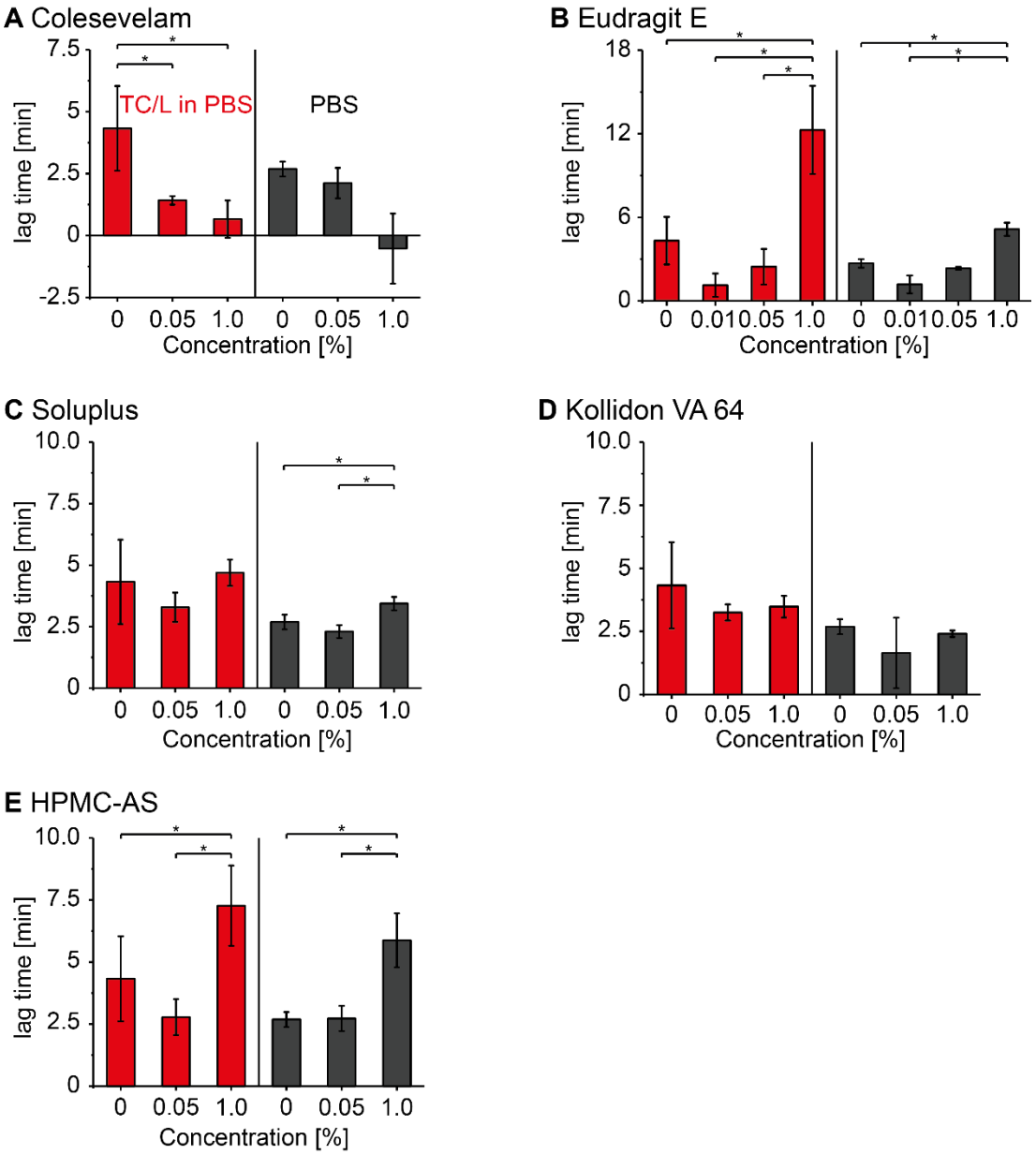

Figure S44: Lag time of Perphenazine with (A) Colesevelam, (B) Eudragit E, (C) Soluplus, (D) Kollidon VA 64, and (E) HPMC-AS in TC/L in PBS (red) and in PBS (black) at concentrations as indicated. The data reported at 0% are identical for all panels and given for comparison. Data for (B) Eudragit E is also shown in Figure 6 in the manuscript. Lag time was calculated by time axis intersect of the extrapolated linear part (**Figure S36**). Data shown as mean ± SD, ANOVA considering $p \leq 0.05$ as statistically significant followed by Tukey post-hoc test for pairwise comparison (significant differences are shown by asterisks).

S7.4.2 Lag time Imatinib

Due to a very high lag time standard deviation of some samples, outlier tests were performed. Lag time of Imatinib in TC/L in PBS, in TC/L in PBS with 1% Eudragit E, in TC/L in PBS with 1% Soluplus, and in TC/L in PBS with 1% HPMC-AS was reevaluated with three additional experimental repetitions (**Table S7**). As a result, one lag time data point for Imatinib in TC/L in PBS was removed from further statistical analysis (**Figure S45**).

Table S7: double-sided Grubb's outlier test for lag time of Imatinib in TC/L in PBS, in TC/L in PBS with 1% Eudragit E, in TC/L in PBS with 1% Soluplus, and in TC/L in PBS with 1% HPMC-AS with a significance level of 0.05. One outcome was excluded as highlighted in bold/italic numbers.

Number	**Lag time Imatinib in TC/L in PBS [min]**	**Lag time Imatinib in TC/L in PBS with 1% Eudragit E [min]**	**Lag time Imatinib in TC/L in PBS with 1% Soluplus [min]**	**Lag time Imatinib in TC/L in PBS with 1% HPMC-AS [min]**
1	3,32	8,33	4,02	6,99
2	3,68	5,10	1,23	2,34
3	*12,16*	14,74	2,46	6,16
4	5,11	6,45	6,15	8,56
5	5,54	8,62	6,63	6,22
6	5,03	8,88	5,33	8,49
Result from Grubb's-test	Outlier (12,16)	No Outlier	No Outlier	No Outlier

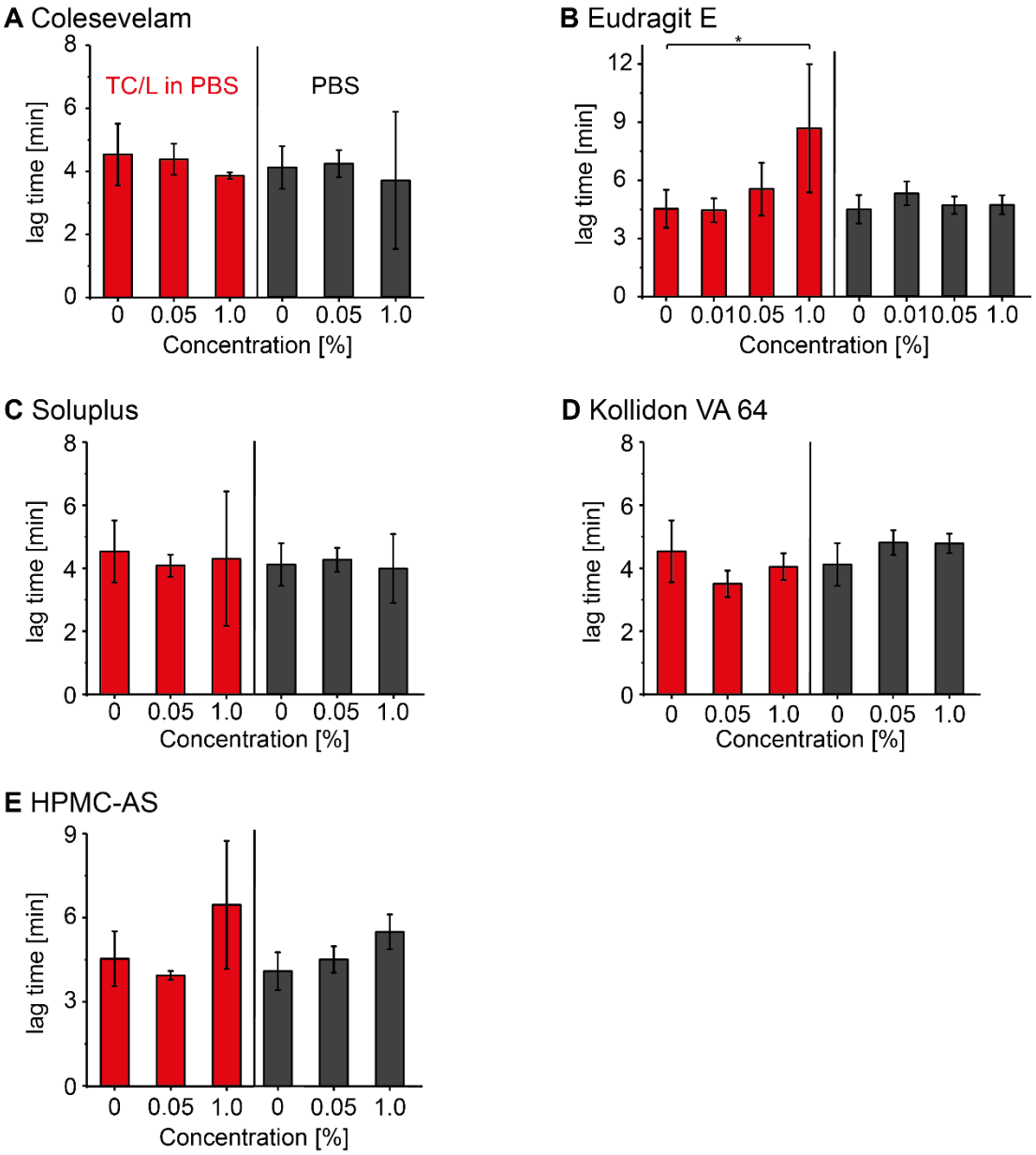

Figure S45: Lag time of Imatinib with (A) Colesevelam, (B) Eudragit E, (C) Soluplus, (D) Kollidon VA 64, and (E) HPMC-AS in TC/L in PBS (red) and in PBS (black) at concentrations as indicated. The first bars 0% are identical for all panels and for comparison. Data for (B) Eudragit E is also shown in Figure 6 in the manuscript. Lag time was calculated by time axis intersect of linear concentration over time extrapolation (**Figure S36**). Data shown as mean ± SD, ANOVA considering $p \leq 0.05$ as statistically significant followed by Tukey Tukey post-hoc test for pairwise comparison (significant differences are shown by asterisks).

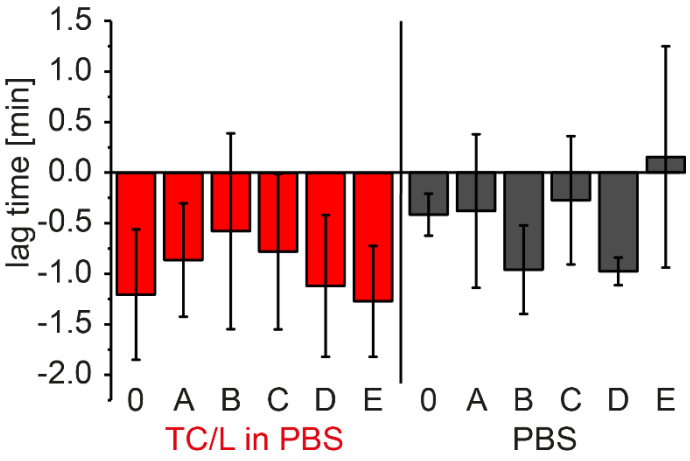

Figure S46: Metoprolol lag time (0) in absence of polymer, with 1% (A) Colesevelam, (B) Eudragit E, (C) Soluplus, (D) Kollidon VA 64, and (E) HPMC-AS in TC/L in PBS (red) and in PBS (black). No difference in lag time between the groups was observed.

S8 Imatinib flux reduction by polymer presence

Flux reduction was calculated at 1% polymer concentration as follows (Eq.1).

$$\text{Flux reduction } [\%] = \left(1 - \frac{Flux_{1\%\ polymer\ in\ TC/L\ in\ PBS}}{Flux_{1\%\ polymer\ in\ PBS}}\right) * 100 \qquad \text{Eq. 1}$$

Imatinib flux in Kollidon VA 64 and HPMC-AS presence was decreased by 23.0% and 20.8%, respectively. In contrast, Eudragit E and Soluplus decreased flux by 35.2% and 42.0%, respectively. This indicated higher affinity of Imatinib to TC/L/polymer MIM than to coexisting species.

References

1. Wiest, J.; Saedtler, M.; Böttcher, B.; Grüne, M.; Reggane, M.; Galli, B.; Holzgrabe, U.; Meinel, L., Geometrical and Structural Dynamics of Imatinib within Biorelevant Colloids. *Mol. Pharmaceutics* **2018**, *15* (10), 4470-4480.
2. Schiller, C.; Fröhlich, C. P.; Giessmann, T.; Siegmund, W.; Monnikes, H.; Hosten, N.; Weitschies, W., Intestinal fluid volumes and transit of dosage forms as assessed by magnetic resonance imaging. *Aliment. Pharmacol. Ther.* **2005,** *22* (10), 971-9.
3. Reker, D.; Blum, S. M.; Steiger, C.; Anger, K. E.; Sommer, J. M.; Fanikos, J.; Traverso, G., "Inactive" ingredients in oral medications. *Sci. Transl. Med.* **2019,** *11* (483).
4. Evonik Nutrition and Care GmbH, Eudragit Polymers for immediate release. https://healthcare.evonik.com/product/health-care/en/products/pharmaceutical-excipients/immediate-release/, 2020 (accessed 01 April 2020).
5. Boni, J. E.; Brickl, R. S.; Dressman, J.; Pfefferle, M. L., Instant FaSSIF and FeSSIF—Biorelevance Meets Practicality. *Dissolut. Technol.* **2009**, *16* (3), 41-45.

Chapter 3: Impact of bile on the intestinal mucus

Simon Hanio[1], Stephanie Möllmert[2], Conrad Möckel[2], Susobhan Choudhury[3], Andreas I. Höpfel[3], Theresa Zorn[4], Sebastian Endres[4], Jonas Schlauersbach[1], Lena Scheller[1], Christoph Keßler[1], Oliver Scherf-Clavel[1], Peter Bellstedt[5, 6], Ulrich S. Schubert[5, 7], Ann-Christin Pöppler[4], Katrin G. Heinze[3], Jochen Guck[2], Lorenz Meinel[1, 8]

[1] University of Würzburg, Institute for Pharmacy and Food Chemistry, University of Wuerzburg, Am Hubland, 97074 Wuerzburg, Germany
[2] Max Planck Institute for the Science of Light and Max-Planck-Zentrum für Physik und Medizin, Staudtstrasse 2, 91058 Erlangen Erlangen, Germany
[3] University of Würzburg, Rudolf Virchow Center for Integrative and Translational Bioimaging, Josef-Schneider-Str. 2, 97080 Wuerzburg, Germany
[4] University of Würzburg, Institute of Organic Chemistry, Am Hubland, 97074 Wuerzburg, Germany
[5] University of Jena, Institute of Organic Chemistry, Humboldtstrasse 10, 07743 Jena, Germany
[6] University of Zürich, Institute for Clinical Chemistry, Rämistrasse 100, 8091 Zurich, Switzerland
[7] University of Jena, Jena Center for Soft Matter (JCSM), Philosophenweg 7, 07743 Jena, Germany
[8] Helmholtz Institute for RNA-based Infection Research (HIRI), Josef-Schneider-Strasse 2, 97080 Wuerzburg, Germany

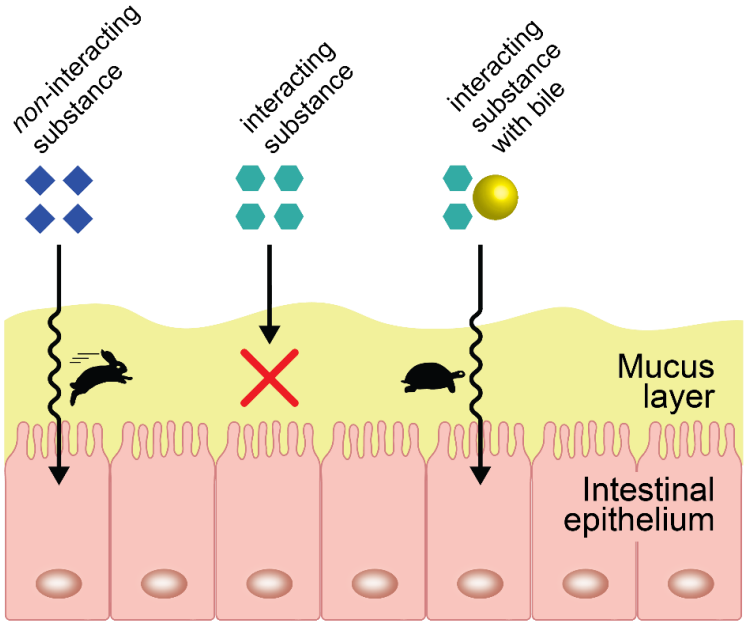

Manuscript submitted.

Abstract

Intestinal mucus impacts the absorption of drugs, however, with a largely unknown role for bile. Here we show that bile transiently stiffens mucus and changes its diffusion kinetics. The presence of bile critically accelerated the mucus kinetics of molecules interacting with bile, whereas the transport of non-bile interacting molecules was unaffected. The critical dependence of bile-interacting drugs on the presence of bile was supported by in vivo bioavailability studies in rats. Collectively, these observations provide insights into the largely overlooked role of the bile-mucus interplay. They point to future studies on the impact of bile on microbiological niches in mucus, the significance of pulsatile gall bladder emptying on mucus biomechanics and diffusion kinetics and provide leverage to improve oral medication and the health-supporting effects of dietary supplements.

Introduction

Bile **s**alt **m**icelles (**BSMs**) critically impact the absorption of fat, dietary components, and pharmaceuticals[1]. These colloidal structures consist of **l**ecithin (**L**) and bile acids, such as **t**auro**c**holate (**TC**) [2]. BSMs, including solubilized molecules, shuttle from the intestinal lumen through the mucus layer to the epithelial surfaces of the intestinal tissues[3, 4]. Hydrophobic and positively charged molecules may have limited mucus permeability and bioavailability[5, 6, 7]. Recent studies linked mucus binding to structural motifs of molecules[7]. The diffusion of supramolecular structures such as micelles, nanoparticles, or pathogens is limited by the pore size (10-200 nm) of the mucus hydrogel[8]. Surface coating of nanoparticles improved mucus transport, including coatings with bile acids[4, 9].

TC, but not L, decreased mucus viscosity and elasticity[10]. At equilibrium, TC lowered mucus viscosity with increasing concentration but only to the point at which BSM were formed[11]. Other studies detailed the binding of TC to mucin at low concentrations. Once TC/L reached levels at which BSM formed, TC binding to mucin substantially decreased[12]. Loss of mucus structure reduced the protection against pathogens and was linked to gut inflammation[13]. Transient destruction of the mucus structure has therapeutic applications with mucolytics or for delivery of larger, transport-hindered drugs such as therapeutic peptides[14].

There is a gap in systematic studies at the bile/mucus interface regarding molecular diffusion patterns or biomechanics. Numerous studies and review articles detail the interaction of molecules with mucus or bile[1, 6, 7, 15]. However, surprisingly little is known about the interaction of all these parameters, i.e., mucus, bile, and molecules' diffusion. We hypothesize that the poor mucus diffusion seen for some bile-interacting molecules may improve in the presence of bile.

We validated our mucus isolates against intact mucus on biopsies by **f**luorescence **c**orrelation **s**pectroscopy (**FCS**). Time-resolved experiments using confocal Brillouin microscopy detailed a transient stiffening front of bile-exposed mucus passing through the hydrogel. At equilibrium, bile had reduced viscosity and elasticity. Analogous to the transient stiffening front, we observed transient diffusion changes upon bile exposure from an anomalous sub-diffusive state to Brownian-like patterns using **d**ifferential **d**ynamic **m**icroscopy (**DMM**). At equilibrium with bile, sub-diffusive patterns were observed. Drugs interacting with bile diffused faster in mucus in the presence of bile, whereas drugs not interacting with bile were not affected by its presence. The value of categorizing drugs as bile-interacting or non-bile-interacting when studying the mucus/bile interface was tested in rats and on more than 50 drugs with known mucin interaction patterns. The study details the impact of bile on mucus biomechanics and diffusion patterns with immediate relevance

for various research directions, e.g., studying the effect of (pulsatile) bile on the biomechanical consequences in microbiological habitats in mucus, predicting malnutrition/impaired bioavailability following cholecystectomy, or leading to improved formulations for drugs.

Results

Mucus isolates are predictive for the molecular diffusion of small molecules in the mucus of full biopsies

We compared four mucus isolates from the small intestine mucosa of pigs (**Fig. 1A, S1**). The isolates had a pH of 6.5 ± 0.2 and a water content of 86 ± 1% (**Tab. S1**).

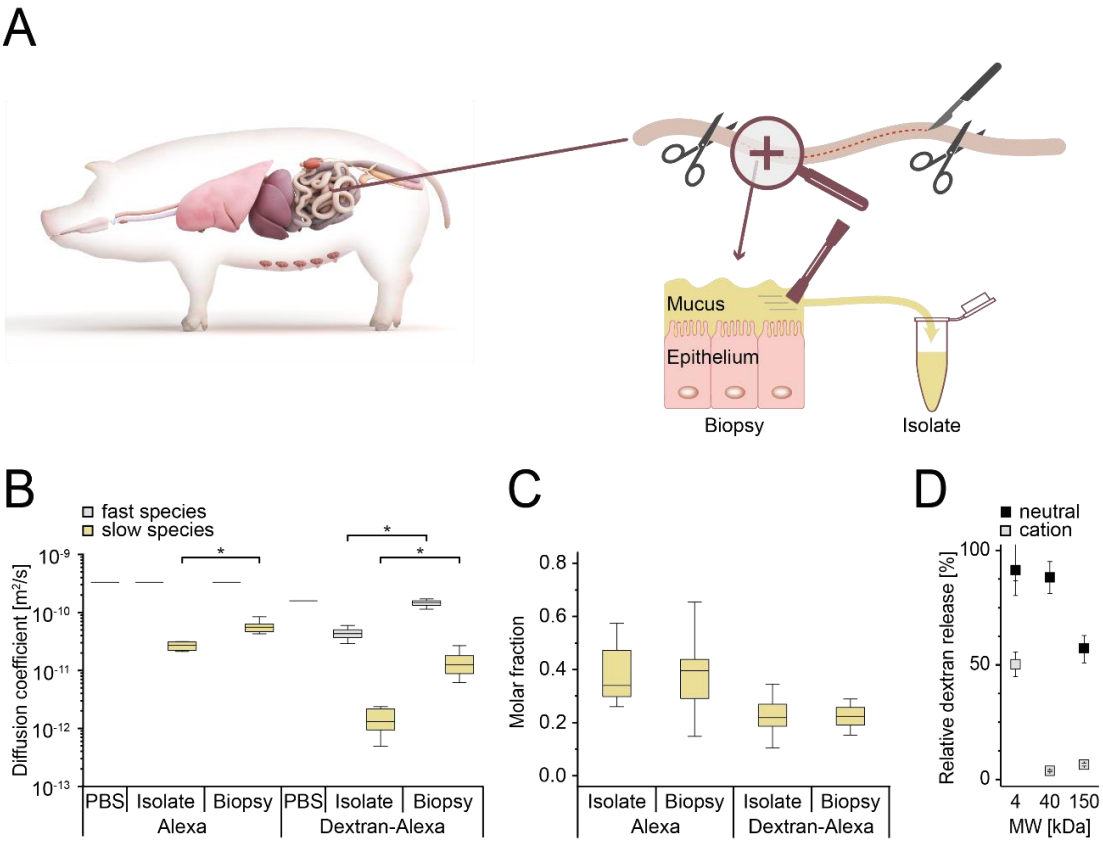

Figure 1. Reconstituted intestinal mucus isolates predict the transport of small molecules within the mucus layer on top of intact biopsies. (A) Collection of the isolates and biopsies from pigs. (B) Fluorescence correlation spectroscopy measurements of a fast (gray) and a slow (yellow) diffusing species of Alexa Fluor 647 (Alexa) and 10 kDa Dextran-AF647 (Dextran-Alexa) within isolates and the mucus on top of the intact biopsies (*p < 0.05, Student's t-test; n ≥ 3). (C) The fraction of the slow diffusing species in the isolates and biopsies. (D) Fluorescein-dextran (no charge; 4, 40, 150 kDa; black) and Fluorescein diethylaminoethyl-dextran (cationic charge; 4, 40, 150 kDa; gray) release from mucus isolates after 48 hours (mean ± standard deviation; n = 3).
Pig illustration in (A) is licensed for use by Sebastian Kaulitzki / Science Photo Library.

Two fluorescent molecules were used to probe the mucus isolates and the biopsies, Alexa Fluor 647 (**Alexa**) and Alexa coupled to a 10-kDa dextran (**Dextran-Alexa**). The temporal changes in the fluorescence emission intensity fit a two-component diffusion model, indicating the presence of a fast and a slow diffusing species for Alexa and Dextran-Alexa (**Fig. 1B-C, S2-3**). Both probes diffused about two to nine times faster in the mucus of the biopsy than in the mucus isolates. The faster diffusing species of Dextran-Alexa was about three times slower in the isolate compared to the biopsy and PBS. The molar ratio of the fast and slow diffusing species was comparable for the isolate and the biopsies. We further studied the impact of size and charge using neutral and positively charged dextrans of 4 kDa, 40 kDa, and 150 kDa (**Fig. 1D, S4**). The cationic dextrans generally interacted stronger with mucus than their neutral counterparts. The release from mucus was comparable for neutral dextrans of 4 and 40 kDa and dropped for the 150 kDa dextrans. In contrast, the release of the cationic dextrans was less, and the larger ones almost exhaustively remained within the mucus. Therefore, the isolates are a valuable proxy for the intact biopsies regarding small molecule diffusion, and we continued the study with the isolates as a model for mucus diffusion.

Bile transiently stiffens mucus and changes its diffusion characteristics

The isolates differed in shear-thinning and yielding properties, time-dependent structural decomposition patterns, partial regeneration, and amplitude and frequency responses (**Fig. 2A, S5, Tab. S2**), and as reported before[1]. We selected one isolate (batch #3; **Fig. 2A**) and observed reduced viscosity after equilibration with 75 mM TC and 18.75 mM L in PBS (**Fig. 2B-C, S6, Tab. S2**). The temporospatial changes leading to these weaker hydrogels were studied by confocal Brillouin microscopy. The mucus was laterally exposed to a TC/L solution at a hydrostatic pressure of about 2 mbar (**Fig. 2D, S7**). Longitudinal scans of the mucus indicated an elevated Brillouin frequency shift indicating mucus stiffening with TC/L but not PBS control (**Fig. 2E, S8-13**). This stiffening front propagated through the mucus with square-root-of-time kinetics and a propagation coefficient of 30 ± 9 $\mu m^2/s$ (mean ± standard deviation, n = 10; **Fig. 2F, S14-15**). The Brillouin frequency shifts decreased again after the stiffening front had passed that particular position, indicating a re-softening of the hydrogel. The individual, unmixed samples, mucus, TC/L in PBS, or PBS did not show such patterns (**Fig. S16**), and all the pooled Brillouin frequency shifts and linewidth values differed among these controls (**Fig. S17**). Mucus incubated with PBS showed a sub-diffusive anomalous diffusion by differential dynamic microscopy (**Fig. S18**). However, like the transient stiffening pattern of TC/L, the diffusion transiently changed from sub-diffusive to Brownian-like diffusion (**Fig. 2G, S19**). With time, the hydrogel returned to sub-diffusive

characteristics. Control experiments with PBS excluded convective disturbances in scattering fluctuations by adding the fluid.

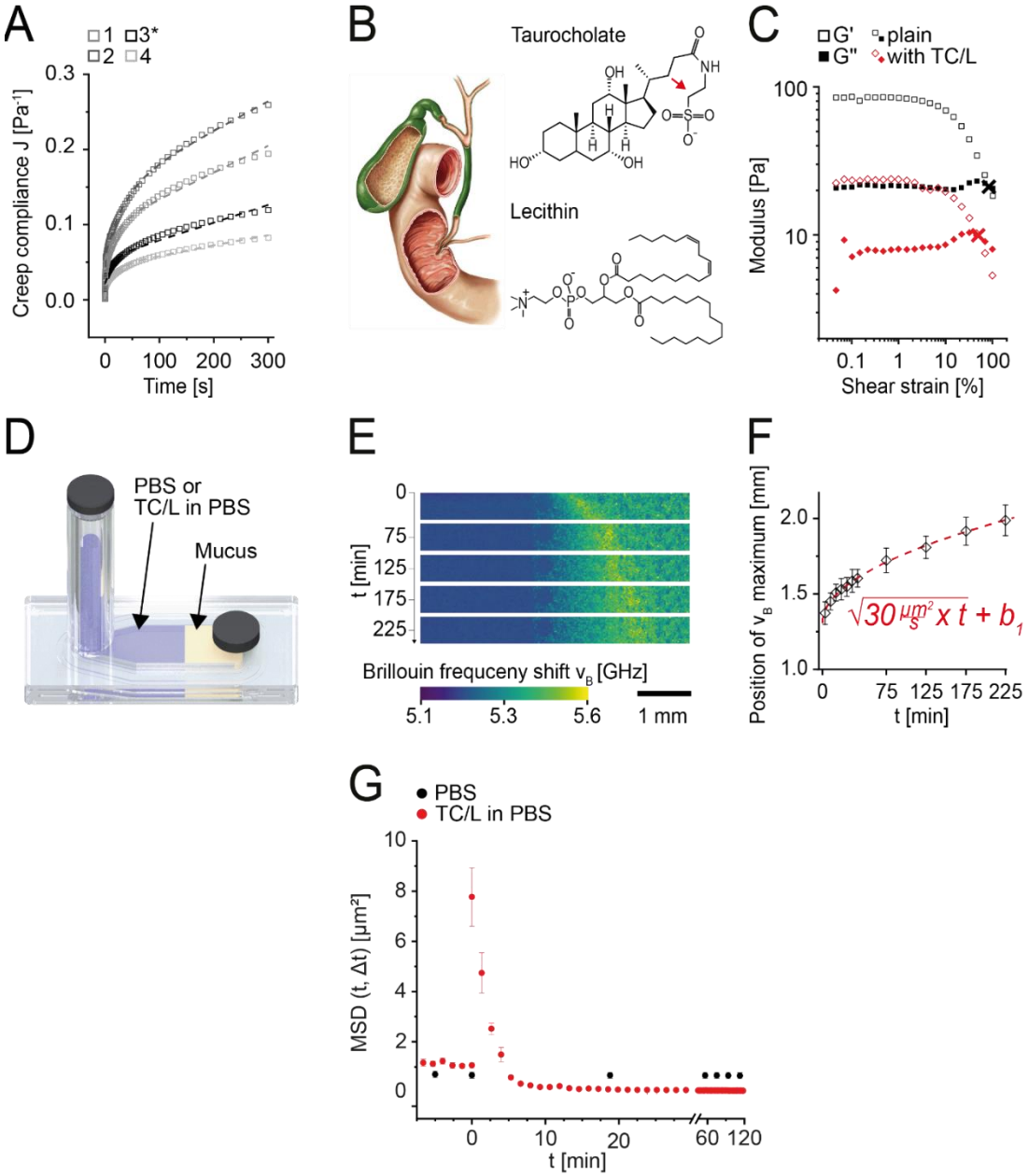

Figure 2. Bile impacts the equilibrium mechanics and mechanodynamics of mucus. (A) Compliance of four independently harvested isolates. Batch 3* was used for the subsequent experiments. (B) Chemical structure of Taurocholate (red arrow indicates the position of the inserted ^{13}C used for NMR spectroscopy) and Lecithin. (C) Storage modulus (G′, open symbols) and loss modulus (G″, closed symbols) of mucus (black) and mucus equilibrated with TC/L (red; crosses are flow points). (D) Sample mounting for confocal Brillouin microscopy. (E) The time-resolved Brillouin frequency shift maxima laterally propagated with (F) square-root-of-time kinetics. (G) Mean square displacement from differential dynamic microscopy in mucus exposed at t = 0 minutes to PBS (black) or TC/L (red) for 10 second time intervals (Δt). Gallbladder illustration in (B) is licensed for use by Asklepios Medical Atlas / Science Photo library.

Bile-interacting molecules profit from the presence of bile with accelerated diffusion in mucus

Diffusion, studied by ^{1}H and ^{19}F DOSY-NMR spectroscopy, was faster in PBS than in mucus, for water 1.7 ± 0.1 (n = 4) times faster, for **tri**fluoro**e**thanol (**TFE**) 1.6 ± 0.1 times faster (n = 4), and for Linezolid 1.7 ± 0.1 times faster (n = 4; **Fig. 3A, S20-S22**). The diffusion of the largest molecule, Linezolid, did not change for two days after the experiment, indicating that the samples had ample time to reach equilibrium (**Fig. S22**). The ^{19}F resonance of TFE and Linezolid was comparable in all mucus samples, and signals broadened in PBS (**Fig. S23-24**). Molecular diffusion was indistinguishable across the four mucus isolates despite their biomechanical differences. We used isolate #3 in the following experiments (**Fig. 3A**). Firstly, we analyzed the presence of amine and carboxyl functional groups tethered to trifluoroethanol on diffusion. The diffusion was about 1.5 times faster in PBS than in mucus for trifluoroethanol, trifluoroethylamine, trifluoroacetic acid, and ethanol (**Fig. S25-26**). The signals of all probes broadened but did not shift in mucus as compared to PBS, except for trifluoroethylamine (**Fig. S27**). These studies established the potential of using ^{19}F DOSY-NMR and the HSQC-iDOSY pulse sequence in the quite viscous mucus.

We now tested equilibrium diffusion dynamics in mucus. Metoprolol diffusion was similar in PBS and mucus (1.3 (± fitting error of 0.2)-fold difference) and increasing TC/L concentrations did not substantially change the diffusion (**Fig. 3B-C, S28-29**). A similar pattern was recorded for water or trifluoroethanol diffusion in PBS and mucus (**Fig. S20-21, S30**). In contrast, Fluphenazine, without bile, diffused about 300-fold slower in mucus than in PBS (**Fig. 3D, S31-32**). Fluphenazine solubilized into bile colloids, reflected by the decreasing diffusion with increasing TC/L concentrations and the corresponding shift to lower ppm values and broadening of the ^{19}F signal (**Fig. S33**). Interestingly, Fluphenazine diffusion in mucus increased abruptly and about 100-fold with the highest TC/L concentration, reaching diffusion in mucus at par with PBS (**Fig. S31-32**). Along with this rise, Fluphenazine's ^{19}F NMR signals sharpened and shifted to higher ppm values (**Fig. 3E, S33**). At the rise (but not before), the diffusion of TC in mucus dropped compared to lower TC/L concentrations (**Fig. 3F, S34-35; Tab. S3**).

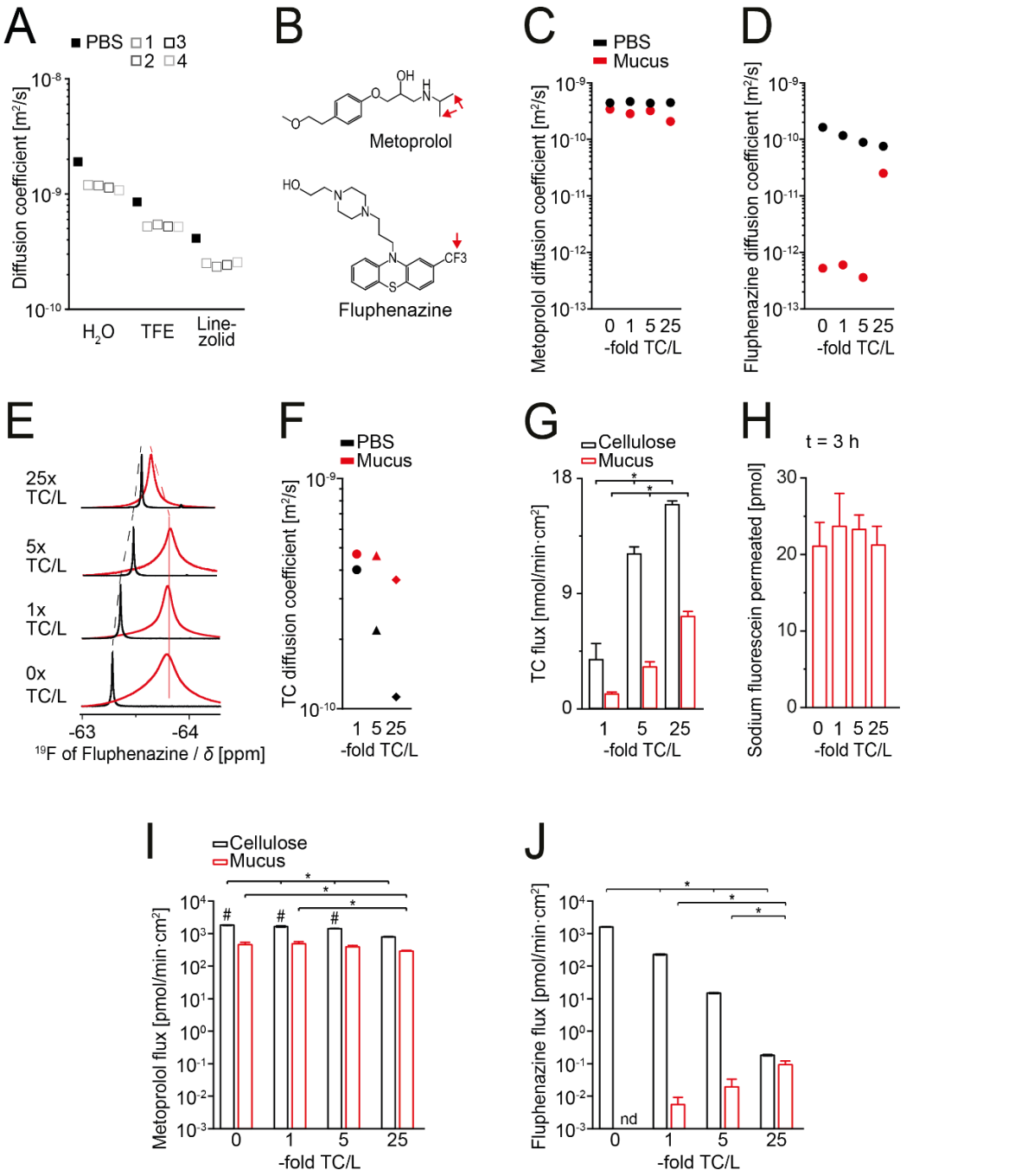

Figure 3. Mucus diffusion of bile-interacting Fluphenazine depends on bile. (A) Diffusion-ordered NMR spectroscopy of water, trifluoroethanol (TFE), and Linezolid in PBS (black) and four isolates. (B) Structures of the drug substances. The red arrows indicate the nuclei used for the NMR studies. (C) Metoprolol and (D) Fluphenazine diffusion in PBS (black) and mucus (red) with bile by Diffusion-ordered NMR spectroscopy as a function of Taurocholate/Lecithin concentration (1-fold bile was 3 mM Taurocholate, 0.75 mM Lecithin). (E) Close-ups of the Fluphenazine ^{19}F NMR spectra in PBS (black) and mucus (red) with bile. (F) Diffusion-ordered NMR spectroscopy of Taurocholate in PBS (black) and mucus (red) in the presence of TC/L. (G) Taurocholate flux across a cellulose membrane (black) and mucus (red; mean ± standard deviation; *p < 0.05, ANOVA with Tukey post hoc test; n = 3). (H) Sodium fluorescein, (I) Metoprolol (bars with the # were reported before[2]), and (J) Fluphenazine permeation across cellulose membranes (black) or mucus in the presence of Taurocholate and Lecithin (red; mean ± standard deviation; *p < 0.05, ANOVA with Tukey *post hoc* test; n = 3; nd = not detected).

These insights were expanded to flux studies across a cellulose membrane or mucus (the polyester-membrane supporting the mucus did not impact the flux; **Fig. 3H, Tab. S4, S36**). Bile did not impact the flux of the bile-non-interacting molecules such as sodium fluorescein (used to control the mucus integrity throughout the experiment; **Fig. 3H, S37**) or Metoprolol in PBS or mucus (**Fig. 3I, S38; S39-40**). However, the flux in PBS/across cellulose membranes of the bile-interacting Fluphenazine (**Fig. S41**) inversely correlated with the bile concentrations (**Fig. 4J, S40**). In contrast, bile enabled Fluphenazine flux across mucus and increased with increasing TC/L concentrations to an extent that flux in mucus approximated the flux in PBS (across cellulose membranes) at 25-fold TC/L (25-fold TC/L equals 75 mM TC, 18.75 mM L; **Fig. 4**). These studies confirmed bile's importance transporting Fluphenazine and possibly other bile-interacting drugs across mucus.

Bile controls the pharmacokinetics of bile-interacting molecules

Perphenazine was bile-interacting (**Fig. S42**). Like Fluphenazine, Perphenazine flux in mucus depended on the presence of bile, correlated with the bile concentrations, and reached the levels of PBS at the highest TC/L concentrations (**Fig. 4A, S39-40**). NMR diffusion studies in mucus using ^{13}C labeled Perphenazine were inconclusive as of insufficient HSQC signals (**Fig. S43**). We concluded that the bile effects in PBS and mucus are similar for Fluphenazine and Perphenazine. We now tested the *in vivo* relevance of these findings in rats (**Fig. 4B, S44**). For that, we conducted bioavailability studies for Metoprolol (non-bile-interacting; **Fig. S38**) and Perphenazine (bile-interacting; **Fig. S42**). The animals received the drugs at relatively low concentrations to maintain stable solutions throughout the animal experiment (24 hours), and to tolerate up-concentration without precipitation as of water absorption during gastrointestinal passage (**Fig. S45**) [3]. These solutions were studied with or without polyallylamine derivatives. These polymers are therapeutically used to bind and lower bile salts, and thereby BSMs and cholesterol levels in the blood[4]. Metoprolol bioavailability was not impacted by the presence of polyallylamine derivatives and the resulting low levels of bile (**Fig. 4B, Tab. S5**). In contrast, Perphenazine bioavailability was critically reduced by the presence of polyallylamine-derivatives (**Fig. S44**). These studies suggested that the presence of bile critically impacted Perphenazine's bioavailability and possibly the bioavailability of other bile-interacting drugs.

We now expanded our hypothesis to other drugs, suggesting that bile (rocket) is responsible for shuttling bile-interacting drugs (turtle) through mucus, whereas it has no impact on non-bile-interacting drugs (rabbit; **Fig. 4C**).

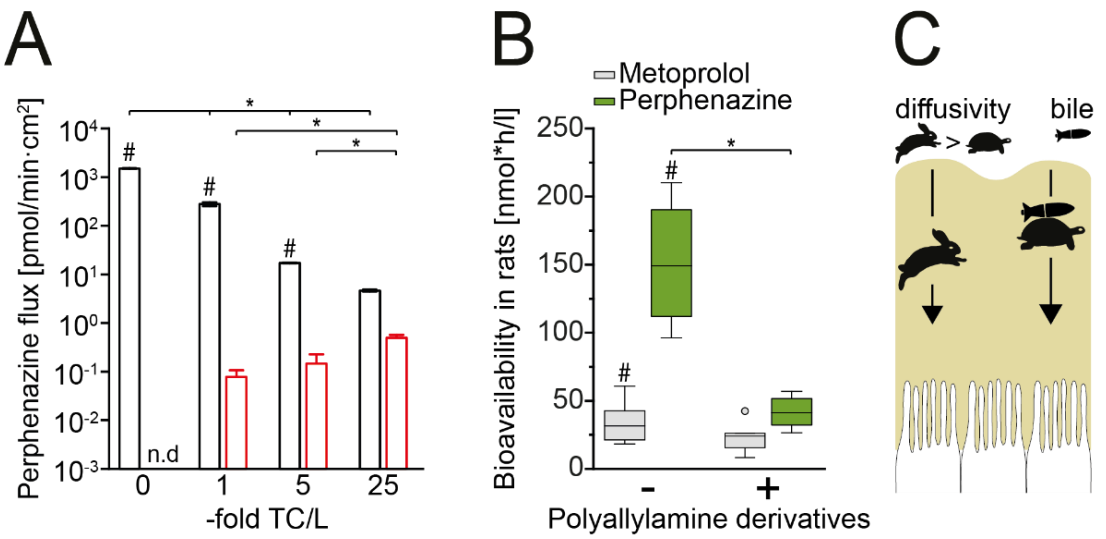

Figure 4. The flux across mucus and the bioavailability of bile-interacting Perphenazine depends on bile. (A) Perphenazine flux across a cellulose membrane (black) or mucus (red) as a function of Taurocholate/Lecithin concentration (1-fold bile was 3 mM Taurocholate, 0.75 mM Lecithin; mean ± standard deviation; *$p < 0.05$, ANOVA with Tukey *post hoc* test; n = 3; n.d. = not detected; bars with the # were reported before[2]). (B) Bioavailability of the non-bile interacting Metoprolol (gray) and bile-interacting Perphenazine (green) with polyallylamine derivative (+) or without (-); median (solid line), circle indicates an outlier, excluded from the comparison, whiskers indicate the upper and lower 25%, respectively (*$p < 0.05$, Student's t-test; n = 5, bars with the # were reported before[5]). (C) Cartoon of our hypothesis, that mucus-diffusion of non-bile interacting drugs (rabbit) is unaffected by bile, whereas bile-interacting drugs (turtle) benefit from the presence of bile (rocket).

Drug-mucus interaction clusters in the group of bile-interacting drugs

We recently linked bile interaction to the chemical structures of drugs[6]. Two descriptors were sufficient, one for lipophilicity (the previous study used h_logD and is now replaced by the logD at pH 7.4) and the other one accounting for molecular size and polarizability (CrippenMR)[7]. The open-access predictive algorithm was used to analyze a set of compounds, for which mucin retention was reported before[8-10] (**Fig. 5A, Tab. S6,** https://github.com/juppifluppi/tclint). Furthermore, we confirmed the predictions of bile interaction at random by NMR spectroscopy (**Fig. 5B; Fig. S46-48**). No molecules were found which had mucin retention and were non-bile interacting (class I). Mucin interacting drugs were also bile-interacting (class II; such as Fluphenazine) but not all bile-interacting drugs interacted with mucin (class III). Many drugs neither interacted with bile nor with mucus (class IV; such as Metoprolol; **Fig. 5B**).

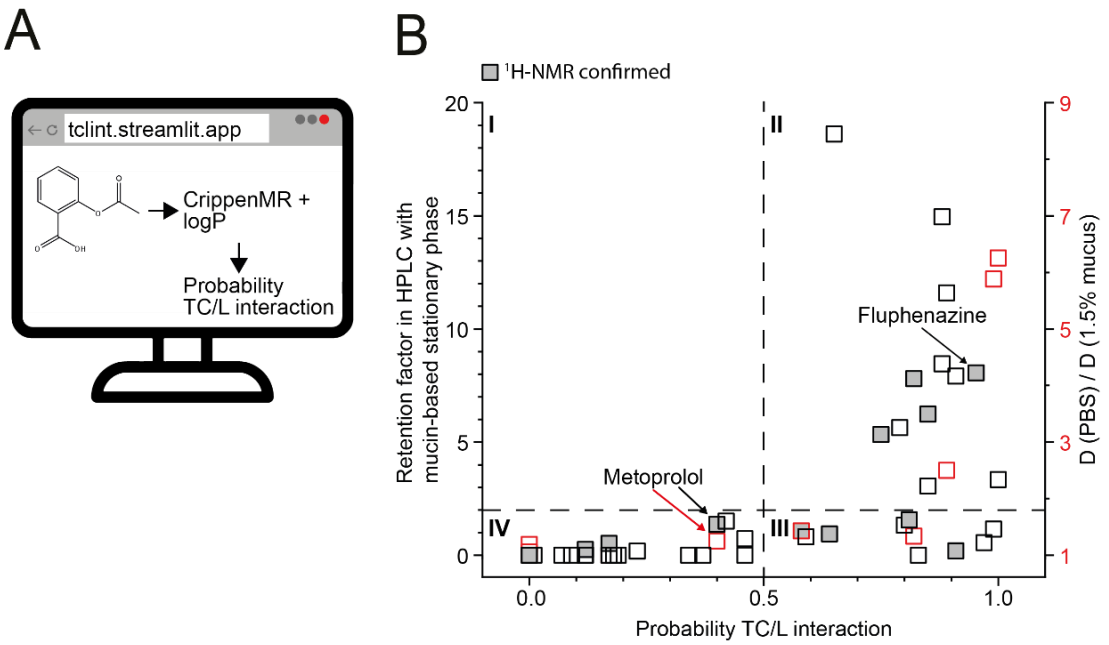

Figure 5. Drugs interacting with mucus interacted with Taurocholate/Lecithin. (A) An open access web tool was used to predict the probability of the molecules for bile interaction using the molecular descriptors Crippen MR and logP. (B) The retention factor of the molecules with mucin (reported before [10]; black squares) and the ratio of diffusion in PBS and diluted mucus (reported before[9]; red squares) against the molecules' probability to interact with TC/L (gray-filled boxes show randomly selected drugs, for which the bile interaction was confirmed by NMR-spectroscopy) [8].

Discussion

Food-triggered stimulation of pulsatile bile flow solubilizes poorly water-soluble drugs and leverages their dissolution and apparent solubility[1,46]. Furthermore, it has been hypothesized that bile facilitates mucus permeability for poorly water-soluble drugs since bile-coated nanoparticles show enhanced transport[24]. What has yet to be clarified is how this phenomenon is induced and how to categorize drugs, whose mucus transport benefits or depends on the presence of bile. Our study shows that drugs interacting with mucin interact with bile and that mucus transport critically depends on bile.

The Brillouin frequency shifts/stiffening and change in scattering fluctuation/diffusion reflect a transient structural change of mucus by TC/L. The square-root-of-time kinetics of the stiffening suggested that the biomechanical changes occurred at lower TC/L concentrations than at equilibrium. At higher concentrations (i.e., later time points) the hydrogel became softer again, a phenomenon being in line with previous reports detailing TC binding to mucin at low but not at concentrations at which BSMs formed[27]. Other studies confirmed the presence of BSMs in mucus above the **c**ritical **m**icelle **c**oncentration (**CMC**) for bile[10]. These insights could link the stiffening front seen in the Brillouin microscopy

experiments to TC/L concentrations below the CMC (**Fig. 2E**). Arguably, the TC bound to mucus increases the negative charge of the hydrogel network, thereby increasing the internal stress that stiffens the hydrogel. TC binding to mucin is supported by previous NMR studies[47]. At concentrations exceeding the CMC the BSMs formed. This is supported by the TC-diffusion data. At high TC/L concentrations, we observed a slower diffusing species, arguably the BSMs diffusing slowly in mucus and as previously suggested (**Fig. 3F**) [10]. Mucus bound TC may at least in part migrate into these BSMs. Thereby, the repulsive charges decline, resulting in a softening towards the levels before TC/L exposure. The concentration dependent interaction of TC/L with mucus might cause the changes in the anomalous diffusion patterns. These changes in diffusion might reflect larger pores because of the transient stiffening/increase in repulsion within the hydrogel network (**Fig. 2F**). The critical impact of BSM for the mucus diffusion of bile-interacting molecules is further evidenced by the rise in Fluphenazine diffusion at high TC/L concentrations (**Fig. 3D**). These biomechanical changes are instantaneous and seem fully reversible, contrasting non-reversive hydrogels, within which modulus changes are associated with cross-links (i.e., not reversible), or unidirectional (i.e., only stiffen or soften), or have long time scales for their response[48,49]. Furthermore, high TC/L concentrations/the presence of BSMs speed up the diffusion of Perphenazine and other bile-interacting drugs. We expanded these *in vitro* studies to bioavailability assessments in rats, and the outcome did not contradict our hypothesis (**Fig. 4**). This cautious interpretation reflects that bile affects several aspects apart from mucus permeability, particularly drug solubilization in the intestinal lumen. We aimed to minimize intestinal solubilization's impact by selecting quite low drug concentrations to minimize precipitation during gastro-intestinal passage, and to remove the need for bile-solubilization to dissolve the drugs. However, solubilization will occur in the lumen and, therefore, bias the interpretation of bile effects on mucus permeability.

Drugs binding to TC/L bind to mucin (class II in **Fig. 5**). Selected samples (Fluphenazine or Perphenazine) suggested that transport in mucus of bile-interacting drugs increases in the presence of bile. Ongoing experiments verify this connection for further drugs. The separation of the classes was based on NMR signal shifts with TC/L of Metoprolol, a non-bile-interacting drug and previous classifications. Any drug exceeding the Metoprolol shifts was defined as bile-interacting[1]. Similarly, chromatographic retention by a factor of 2 or more on columns with mucin as the stationary phase were defined as relevant[45].

In summary, the results define a critical role of bile on the mucus transport of bile-interacting drugs. Drugs interacting with mucin interact with bile. These findings may trigger future studies, expanding the benefit of bile on drug diffusion in mucus to more drugs. The prompt and transient stiffening of mucus at low TC/L concentrations followed by softening at higher

TC/L concentrations may also stimulate exploration of the role of (the pulsatile release of) bile on the biomechanics of microbiological habitats in mucus, nanoparticle/colloid transport, or pharmaceutical and dietary consequences for cholecystectomy patients[50-54].

Materials and Methods

Materials

Sodium ^{13}C2-TC was obtained from Eurisotop (Saarbrücken, Germany). ^{13}C3-Metoprolol and ^{13}C3-Perphenazine were synthesized in-house following previous reports[55,56]. Other chemicals and laboratory consumables were obtained from VWR (Ismaning, Germany) or Merck (Darmstadt, Germany).

Collection of porcine intestinal mucus

2-3 m long jejunual section were excised from pig small intestines at a local slaughterhouse (Staatsgut Schwarzenau - Versuchs- und Bildungszentrum für Schweinehaltung, Schwarzach am Main, Germany). The jejuna were transported on ice to the lab, gently flashed with ice-cold water and cut transversely into sections about 25 cm in length. The sections were opened longitudinally along the mesenteric line followed by mucus collection using plastic scrapers. 8-10 muci were pooled to one batch to reduce biological variations[57]. 0.4% (w/w) sodium azide (nominal end concentration: 60 µM) and SIGMAFAST™ Protease Inhibitor Tablets (1 tablet per 100 mL) were added. The pooled mucus was stirred for 24 h, at 50 rpm, at 4 °C. On the next day, the samples were frozen in aliquots at -20 °C. The samples were incubated for at least 30 min at room temperature before experimentation.

Media preparation

Modified phosphate-buffered saline with a pH value of 6.50 ± 0.05 (PBS – identical with FaSSIF-V1 without TC and L) and FaSSIF-V1 (TC/L in PBS, i.e., 3 mM TC and 0.75 mM L in PBS) were prepared according to the Biorelevant.com (London, U.K.) protocol. 5- and 25-fold TC/L in PBS were made analogous to TC/L in PBS but with the 5- and 25-fold amount of FaSSIF powder (Biorelevant.com), respectively. 19 volume parts of mucus were supplemented with 1 volume part of 500-, 100-, and 20-fold TC/L in PBS, resulting in Mucus with 25-, 5-, 1-fold TC/L, respectively. Samples were equilibrated at room temperature for 2 hours before further use.

pH value and water content determination of isolated mucus

The pH-value of the mucus was measured. The water content was determined by weighing before and after freeze-drying (CoolSafe 110-4 Pro, ScanLaf, Denmark) in triplicate.

Fluorescence correlation spectroscopy

Fluorescence correlation spectroscopy (FCS) measurements were done in a custom build confocal setup based on an Olympus IX 71 stand (Olympus, Hamburg, Germany). We used the reported diffusion coefficient value of Alexa Fluor 647 to determine the effective confocal volume of the setup[58]. See *SI Experimental Section* for the detailed experimental protocols.

Fluorescein isothiocyanate-dextran release

The release kinetic of (DEAE-)dextrans labeled with FITC from mucus was studied on a Cary Eclipse fluorescence spectrophotometer (Agilent Technologies, Waldbronn, Germany). Release studies were done in triplicate. See *SI Experimental Section* for the detailed experimental protocols.

Rheology

The rheological properties were studied on a Modular Compact Rheometer MCR-302 (Anton Paar, Ostfildern, Germany) equipped with a solvent trap and a Peltier hood H-PTD200 (Anton Paar). The rheological data were analyzed with RheoCompass™ (Anton Paar). See *SI Experimental Section* for the detailed experimental protocols.

Nuclear magnetic resonance spectroscopy

NMR spectra were recorded on a Bruker Avance III HD 600 MHz, a Bruker Avance IV NEO 500 MHz, and a Bruker Avance 400 MHz spectrometer operating at 600.4, 470.6, and 400.1 MHz, respectively, and equipped with a 5 mm BBFO, a Diff50, and a BBI BB-H 5 mm probe, respectively. DOSY-NMR spectra were acquired using the pulse sequences ledbpgp2s[59], ledgp2s[60], dstebpgp3s[61,62], or idosyhsqc3d[63]. DOSY decay curves were fitted using a mono-exponential fit[64]. Spectra were analyzed using TopSpin 4.0.6. (Bruker BioSpin). See *SI Experimental Section* for the detailed experimental protocols.

Confocal Brillouin microscopy

Brillouin microscopy was performed on a custom-built confocal Brillouin microscope based on a two-stage virtually imaged phase array. The working principle was previously detailed.[65-67] Data were analyzed with the custom-made software bmlab [Raimund Schlüßler and others (2022), a Python library for the post-measurement analysis of Brillouin microscopy data v.0.3.0, available at https://github.com/BrillouinMicroscopy/bmlab] and BMicro [Raimund Schlüßler and others (2022), Python GUI for post-measurement Brillouin microscopy analysis v.0.4.0, available at https://github.com/BrillouinMicroscopy/BMicro]. Raincloud plots were generated as previously described[68]. All effect size estimates were calculated based on a previous report[69]. See *SI Experimental Section* for the details on data acquisition, data analysis and representation.

Differential dynamic microscopy

Differential dynamic microscopy was performed on a custom-built setup. DDM is a computational method to study the inherent intensity fluctuations of a system, obtained from time-lapse images measured by optical microscopy[70-73]. Formally, these fluctuations can be described in spatial Fourier space by the 'intermediate scattering function' (ISF), which is the key observable obtained by DDM. The ISF is connected to the mean-squared-displacement in dependence of spatial frequency and lag time. DDM provides a way of characterizing the diffusive properties of a specimen optically, without the immediate need for particle tracking. All data was analysed with a custom Mathemtica script (https://support.wolfram.com/472).

See *SI Experimental Section* for the details on data acquisition, data analysis and representation.

Flux

Side-by-side diffusion cells (PermeGear Inc., Hellertown, PA, USA) with cellulose membranes (innoME GmbH, Espelkamp, Germany) were used to determine the free drug concentration, as previously reported[2]. Here, we extend our previously reported data set[2]. The Transwell diffusion model was applied to determine the drug permeation through mucus[74]. The permeated amount of sodium fluorescein was quantified with a Tecan Reader Infinite 200 pro plate reader (Tecan Group, Maennedorf, Switzerland). Drug concentrations were quantified preferably by High Pressure Liquid Chromatography (HPLC) on an Agilent 1260 infinity II HPLC using calibration curves. Fluphenazine und Perphenazine samples, which were not quantifiable by HPLC, were analyzed by liquid chromatography-tandem mass spectrometry (LC-MS/MS) based on previously published methods[75,76]. For that, ultra-high performance liquid chromatography (UHPLC) was performed on an Agilent 1200 Series with effluent channeled to an Agilent 6460 triple quadrupole. Quantification was done by calibration curves with ^{13}C3-labeled Perphenazine as internal standard. Data was acquired and analyzed with MassHunter software (Agilent Technologies). The flux experiments were done in triplicate. See **Table S7** for the LC-MS/MS analytical conditions and *SI Experimental Section* for the detailed experimental protocols.

Pharmacokinetic studies in rats

A pharmacokinetic (PK) study in rats was conducted at Aurigon (Dunakeszi, Hungary). Together with Metoprolol or Perphenazine, a PBS solution containing polyallylamines derivatives (Colesevelam) was administered orally. We reused the control groups from a previous report[3]. See *SI Experimental Section* for the detailed experimental protocols.

Data processing and Visualization Statistics

Data were processed with OriginPro 2020 (OriginLab Corporation, Northampton, MA). Figures were created with Adobe Illustrator 2022 (Adobe Inc., San Jose, CA).

Statistics

Statics were performed with OriginPro 2020. P-values ≤ 0.05 were considered statistically significant. The flux data were analyzed by a one-way Analysis of variance followed by post hoc Tukey for pairwise comparison. The unpaired two-sample t-test was used for all other pairwise comparison.
See *SI Experimental Section* for details on the statistical analysis of the Brillouin microscopy data.

Acknowledgments

We thank the Staatsgut Schwarzenau, and Bettina Lenz for the help with the isolation of mucus, Kyoohyun Kim, Paul Müller, and Raimund Schlüßler for excellent technical support and proof reading with the Brillouin microscopy data. We thank David Ort for technical support and Josef Kehrein for his work on the webtool. The NMR used for the diffusion measurement at the NMR Platform Jena was partially funded by the German Research Foundation grant INST 275/442-1 FUGG.

Conflict of interest

The authors have no conflict of interest.

References

1 Schlauersbach, J. *et al.* Predicting Bile and Lipid Interaction for Drug Substances. *Mol Pharm* **19**, 2868-2876, doi:10.1021/acs.molpharmaceut.2c00227 (2022).

2 Schlauersbach, J. *et al.* Leveraging bile solubilization of poorly water-soluble drugs by rational polymer selection. *J Control Release* **330**, 36-48, doi:10.1016/j.jconrel.2020.12.016 (2021).

3 Schlauersbach, J. *et al.* Bile and excipient interactions directing drug pharmacokinetics in rats. *Eur J Pharm Biopharm*, doi:10.1016/j.ejpb.2022.07.016 (2022).

4 Malik, N. A. Solubilization and Interaction Studies of Bile Salts with Surfactants and Drugs: a Review. *Appl. Biochem. Biotechnol.* **179**, 179-201, doi:10.1007/s12010-016-1987-x (2016).

5 Boyer, J. L. Bile formation and secretion. *Compr. Physiol.* **3**, 1035-1078, doi:10.1002/cphy.c120027 (2013).

6 Monte, M. J., Marin, J. J., Antelo, A. & Vazquez-Tato, J. Bile acids: chemistry, physiology, and pathophysiology. *World J. Gastroenterol.* **15**, 804-816, doi:10.3748/wjg.15.804 (2009).

7 Esteller, A. Physiology of bile secretion. *World J Gastroenterol* **14**, 5641-5649, doi:10.3748/wjg.14.5641 (2008).

8 Riethorst, D. *et al.* Characterization of Human Duodenal Fluids in Fasted and Fed State Conditions. *J Pharm Sci* **105**, 673-681, doi:10.1002/jps.24603 (2016).

9 Westergaard, H. & Dietschy, J. M. The mechanism whereby bile acid micelles increase the rate of fatty acid and cholesterol uptake into the intestinal mucosal cell. *J Clin Invest* **58**, 97-108, doi:10.1172/JCI108465 (1976).

10 Yildiz, H. M., McKelvey, C. A., Marsac, P. J. & Carrier, R. L. Size selectivity of intestinal mucus to diffusing particulates is dependent on surface chemistry and exposure to lipids. *J Drug Target* **23**, 768-774, doi:10.3109/1061186X.2015.1086359 (2015).

11 Witten, J., Samad, T. & Ribbeck, K. Selective permeability of mucus barriers. *Curr Opin Biotechnol* **52**, 124-133, doi:10.1016/j.copbio.2018.03.010 (2018).

12 Sigurdsson, H. H., Kirch, J. & Lehr, C. M. Mucus as a barrier to lipophilic drugs. *Int J Pharm* **453**, 56-64, doi:10.1016/j.ijpharm.2013.05.040 (2013).

13 Huang, J. X. *et al.* Mucin Binding Reduces Colistin Antimicrobial Activity. *Antimicrob Agents Chemother* **59**, 5925-5931, doi:10.1128/AAC.00808-15 (2015).

14 Larhed, A. W., Artursson, P., Grasjo, J. & Bjork, E. Diffusion of drugs in native and purified gastrointestinal mucus. *J Pharm Sci* **86**, 660-665, doi:10.1021/js960503w (1997).

15 Lock, J. Y., Carlson, T. L. & Carrier, R. L. Mucus models to evaluate the diffusion of drugs and particles. *Adv Drug Deliv Rev* **124**, 34-49, doi:10.1016/j.addr.2017.11.001 (2018).

16 Boegh, M. & Nielsen, H. M. Mucus as a barrier to drug delivery - understanding and mimicking the barrier properties. *Basic Clin Pharmacol Toxicol* **116**, 179-186, doi:10.1111/bcpt.12342 (2015).

17 Larhed, A. W., Artursson, P. & Bjork, E. The influence of intestinal mucus components on the diffusion of drugs. *Pharm Res* **15**, 66-71, doi:10.1023/a:1011948703571 (1998).

18 Witten, J., Samad, T. & Ribbeck, K. Molecular Characterization of Mucus Binding. *Biomacromolecules* **20**, 1505-1513, doi:10.1021/acs.biomac.8b01467 (2019).

19 Murgia, X., Loretz, B., Hartwig, O., Hittinger, M. & Lehr, C. M. The role of mucus on drug transport and its potential to affect therapeutic outcomes. *Adv Drug Deliv Rev* **124**, 82-97, doi:10.1016/j.addr.2017.10.009 (2018).

20 Lai, S. K., Wang, Y. Y., Wirtz, D. & Hanes, J. Micro- and macrorheology of mucus. *Adv Drug Deliv Rev* **61**, 86-100, doi:10.1016/j.addr.2008.09.012 (2009).

21 Lai, S. K. *et al.* Rapid transport of large polymeric nanoparticles in fresh undiluted human mucus. *Proc Natl Acad Sci U S A* **104**, 1482-1487, doi:10.1073/pnas.0608611104 (2007).

22 Bajka, B. H., Rigby, N. M., Cross, K. L., Macierzanka, A. & Mackie, A. R. The influence of small intestinal mucus structure on particle transport ex vivo. *Colloids Surf B Biointerfaces* **135**, 73-80, doi:10.1016/j.colsurfb.2015.07.038 (2015).

23 Kirch, J. *et al.* Optical tweezers reveal relationship between microstructure and nanoparticle penetration of pulmonary mucus. *Proc Natl Acad Sci U S A* **109**, 18355-18360, doi:10.1073/pnas.1214066109 (2012).

24 Macierzanka, A. *et al.* Adsorption of bile salts to particles allows penetration of intestinal mucus. *Soft Matter* **7**, doi:10.1039/c1sm05888f (2011).

25 Martin, G. P., Marriott, C. & Kellaway, I. W. Direct effect of bile salts and phospholipids on the physical properties of mucus. *Gut* **19**, 103-107, doi:10.1136/gut.19.2.103 (1978).

26 Poelma, F. G. J., Breäs, R. & Tukker, J. J. Intestinal absorption of drugs. IV. The influence of taurocholate and l-cysteine on the barrier function of mucus. *International Journal of Pharmaceutics* **64**, 161-169, doi:10.1016/0378-5173(90)90265-6 (1990).

27 Wiedmann, T. S., Liang, W. & Herrington, H. Interaction of bile salts with gastrointestinal mucins. *Lipids* **39**, 51-58, doi:10.1007/s11745-004-1201-y (2004).

28 Celli, J. P. *et al.* Helicobacter pylori moves through mucus by reducing mucin viscoelasticity. *Proc Natl Acad Sci U S A* **106**, 14321-14326, doi:10.1073/pnas.0903438106 (2009).

29 Sun, J. *et al.* Therapeutic Potential to Modify the Mucus Barrier in Inflammatory Bowel Disease. *Nutrients* **8**, doi:10.3390/nu8010044 (2016).

30 Sheffner, A. L. The reduction in vitro in viscosity of mucoprotein solutions by a new mucolytic agent, N-acetyl-L-cysteine. *Ann N Y Acad Sci* **106**, 298-310, doi:10.1111/j.1749-6632.1963.tb16647.x (1963).

31 Srinivasan, S. S. *et al.* RoboCap: Robotic mucus-clearing capsule for enhanced drug delivery in the gastrointestinal tract. *Sci Robot* **7**, eabp9066, doi:10.1126/scirobotics.abp9066 (2022).

32 Khanvilkar, K., Donovan, M. D. & Flanagan, D. R. Drug transfer through mucus. *Adv Drug Deliv Rev* **48**, 173-193, doi:10.1016/s0169-409x(01)00115-6 (2001).

33 Leal, J., Smyth, H. D. C. & Ghosh, D. Physicochemical properties of mucus and their impact on transmucosal drug delivery. *Int J Pharm* **532**, 555-572, doi:10.1016/j.ijpharm.2017.09.018 (2017).

34 Hanio, S. *et al.* Drug-Induced Dynamics of Bile Colloids. *Langmuir* **37**, 2543-2551, doi:10.1021/acs.langmuir.0c02282 (2021).

35 Holm, R., Mullertz, A. & Mu, H. Bile salts and their importance for drug absorption. *Int J Pharm* **453**, 44-55, doi:10.1016/j.ijpharm.2013.04.003 (2013).

36 Augustijns, P. *et al.* A review of drug solubility in human intestinal fluids: implications for the prediction of oral absorption. *Eur J Pharm Sci* **57**, 322-332, doi:10.1016/j.ejps.2013.08.027 (2014).

37 Klein, S. The use of biorelevant dissolution media to forecast the in vivo performance of a drug. *AAPS J* **12**, 397-406, doi:10.1208/s12248-010-9203-3 (2010).

38 Boegh, M., Baldursdottir, S. G., Mullertz, A. & Nielsen, H. M. Property profiling of biosimilar mucus in a novel mucus-containing in vitro model for assessment of intestinal drug absorption. *Eur J Pharm Biopharm* **87**, 227-235, doi:10.1016/j.ejpb.2014.01.001 (2014).

39 Mudie, D. M. *et al.* Quantification of Gastrointestinal Liquid Volumes and Distribution Following a 240 mL Dose of Water in the Fasted State. *Mol Pharmaceut* **11**, 3039-3047, doi:10.1021/mp500210c (2014).

40 Davidson, M. H. *et al.* Colesevelam hydrochloride (cholestagel): a new, potent bile acid sequestrant associated with a low incidence of gastrointestinal side effects. *Arch Intern Med* **159**, 1893-1900, doi:10.1001/archinte.159.16.1893 (1999).

41 Molecular Operating, E. (MOE Montreal, QC, 2019).

42 Wildman, S. A. & Crippen, G. M. Prediction of Physicochemical Parameters by Atomic Contributions. *Journal of Chemical Information and Computer Sciences* **39**, 868-873, doi:10.1021/ci990307l (1999).

43 Yang, Z. Y., Yang, Z. J., Lu, A. P., Hou, T. J. & Cao, D. S. Scopy: an integrated negative design python library for desirable HTS/VS database design. *Brief Bioinform* **22**, doi:10.1093/bib/bbaa194 (2021).

44 Kehrein, J. & Hanio, S. *TC/L interaction probability model*, <https://tclint.streamlit.app> (2022).

45 Gargano, A. F., Lammerhofer, M., Lonn, H., Schoenmakers, P. J. & Leek, T. Mucin-based stationary phases as tool for the characterization of drug-mucus interaction. *J Chromatogr A* **1351**, 70-81, doi:10.1016/j.chroma.2014.05.031 (2014).

46 Kawai, Y. *et al.* Profiling and trend analysis of food effects on oral drug absorption considering micelle interaction and solubilization by bile micelles. *Drug Metab Pharmacokinet* **26**, 180-191, doi:10.2133/dmpk.dmpk-10-rg-098 (2011).

47 Wiedmann, T. S., Deye, C. & Kallick, D. Interaction of bile salt and phospholipids with bovine submaxillary mucin. *Pharm Res* **18**, 45-53, doi:10.1023/a:1011022626030 (2001).

48 Guvendiren, M. & Burdick, J. A. Stiffening hydrogels to probe short- and long-term cellular responses to dynamic mechanics. *Nat Commun* **3**, 792, doi:10.1038/ncomms1792 (2012).

49 Liu, H. Y., Korc, M. & Lin, C. C. Biomimetic and enzyme-responsive dynamic hydrogels for studying cell-matrix interactions in pancreatic ductal adenocarcinoma. *Biomaterials* **160**, 24-36, doi:10.1016/j.biomaterials.2018.01.012 (2018).

50 Oldham-Ott, C. K. & Gilloteaux, J. Comparative morphology of the gallbladder and biliary tract in vertebrates: Variation in structure, homology in function and gallstones. *Microscopy Research and Technique* **38**, 571-597, doi:10.1002/(sici)1097-0029(19970915)38:6<571::Aid-jemt3>3.0.Co;2-i (1997).

51 Nahrwold, D. L. & Grossman, M. I. Effect of cholecystectomy on bile flow and composition in response to food. *Am J Surg* **119**, 30-34, doi:10.1016/0002-9610(70)90007-3 (1970).

52 Hassler, K. R., Collins, J. T., Philip, K. & Jones, M. W. *Laparoscopic Cholecystectomy.* (StatPearls Publishing, Treasure Island (FL), 2022).

53 Di Ciaula, A., Garruti, G., Wang, D. Q. & Portincasa, P. Cholecystectomy and risk of metabolic syndrome. *Eur J Intern Med* **53**, 3-11, doi:10.1016/j.ejim.2018.04.019 (2018).

54 Fathi, M., Soori, M., Rashnoo, F. & Hajinasrollah, E. Cholecystectomy: Long term effect on serum lipid profile and Vitamin D. *Researcher Bulletin of Medical Sciences* **24**, e9 (2020).

55 Moura-Letts, G. & Lizza, J. Solvent-Directed Epoxide Opening with Primary Amines for the Synthesis of β-Amino Alcohols. *Synthesis* **49**, 1231-1242, doi:10.1055/s-0036-1588356 (2016).

56 Kohiki, T., Nishikawa, Y., Inokuma, T., Shigenaga, A. & Otaka, A. Chemical Synthetic Platform for Chlorpromazine Oligomers That Were Reported as Photo-degradation Products of Chlorpromazine. *Chem Pharm Bull (Tokyo)* **65**, 1161-1166, doi:10.1248/cpb.c17-00692 (2017).

57 Schömig, V. J. *et al.* An optimized purification process for porcine gastric mucin with preservation of its native functional properties. *RSC Advances* **6**, 44932-44943, doi:10.1039/c6ra07424c (2016).

58 Weidemann, T. & Schwille, P. Dual-color fluorescence cross-correlation spectroscopy with continuous laser excitation in a confocal setup. *Methods Enzymol* **518**, 43-70, doi:10.1016/B978-0-12-388422-0.00003-0 (2013).

59 Wu, D. H., Chen, A. D. & Johnson, C. S. An Improved Diffusion-Ordered Spectroscopy Experiment Incorporating Bipolar-Gradient Pulses. *Journal of Magnetic Resonance, Series A* **115**, 260-264, doi:10.1006/jmra.1995.1176 (1995).

60 Gibbs, S. J. & Johnson, C. S. A Pfg Nmr Experiment for Accurate Diffusion and Flow Studies in the Presence of Eddy Currents. *Journal of Magnetic Resonance* **93**, 395-402, doi:Doi 10.1016/0022-2364(91)90014-K (1991).

61 Jerschow, A. & Müller, N. 3D Diffusion-Ordered TOCSY for Slowly Diffusing Molecules. *Journal of Magnetic Resonance, Series A* **123**, 222-225, doi:10.1006/jmra.1996.0241 (1996).

62 Jerschow, A. & Müller, N. Suppression of Convection Artifacts in Stimulated-Echo Diffusion Experiments. Double-Stimulated-Echo Experiments. *Journal of Magnetic Resonance* **125**, 372-375, doi:10.1006/jmre.1997.1123 (1997).

63 McLachlan, A. S., Richards, J. J., Bilia, A. R. & Morris, G. A. Constant time gradient HSQC-iDOSY: practical aspects. *Magn Reson Chem* **47**, 1081-1085, doi:10.1002/mrc.2518 (2009).

64 Endres, S. *et al.* Concentration and composition dependent aggregation of Pluronic- and Poly-(2-oxazolin)-Efavirenz formulations in biorelevant media. *J Colloid Interface Sci* **606**, 1179-1192, doi:10.1016/j.jcis.2021.08.040 (2022).

65 Schlussler, R. *et al.* Mechanical Mapping of Spinal Cord Growth and Repair in Living Zebrafish Larvae by Brillouin Imaging. *Biophys J* **115**, 911-923, doi:10.1016/j.bpj.2018.07.027 (2018).

66 Scarcelli, G. & Yun, S. H. Multistage VIPA etalons for high-extinction parallel Brillouin spectroscopy. *Opt Express* **19**, 10913-10922, doi:10.1364/OE.19.010913 (2011).

67 Prevedel, R., Diz-Munoz, A., Ruocco, G. & Antonacci, G. Brillouin microscopy: an emerging tool for mechanobiology. *Nat Methods* **16**, 969-977, doi:10.1038/s41592-019-0543-3 (2019).

68 Allen, M. *et al.* Raincloud plots: a multi-platform tool for robust data visualization. *Wellcome Open Research* **4**, doi:10.12688/wellcomeopenres.15191.2 (2021).

69 Tomczak, M. & Tomczak, E. The need to report effect size estimates revisited. An overview of some recommended measures of effect size. **21**, 19-25 (2014).

70 Edera, P., Bergamini, D., Trappe, V., Giavazzi, F. & Cerbino, R. Differential dynamic microscopy microrheology of soft materials: A tracking-free determination of the frequency-dependent loss and storage moduli. *Physical Review Materials* **1**, 073804 (2017).

71 Cerbino, R., Giavazzi, F. & Helgeson, M. E. Differential dynamic microscopy for the characterization of polymer systems. *Journal of Polymer Science* **60**, 1079-1089, doi:10.1002/pol.20210217 (2021).

72 Gu, M., Luo, Y., He, Y., Helgeson, M. E. & Valentine, M. T. Uncertainty quantification and estimation in differential dynamic microscopy. *Phys Rev E* **104**, 034610, doi:10.1103/PhysRevE.104.034610 (2021).

73 Cerbino, R. & Cicuta, P. Perspective: Differential dynamic microscopy extracts multi-scale activity in complex fluids and biological systems. *J Chem Phys* **147**, 110901, doi:10.1063/1.5001027 (2017).

74 Friedl, H. *et al.* Development and evaluation of a novel mucus diffusion test system approved by self-nanoemulsifying drug delivery systems. *J Pharm Sci* **102**, 4406-4413, doi:10.1002/jps.23757 (2013).

75 Slawson, M. H. & Johnson-Davis, K. L. Quantitation of Haloperidol, Fluphenazine, Perphenazine, and Thiothixene in Serum or Plasma Using Liquid Chromatography-Tandem Mass Spectrometry (LC-MS/MS). *Methods Mol Biol* **1383**, 49-57, doi:10.1007/978-1-4939-3252-8_6 (2016).

76 Juenke, J. M., Brown, P. I., Urry, F. M., Johnson-Davis, K. L. & McMillin, G. A. Simultaneous UPLC-MS/MS assay for the detection of the traditional antipsychotics haloperidol, fluphenazine, perphenazine, and thiothixene in serum and plasma. *Clin Chim Acta* **423**, 32-34, doi:10.1016/j.cca.2013.04.014 (2013).

Supporting Information

Table S1. Water content (mean ± standard deviation; n=3) and pH value of mucus isolates harvested from the small intestinal mucosa of four pigs.

	Isolated mucus batch			
	#1	**#2**	**#3**	**#4**
Water content [%]	85.1 ± 0.4	86.0 ± 0.1	86.1 ± 0.2	85.1 ± 0.1
pH value	6.24	6.55	6.45	6.72

Table S2. Rheological fitting parameters, with a power-law model fitted to the steady shear viscosity curve for obtaining the flow behaviour index (n) and flow consistency index (K). Yield stress (τy) was approximated by the tangent intersection point method on the steady stress sweep data. A Maxwell-Voigt model was fitted to the creep curves obtaining instantaneous compliance (J0), viscoelastic compliance (Jm), mean retardation times (TM), zero-shear rate viscosities (η0), and the correlation coefficient (Rxy). The onset of the decrease in the storage modulus and the cross-over point of the storage and loss moduli indicate the limit of the linear viscoelastic region (γLVR) and the flow point (γflow), respectively. 25-fold TC/L corresponds to 75 mM TC and 18.75 mM L.

Experiment	**Value**	**Isolated mucus batch**				
		#1	**#2**	**#3**	**#3 with 25-fold TC/L**	**#4**
Steady shear viscosity	n [1]	0.21	0.23	0.24	0.26	0.27
	K [Pa·sn]	11.3	10.2	13.7	9.45	12.5
Steady stress sweep	τy [Pa]	1.9	2.2	5.8	1.9	5.4
Creep test	J0 [kPa-1]	39	40	23	24	18
	JM1 [kPa-1]	57	85	31	33	26
	TM1 [s]	18	37	14	5	23
	JM2 [kPa-1]	-	19	-	-	-
	TM2 [s]	-	1	-	-	-
	η0 [Pa·s]	2855	2614	4321	3851	7401
	Rxy	0.997	0.999	0.993	0.979	0.998
Shear strain amplitude sweep	γLVR [%]	1.56	1.25	1.26	1.08	1.24
	γflow [%]	46	58	84	50	74

Table S3. Colloidal size of mixed Taurocholate/Lecithin colloids in PBS. Hydrodynamic diameter (mean ± standard deviation, n = 3) and PDI (mean ± standard deviation, n = 3) were measured by dynamic light scattering. Diffusion coefficients were determined by ^{1}H NMR DOSY experiments. NA = not available, too low signal for robust NMR diffusion measurements. 1-fold TC/L corresponds to 3 mM TC and 0.75 mM L.

Medium	**Z-Average hydrodynamic diameter [nm]**	**PDI**	**Diffusion coefficient [10^{-10} m^2/s]**	
			Taurocholate-H26	**Lecithin-H4**
1-fold TC/L in PBS	53 ± 5	0.029 ± 0.007	4.12	NA
5-fold TC/L in PBS	6 ± 1	0.009 ± 0.001	2.25	0.74
25-fold TC/L in PBS	4 ± 1	0.007 ± 0.003	1.16	0.76

Table S4. The barrier resistance of the polyester-membrane without mucus in the Transwell diffusion experiments (concentration in the acceptor compartment is given as mean ± standard deviation, n =3). The nominal concentration for an assumed homogeneously distributed solution was 0.25 mM for the drug substances and 18.75 mM for Taurocholate. 25-fold TC/L corresponds to 75 mM TC and 18.75 mM L.

Substance	**Medium in donor compartment**	**Concentration in acceptor compartment after 5 min [mM]**
Metoprolol	PBS	0.19 ± 0.02
	25-fold TC/L in PBS	0.13 ± 0.01
Perphenazine	PBS	0.13 ± 0.02
	25-fold TC/L in PBS	0.17 ± 0.01
Fluphenazine	PBS	0.12 ± 0.01
	25-fold TC/L in PBS	0.14 ± 0.01
Taurocholate	25-fold TC/L in PBS	11.4 ± 1.8

Table S5. Non-compartmental PK analysis of rat study. Maximum of plasma concentration (c_{max}), Area under the curve to last nonzero concentration using linear up and down method (AUC_{last}), estimated terminal rate constant (λ_z), and apparent clearance (CL/F) are shown as mean ± standard deviation, n = 5. Time to peak drug concentration (t_{max}) is shown as median and range in brackets. Analysis was applied to plasma concentrations using R version 4.0.5 with the package 'NonCompart' V 0.4.9 (Kyun-Seop Bae). One rat in the Perphenazine control group was excluded from analysis as it was, in contrast to the protocol, not pre-treated with Omeprazole. Control group was reported before[1].

Drug	**Treatment**	**c_{max} [nmol/L]**	**t_{max} [h]**	**AUC_{last} [nmol*h/L]**	**λ_z [1/h]**	**CL/F [L/h]**
Metoprolol	Control	50 ± 34	0.25 (0.25)	35 ± 17	0.48 ± 0.28	272 ± 90
	Colesevelam	30 ± 20	0.25 (0.25)	23 ± 13	0.65 ± 0.46	443 ± 192
Perphenazine	Control	31 ± 12	1 (1)	151 ± 50	0.16 ± 0.02	57 ± 22
	Colesevelam	7 ± 3	1 (1)	38 ± 11	0.16 ± 0.07	213 ± 47

Table S6. Predicted molecular descriptors, TC/L interaction probability as well as experimental results from compounds from two literature datasets[2,3]. A TC/L interaction probability > 0.5 was classified as bile-interacting (BI). Asterisk (*) mark compounds with pairs of values of CrippenMR and logP that are different from the set of drugs used in the modelling. Therefore, the prediction of these drugs is questionable. A retention factor in HPLC with mucin-based stationary phase > 2 was classified as mucus-interacting (MI) [2]. Accordingly, the compounds were sorted into four classes (I: non-MI, non-BI; II: MI, non-BI; III: MI, BI; IV: non-MI, BI). Compounds that were analysed by ^{1}H NMR are shown in italics, see Figure S46-48 for spectra, n/a stands for not available.

	Model prediction			**Experimental outcome**		
Compound	**Crippen's Molar refractivity**	**log D at pH 7**	**TC/L interaction probability**	**Retention factor in HPLC with mucin-based stationary phase**	**D (PBS) / D (1.5% mucus)**	**Region**
Pyrazinamide	30.55	0.38	0.01	0	n/a	IV
Acetylsalicylic acid	42.08	-0.82	0	0	n/a	IV
5-Fluorouracil	27.64	-0.36	0	0	n/a	IV
Salicylic acid	32.44	-0.88	0	0	n/a	IV
Aminophenazone	70.07	1.48	0.37	0	n/a	IV
Ketoprofen	69.74	0.53	0.18	0	n/a	IV
Fenoprofen	66.38	0.83	0.19	0	n/a	IV
Suprofen	67.62	0.63	0.17	0	n/a	IV
Ketorolac	66.67	-0.02	0.09	0	n/a	IV
Naproxen	63.92	0.47	0.12	0	n/a	IV
4-Aminosalicyclic acid	36.85	-1.06	0.00	0	n/a	IV
Capecitabine	84.55	0.81	0.46	0	n/a	IV
Phenobarbital	60.54	0.71	0.12	0	n/a	IV
Mephenytoin	58.84	0.2	0.07	0	n/a	IV
Lidocaine	71.46	1.25	0.34	0	n/a	IV
Nandrolone	78.1	3.01	0.83	0	n/a	III
Indoprofen	76.82	0.31	0.23	0.18	n/a	IV
Warfarin	87.73	3.06	0.91	0.19	n/a	III
Salbutamol	65.53	0.39	0.12	0.25	n/a	IV
Phenazone	55.75	1.41	0.17	0.52	n/a	IV
Budesonide	112.87	2.5	0.97	0.56	n/a	III
Diclofenac	74.9	1.48	0.46	0.72	n/a	IV
Venlafaxine	81.45	1.53	0.59	0.82	n/a	III
Oxazepam	78.17	2.01	0.64	0.94	n/a	III
Rifampicin*	218.73	1.14	0.99	1.16	n/a	III
Lorazepam	83.18	2.5	0.80	1.32	n/a	III
Metoprolol	75.45	1.2	0.40	1.36	~1.3	IV
Spironolactone	86.57	0.52	0.42	1.51	n/a	IV
Diazepam	81.81	2.6	0.81	1.56	n/a	III
Quinine	94.15	2.07	0.85	3.06	n/a	II
Docetaxel	203.6*	2.83	1	3.34	n/a	II
Doxepin	86.59	1.91	0.75	5.33	n/a	II

Compound	Model prediction			Experimental outcome		Region
	Crippen's Molar refractivity	log D at pH 7	TC/L interaction probability	Retention factor in HPLC with mucin-based stationary phase	D (PBS) / D (1.5% mucus)	
Desipramine	84.63	2.29	0.79	5.64	n/a	II
Imipramine	89.59	2.41	0.85	6.24	n/a	II
Amitriptyline	89.67	2.15	0.82	7.80	n/a	II
Trimipramine	94.14	2.64	0.91	7.91	n/a	II
Fluphenazine	2.18	111.8	0.95	8.14	n/a	II
Dosulepin	91.82	2.48	0.88	8.45	n/a	II
Doxorubicin	130.46	-0.18	0.89	11.59	n/a	II
Cyclobenzaprine	91.19	2.54	0.88	14.95	n/a	II
Pentamidine	98.17	0.63	0.65	18.61	n/a	II
Glucosamine	36.66	-2.01	0	n/a	~1.2	n/a
Mannitol	38.2	-1.64	0	n/a	~1	n/a
Glucuronic acid	33.91	-3.26	0	n/a	~1.1	n/a
Glucose	35.99	-1.3	0	n/a	~1	n/a
Antipyrine	55.75	1.41	0.17	n/a	~1	n/a
Propranolol	77.38	1.8	0.58	n/a	~1.4	n/a
Hydrocortisone	95.14	1.76	0.82	n/a	~1.3	n/a
Testosterone	82.72	3.25	0.89	n/a	~2.5	n/a
Cyclosporin A*	317.69	-3.37	1	n/a	~6.3	n/a
Desmopressin*	269.82	-2.63	0.99	n/a	~5.9	n/a

Table S7. LC-MS/MS analytical conditions for flux determination. Methods are based on previously published protocols[4,5]. Drugs were quantified with ^{13}C-Perphenazine for internal standard pairing using calibration curves, n/a stands for not available. Q3 ion used for quantification is marked with an asterisk.

Ultra high-pressure liquid chromatography

Instrument	Agilent 1200				
Column	XBridge C18 3.5 µm 2.1 x 50 mm				
Mobile phase	A: 10 mM ammonium hydrogen carbonate in water/methanol 90/10 (v/v)				
	B: 10 mM ammonium hydrogen carbonate in methanol/water 90/10 (v/v)				
Gradient table	Time [min]	A [%]	B [%]		
	0.00	30	70		
	0.33	30	70		
	2.00	10	90		
	2.70	10	90		
	2.80	30	70		
	3.60	30	70		
Flow rate	600 µL/min				
Injection volume	5 µL				
Column temperature	20 ± 0.8 °C				
Tandem mass spectrometry					
Instrument	Agilent 6460 triple quadrupole operating with an electrospray ionization interface and in multiple reaction monitoring (MRM) mode				
Settings	Compound	Retention time [min]	MRM pair Q1 [m/z]	MRM pair Q3 [m/z]	Collision energy [V]
	Perphenazine	1.9	404.0	143.0*	28
				171.0	24
	Fluphenazine	2.1	438.0	143.0*	32
				171.0	24
	^{13}C3-Perphenazine (Internal Standard)	1.9	407.0	144.0	28
				174.1*	24
Ion Polarity	Positive				
Dwell time	125 ms				
Fragmentor	135 V				
Cell Accelerator voltage	4 V				

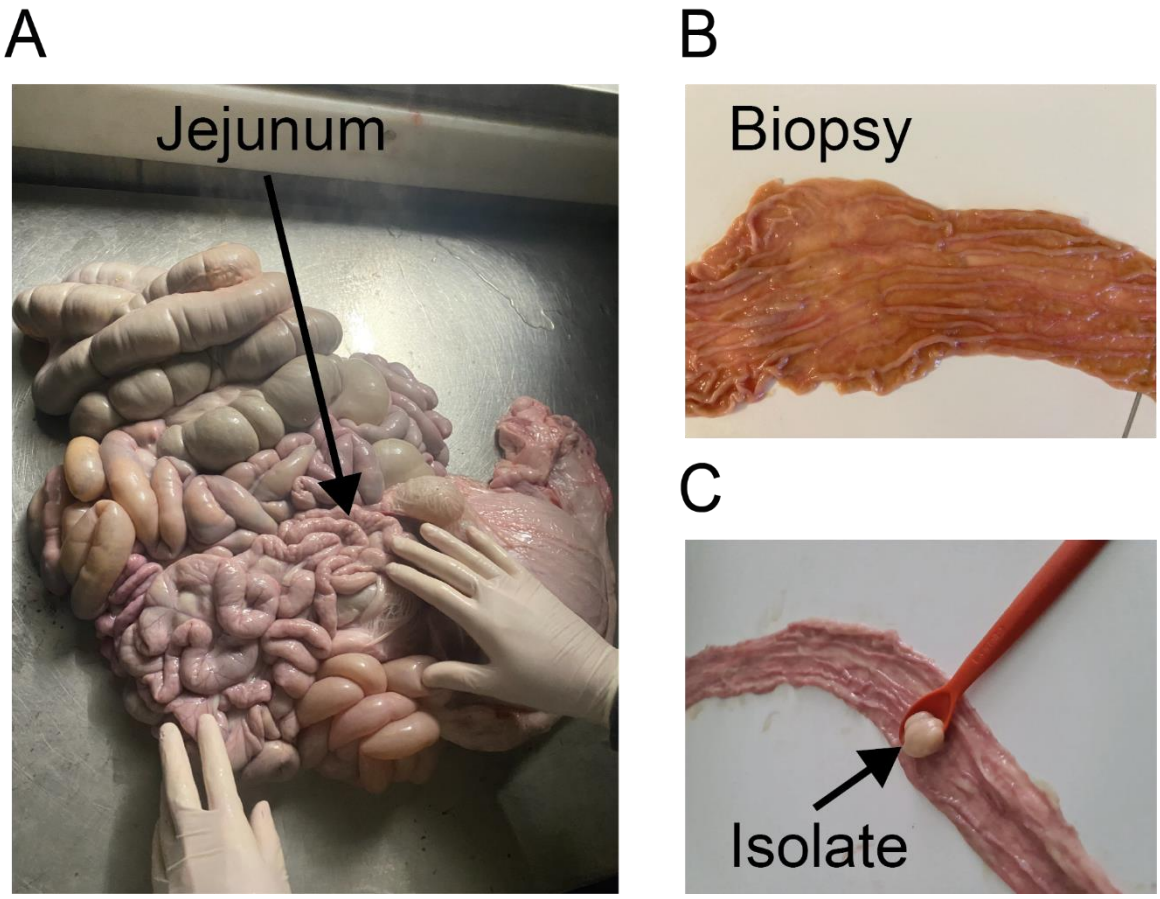

Figure S1. Mucus collection from pig jejunum with a picture taken from (A) the site of harvest, (B) a longitudinal view of the opened tract, and (C) an example of the mucus scraped from the biopsy which is referred to as mucus isolate in this manuscript.

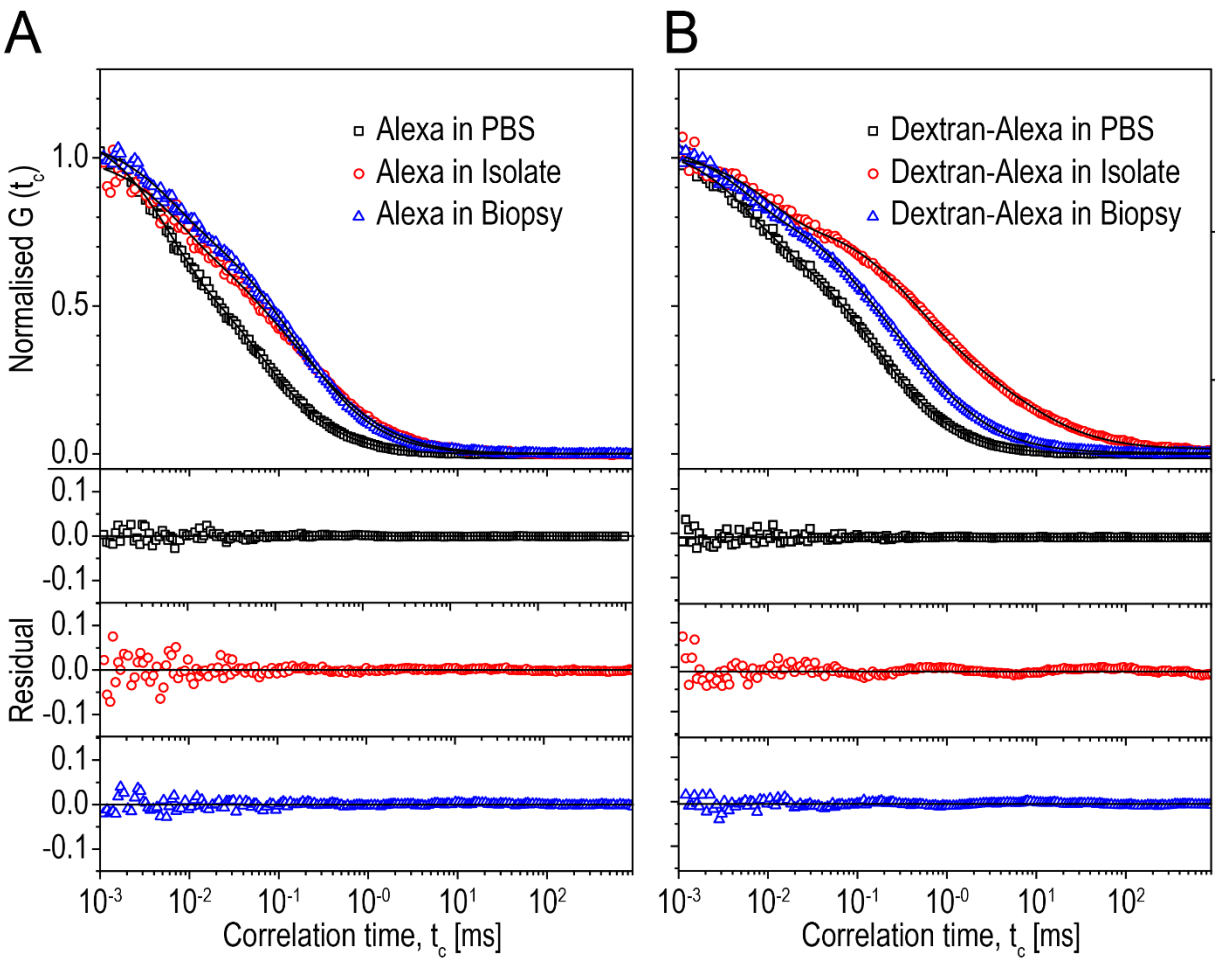

Figure S2. FCS curves of (A) Alexa and (B) Dextran-Alexa with residuals in PBS (squares, black), isolate (circles, red), and in biopsy (up-pointing triangles, blue), respectively. FCS curve from Alexa and Dextran-Alexa in PBS fitted with single three-dimensional diffusion model with an additional relaxation component (A31DT) for the photophysics. For FCS curves in isolate and biopsy, the introduction of another diffusion component (A32DT) resulted in better fits, see "FCS data acquisition and analysis" section for details.

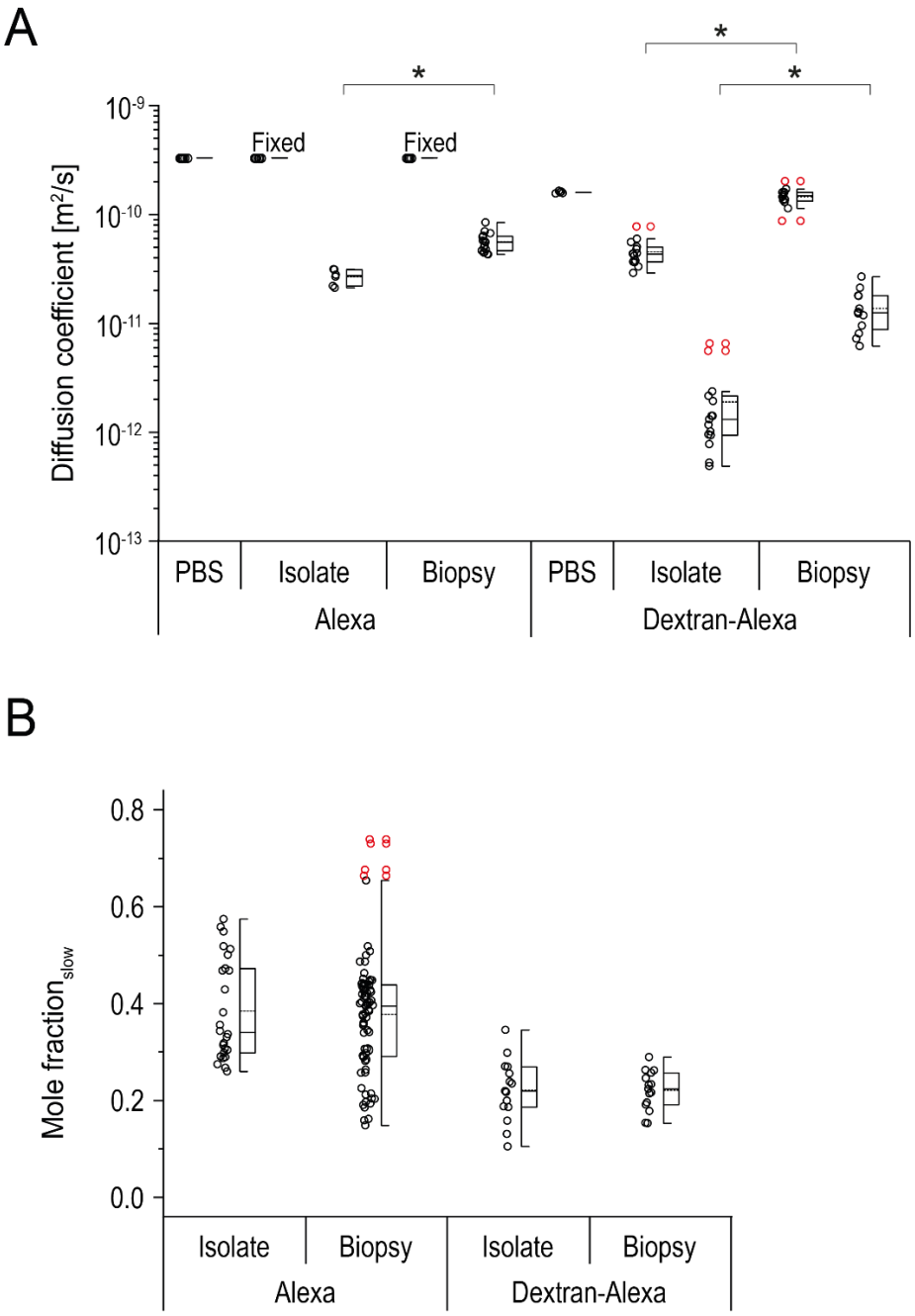

Figure S3. Diffusion coefficients and molar fraction of Alexa and 10 kDa Dextran-Alexa. (A) Diffusion coefficients, D_{fast} and D_{slow}, of Alexa and Dextran-Alexa in phosphate buffered saline (PBS), mucus isolate, and within the mucus on undisturbed biopsies with (B) outlining the molar fractions with slow diffusion. FCS data shown as half scatterplot and half box/whisker plot with median (solid line), mean (dotted line), red circles indicating outliers, and whiskers indicate the upper and lower 25%, respectively (*$p < 0.05$, Student's t-test; n ≥ 3, outlier is any data point more than 1.5 interquartile ranges below the first or above the third quartile). The slower diffusion component of Alexa (D_{slow}) were 0.28 (± 0.04) x 10^{-10} m^2/s and 0.56 (± 1.13) x 10^{-10} m^2/s for isolated and biopsy mucus, respectively. The diffusion coefficient of Dextran-Alexa in PBS 1.60 (± 0.04) x 10^{-10} m^2/s was slower compared to Alexa in PBS. The D_{fast} component for isolated and biopsy mucus were 0.45 ± 0.12 x 10^{-10} m^2/s and 1.46 (± 0.29) x 10^{-10} m^2/s, respectively. Isolated mucus showed much slower D_{slow} 0.016 (± 0.015) x 10^{-10} m^2/s compared to biopsy 0.14 (± 0.06) x 10^{-10} m^2/s. The data is also shown in modified form in Fig. 1B-C.

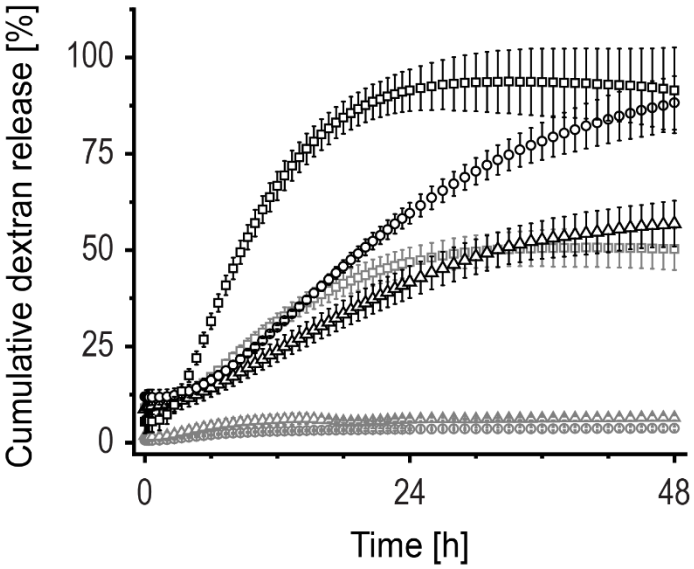

Figure S4. Dextran release from isolates. Release profiles of fluorescein isothiocyanate (FITC)-dextrans (black) and FITC-Diethylaminoethyl (DEAE)-dextrans (gray) with molecular weight of 4 kDa (squares), 40 kDa (circles), and 150 kDa (up-pointing triangle). Data shown as mean ± standard deviation, n = 3.

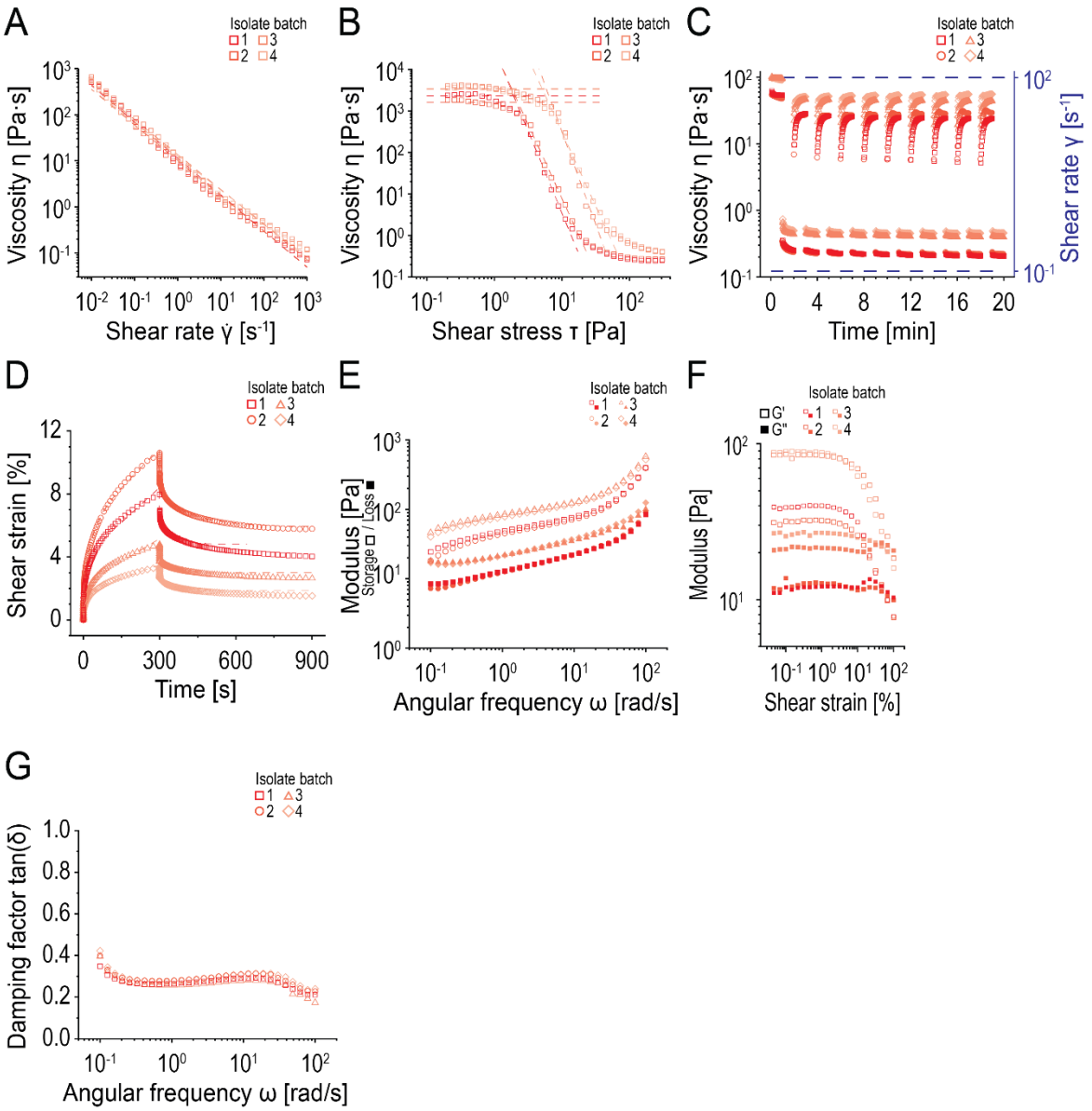

Figure S5. Bulk rheology of four isolated porcine intestinal mucus samples. (A) Viscosity as a function of shear rate and fitted with a power law model fit (dotted line). (B) Viscosity as a function of shear stress. The intersection of the tangents (dotted lines) designates the yield stress. (C) Viscosity as a function of time with alternating high- and low-shear phases. (D) Shear strain at creep and stress relaxation as a function of time. Materials' responses to constant applied stress fitted to a Maxwell-Voigt model. The corresponding creep and creep recovery compliance function fits are shown by dashed lines. (E) Frequency sweep test with the storage modulus (open symbols) and loss modulus (closed symbols) shown as a function of the angular frequency at fixed shear strain. (F) Amplitude sweep test with the storage modulus (open symbols) and loss modulus (closed symbols) shown as a function of the shear strain at fixed angular frequency. (G) Damping factor as a function of angular frequency.

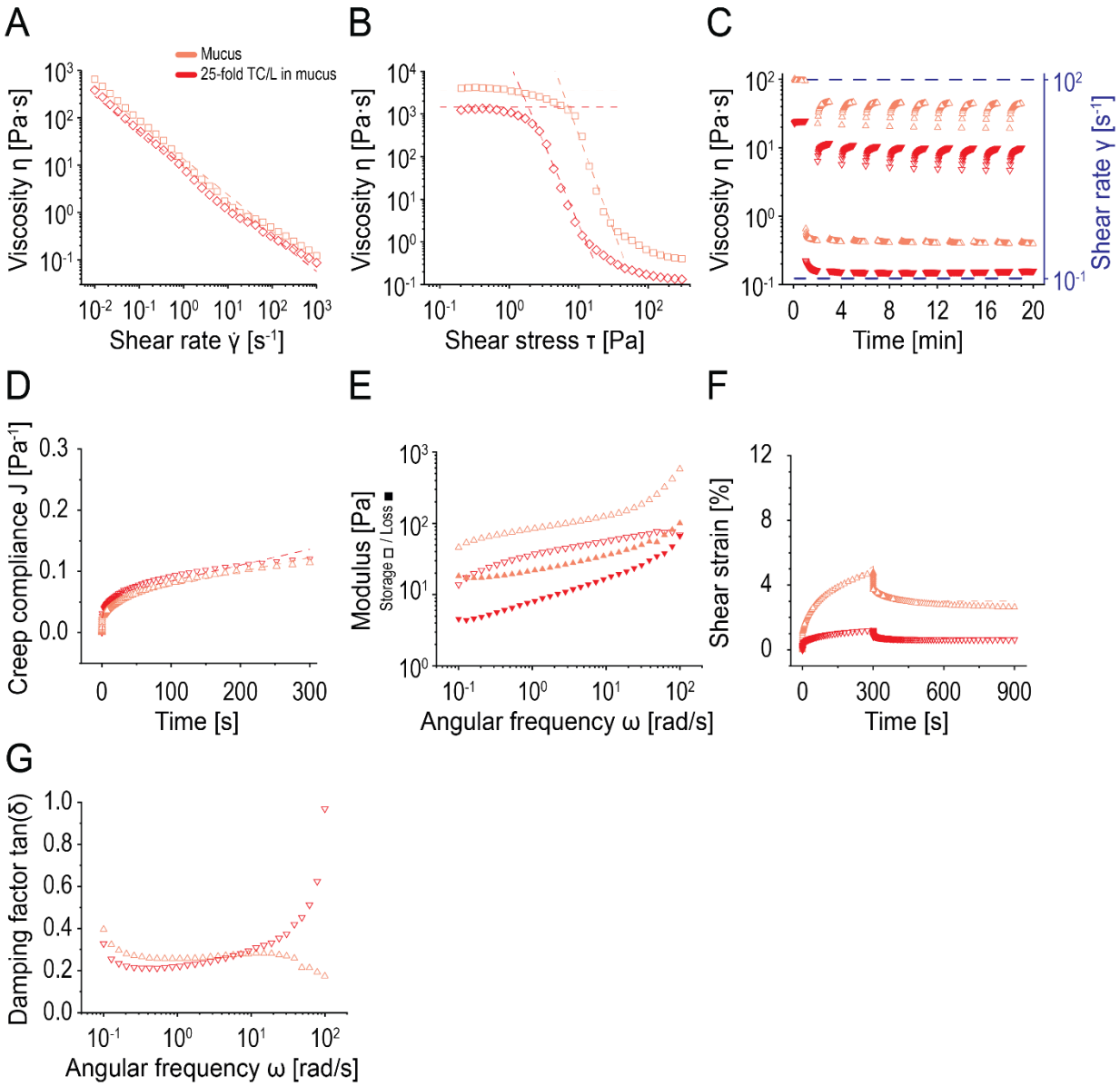

Figure S6. Impact of bile (75 mM TC and 18.75 mM L) on bulk rheology of isolated porcine intestinal mucus samples. (A) Viscosity as a function of shear rate and fitted with a power law model (dotted line). (B) Viscosity as a function of shear stress. The intersection of the tangents (dotted lines) designates the yield stress. (C) Viscosity as a function of time with alternating high- and low-shear phases. (C) Creep compliance against time. (E) Frequency sweep test with the storage modulus (open symbols) and loss modulus (closed symbols) shown as a function of the angular frequency at fixed shear strain. (F) Shear strain at creep and stress relaxation as a function of time. Materials' responses to constant applied stress fitted to a Maxwell-Voigt model. The corresponding creep and creep recovery compliance function fits are shown by dashed lines. (G) Damping factor as a function of angular frequency.

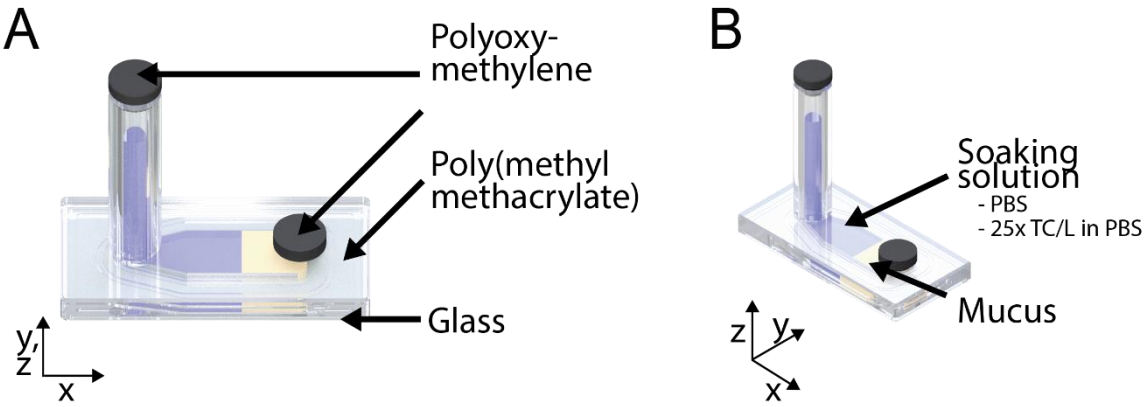

Figure S7. Construction of setup for Brillouin microscopy. Schematic (A) frontal and (B) isometric projection of the measuring cell. (A) is shown modified in Fig. 2D.

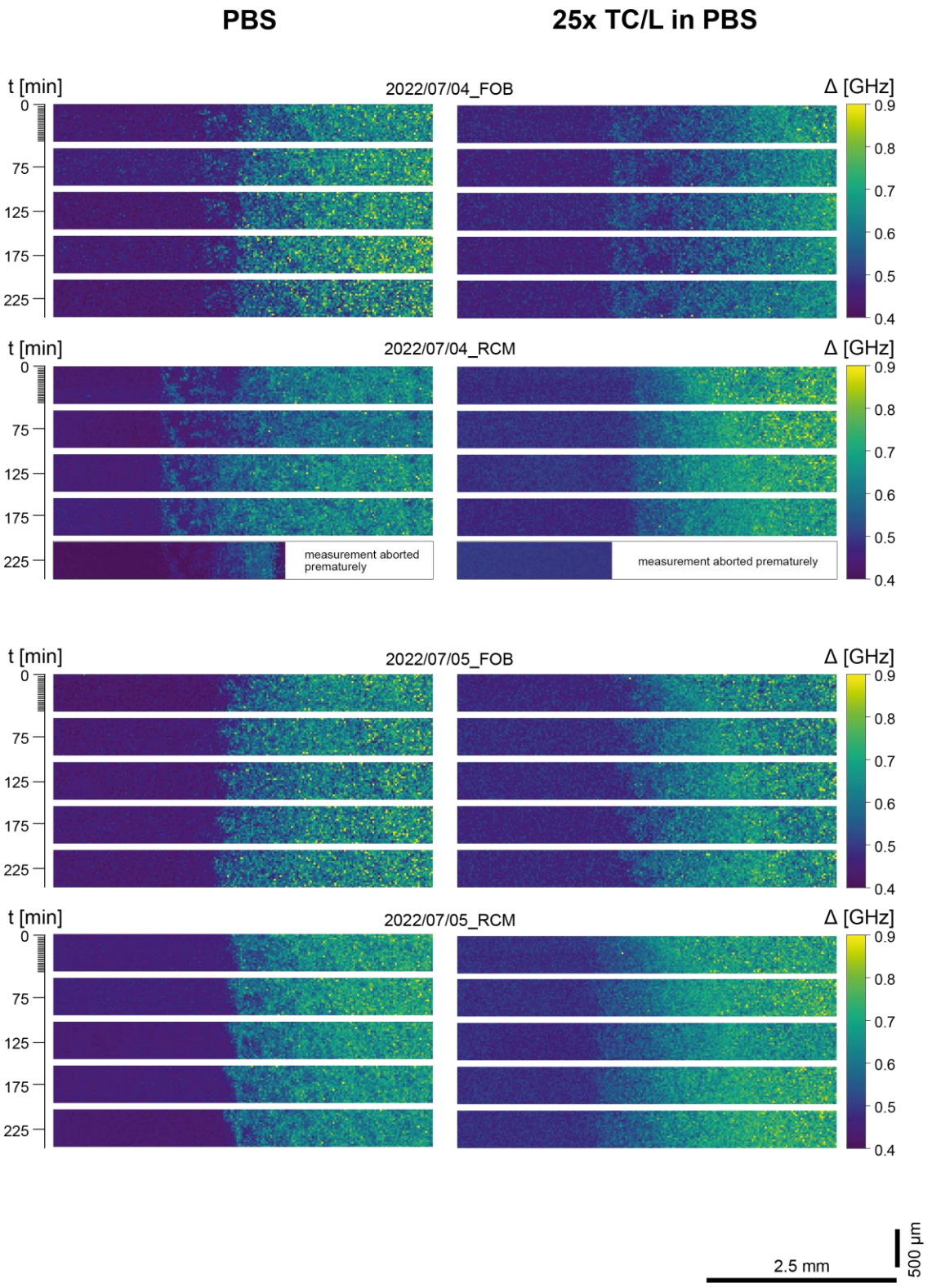

Figure S8. Brillouin linewidth maps, part 1 of 3. Brillouin microscopy sequences of the linewidth for mucus exposed to PBS (left) and 25-fold TC/L (corresponds to 75 mM TC and 18.75 mM L) in PBS (right).

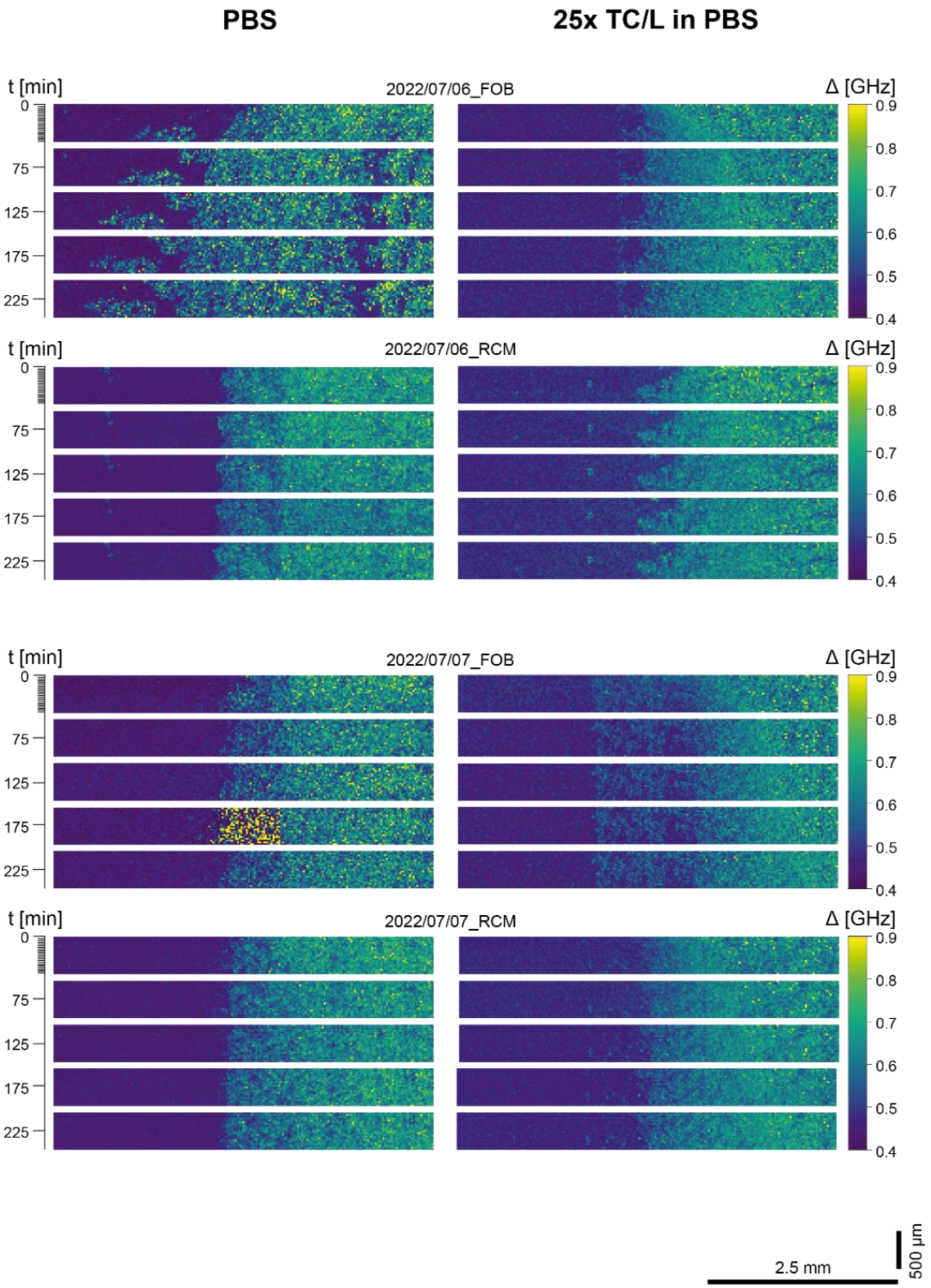

Figure S9. Brillouin linewidth maps, part 2 of 3. Brillouin microscopy sequences of the linewidth for mucus exposed to PBS (left) and 25-fold TC/L (corresponds to 75 mM TC and 18.75 mM L) in PBS (right).

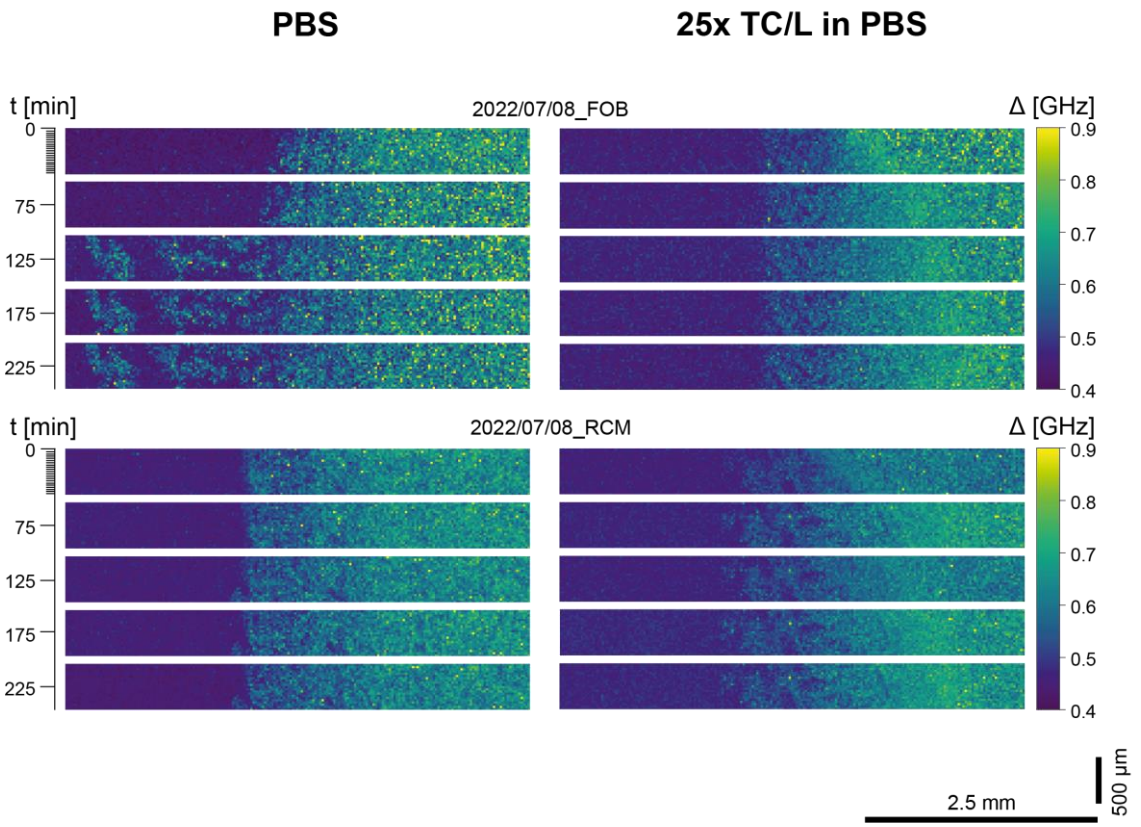

Figure S10. Brillouin linewidth maps, part 3 of 3. Brillouin microscopy sequences of the linewidth for mucus exposed to PBS (left) and 25-fold TC/L (corresponds to 75 mM TC and 18.75 mM L) in PBS (right).

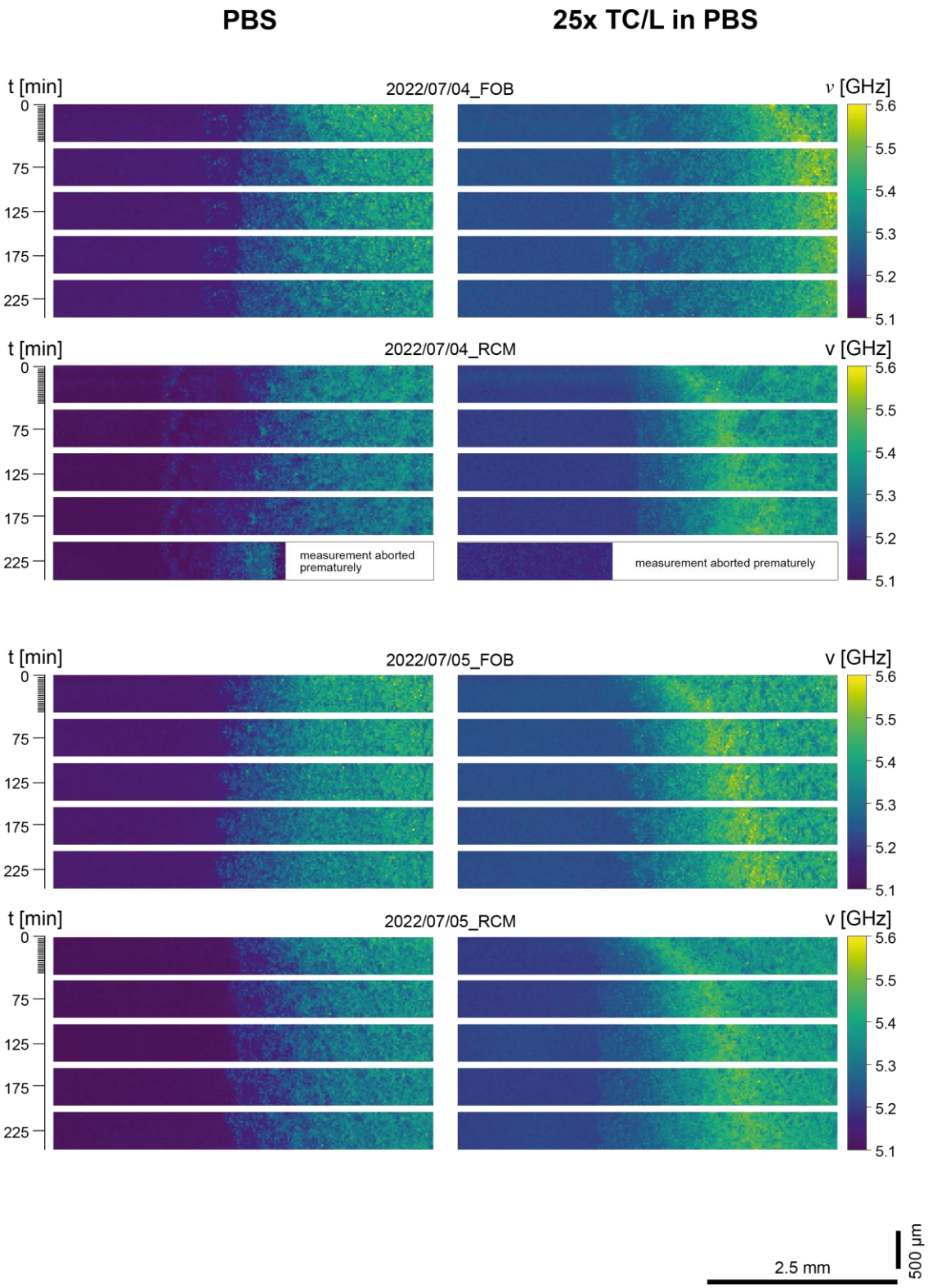

Figure S11. Brillouin frequency shift maps, part 1 of 3. Brillouin microscopy sequences of the frequency shifts for mucus exposed to PBS (left) and 25-fold TC/L (corresponds to 75 mM TC and 18.75 mM L) in PBS (right).

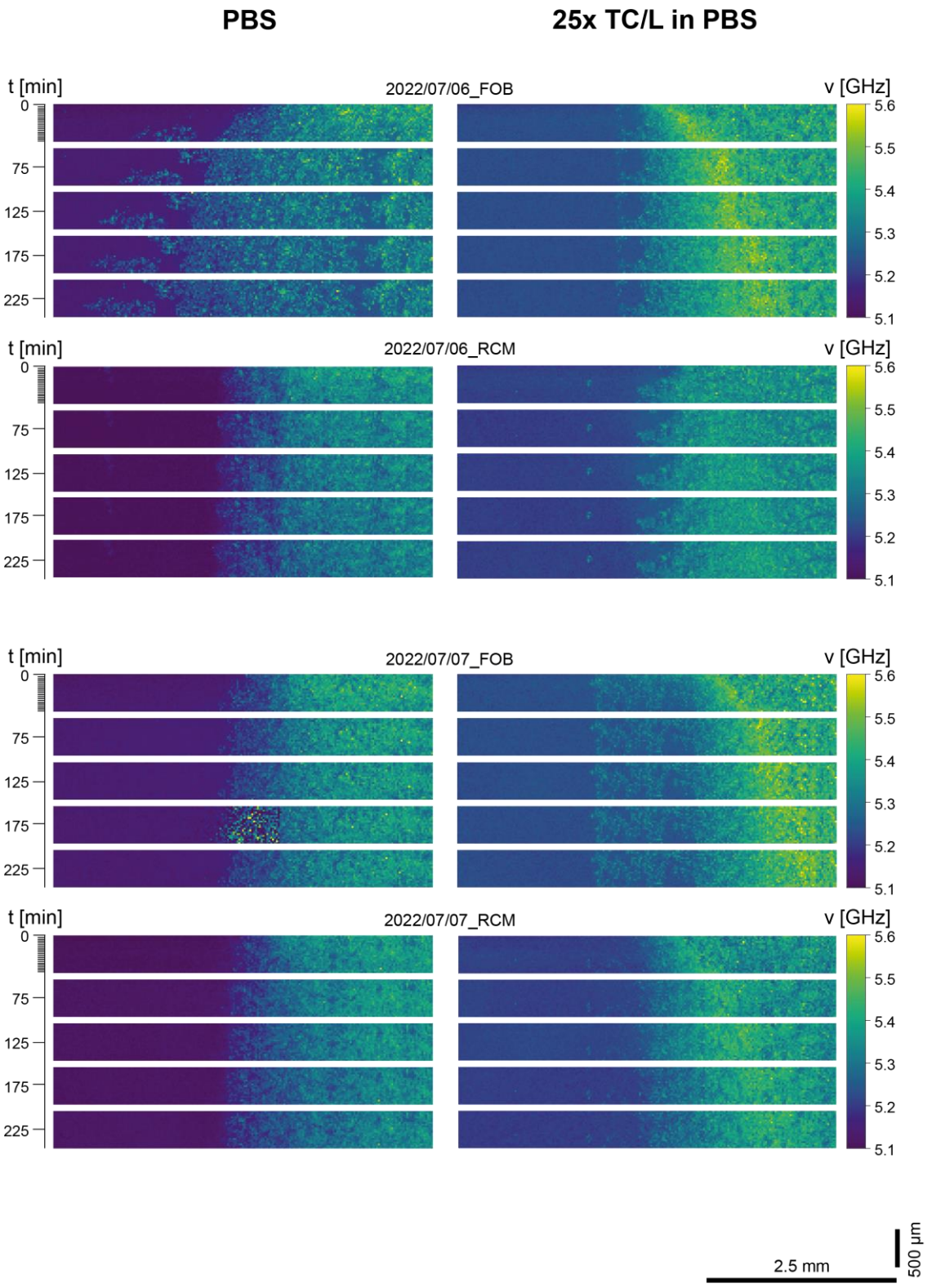

Figure S12. Brillouin frequency shift maps, part 2 of 3. Brillouin microscopy sequences of the frequency shifts for mucus exposed to PBS (left) and 25-fold TC/L (corresponds to 75 mM TC and 18.75 mM L) in PBS (right). Maps of 2022/07/06_FOB exposed to 25-fold TC/L in PBS are modified shown in Fig. 2E.

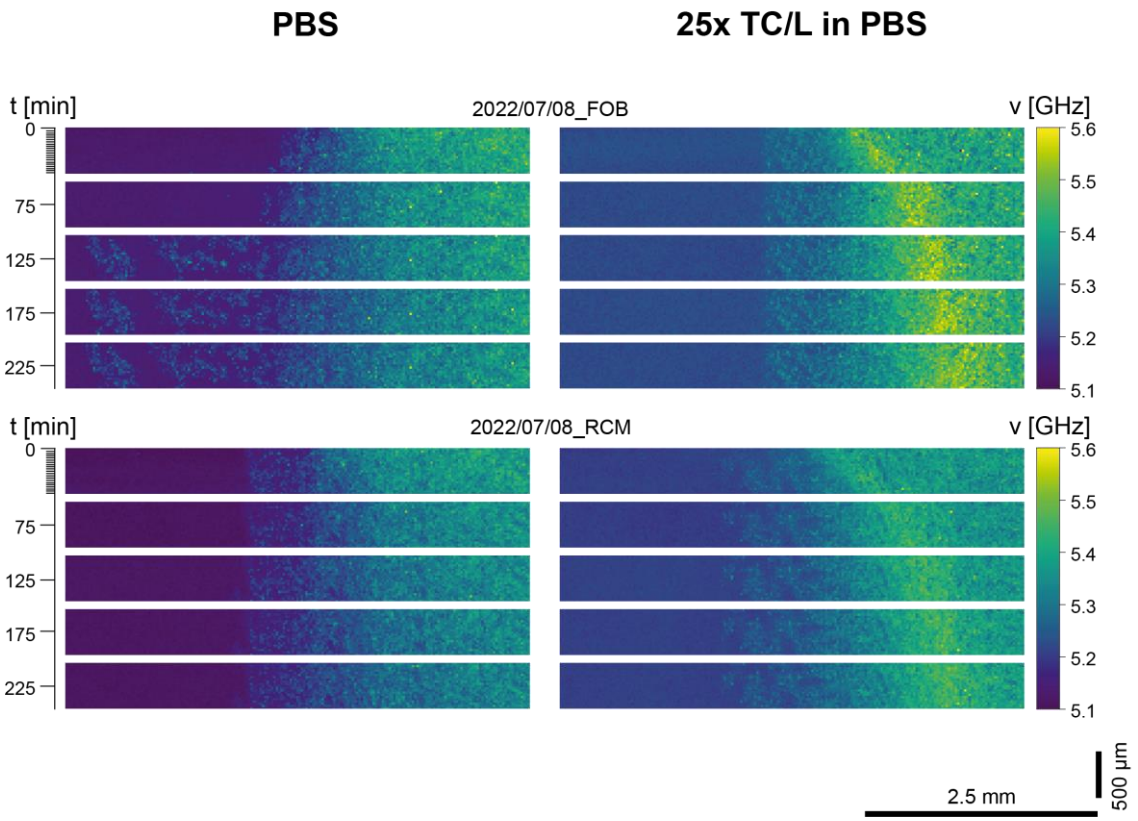

Figure S13. Brillouin frequency shift maps, part 3 of 3. Brillouin microscopy sequences of the frequency shifts for mucus exposed to PBS (left) and 25-fold TC/L (corresponds to 75 mM TC and 18.75 mM L) in PBS (right).

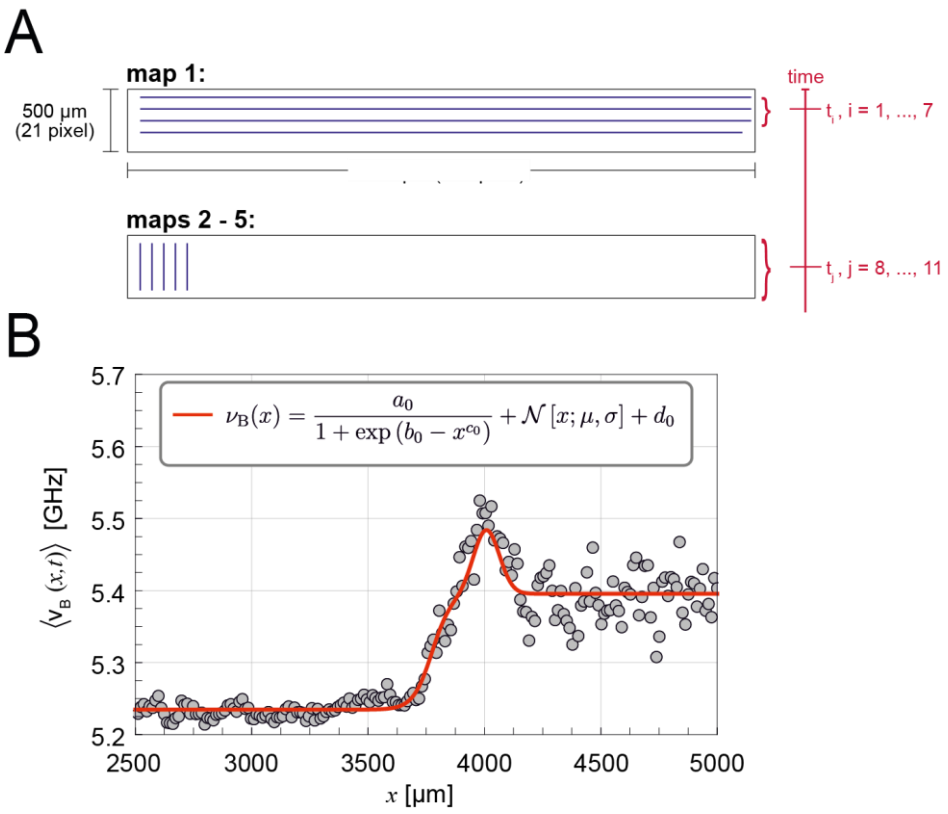

Figure S14. Measurement scheme and workflow to quantify the dynamic mechanical changes of the mucus exposed to 25-fold TC/L (corresponds to 75 mM TC and 18.75 mM L) in PBS (right). in PBS mixture. (A) Each chamber, filled with either mucus and PBS or with mucus and 25-fold TC/L in PBS, was subjected to a sequence of five consecutive Brillouin microscopy scans. Each scan yielded one map. The first respective maps of each sequence were scanned along the long axis first (from PBS/25-fold TC/L in PBS to mucus) to capture potentially fast dynamics. The four consecutive maps were scanned along the shorter axis first. Each map consists of 21 pixel (= measurement points) x 201 pixel spanning an area of 500 µm to 5000 µm. (B) In the first Brillouin microscopy maps, three line scans were averaged and yielded seven average line scans in which a fitting function determined the position of the respective Brillouin frequency shift maximum. Thus, the first maps gave rise to seven pairs of positions of Brillouin frequency shift maxima and corresponding time points. The four subsequent maps were averaged entirely giving rise to one additional such pair per map. The resulting curve of all positions of the respective Brillouin frequency shift maxima and their corresponding time points are given in Fig. 2F.

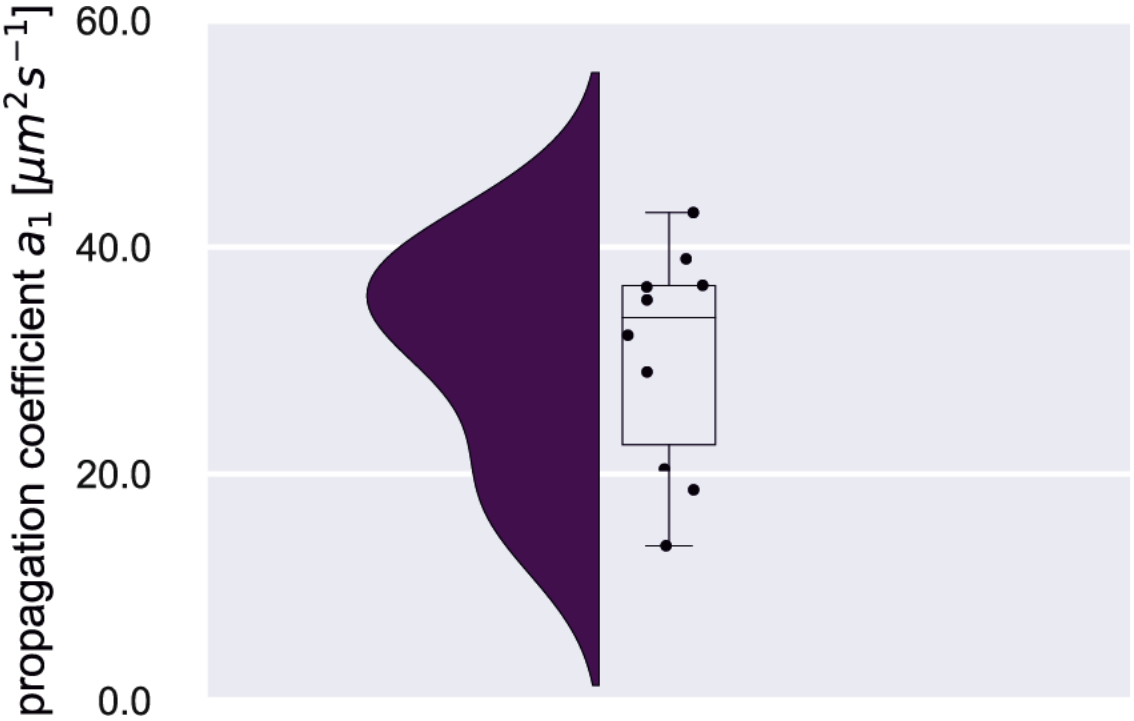

Figure S15. Distribution of the propagation coefficient of the elevated Brillouin frequency shift values traveling through the mucus when exposed to 25-fold TC/L (corresponds to 75 mM TC and 18.75 mM L) in PBS (right). Data shown as raincloud plot (left) and box plot with scatterplot (right), box/whisker plot with median (solid line), and whiskers indicate the upper and lower 25%, respectively.

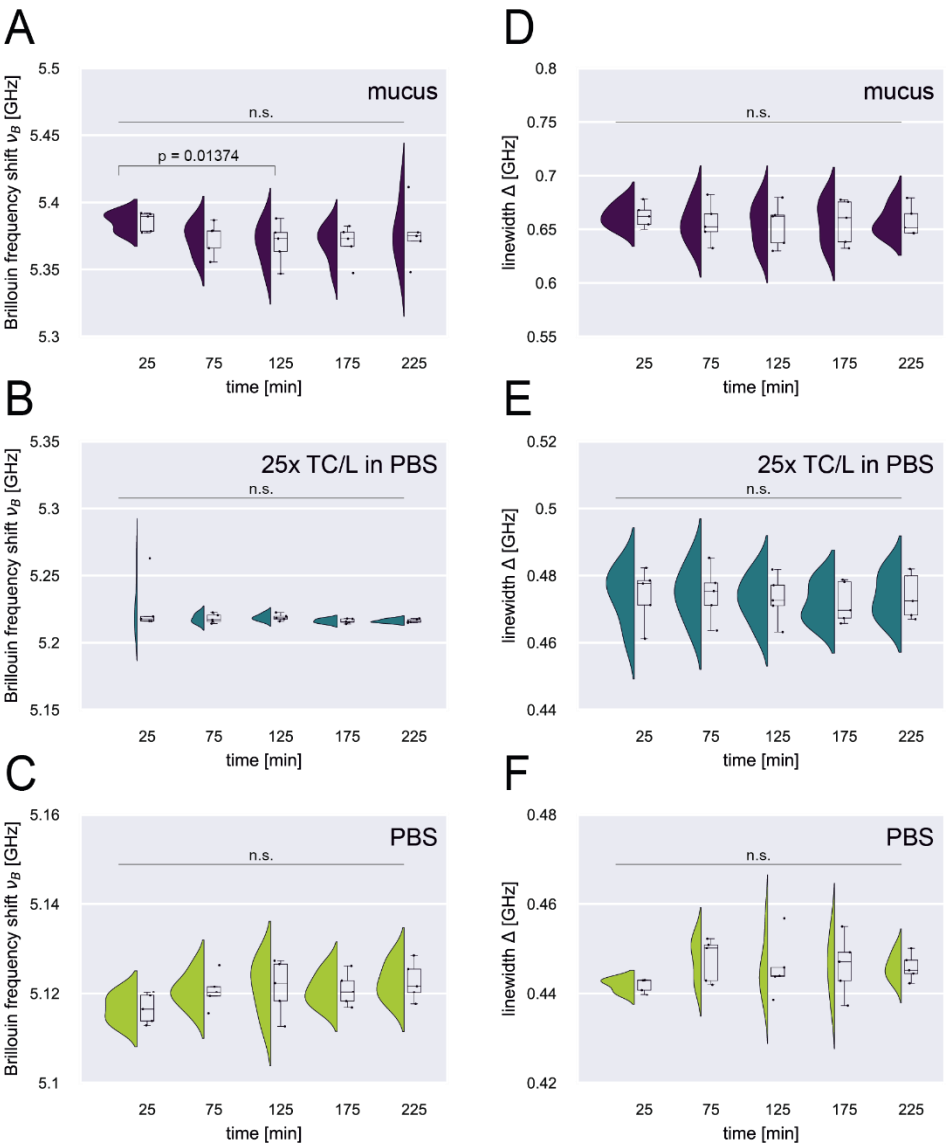

Figure S16. Temporal evolution of the Brillouin frequency shift and linewidth of mucus, 25-fold TC/L (corresponds to 75 mM TC and 18.75 mM L) in PBS and PBS. (A) – (C) Brillouin frequency shift and (D) – (E) linewidth of unmixed mucus, unmixed 25-fold TC/L in PBS and unmixed PBS over time, respectively. One datum represents the mean Brillouin frequency shift or mean linewidth obtained by close-uping and averaging the 210 spectra (10 measurement columns) that are farthest to the right (for unmixed mucus) or left (for unmixed 25-fold TC/L in PBS or unmixed PBS) in each Brillouin microscopy map. Data shown as raincloud plot (left) and box plot with scatterplot (right), box/whisker plot with median (solid line), and whiskers indicate the upper and lower 25%, respectively.

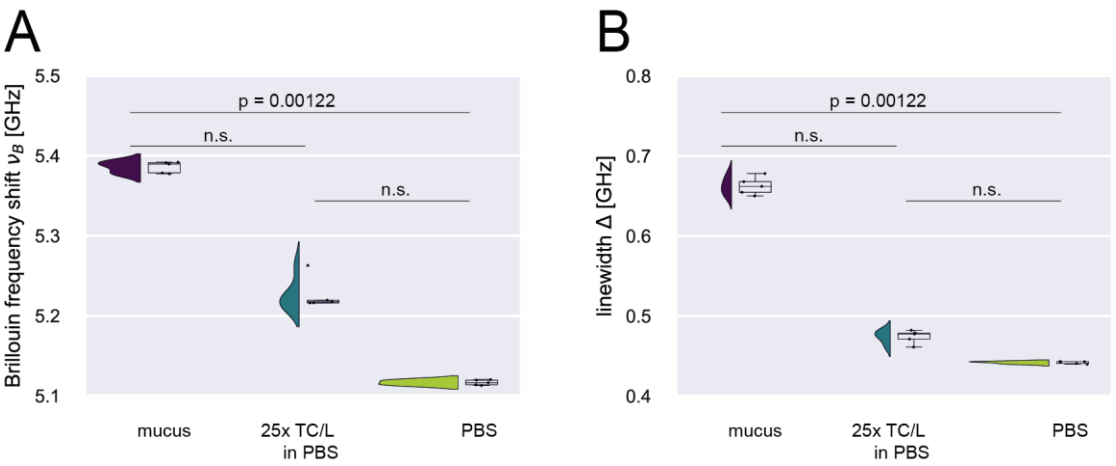

Figure S17. Direct comparison of the initial Brillouin frequency shifts and linewidths of mucus, 25-fold TC/L (corresponds to 75 mM TC and 18.75 mM L) in PBS (right) and PBS. A) Brillouin frequency shift and B) linewidth of unmixed mucus, unmixed 25-fold TC/L in PBS, and unmixed PBS obtained from the first respective Brillouin microscopy maps, i.e. on average 25 minutes after measurement start. One datum represents the mean Brillouin frequency shift or mean linewidth obtained by close-uping and averaging the 210 spectra (10 measurement columns) that are farthest to the right (unmixed mucus) or left (unmixed 25-fold TC/L in PBS or unmixed PBS) in the first Brillouin microscopy maps of each measurement sequence. Data shown as raincloud plot (left) and box plot with scatterplot (right), box/whisker plot with median (solid line), and whiskers indicate the upper and lower 25%, respectively.

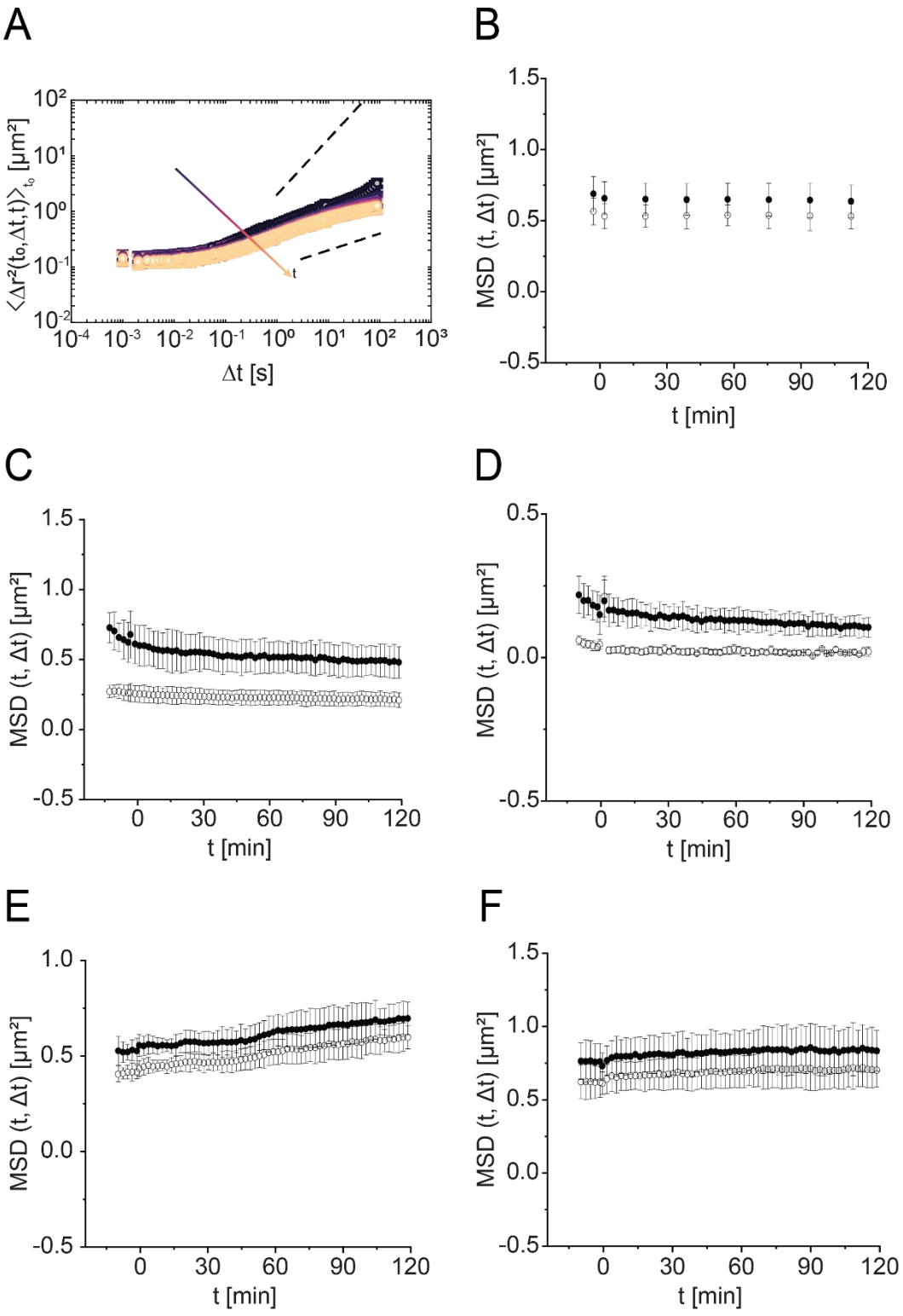

Figure S18. (A) Mean-squared displacements in dependence of lag time (Δt) and age (t) after the addition of PBS. The upper dashed line indicates a slope of Δt of 1 which indicates Brownian motion and the lower gray dashed line a slope of Δt of 0.3 which indicates the sub-diffusive state. (B-F) Mean square displacement of five independent experiments from differential dynamic microscopy in mucus exposed at t = 0 minutes to PBS for 1 second (filled) and 10 second /unfilled) time intervals (Δt). (B) is modified shown in Fig. 2G.

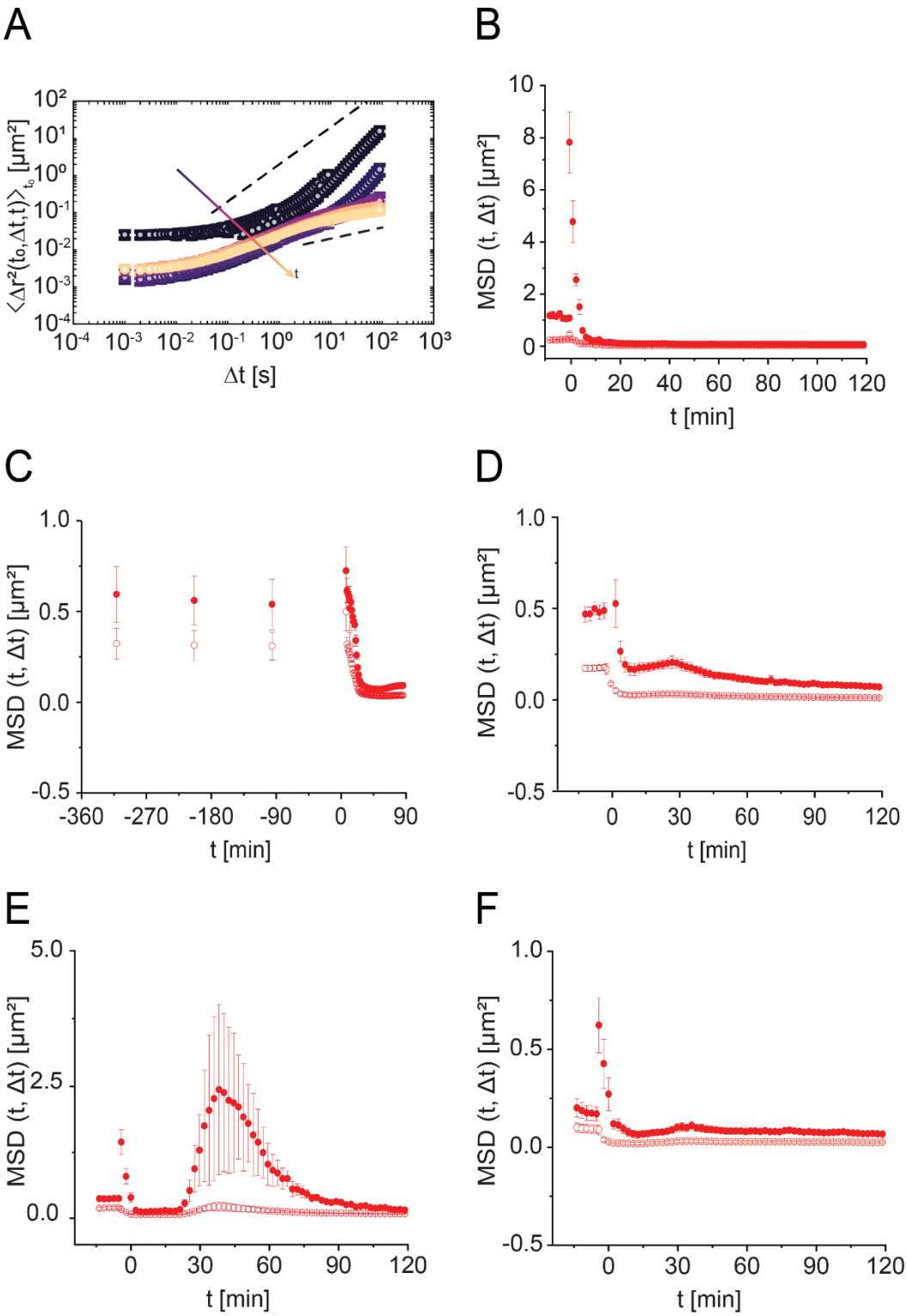

Figure S19. (A) Mean-squared displacements in dependence of lag time (Δt) and age (t) after the addition of 25-fold TC/L (corresponds to 75 mM TC and 18.75 mM L) in PBS. The upper dashed line indicates a slope of Δt of 1 which indicates Brownian motion and the lower gray dashed line a slope of Δt of 0.3 which indicates the sub-diffusive state. (B-F) Mean square displacement of five independent experiments from differential dynamic microscopy in mucus exposed at t = 0 minutes to 25-fold TC/L in PBS for 1 second (filled) and 10 second /unfilled) time intervals (Δt). (B) is modified shown in Fig. 2G.

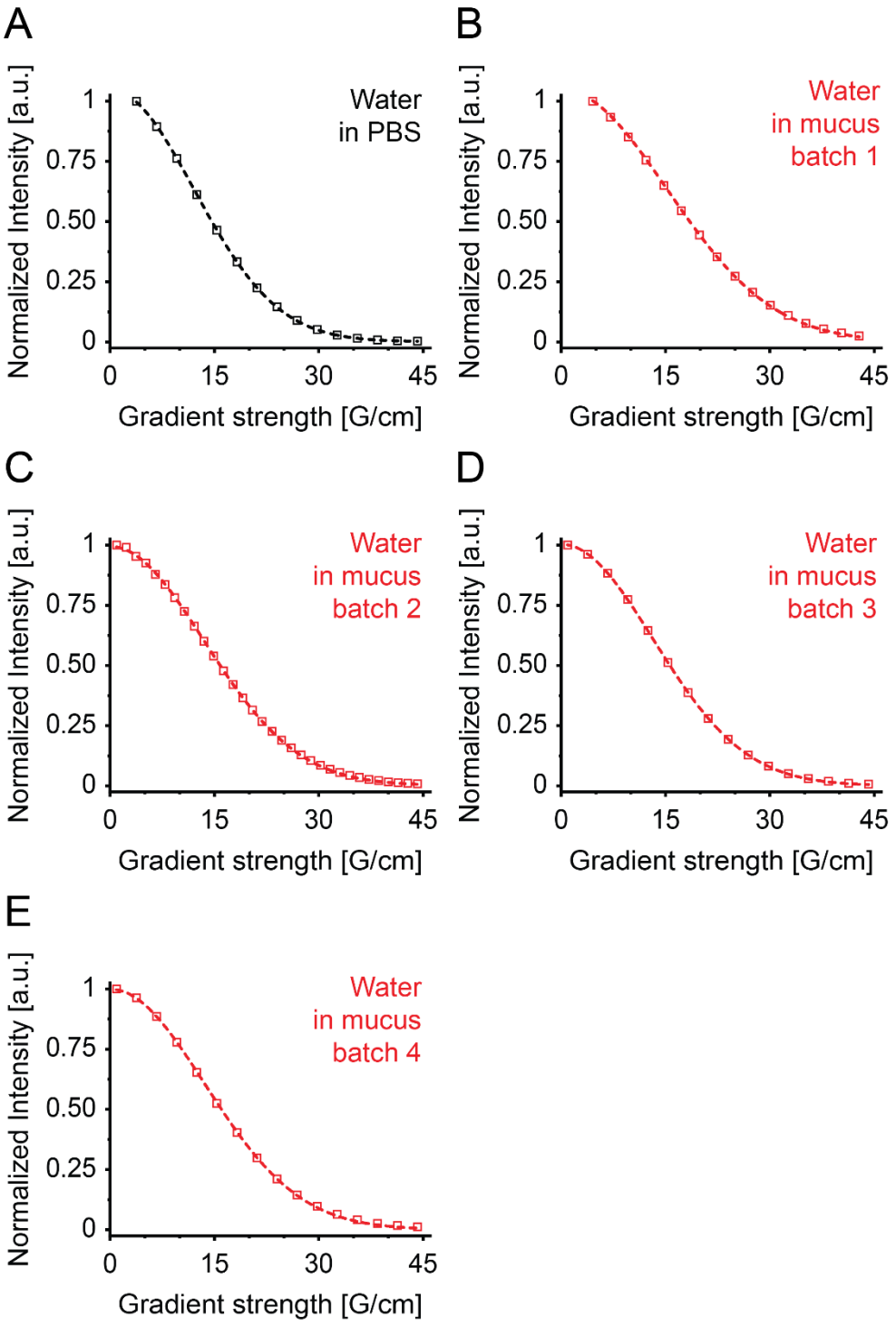

Figure S20. Water DOSY decay curves in PBS and mucus. Normalized DOSY attenuation curves of the ^{1}H NMR signal of water in (A) PBS, (B-E) mucus batch 1-4. Data points and the corresponding mono-exponential fit curves are shown by open squares and dotted lines, respectively.

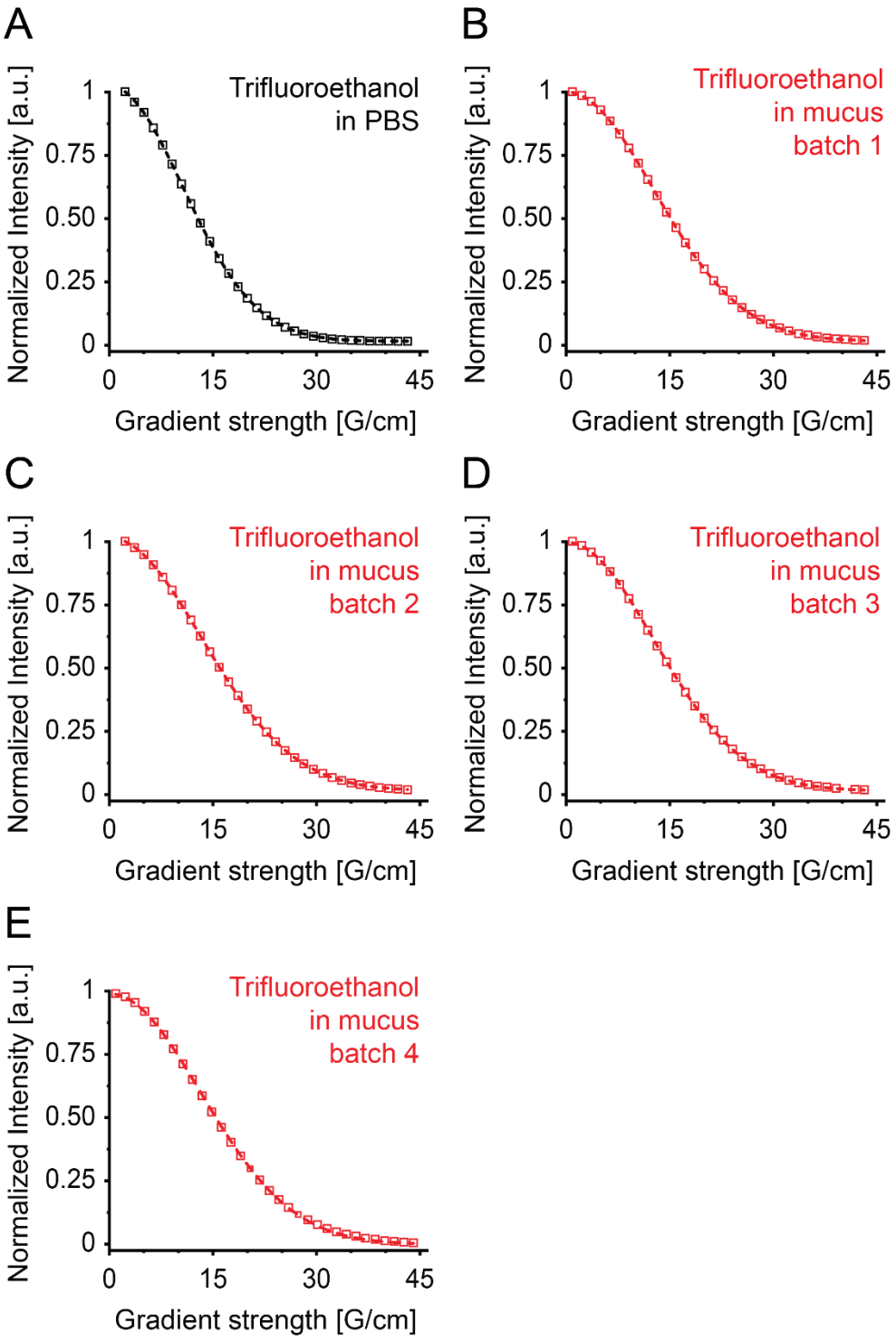

Figure S21. Trifluoroethanol DOSY decay curves in PBS and mucus. Normalized DOSY attenuation curves of the ^{19}F NMR signal of Trifluoroethanol in (A) PBS, (B-E) mucus batch 1-4. Data points and the corresponding mono-exponential fit curves are shown by open squares and dotted lines, respectively.

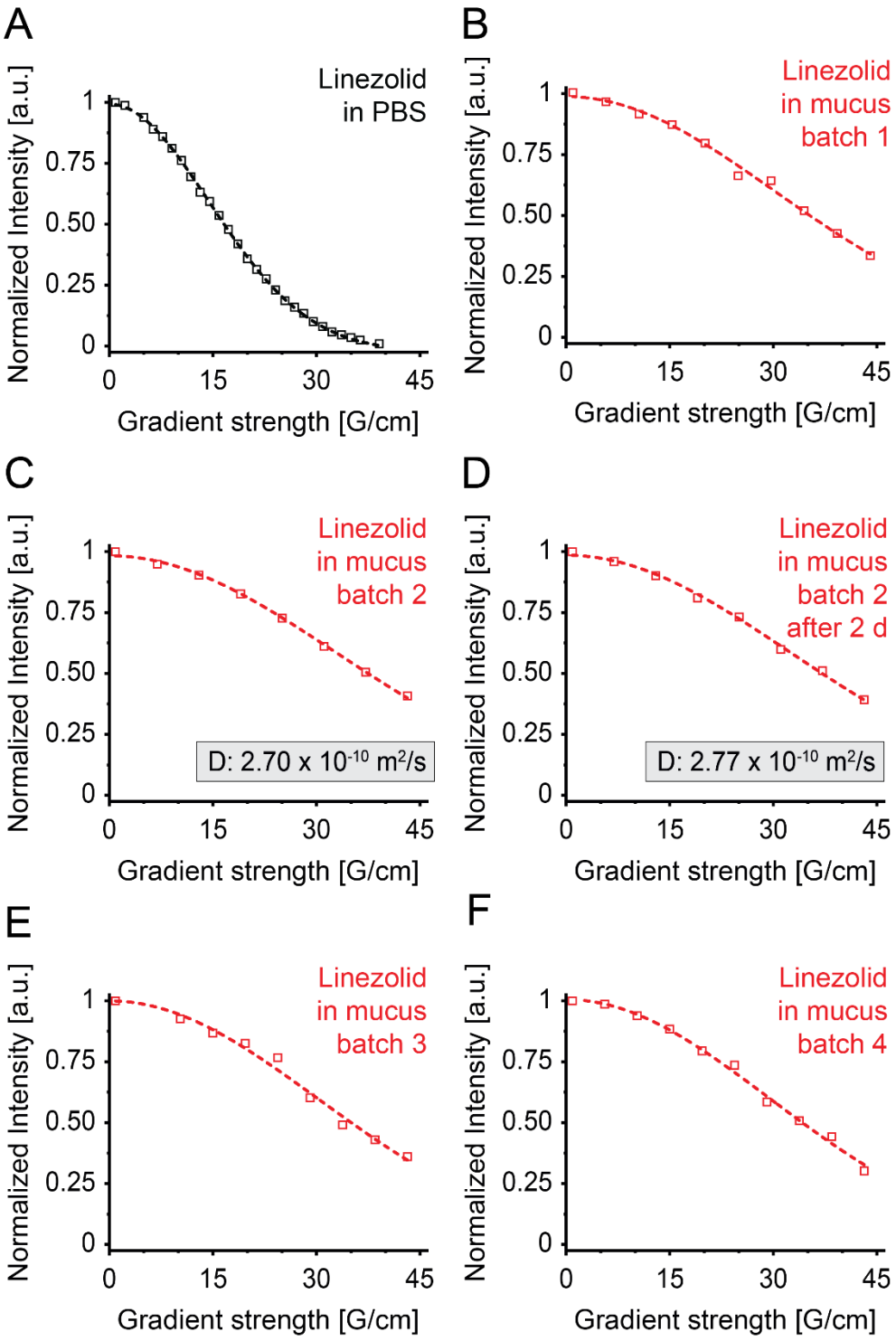

Figure S22. Linezolid DOSY decay curves in PBS and mucus. Normalized DOSY attenuation curves of the ^{19}F NMR signal of Linezolid in (A) PBS, (B, C, E, F) mucus batch 1-4, and (D) mucus batch 2 after 2 days equilibration. Data points and the corresponding mono-exponential fit curves are shown by open squares and dotted lines, respectively. The Diffusion coefficient of (C, D) is given in the grey boxes within the respective panel.

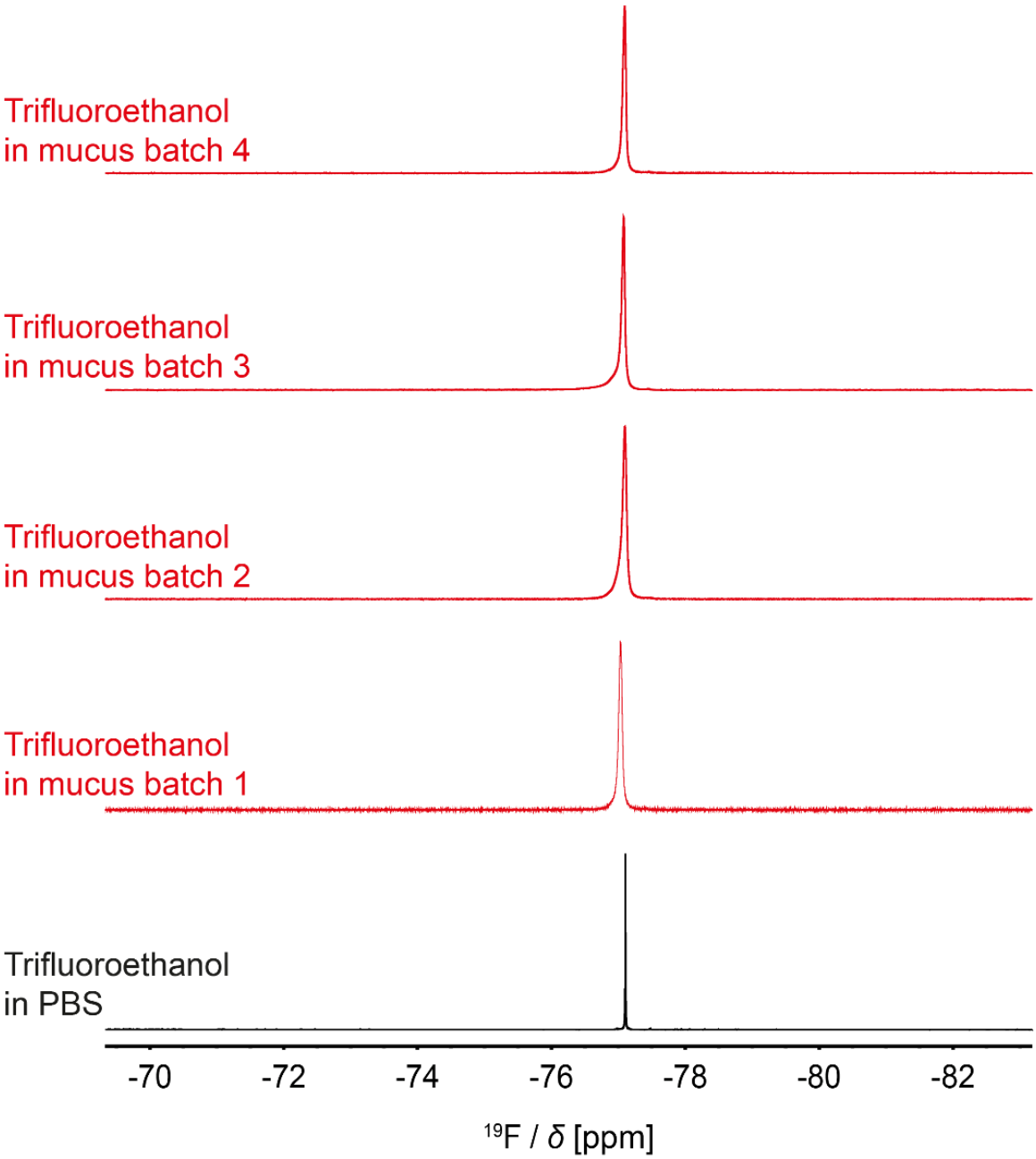

Figure S23. Close-ups of ^{19}F NMR spectra of Trifluoroethanol in PBS (black, lowest spectrum) and mucus batches 1-4 (red, in ascending batch order from second lowest spectrum to the top).

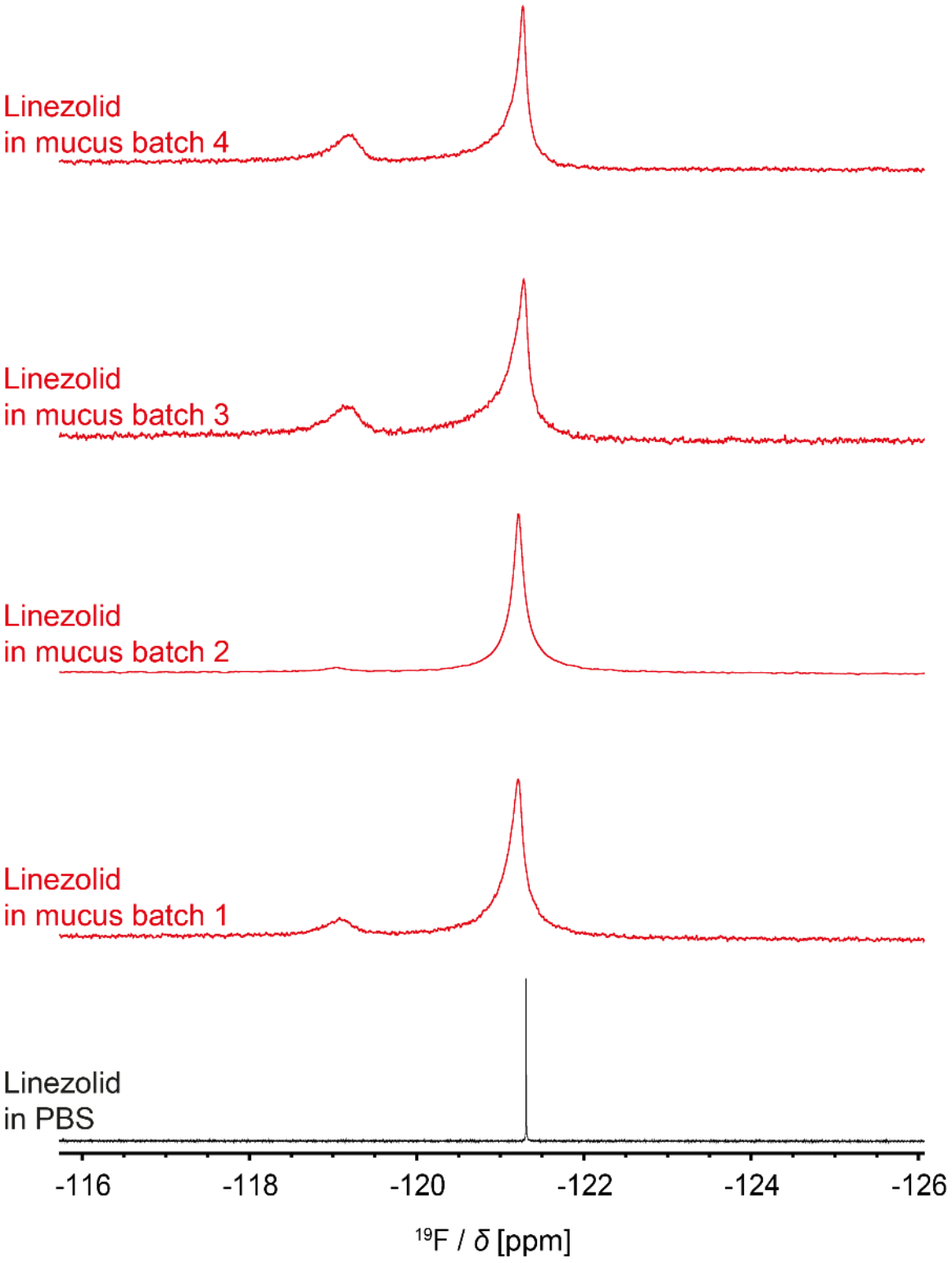

Figure S24. Close-ups of ^{19}F NMR spectra of Linezolid in PBS (black, lowest spectrum) and mucus batch 1-4 (red, in ascending batch order from second lowest spectrum to the top), respectively. The signal with a shift of ca. -121 ppm was used to determine the DOSY decay curves.

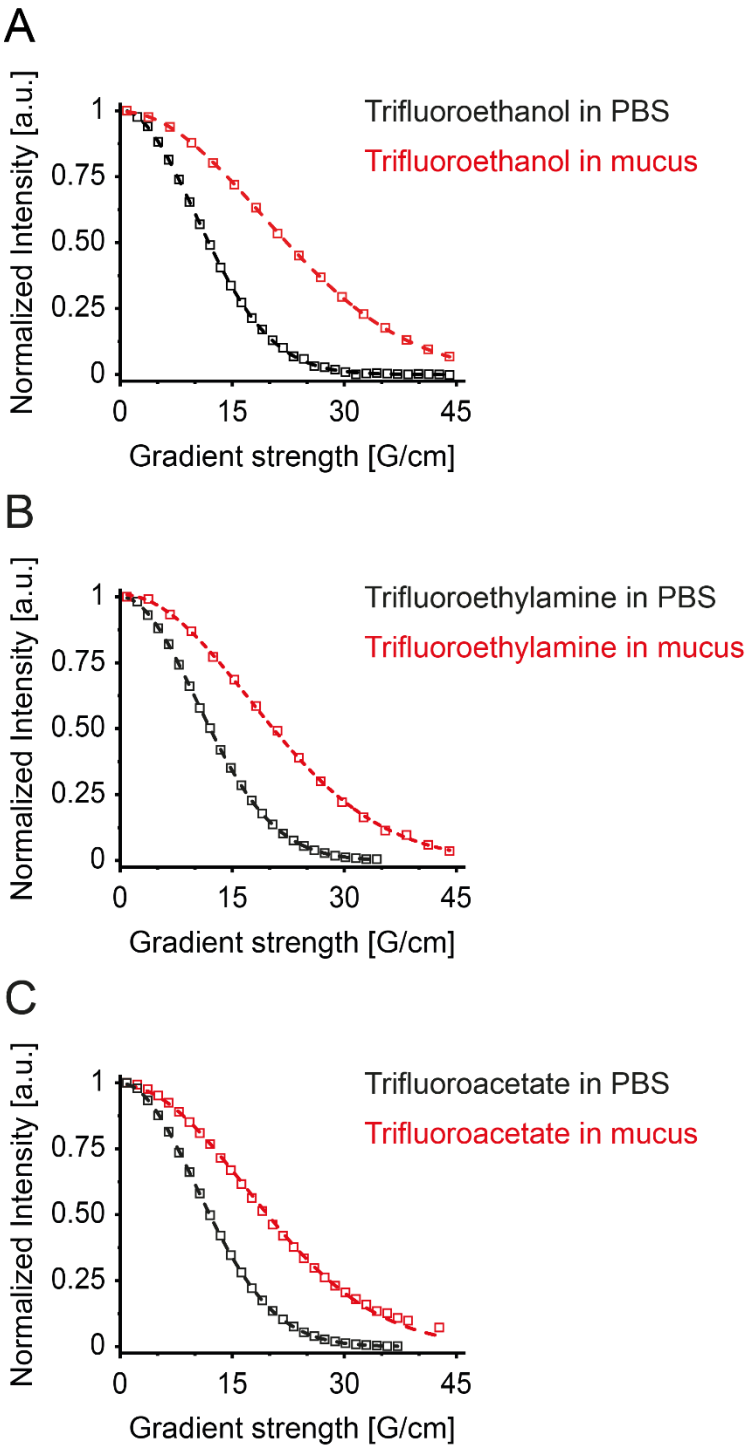

Figure S25. Normalized DOSY attenuation curves of the ^{19}F NMR signal of (A) Trifluoroethanol, (B) Trifluoroethylamine, and (C) Trifluoroacetate in PBS (black) and mucus (red). Data points and the corresponding mono-exponential fit curves are shown by open squares and dotted lines, respectively.

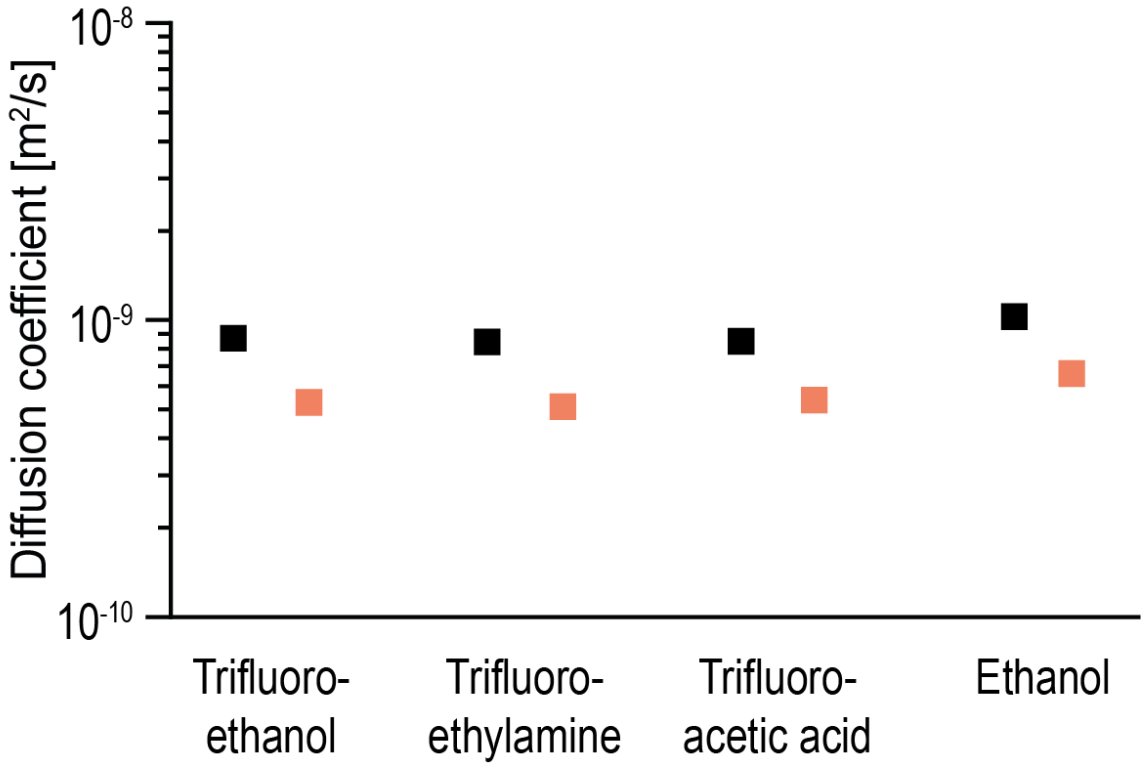

Figure S26. DOSY-diffusion coefficients of Trifluoroethly compounds in PBS (black) and mucus (orange).

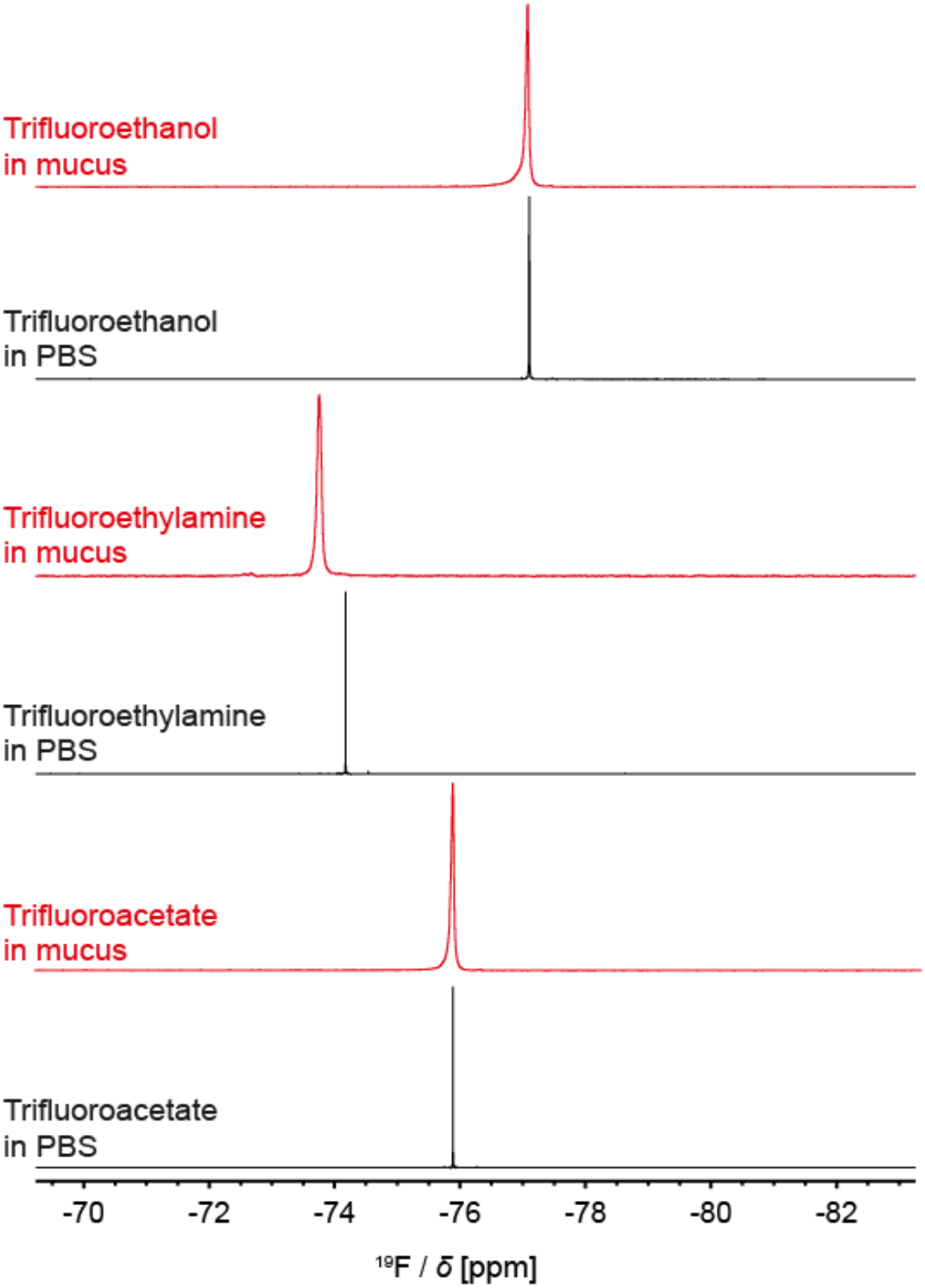

Figure S27. Close-ups of ^{19}F NMR spectra of Trifluoroethanol, Trifluoroethylamine, and Trifluoroacetate, in mucus (red) and in PBS (black).

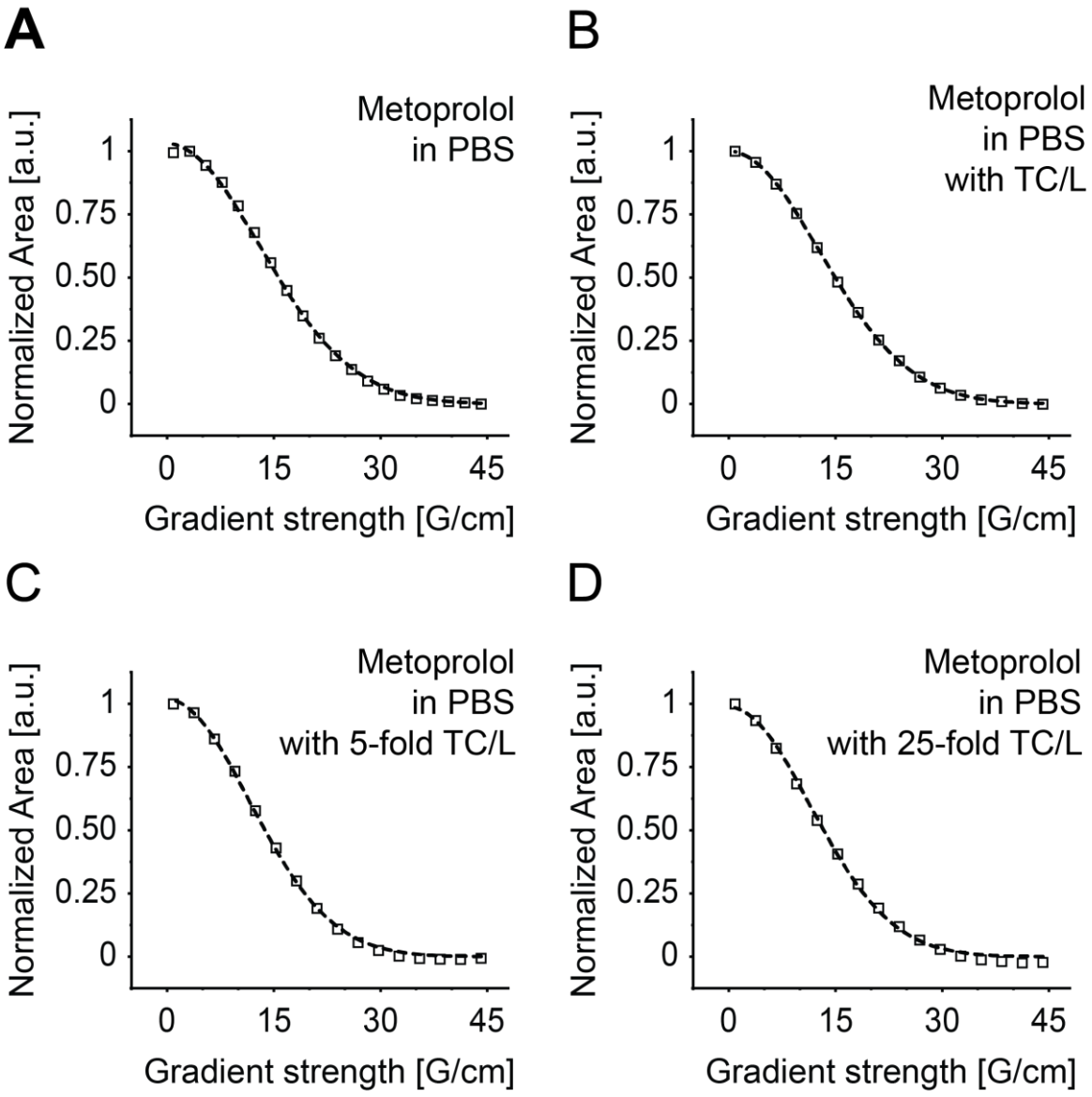

Figure S28. Metoprolol DOSY decay curves in PBS. Normalized DOSY attenuation curves of the aromatic ^{1}H NMR signals of Metoprolol in (A) PBS, (B) in TC/L in PBS, (C) 5-fold TC/L in PBS, and (D) 25-fold TC/L in PBS. Data points and the corresponding mono-exponential fit curves are shown by open squares and dotted lines, respectively. 1-fold TC/L corresponds to 3 mM TC and 0.75 mM L.

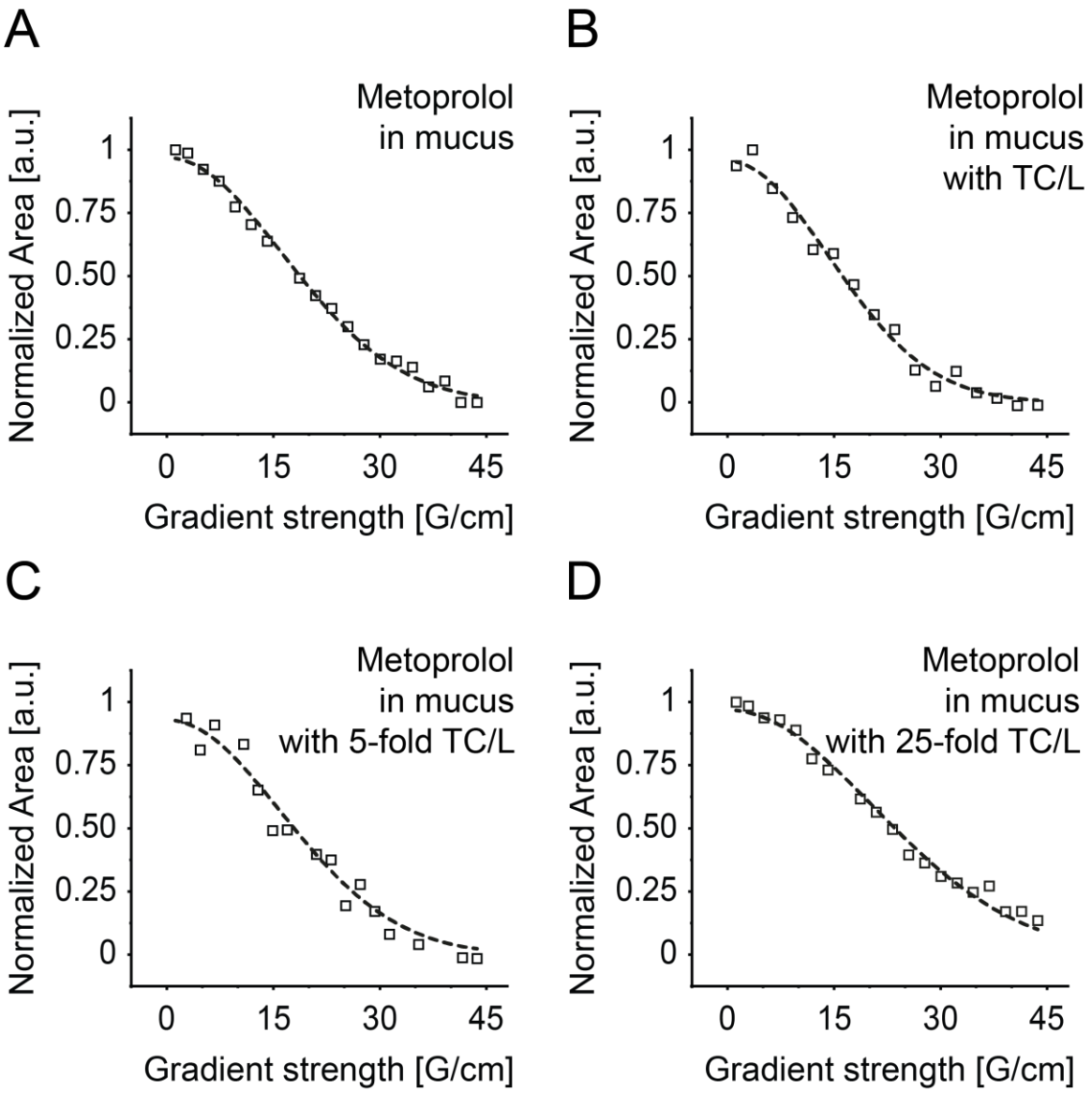

Figure S29. Metoprolol DOSY decay curves in mucus. Normalized DOSY attenuation curves of the ^{1}H-^{13}C-HSQC NMR signal of Metoprolol H18/H19 in (A) mucus, (B) mucus with TC/L, (C) mucus with 5-fold TC/L, and (D) mucus with 25-fold TC/L. Data points and the corresponding mono-exponential fit curves are shown by open squares and dotted lines, respectively. 1-fold TC/L corresponds to 3 mM TC and 0.75 mM L.

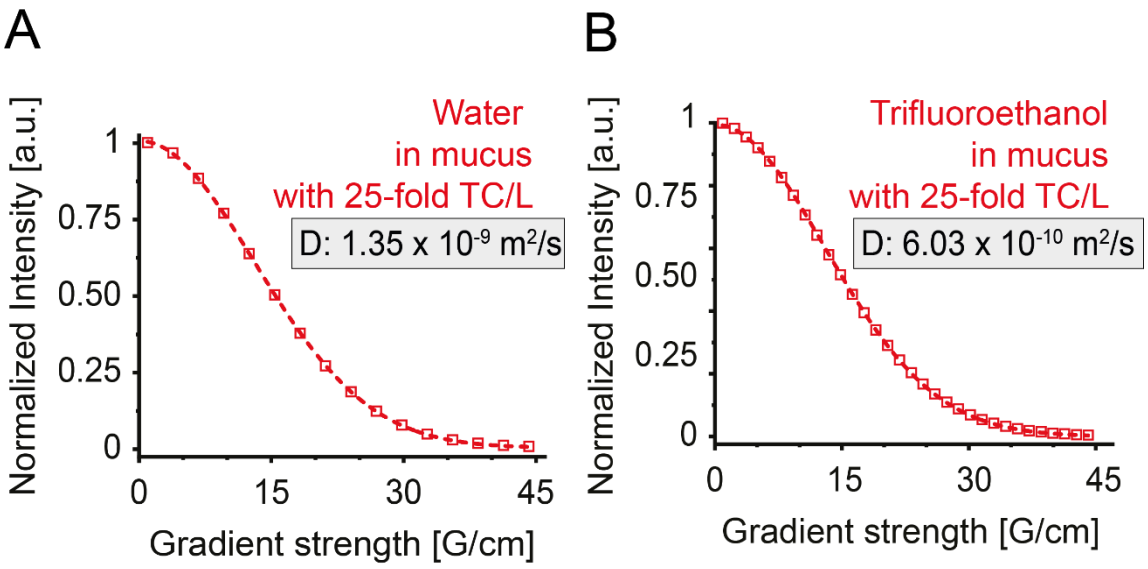

Figure S30. Normalized DOSY attenuation curves of the (A) ^{1}H NMR signal of water and (B) ^{19}F NMR signal of Trifluoroethanol, respectively. Data points and the corresponding mono-exponential fit curves are shown by open squares and dotted lines, respectively. 1-fold TC/L corresponds to 3 mM TC and 0.75 mM L.

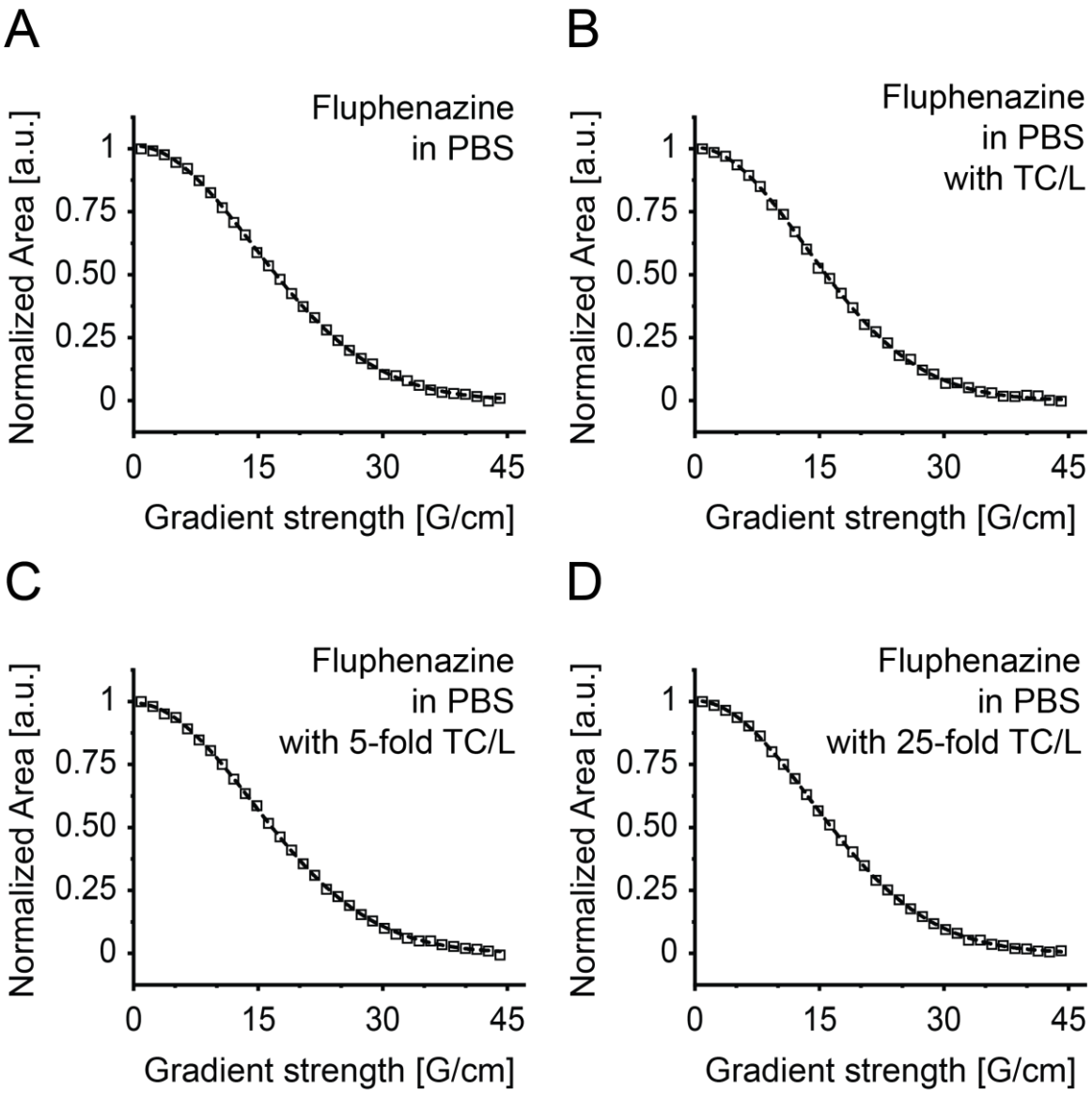

Figure S31. Normalized DOSY attenuation curves of the ^{19}F NMR signal of Fluphenazine in (A) PBS, (B) TC/L in PBS, (C) 5-fold TC/L in PBS, and (D) 25-fold TC/L in PBS. Data points and the corresponding mono-exponential fit curves are shown by open squares and dotted lines, respectively. 1-fold TC/L corresponds to 3 mM TC and 0.75 mM L.

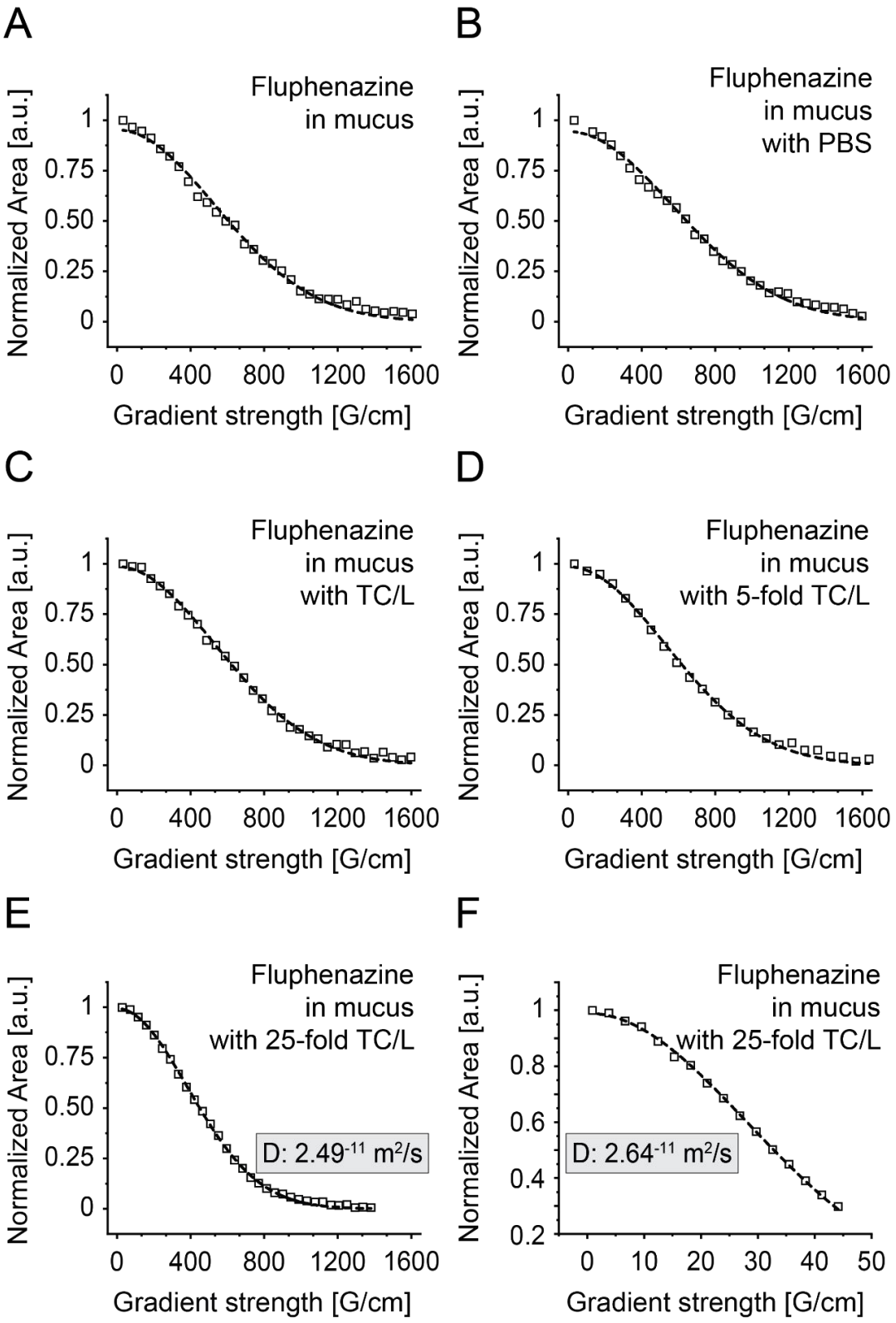

Figure S32. Normalized DOSY attenuation curves of the ^{19}F NMR signal of Fluphenazine in (A) mucus, (B) mucus with PBS, (C) mucus with TC/L, (D) mucus with 5-fold TC/L, and (E, F) two separate samples of mucus with 25-fold TC/L. (F) was measured with a different spectrometer than (A-E). Data points and the corresponding mono-exponential fit curves are shown by open squares and dotted lines, respectively. 1-fold TC/L corresponds to 3 mM TC and 0.75 mM L.

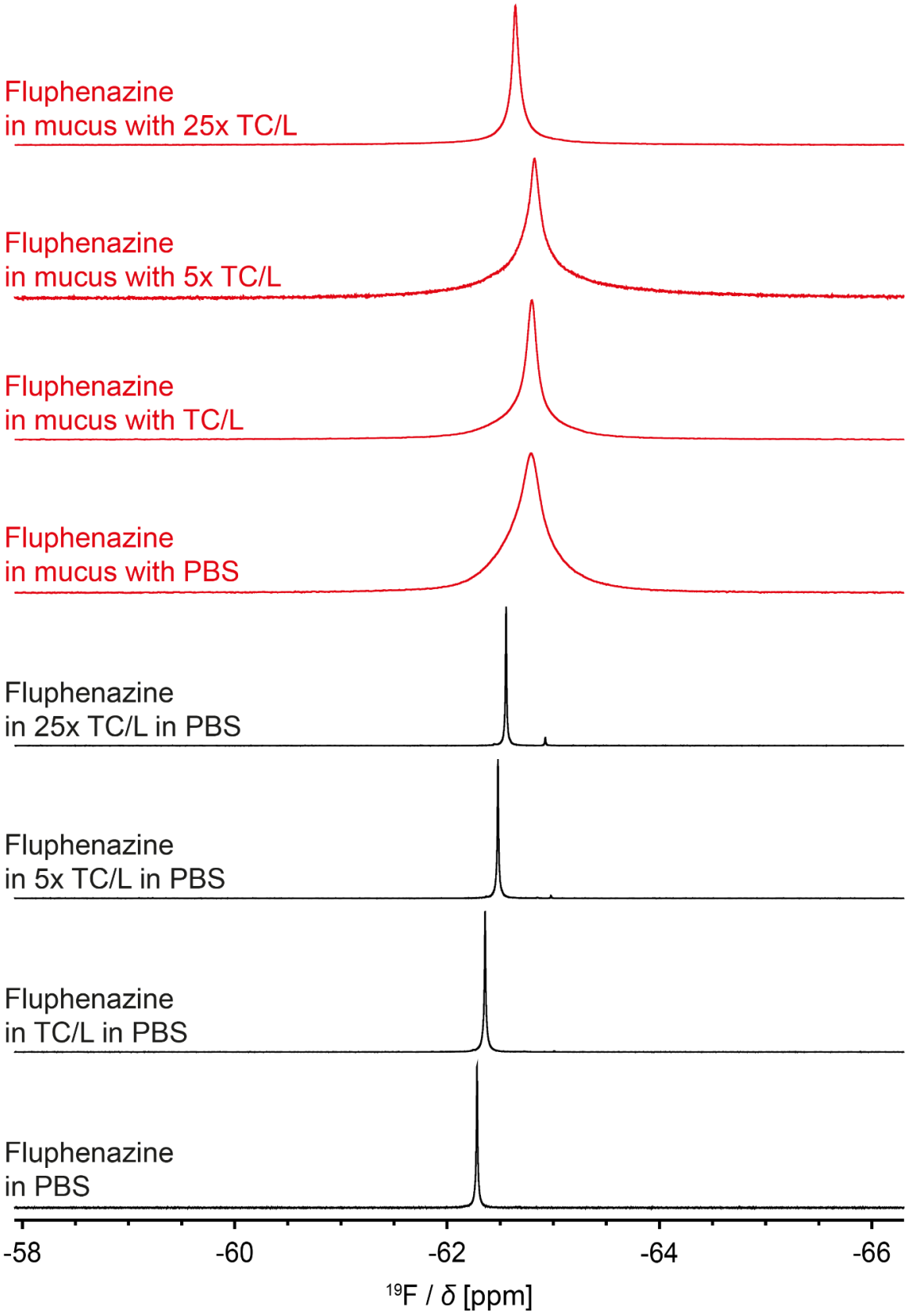

Figure S33. Close-ups of Fluphenazine ^{19}F NMR spectra in PBS (black) and mucus (red) at TC/L concentrations as indicated. 1-fold TC/L corresponds to 3 mM TC and 0.75 mM L. Extracts of these spectra are shown in Fig. 3E.

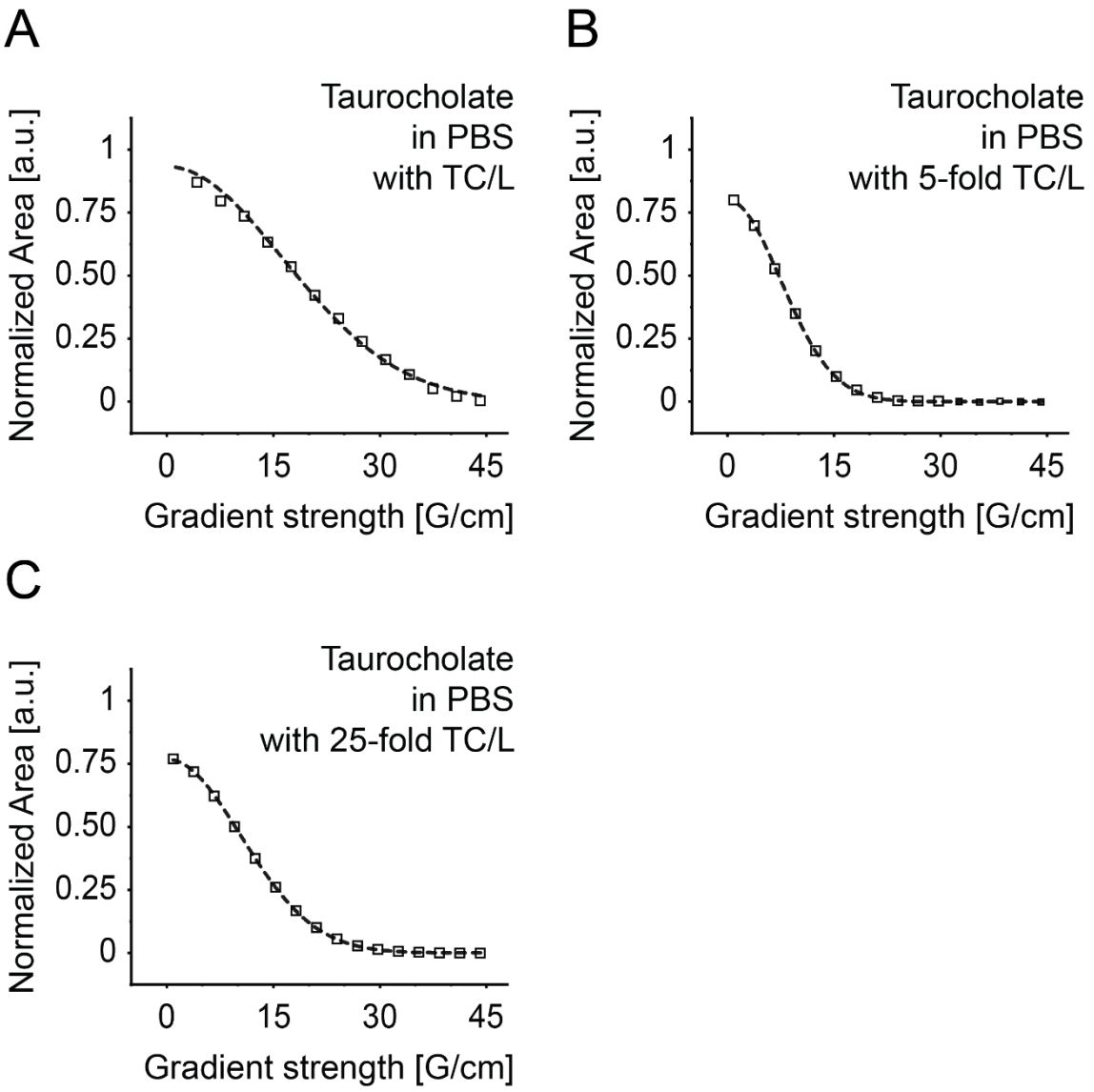

Figure S34. Normalized DOSY attenuation curves of the ^{1}H-^{13}C-HSQC NMR signal of Taurocholate H26 in (A) TC/L in PBS, (B) 5-fold TC/L in PBS, and (C) 25-fold TC/L in PBS. Data points and the corresponding mono-exponential fit curves are shown by open squares and dotted lines, respectively. 1-fold TC/L corresponds to 3 mM TC and 0.75 mM L.

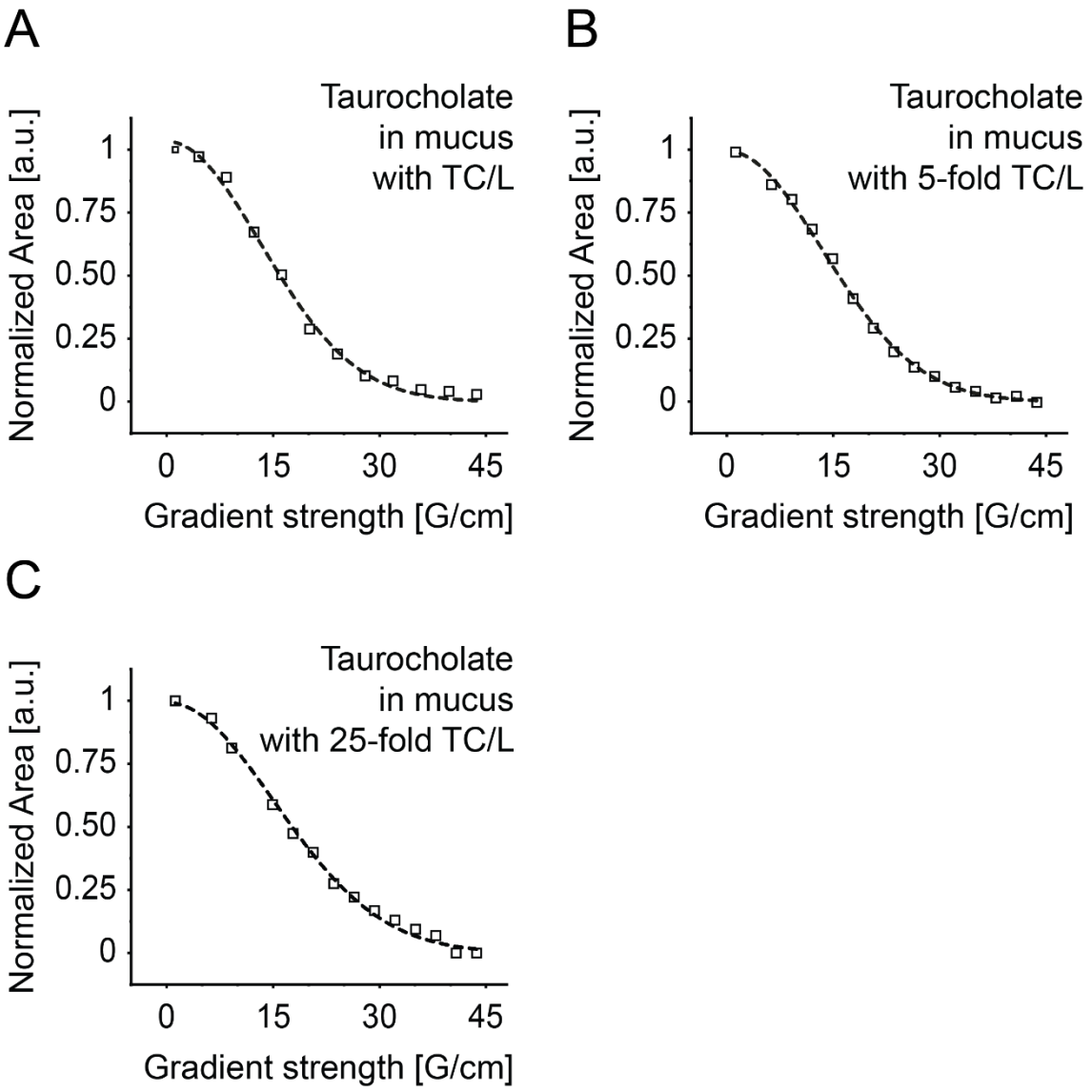

Figure S35. Normalized DOSY attenuation curves of the ^{1}H-^{13}C-HSQC NMR signal of Taurocholate H26 in (A) TC/L in mucus, (B) 5-fold TC/L in mucus, and (C) 25-fold TC/L in mucus. Data points and the corresponding mono-exponential fit curves are shown by open squares and dotted lines, respectively. 1-fold TC/L corresponds to 3 mM TC and 0.75 mM L.

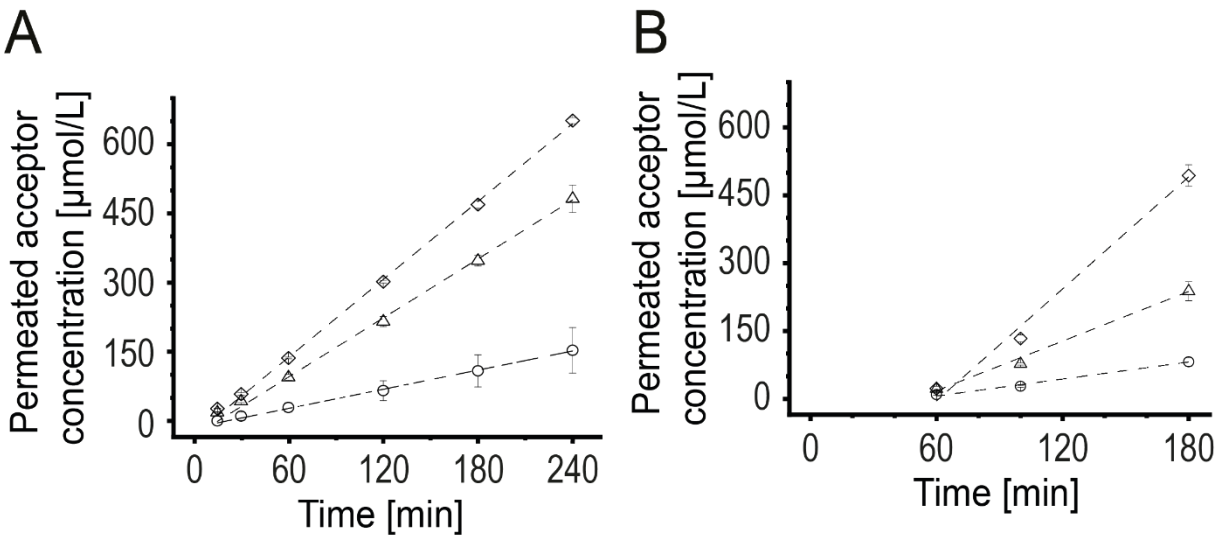

Figure S36. Time-concentration profiles of Taurocholate permeation across a (A) cellulose membranes and (B) mucus. Taurocholate concentration in the receiver compartment over time in PBS (square), TC/L in PBS (circle), 5-fold TC/L in PBS (triangles), and in 25-fold TC/L in PBS (open diamonds). Data shown as mean ± standard deviation, linear fits are shown by dashed lines. 1-fold TC/L corresponds to 3 mM TC and 0.75 mM L.

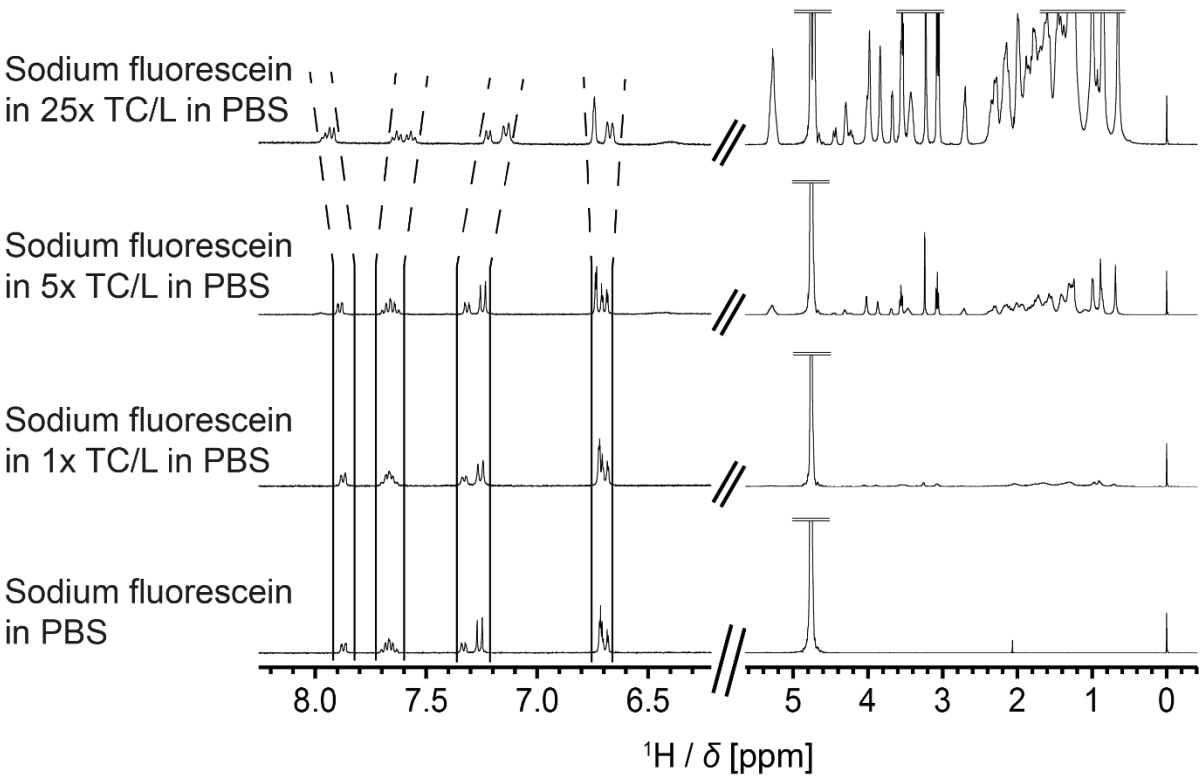

Figure S37. Close-ups of ^{1}H NMR spectra of Fluphenazine in 25-fold TC/L in PBS, 5-fold TC/L in PBS, TC/L in PBS, and in PBS (from the top to the lowest), respectively. 1-fold TC/L corresponds to 3 mM TC and 0.75 mM L.

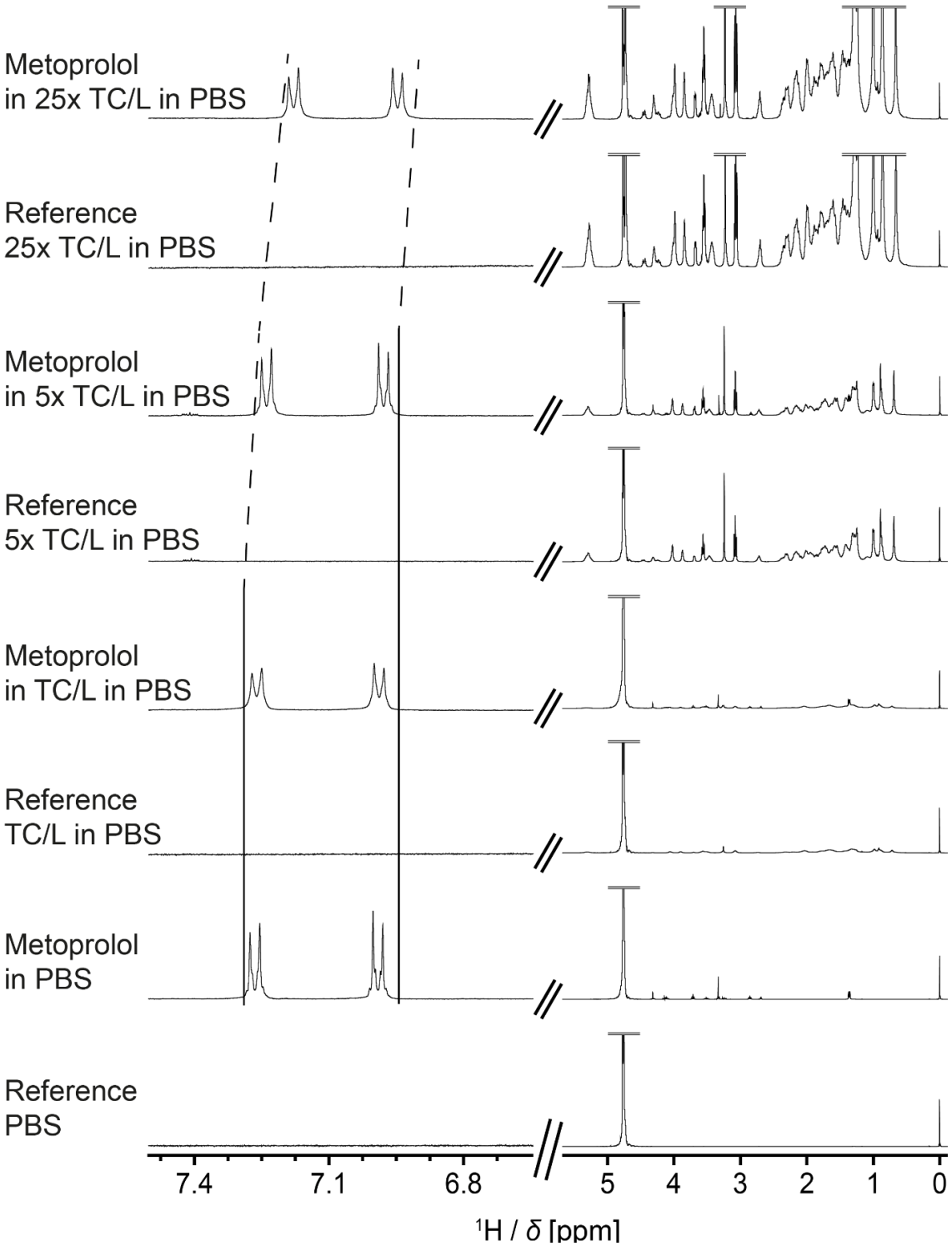

Figure S38. Close-ups of ^{1}H NMR spectra of Metoprolol in 25-fold TC/L in PBS, 5-fold TC/L in PBS, TC/L in PBS, and in PBS (every second spectrum from the top to the second lowest), respectively and of 25-fold TC/L in PBS, 5-fold TC/L in PBS, TC/L in PBS, and PBS (every second spectrum from the second top to the lowest). Dotted lines indicate shifts. The ^{1}H aromatic resonances of Metoprolol shifted in PBS at higher TC/L concentration compared to those of Perphenazine and Fluphenazine, referenced to the respective PBS spectra. 1-fold TC/L corresponds to 3 mM TC and 0.75 mM L.

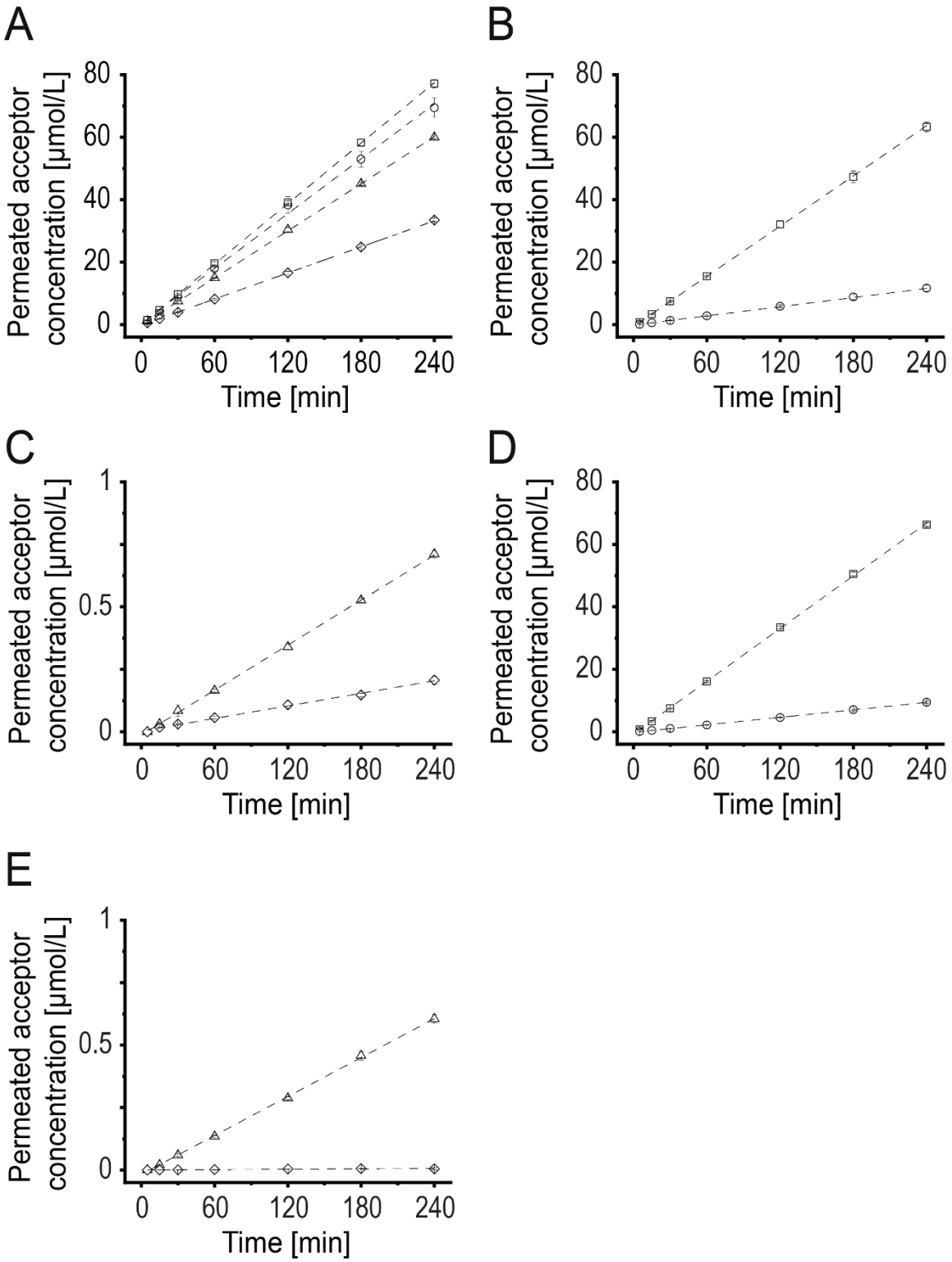

Figure S39. Time-concentration profiles of permeation experiments across cellulose membranes for drug substances. A) Metoprolol, (B, C) Perphenazine, (D, E) Fluphenazine concentration in the receiver compartment over time in PBS (squares), TC/L in PBS (circles), 5-fold TC/L in PBS (up-pointing triangles), and in 25-fold TC/L in PBS (diamonds). Data shown as mean ± standard deviation, n = 3, linear fits are shown by dashed lines. Previously, the profiles of metoprolol and perphenazine were reported[6], except in 25-fold TC/L in PBS. 1-fold TC/L corresponds to 3 mM TC and 0.75 mM L.

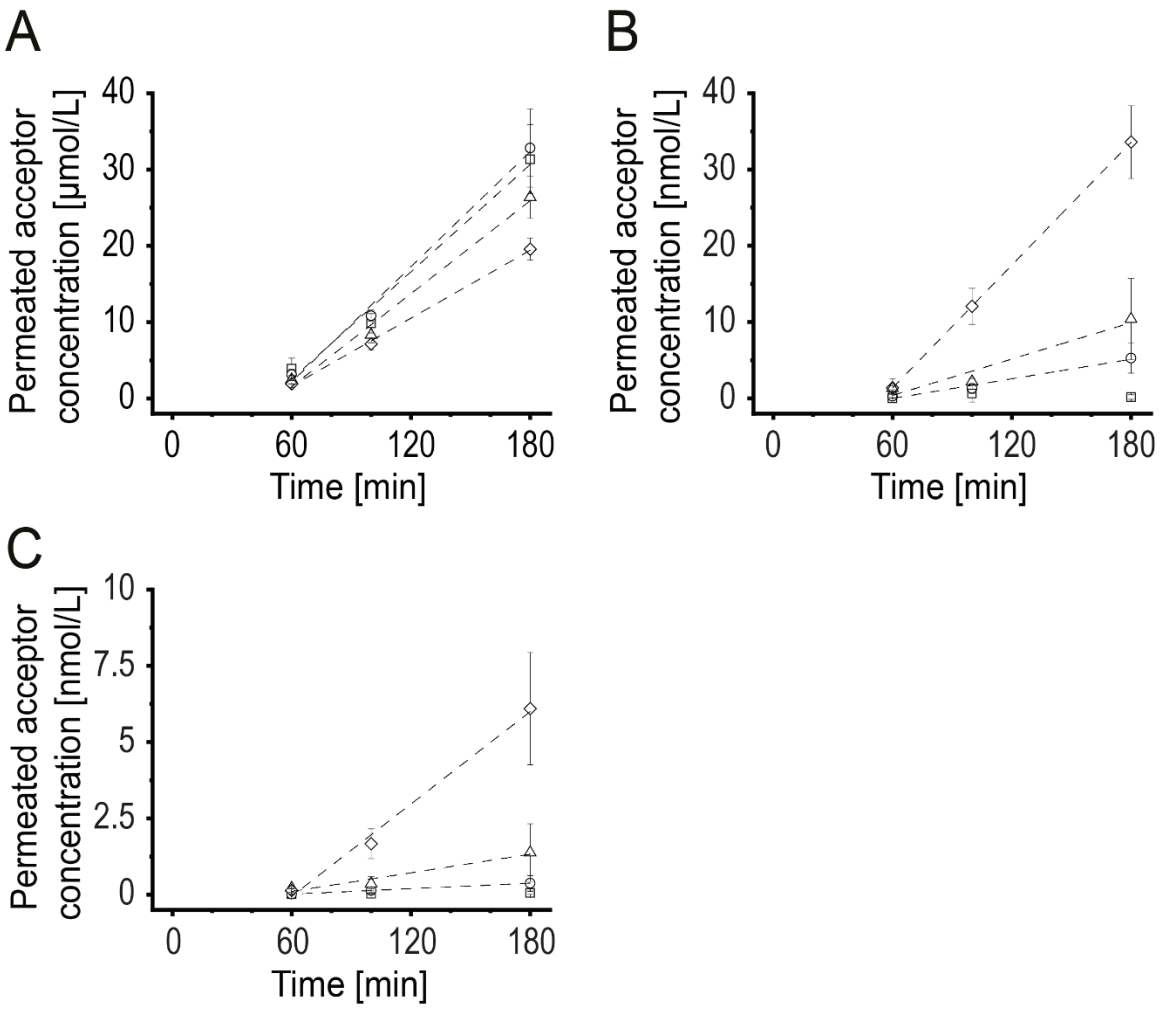

Figure S40. Time-concentration profiles of permeation experiments across mucus for drug substances. (A) Metoprolol, (B) Perphenazine, and (C) Fluphenazine concentration in the receiver compartment over time in PBS (squares), TC/L in PBS (circles), 5-fold TC/L in PBS (triangles), and in 25-fold TC/L in PBS (diamonds). Data shown as mean ± standard deviation, n = 3, linear fits are shown by dashed lines. 1-fold TC/L corresponds to 3 mM TC and 0.75 mM L.

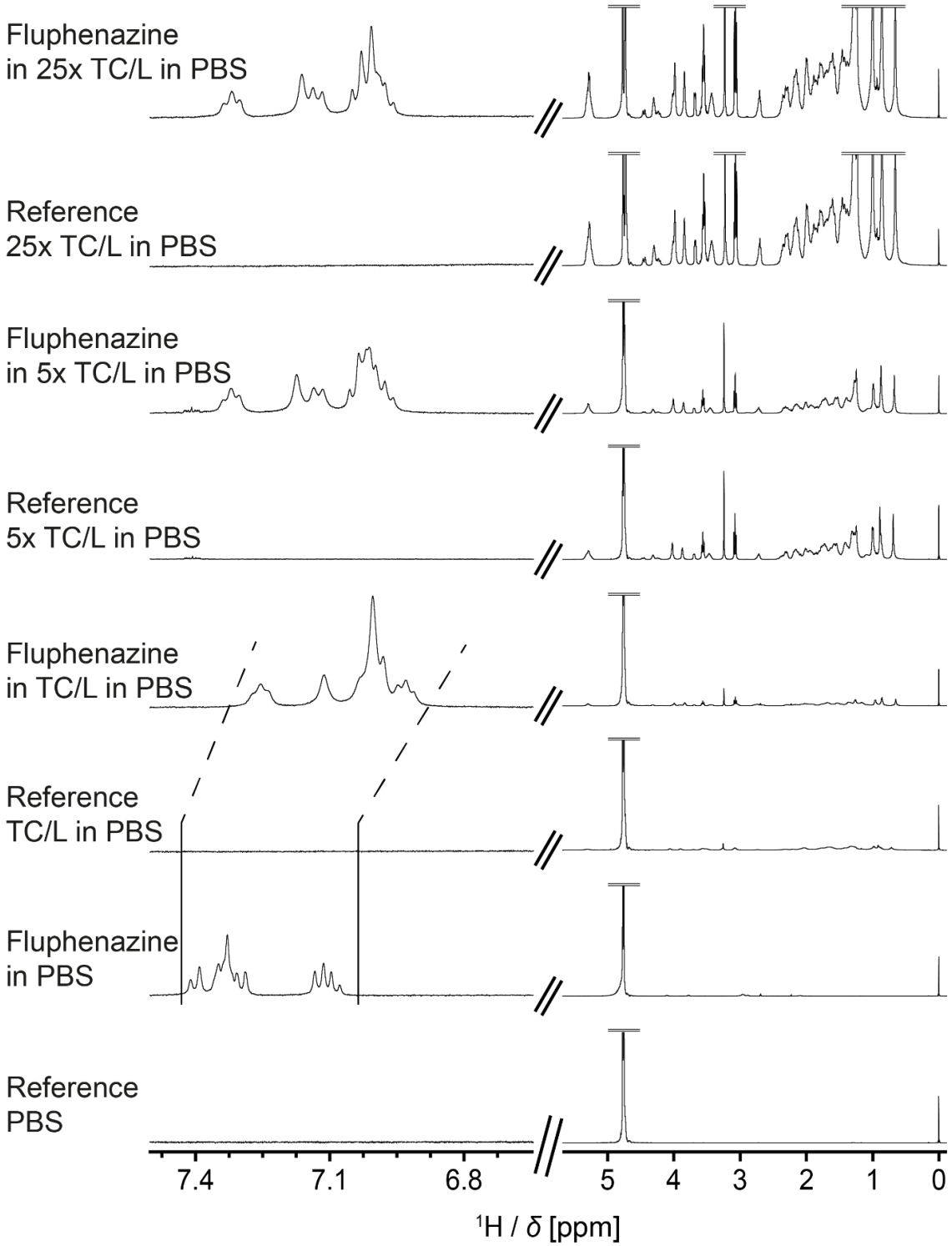

Figure S41. Close-ups of ^{1}H NMR spectra of Fluphenazine in 25-fold TC/L in PBS, 5-fold TC/L in PBS, TC/L in PBS, and in PBS (every second spectrum from the top to the second lowest), respectively and of 25-fold TC/L in PBS, 5-fold TC/L in PBS, TC/L in PBS, and PBS (every second spectrum from the second top to the lowest). Dotted lines indicate shifts. The ^{1}H aromatic resonances of Fluphenazine shifted in PBS at lower TC/L concentration compared to those of Metoprolol, referenced to the respective PBS spectra. 1-fold TC/L corresponds to 3 mM TC and 0.75 mM L

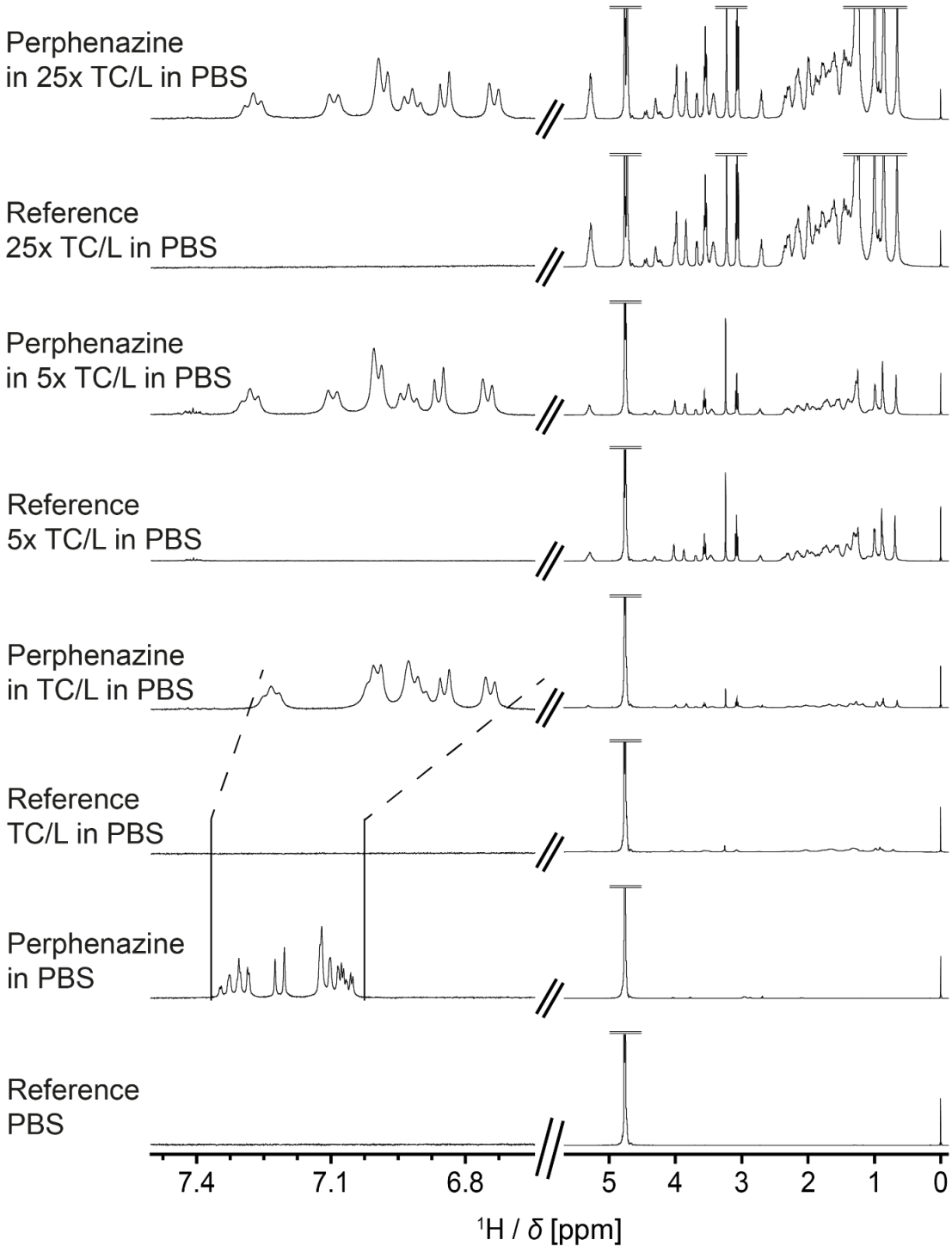

Figure S42. Close-ups of ^{1}H NMR spectra of Perphenazine in 25-fold TC/L in PBS, 5-fold TC/L in PBS, TC/L in PBS, and in PBS (every second spectrum from the top to the second lowest), respectively and of ^{1}H NMR spectra of 25-fold TC/L in PBS, 5-fold TC/L in PBS, TC/L in PBS, and PBS (every second spectrum from the second top to the lowest). Dotted lines indicate shifts. The ^{1}H aromatic resonances of Perphenazine shifted in PBS at lower TC/L concentration compared to those of Metoprolol, referenced to the respective PBS spectra. 1-fold TC/L corresponds to 3 mM TC and 0.75 mM L.

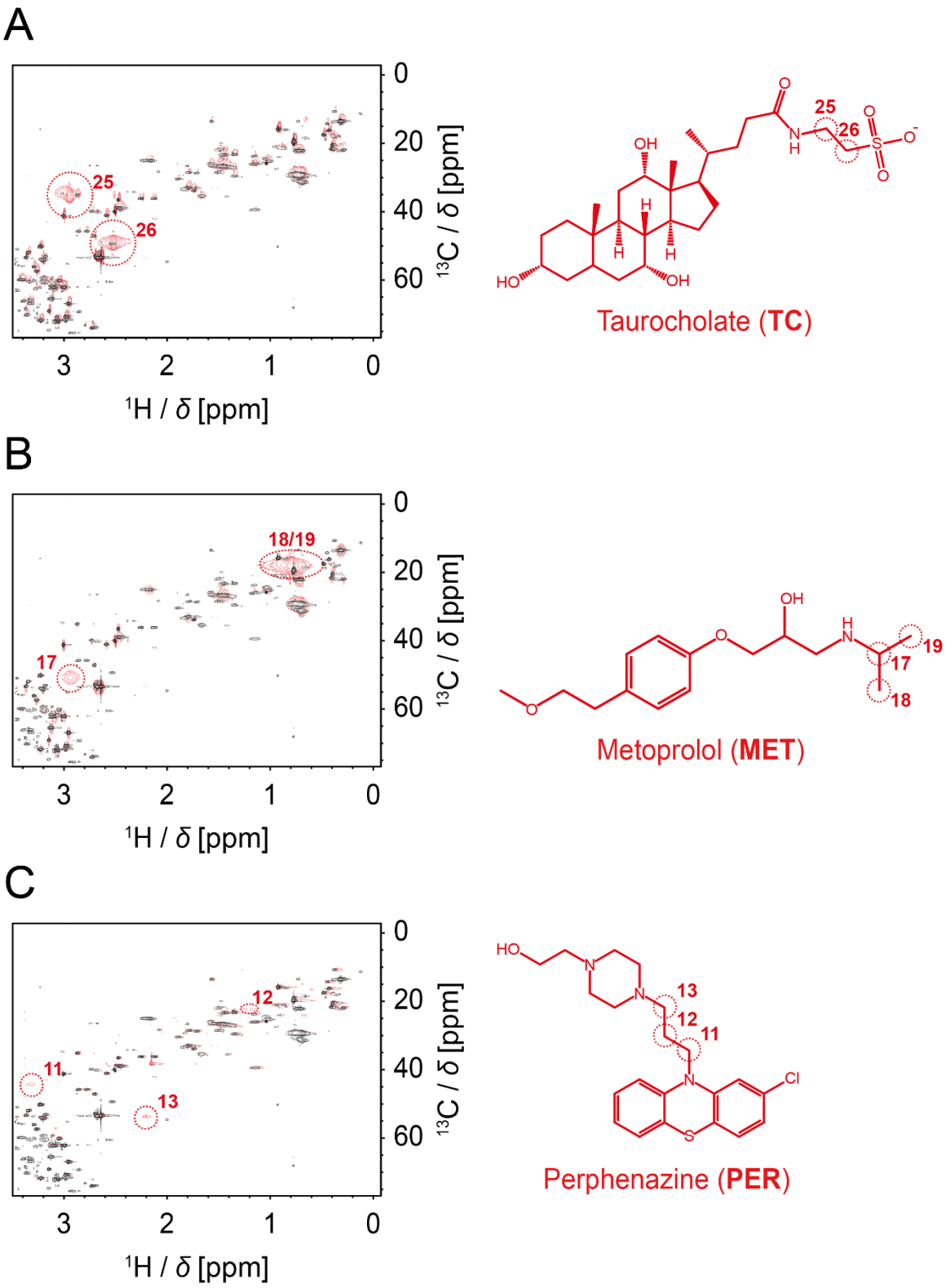

Figure S43. ^{1}H-^{13}C-HSQC-spectra of (A) Taurocholate, (B) Metoprolol, and (C) Perphenazine in mucus (red, left side; ^{1}H-^{13}C-HSQC-spectrum of mucus (black) is given for comparison in each panel) The molecular structures with numbering are given on the right side. The NMR signals of the ^{13}C nuclei are highlighted by red circles and numbered.

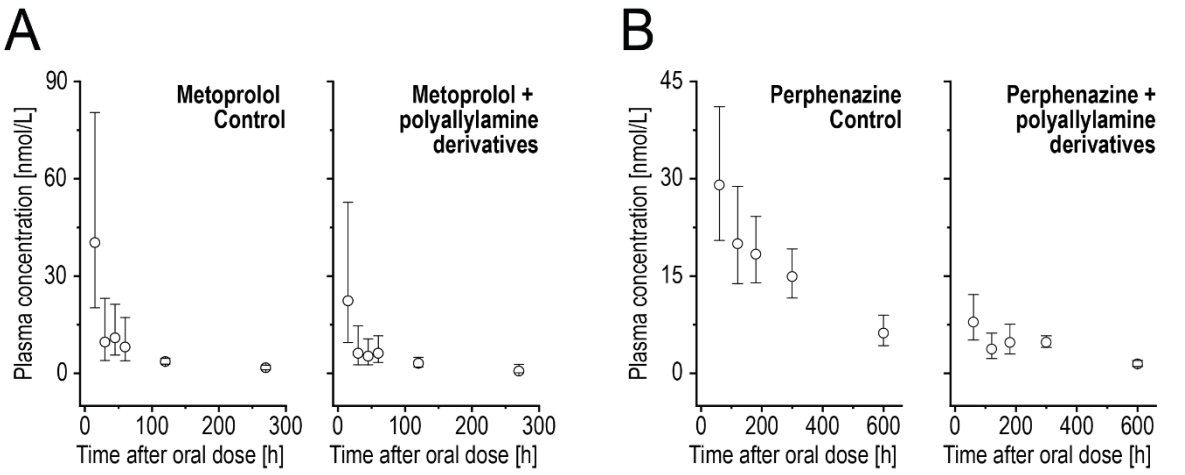

Figure S44. (A) Metoprolol and (B) Perphenazine plasma-time curves in rats after oral administration of 10 µmol/kg drug substance in PBS (left, control) and with polyallylamine derivatives (right). Data shown as geometric mean ± geometric standard deviation, n = 5. One rat in the Perphenazine control group was excluded from analysis as it was not pre-treated with Omeprazole.

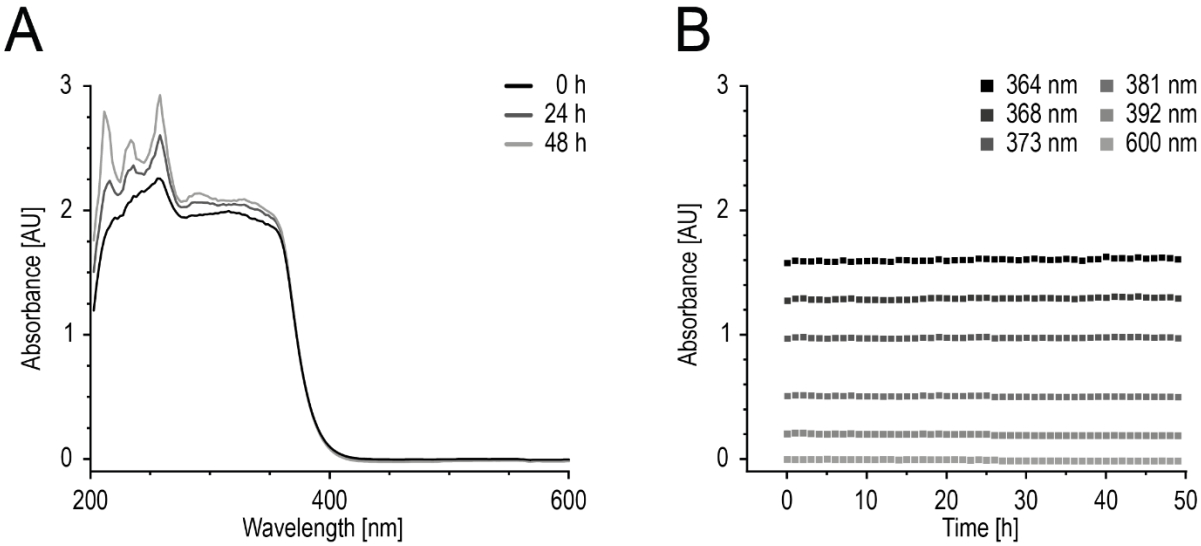

Figure S45. (A) UV spectra of 4 mM Perphenazine in PBS after 0 h, 24 h, and 48 h (black to gray) and (B) absorbance at 364 nm, 368 nm, 373 nm, 381 nm, 392 nm, and 600 nm (black to gray) over time. The spectra were recorded using a Sirius T3 instrument with the stirrer controlled to 30% and at room temperature. The integration time was 27 ms, 25 scans per time point were averaged.

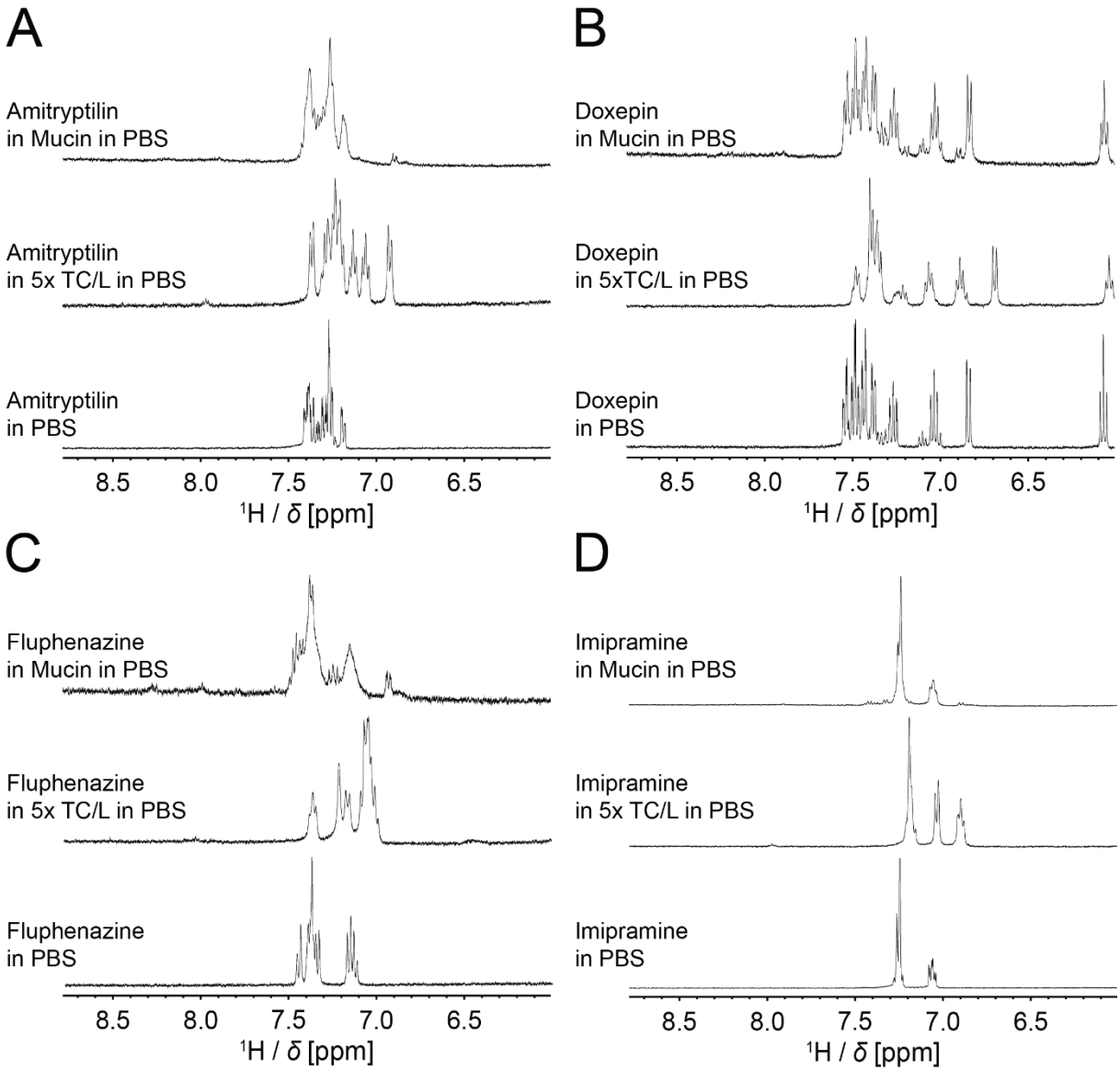

Figure S46. Extracts from the ^{1}H NMR spectra of region II drug compounds. (A) Amitriptyline, (B) Doxepin, (C) Fluphenazine, and (D) Imipramine in PBS (bottom), in 5-fold TC/L in PBS (middle), and Mucin in PBS (top). 5-fold TC/L corresponds to 15 mM TC and 3.75 mM L. Mucin in PBS was prepared by dissolving 0.2 g mucin from porcine stomach type II (Merck) in 100 mL PBS.

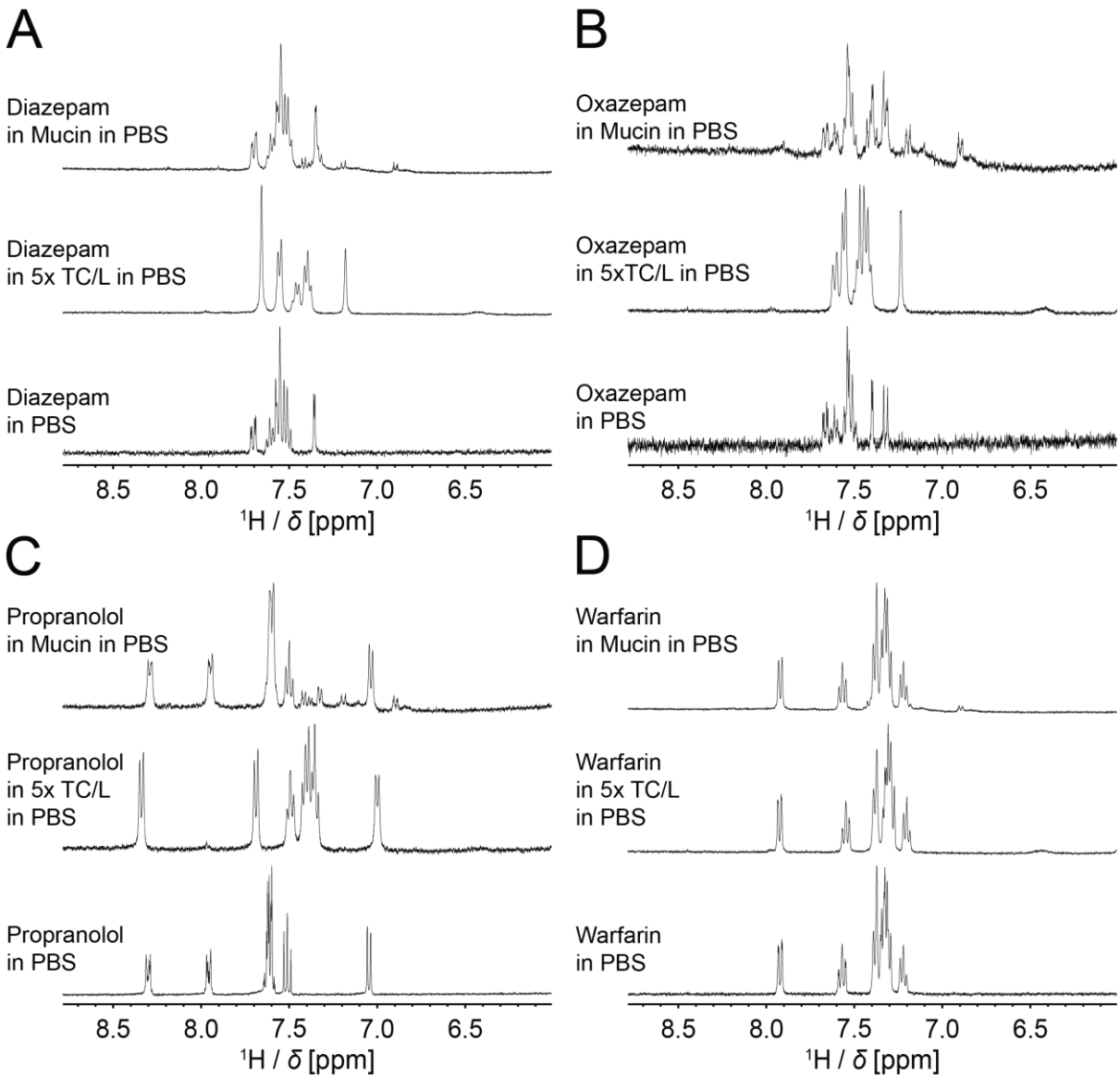

Figure S47. Extracts from the ^{1}H NMR spectra of region III drug compounds. (A) Diazepam, (B) Oxazepam, (C) Propranolol, and (D) Warfarin in PBS (bottom), in 5-fold TC/L in PBS (middle), and Mucin in PBS (top). 5-fold TC/L corresponds to 15 mM TC and 3.75 mM L. Mucin in PBS was prepared by dissolving 0.2 g mucin from porcine stomach type II (Merck) in 100 mL PBS.

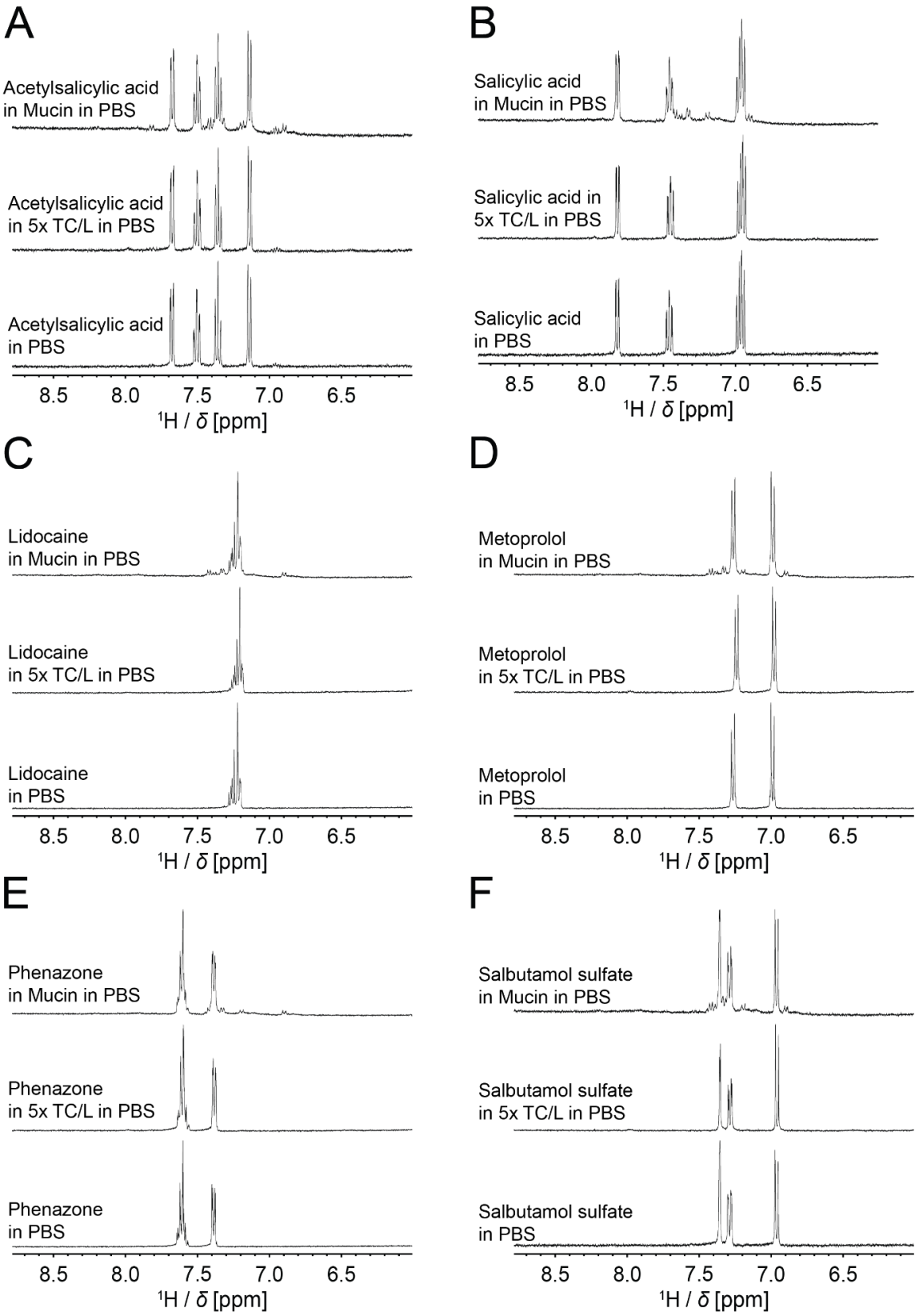

Figure S48. Extracts from the ^{1}H NMR spectra of region IV drug compounds. (A) Acetylsalicylic acid, (B) Salicylic acid, (C) Lidocaine, (D) Metoprolol, (E) Phenazone, and (F) Salbutamol sulfate in PBS (bottom), in 5-fold TC/L in PBS (middle), and Mucin in PBS (top). 5-fold TC/L corresponds to 15 mM TC and 3.75 mM L. Mucin in PBS was prepared by dissolving 0.2 g mucin from porcine stomach type II (Merck) in 100 mL PBS.

Supporting Information, Experimental Section

Fluorescence correlation spectroscopy

Labeling of isolated mucus or biopsy

To probe the diffusion in isolated mucus or biopsies, we labeled the mucus samples with AlexaFluor 647 (AF647) (ThermoFisher scientific, Dreieich, Germany) and 10 kDa Dextran-AF647 (ThermoFisher scientific, Dreieich, Germany). For isolated mucus, the sample was stained with the fluorophore (AF647 or Dextran-AF647) at the final dye concentration of 10 nM. The mixture was homogenized by pipetting. Ca. 30 µL aliquot was placed on top of a cleaned glass coverslip (Menzel-Gläser, Braunschweig, Germany; 24 x 40 mm, 1.5# thick).
To label the biopsies, fresh biopsy samples were soaked in a 100 nM 3 mL solution of AF647 or Dextran-AF647 in PBS in a small petri dish (35 x 10 mm) for 1 hour and then washed 7 times with 3 mL phosphate buffered saline (PBS) in 7 petri dishes to remove any unbound dye. Afterwards, biopsies were transferred to an 8 chambered well chamber (Cellvis, Mountain View, California) keeping the mucus side of the biopsy facing downwards. To prevent desiccation 20 µl of PBS had been added to each chamber.

Fluorescence correlation spectroscopy setup

Fluorescence correlation spectroscopy (FCS) measurements were done in our custom build confocal setup based on an Olympus IX 71 stand (Olympus, Hamburg, Germany). A laser beam of wavelength 640 nm was coupled into an optical fiber and expanded with a telescope to fill the back aperture of the objective (water objective, 60x, 1.20 W) to create a diffraction-limited spot. Before reaching the sample, the beam was reflected from a dichroic mirror (Quad 405/488/560/647) to separate the excitation and emission light effectively in the beam path. After that, the emission from the sample passed through 50 µm pinhole to reject out of focus light and projected on photon counting detectors (2x Avalange Photodiode, SPCM-AQR-14, PerkinElmer, Germany) by a telescope in a 4f configuration (focal length of lenses: 60 mm, G063126000, Qioptiq, Rhyl, UK). To detect in two detectors, we used polarizing beam splitter (10FC16PB.3, Newport, Darmstadt, Germany) and specific wavelengths were selected by using Emission filters (band pass filter Brightline ET 685/70 AHF, Tübingen, Germany).

FCS data acquisition and analysis

During all FCS measurements laser pulsed was set to 40 MHz and the sample binning was set to 4 ps. Calibration was performed using AF647. From a single spot of a single sample (isolated mucus/biopsy) at least 5 measurements were taken for 2-3 minutes depending on the photon count rate. The averaged values were autocorrelated and exported to text files

using SymPhoTime 64 (PicoQuant, Berlin, Germany). Correlation curves were normalized to 1 for better comparison and fits were performed using Origin2021b (OriginLab, MA) with two different models.

Model 1: A31DT (Auto correlation, one 3D diffusion and one triplet state)

Model 2: A32DT (Auto correlation, two 3D diffusion and one triplet state)

The overall equation for fitting is

$$G(t_C) = b + \frac{1}{N} \cdot \left(\frac{x_1}{\left(1+\frac{t_c}{\tau_{D1}}\right)} \cdot \left(\frac{1}{\sqrt{1+1/S^2(\frac{t_c}{\tau_{D1}})}} \right) + \frac{1-x_1}{(1+\frac{tc}{\tau_{D2}})} \cdot \left(\frac{1}{\sqrt{1+1/S^2(\frac{t_c}{\tau_{D2}})}} \right) \right) \cdot \left(1 - T + T \cdot e^{-\frac{t_c}{\tau_T}}\right) \quad \text{eq (1)}$$

Where N is the average number of molecules in the detection volume, t_c is the delay time, τ_{D1} and τ_{D2} are two diffusion times. x_1 is the fraction of the first diffusion component. T is the triplet state fraction and τ_T is the triplet state relaxation time. S is the structural parameter of the instrumental setup $S=z_0/\omega_0$, where z_0 and ω_0 are the axial width and lateral 1/e2 beam radius of the confocal volume, respectively.

With the previous reported value of diffusion coefficient of AF647 3.30 x 10^{-10} m^2/s[7] the effective confocal volume of the setup was determined by extracting the value of S from diffusion measurement of 2 nM AF647 in PBS using A31DT and following equation

$$V_{eff} = \pi^{\frac{3}{2}} \cdot z_0 \cdot \omega_0 \quad \text{eq (2)}$$

Having V_{eff} calibrated, one can calculate the diffusion coefficients of corresponding extracted diffusion times from the fitting of isolated mucus and biopsies, ω_0 from calibration using following equation

$$D = \frac{\omega_0^2}{4 \cdot \tau_D} \quad \text{eq (3)}$$

Where D is the diffusion coefficient.

To fit the Alexa curves in isolate and biopsies, the diffusion time of the fast component was fixed to the value observed in PBS. Here we have assumed that the fast component of Alexa diffusion in isolate and biopsies is originating from the void space of mucus similar to the diffusion in PBS.

Fluorescein isothiocyanate-dextran release

The release kinetic of (Diethylaminoethyl (DEAE))-dextran labelled with fluorescein isothiocyanate (FITC) from mucus was studied by fluorescence measurements. 495 µL mucus was mixed with 5 µL of a 10 g/L dextran stock solution in PBS followed by an equilibration phase for 24 h at 25 °C without shaking on a Thermomixer F1.5 (Eppendorf, Hamburg, Germany). Next, 200 µL of the mucus containing 0.1 g/L dextran was transferred

to the bottom of a 10.0 x 10.0 mm^2 quartz glass cell (Hellma, Müllheim, Germany). The cuvette was placed in a 50 mL falcon tube equipped with a self-built holder and centrifuged on an Allegra X15 R (Beckman Coulter, Brea, CA) at 4000 g, for 10 min, at 25 °C. At the beginning of the release experiment, 1500 µL of PBS was gently added to the evenly distributed mucus and the cuvette was placed in a Cary Eclipse fluorescence spectrophotometer (Agilent Technologies, Waldbronn, Germany). The fluorescence signal was recorded over 48 h at an excitation wavelength λ_{ex} of 489 nm, an excitation slit of 5 nm, at an emission wavelength λ_{emi} of 515 nm, an emission slit of 5 nm, an integration time of 1 s per measurement point, and a photomultiplier tube (PMT) voltage of 600 V. The signal intensities were converted to dextran concentrations by calibration curves. Experiments were carried out under light protection. The release studies were done in triplicate. Data were recorded using the Cary Eclipse Software (Agilent Technologies).

Rheology

The rheological properties of different mucus batches were studied on a Modular Compact Rheometer MCR-302 (Anton Paar, Ostfildern, Germany) equipped with a solvent trap and an actively heated Peltier hood H-PTD200 (Anton Paar). The measurements were performed using a plate-plate geometry with a diameter of 25 mm (PP25, Anton Paar) at a constant temperature of 25 ± 0.1 °C. The rheological data were analysed with RheoCompass™ Version 1.23.378 (Anton Paar).

Rotational mode

The steady shear viscosity η was recorded as a function of the applied shear rates $\dot{\gamma}$ 0.01 → 1000 s^{-1}. The shear-thinning properties were evaluated using the power law model. Steady stress sweeps were performed increasing the shear stress τ 0.2 → 307 Pa to determine the apparent yield stress τ_0 as the onset of decreasing η values using the tangent intersection point method. In addition, the structural decomposition and regeneration were characterized by structure-recovery tests alternating the $\dot{\gamma}$ from 0.1 to 100 s^{-1} ten times at one-minute intervals. The viscoelastic properties were addressed by creep-recovery experiments. Here a constant stress – within the LVR for a given sample – was applied at the creep interval (0-300 s) followed by the creep-recovery interval (300-900 s) after the removal of stress. The shear strain γ was monitored over time obtaining the creep compliance J as the ratio of γ and τ. The creep curves were fitted to the generalized Kelvin-Voigt model with up to 2 voigts units.

Oscillatory mode

Shear strain amplitude sweeps were conducted with controlled strain deformation γ from 0.03% to 101% at a fixed angular frequency ω of 10 rad/s. The data were used to assess the limit of the linear viscoelastic region (LVR) γ_{LVR} and the flow point γ_{flow} defined as the onset of the decrease of the storage modulus G' and the cross-over of the storage modulus G' with the lost modulus G", respectively. Next, frequency sweep was conducted within the LVR for a given sample. Oscillatory frequency sweeps were conducted from ω of 0.1 to 100 rad/s with controlled shear strain and the damping factor tan δ was calculated as the ratio of G" and G'.

Nuclear magnetic resonance spectroscopy

Nuclear magnetic resonance (NMR) samples were prepared by adding stock solutions of the small molecule (in DMSO or PBS) of interest to the respective medium. The DMSO concentration did not exceed 1% (v/v) and the maximum nominal concentration of the species of interest was 15 mM. The samples were initially mixed and then equilibrated for 2 h at a temperature of 25 °C without shaking on a Thermomixer F1.5. Spectra of proton NMR (^{1}H NMR), proton-diffusion-ordered spectroscopy NMR (^{1}H-DOSY NMR), fluorine NMR (^{19}F NMR), fluorine-diffusion ordered spectroscopy NMR (^{19}F-DOSY NMR), proton-carbon heteronuclear single quantum coherence NMR (HSQC NMR), and proton-carbon heteronuclear single quantum coherence incorporated diffusion ordered spectroscopy NMR (HSQC-iDOSY NMR) were recorded on a Bruker Avance III HD 600 MHz spectrometer operating at 600.4 MHz with a 5 mm BBFO probe or a Bruker Avance IV NEO 500 MHz spectrometer operating at 470.6 MHz with a Diff50 probe. The probe temperature was set to 295.6 K. Coaxial inserts filled with DMSO-d_6 were used for locking. ^{1}H-DOSY,^{19}F-DOSY, and HSQC-iDOSY NMR spectra were measured by using the pulse sequences ledbpgp2s, ledgp2s, dstebpgp3s, and idosyhsqc3d. The diffusion gradients were linearly incremented in up to 32 steps. The diffusion time (d20) and the length of the gradient pulse (p30) were adjusted to achieve an adequate signal attenuation, except for Linezolid in mucus, for which the decay curve only dropped to 25-50%. DOSY decay curves were fitted using a mono-exponential fit as previously described[8].

In addition, we studied samples reflecting the donor solutions used within the flux experiments. Here, deuterated water was used for media preparation. For pH adjustment in deuterated water, a correction factor was used adjusting pD to 6.91 using DCl and NaOD. Deuterated DMSO drug stock solutions were added to PBS, TC/L in PBS, 5-fold TC/L in PBS, and 25-fold TC/L in PBS, obtaining a nominal drug concentration of 1 mmol/L and a maximum of 1.0% (v/v) DMSO. The samples were vortexed for at least 30 s using a VTX-3000 L. Subsequently, ^{1}H NMR spectra were recorded on a Bruker Avance 400 MHz

spectrometer operating at 400.1 MHz with a BBI BB-H 5mm probe at a temperature of 300 K. The chemical shifts were referenced to the external standard of 0.05% TSP-d_4 in D_2O filled in a coaxial insert tube.
All spectra were analyzed using TopSpin 4.0.6. (Bruker BioSpin). An automatic baseline correction and manual phasing were performed.

Brillouin microscopy

Generals

We introduce the application of confocal Brillouin microscopy to detect and quantify mechanical changes of the mucus evoked by the immediate reaction with bile. Confocal Brillouin microscopy is an optical, contact and label-free technique that probes viscoelastic properties in three dimensions as previously reviewed[9]. It utilizes inelastic light scattering by inherent, thermally induced density fluctuations. The density fluctuations are spontaneous acoustic waves that occur in all materials at a temperature above absolute zero. The energy transfer between acoustic waves and incident light, caused by the inelastic scattering, is detectable as a frequency change (Brillouin frequency shift). While the BFS closely connected to the longitudinal modulus and therefore the elastic properties of the sample, the line-width of the spectral peak (i.e. attenuation coefficient of the acoustic wave) is connected to the viscosity of the scattering volume, as previously shown[9]. In this work, we quantified both the Brillouin frequency shift (~ longitudinal modulus) and the linewidth (~ viscosity) as mechanical parameters accompanying the chemical changes induced within the mucus-bile mixture. Our results document a locally confined, transient increase in the Brillouin frequency shift, but not linewidth, of the two-component mixture that propagates as a wave front through the mucus portion of the chamber with diffusive characteristics.

Chamber setup and sample preparation

A 24 x 50 mm cover glass (made of pure white hydrolytic class 1 glass) with a thickness of 0.17 mm was glued to a custom-made chamber made of poly(methylmetacrylate) with a multi-purpose, one component silicone sealant (Dow Corning, Mfr. Part #4103096, **Fig. 2D, Fig. S7**). 200 µL of mucus was added to the chamber through the right hole which was sealed with a polyoxymethylene stopper or adhesive tape. At the beginning of the experiment, PBS or 25-fold TC/L in PBS was pipetted through the left orifice as a soaking solution. The column was attached and sealed with a polyoxymethylene stopper. The liquid level of the soaking solution in the column was 2 cm along all experiments (ρ (25-fold TC/L) = 1.017 g/cm^3). Measuring cells were used once.

Brillouin microscopy data acquisition

Brillouin microscopy was performed using a custom-built confocal Brillouin microscope based on a two-stage virtually imaged phase array (VIPA). The detailed working principle was previously described[10]. Briefly, a frequency-modulated diode laser beam (l = 780.24 nm, DLC TA PRO 780, Toptica Photonics AG, Germany) served as an illumination source. The central frequency of the beam was stabilized to the D2 transition of 85Rb by monitoring the intensity of the probe beam after it passed through a rubidium molecular absorption cell (TG-ABRB-I85-Q, Precision Glassblowing Inc., USA). The suppression of amplified spontaneous emission (ASE) and the cleaning of the laser spectrum was facilitated by a Fabry-Pérot interferometer (FPI) in the illumination path with the cavity length of a piezo-tuneable etalon (OP-1986-102, LightMachinery Inc., Canada) stabilized to the central laser frequency. The FPI reduced the laser mode to ASE ratio by 20 to ~85 dB, and the ASE was further suppressed by a monochromatic detector (DFC MD, Toptica).

Then, the laser beam was coupled into a single-mode fiber and guided to a custom-built inverse confocal microscope. An inverted microscope stand (Axio Observer 7, Carl Zeiss AG, Germany) served as a basis for the confocal microscope. The laser beam was focused in the sample by an objective lens (NA 0.5, 20´, EC Plan-Neofluar, Carl Zeiss) achieving a resolution of 1 µm in lateral and 5 µm in axial direction. Sample positioning and translation during the scanning process was facilitated by a motorized stage. Finally, the backscattered light was collected by the same objective lens and coupled into a second single-mode fiber achieving confocal sectioning. The fiber-coupled light was then guided to the Brillouin spectrometer. In the spectrometer, the light was collimated and passed through the same rubidium molecular absorption cell for frequency stabilization and attenuation of the elastically scattered Rayleigh and reflected light. Then, the beam was guided to two-stage VIPA etalons (OP-6721-6743-4, LightMachinery) with 15.2 GHz free spectral range. The VIPA etalons led to angular dispersion of light with different frequencies (Opt. Express. 19, 10913 (2011)). Per Pixel, two spectra were recorded by a scientific complementary metal-oxide-semiconductor camera (Prime BSI, Teledyne Photometrics, USA) with an acquisition time of 0.2 s each. Each pixel was timestamped. Image acquisition and microscope control were facilitated by custom-made software BrillouinAcquisition [Raimund Schlüßler and others (2017), BrillouinAcquisition version 0.2.2: C++ program for the acquisition of FOB microscopy data sets, available at https://github.com/BrillouinMicroscopy/BrillouinAcquisition].

Samples were subjected to a sequence of five consecutive Brillouin microscopy scans. Each scan yielded one map and covered 500 µm (21 pixel) x 5000 µm (201 pixel). The first respective maps of each sequence were scanned along the long axis first (from PBS/25-fold

TC/L PBS to mucus) to capture potentially fast dynamics. The four consecutive maps were scanned along the shorter axis first.

The penetration depth of the laser beam inside the sample was determined based on the maximum distance from the cover slip at which the live spectra still displayed a high intensity in the mucus filled region of the measurement chamber (~ 30 to 40 µm). The power of the focused laser beam on the sample was 10 mW. The temperature of the calibration media and the rooms in which the measurements took place were monitored and kept constant at 23˚C throughout the entire experiment series.

Brillouin microscopy data acquisition

Brillouin microscopy data was analyzed using custom-made software bmlab [Raimund Schlüßler and others (2022)]. A Python library was used for the post-measurement analysis of Brillouin microscopy data v.0.3.0, available at https://github.com/BrillouinMicroscopy/bmlab and BMicro [Raimund Schlüßler and others (2022), Python GUI for post-measurement Brillouin microscopy analysis v.0.4.0, available at https://github.com/BrillouinMicroscopy/BMicro]. In brief, one-dimensional Brillouin spectra displaying the Brillouin and Rayleigh peaks were close-uped from the recorded images. The position, width, and intensity of the Brillouin and Rayleigh peaks were determined by fitting Lorentzian functions. Reference measurements of methanol and water positioned in the calibration beam path were acquired every 10 min by moving a motorized mirror into the calibration beam path and served to calibrate the frequency axis, which facilitated the collection of absolute Brillouin frequency shift values and the compensation for potential drifts of the VIPA setup during the measurements. All Brillouin frequency shift and linewidth maps were generated using bmlab and BMicro.

To compare the evolution of the mechanical properties of the individual, unmixed components during an entire sequence of five consecutive Brillouin microscopy scans, we close-uped and averaged the 210 spectra (10 measurement columns) that are farthest to the right (for unmixed mucus) or left (for unmixed 25-fold TC/L in PBS or unmixed PBS) in each Brillouin microscopy map. The close-ups of those discrete regions of interest from each Brillouin frequency shift or linewidth map was done with the custom-made software Impose [Paul Müller and others (2021), impose version 0.1.2: Graphical user interface for superimposing and quantifying data from different imaging modalities, available at https://github.com/GuckLab/impose].

To describe and quantify the dynamic mechanical changes observed in the Brillouin frequency shift maps of mucus-25-fold TC/L in PBS mixtures, we averaged three line-scans in the first map of each sequence. For the 21 measured line scans, this yielded seven average

line scans and, hence, seven average time points. Each of those seven averaged line scans was fitted using Wolfram Mathematica's NonlinearModelFit (version 12.2) to determine the maximum Brillouin frequency shift for that time point using the empirical functional relation $\nu_B(x) = a_0/(1 + \exp(b_0 - x^{c_0})) + \mathcal{N}[x; \mu, \sigma] + d_0$, where $\nu_B(x)$ denotes the Brillouin frequency shift in dependence of the channel position. This model is divided in two parts; i) the sigmoidal term $a_0/(1 + \exp(b_0 - x^{c_0})) + d_0$ that describes the bi-phasic structure of the sample and the mixing between both, where $(a_0 + d_0)$ is the Brillouin frequency shift of the mucin, b_0 represents the central transition position from bile to mucin, c_0 is a scaling parameter, d_0 is Brillouin frequency shift of the bile and ii) the probability density function of a Normal distribution $\mathcal{N}[x; \mu, \sigma]$, corresponding to the Brillouin frequency shift peak with mean μ and standard deviation σ. The four subsequent maps of each sequence were averaged entirely and subjected to the same fitting procedure as described for the first seven line-scans. Thus, per map and per sample, allowing for correlating 11 Brillouin frequency shift maxima with their corresponding time points. When plotted, these pairs display a square-root-of-time dependency which we fitted using $\mu(t) = \sqrt{a_1 t} + b_1$ where $\mu(t)$ denotes the position of the Brillouin frequency shift maxima, a_1 denotes the propagation coefficient, t represents time and b_1 represents an offset to account for differences in the initial peak position ($\mu(t = 0)$) simply caused by different absolute measurement positions for each sample. Thereby we close-uped one characteristic propagation coefficient a_1 per measurement sequence. For all fits a coefficient of determination R^2>0.99 was found. Since all measurement sequences performed on the same day (4 sequences, see overview Fig. S8-13) used the same mucus sample and can be regarded as technical replicates, we averaged all reported values for each day.
Raincloud plots were generated as previously described[11]. Maps, plots, and graphs in figures were assembled using CorelDraw 2019.

Statistical analysis for Brillouin microscopy data

Statistical analysis was carried out using Origin Lab Pro 2021b. All Brillouin microscopy data were subjected to non-parametric tests for statistical analyses, because the available sample sizes of N = 5 for each material (mucus, 25-fold TC/L in PBS, PBS) were too small to determine the quality of their respective distribution with certainty. **Fig. S16A** comprises five repeated measures of the same specimens, which requires the Friedman ANOVA. The test yields a test statistic X^2 (4) = 12.8 with a probability p = 0.0123. Post-hoc analysis with Dunn's test revealed a significant statistical difference between "25 min" and "125 min" (p = 0.01374), but not between any other pairings. The effect size was determined using Kendall's W test with W = X^2/(N_ *(k-1)); where X^2 is the Friedman test statistic value, N is the

sample size, k is the number of measurements per subject x). In our case W = 0.64 (large effect size). The same statistical analysis for the other subfigures yielded no statistically significant differences among the respective repeated measures: (**Fig. S16B**): X^2 (4) = 6.88 with p = 0.14237 and W = 0.34 (medium effect size). (**Fig. S16C**): X^2 (4) = 7.2 with p = 0.12569 and W = 0.36 (medium effect size). (**Fig. S16D**): X^2 (4) = 1.76 with p = 0.77979 and W = 0.088 (low effect size). (**Fig. S16E**): X^2 (4) = 3.36 with p = 0.49948 and W = 0.17 (low effect size). (**Fig. S16F**): X^2 (4) = 5.6 with p = 0.23108 and W = 0.28 (medium effect size).

The data in (**Fig. S17**) comprises N = 5 independent samples for each subfigure and material obtained from the first respective Brillouin microscopy maps of each sequence, i.e. on average 25 minutes after measurement start. Here, a Kruskal-Wallis ANOVA is required followed by Dunn's post-hoc analysis. For (**Fig. S17A**) this analysis yielded a test statistic $\chi 2$ (2) = 12.5 with a probability p = 0.00193. Dunn's post-hoc analysis revealed a statistically significant difference between the samples "mucus" and "PBS" (p = 0.00122), but not any other pairings. The Kruskal-Wallis effect size $\eta 2$ was calculated using η^2= X^2-k+1/n-k; where $\chi 2$ is the Kruskal-Wallis test statistic value; k is the number of groups and n is the total number of observations. In our case $\eta 2$ = 0.88 (large effect size). In analogy, the data displayed in subfigure (**Fig. S17B**) yielded the following: $\chi 2$ (2) = 12.5 with p = 0.00193 and $\eta 2$ = 0.88 (large effect size). Dunn's post-hoc analysis revealed a statistically significant difference between the samples "mucus" and "PBS" (p = 0.00122), but not any other pairings. All effect size estimates were done according to a previous report[12].

Differential dynamic microscopy

Theory

Given a set of 2D images $I(\boldsymbol{x}, t_0)$, the intermediate scattering function at time (i.e., age of the system) t is estimated by

$$f(q, \Delta t, t_0) = 1 - \langle \frac{D(\boldsymbol{q}, \Delta t, t_0) - B(\boldsymbol{q})}{A(\boldsymbol{q})} \rangle_{\boldsymbol{q}=q},$$

where

$$D(\boldsymbol{q}, \Delta t, t_0) = \langle \left| \hat{I}(\boldsymbol{q}, t_0 + \Delta t, t) - \hat{I}(\boldsymbol{q}, t_0, t) \right|^2 \rangle_{t_0},$$

$$A(\boldsymbol{q}) + B(\boldsymbol{q}) \approx 2 \langle \left| \hat{I}(\boldsymbol{q}, t_0) \right|^2 \rangle_{t_0} \text{ and}$$

$$B(\boldsymbol{q}) = 2 \langle \left| \hat{I}_0(\boldsymbol{q}, t_0) \right|^2 \rangle_{t_0}.$$

Here, $\hat{I}(\boldsymbol{q})$ is the Fourier transform of $I(\boldsymbol{x})$, $I_0(\boldsymbol{x}, t_0)$ are the background time lapse images, $A(\boldsymbol{q})$ and $B(\boldsymbol{q})$ are time independent estimates of the structure factor of the sample and spatial background noise of the camera and $q = \sqrt{{q_x}^2 + {q_y}^2}$ is the norm of the wave vector. In this context $\langle \dots \rangle_{\boldsymbol{q}=q}$ denotes azimuthal averaging in spatial Fourier space and $\langle \dots \rangle_{t_0}$ denotes the temporal average. The mean-squared-displacement (MSD) in dependence of spatial frequency magnitude, lag time and age is then obtained by

$\Delta r^2(q, \Delta t, t_0) = -\frac{4}{q^2} \ln f(q, \Delta t, t_0)$.

Further details are detailed in previous report[13,14].

Sample preparation

The samples for the DDM measurements were mounted in an ibidi µ-Dish 35 mm, high Glass Bottom using a silicone spacer (4.5 mm) to prevent the mucus from spreading during the measurements. In order to speed up the initial spreading, the dish was taped on an Eppendorf ThermoMixer C, vibrating at 1000 rpm for at least 10 minutes. The dish was then flooded with 2 ml PBS, covering the mucus, and left to further equilibrate for at least 45 minutes. After that, an initial set of time lapse measurements were initiated. Once the measurements were finished, 1ml of 25-fold TC/L or PBS was added, respectively, for conditional and control measurements, followed by immediate further measurements. The room temperature and hence assumed sample temperature was fixed to 22 °C for all measurements.

Data acquisition

The time lapse images (400x400 px^2) of respective samples were recorded at 1000, 100 and 10 fps (Mikrotron EoSense CL 1362) on an inverted microscope (Zeiss Axio Observer.A1 equipped with a N-Achroplan 20x/0.45), using a custom python script employing pyLabLib [https://github.com/SandoghdarLab/pyLabLib-cam-control]. For every frame rate 1000

images were acquired. The individual measurements at different frame rates were consecutively chained, starting at 1000 fps, resulting in a total measurement time of 111s. Multiple of these measurement cycles were performed with a 19 s wait time in between. For each measurement session background time lapses (dish flooded with PBS; no sample) were acquired. The data was then stored as a HDF5 file for further analysis.
For each, control and TC/L addition, 5 different samples of mucus were measured.

Data analysis

The time lapse images were evaluated with a custom Mathematica script using the formulas stated above and for each measurement cycle the MSD was computed. The ergodicity of the system was investigated by evaluating the overlap between the MSDs acquired at different frame rates of the same cycle and it was found to be safe to assume for the measurement times stated above. Hence, the time averaged MSD coincides with the ensemble averaged MSD. We report the median and median deviations of the time averaged MSD in dependence of the age of the system t at representative lag times $\Delta t = 1$ s and $\Delta t = 10$ s. The median and median deviation of the time averaged MSD were calculated over a range of spatial frequency magnitudes from $q = 0.1\ \mu m^{-1}$ to $1\ \mu m^{-1}$, where the signal to noise ratio was sufficiently high, i.e. $A(q)/B(q) > 10$.

Flux

Flux across cellulose membranes

A side-by-side diffusion cell (PermeGear Inc., Hellertown, PA, USA) was used to determine the free drug concentration as well as the permeated amount of Taurocholate. The donor and receiver compartments were separated by a cellulose membrane (innoME GmbH, Espelkamp, Germany) with an average pore size of 33 nm and a surface area of 1.77 cm^2. The donor compartment contained 10 mL of PBS, TC/L in PBS, 5-fold TC/L in PBS, or 25-fold TC/L in PBS. The receiver compartment was filled with 10 mL of PBS containing 0.2% (w/v) Vitamin E TPGS. The temperature was held at 298 K using a Haake Fisons C1 water circulator (Thermo Fisher Scientific Inc., Karlsruhe, Germany) with a DLK 1002 cooling unit (FRYKA GmbH, Esslingen, Germany). The fluids in the cells were stirred at a stirring speed of 500 rpm on a H9-CB-02 stirring apparatus (SES GmbH, Bechenheim, Germany). At the beginning of the diffusion experiment, 100 µL of a 0.1 mol/l drug stock solution in DMSO was added to the donor. After 15, 30, 60, 120, 180, and 240 min aliquots of 100 µL were taken from the receiver medium and replaced with fresh medium. Subsequently, the samples were diluted with Acetonitrile (ACN) with 0.1% trifluoroacetic acid (TFA) and ACN with 0.1% formic acid (FA) for HPLC and LC-MS/MS analysis, respectively. The samples were

vortexed for at least 30 s (VTX-3000 L, LMSCO. LTD., Tokyo, Japan) and centrifuged with a MiniSpin centrifuge (Eppendorf) at 13000 rpm for 10 min. Perphenazine and Fluphenazine experiments were carried out under light protection. In all experiments, the maximum drug concentration in the receiver cell was less than one tenth of the starting drug concentration in the donor.

Flux across mucus

The Transwell diffusion model was used to characterize the bulk diffusion through mucus. 600 µL of PBS was filled in a well of a 24-well cell culture multiwell plate (Greiner Bio-One, Frickenhausen, Germany) working as the receiver compartment. 50 µL of mucus was evenly layered on the polyester-membrane with a pore diameter of 3.0 µm of a translucent cell culture insert (Greiner Bio-One). Donor solutions with 1 mmol/L of drug (out of DMSO stock solutions) and 2.66 µmol/L of sodium-fluorescein (out of PBS stock solution) were prepared in PBS, TC/L in PBS, 5-fold TC/L in PBS, and 25-fold TC/L in PBS. At the beginning of the experiment, 200 µL of the donor solution was gently added to the mucus layering the membrane. Multiwell plate was shaken at a shaking speed of 300 rpm on a Noctua KV2/1500. After 60, 100, and 180 min aliquots of 100 µL were taken from the receiver compartment followed by replacement with fresh medium. Subsequently, samples were diluted with ACN with 0.1% TFA for high pressure liquid chromatography (HPLC) analysis. ACN with 0.1% FA containing ^{13C}Perphenazine as the internal standard was added to the samples analyzed by liquid chromatography-tandem mass spectrometry (LC-MS/MS). The diluted samples were vortexed for at least 30 s using a VTX-3000 L (LMSCO. LTD, Tokyo, Japan) and centrifuged with a MiniSpin centrifuge (Eppendorf) at 13000 rpm for 10 min. In all experiments, the maximum drug concentration in the receiver compartment was less than one tenth of the starting donor drug concentration. The flux experiments were done at room temperature. After the flux experiment, the membrane integrity was assessed measuring the fluorescence of sodium fluorescein in the receiver compartment on a Tecan Reader Infinite 200 pro plate reader (Tecan Group, Maennedorf, Switzerland) at an excitation and emission wavelength of 489 nm and 520 nm, respectively. Quantification of permeated sodium fluorescein was done by calibration curves. Flux experiments were carried out in triplicate. Fluphenazine and Perphenazine experiments were carried out under light protection. In all experiments, the maximum drug concentration in the receiver cell was less than one tenth of the starting drug concentration in the donor.

High pressure liquid chromatography analysis

High Pressure Liquid Chromatography (HPLC) was used to determine the receiver compartment concentration change over time for the flux across cellulose membranes of

Metoprolol in all media and of Perphenazine and Fluphenazine in all media but 25-fold TC/L in PBS. In addition, the flux across mucus of Metoprolol in all media was quantified by HPLC analysis. The samples were analyzed on an Agilent 1260 infinity II HPLC (Agilent Technologies Inc., Waldbronn, Germany) using a Zorbax Eclipse XDB-C18 analytical 80 Å 4.6 x 150 mm HPLC column (Agilent) and a Synergi™ 4 µm Hydro-RP18 80 Å 150 × 4.6 mm LC column (Phenomenex LTD, Aschaffenburg, Germany), respectively. The device was equipped with a variable wavelength detector (G7114A, Agilent), an automatic vialsampler (G7129C, Agilent), flexible Pump (G7104C, Agilent), and multicolumn oven (G7116A, Agilent). Mobile phase A was 0.1% TFA in Millipore water. Mobile phase B was ACN with 0.1% TFA, flow was set to 1 mLmin, injection volume was 50 µL, and the wavelength of the detector was set to λ = 275 nm for Metoprolol, λ = 255 nm for Perphenazine, and λ = 255 nm for Fluphenazine. For the analysis of the flux across cellulose membrane, the gradient started at 20% B increasing to 100% within 6 min, held for 4 min, then back to 20% B within 1 min, and held for 4 min. For the analysis of the flux across mucus, the gradient profile was adjusted aiming at separating the Metoprolol peak from mucus signals. Here, the gradient started at 5% B, held for 1 min, increasing to 55% B within 8 min, further increasing to 100% B within 1 min, held for 3 min, then back to 5% B within 2 min, and held for 4 min. Taurocholate samples were analysed using a Zorbax Eclipse XDB-C18 analytical 80 Å 4.6 x 150 mm HPLC column (Agilent). Phase A and B were equivalent to the drug analysis. The column temperature was set to 50 °C. Quantification was done with an evaporative light scattering detector (G4260B, Agilent). The evaporator and nebulizer temperature of the detector were set to 80 °C and 30 °C, respectively. The elution experiment started at 5% B, was held for 1 min, up to 45% B within 9 min, and to 100% B within another 1 min. 100% B was held constant for 3 min, and then the mobile phase composition was adjusted back to the initial gradient within 2 min. After a 4 min column equilibration time, the next elution experiment was started. Quantification was done by calibration curves. The flux was obtained from the slope of the resulting concentration versus time profile using linear regression per permeated area.

Liquid chromatography-tandem mass spectrometry

Liquid chromatography-tandem mass spectrometry (LC-MS/MS) was used to determine the receiver compartment concentration change over time for the flux across cellulose membrane of Perphenazine and Fluphenazine in 25-fold TC/L in PBS. In addition, the flux across mucus of Fluphenazine and Perphenazine in all media was quantified by LC-MS/MS analysis. Ultra-high performance liquid chromatography (UHPLC) was performed on an Agilent 1200 Series HPLC system equipped with a XBridge C18 3.5 µm 2.1 x 50 mm (Waters

Corporation, Milford, MA) column. The column compartment temperature was set to 20 °C. LC-MS grade solvents were used. Mobile phase A was 10 mM NH_4HCO_3 in water/methanol 90/10 (v/v). Mobile phase B was 10 mM NH_4HCO_3 in 90/10 (v/v) methanol/water. The flow rate was set to 0.6 mL/min and the injection volume was 5 µL. The gradient started at 70% B, held for 20 s, increased to 90% B within 100 s, held for 42 s, and then back to 70% B within 6 s, and held for 60 s. The UHPLC effluent was channelled to an Agilent 6460 triple quadrupole operating with an electrospray ionization (ESI) interface, in multiple reaction monitoring (MRM) and positive ion mode. Quantification was done by calibration curves using ^{13C}Perphenazine as an internal standard. The method quantification limit was estimated using the signal-to-noise-ratio and was 0.5 nM for Perphenazine and 0.1 nM for Flupheanzine[15]. Data was acquired with MassHunter software (Agilent Technologies) and further analyzed with MassHunter Quantitative and Qualitative Analysis Version B.08.00 for QQQ (Agilent Technologies). The flux was obtained from the slope of the resulting concentration versus time profile using linear regression per permeated area.

Pharmacokinetic studies in rats

A comparative pharmacokinetic study in male wistar rats (Toxi Coop zrt., Budapest, Hungary) was done in accordance with the animal welfare directive 2010/63/EU at Aurigon Toxicological Research Center Ltd. (Dunakeszi, Hungary). Each treatment group consisted of 5 rats that were fasting overnight and received 20 mg/kg Omeprazole in PBS 2 h prior to treatment. For the treatment solutions, 10% w/v Colesevelam x Hydrochloride was equilibrated in PBS and supplemented with Metoprolol or Perphenazine from a DMSO stock solution. Drug substance concentration was 2 mmol/L and the amount of DMSO was 1% (v/v). The nominal ionic strength and pH were the same for the intervention group (Colesevelam) and the control group (PBS). 5 mL/kg of the treatment solution was administered orally by gavage. Metoprolol and Perphenazine doses were 10 µmol/kg. Blood collection, sample preparation and sample analysis by LC-MS/MS were the same as previously reported[1]. In brief, 200 µL blood was withdrawn and plasma was obtained by centrifugation (3000 g, 10 min, room temperature). Next, plasma was extracted with ice-cold acetonitrile including internal standard (Perphenazine-^{13}C3 or Metoprolol-d7, respectively), vortexed, and centrifuged (24900 g, 15 min, 4 °C). The supernatant was diluted with the mobile phase, again vortexed and centrifuged. Samples were measured using the LC-MS/MS system as described in the flux section. The perphenazine samples were measured under the experimental conditions as described in the flux section and shown in Tab. S7. Chromatographic settings for Metoprolol samples were identical to those for Perphenazine and Fluphenazine, see also Tab. S7. For Metoprolol transitions from 268.1 to 159 m/z with a

collision energy of 17 eV was used and for Metoprolol-d7 transitions from 279.1 to 123 m/z with a collision energy of 20 eV. The method quantification limit was estimated using the signal-to-noise-ratio and was 1.8 nM for Perphenazine and 3.2 nM for Metoprolol[1,15].

Dynamic light scattering

DLS experiments were performed on a DelsaNanoHC particle analyzer from Beckman Coulter, as previously described[16]. Briefly, the unfiltered samples were transferred to disposable 1.5 mL UV-cuvettes (Brand, Wertheim, Germany) and measured in triplicate with an accumulation of 70 scans. Data was analyzed by the CUMULANT method with a refractive index of 1.333 and a dynamic viscosity of 0.9227 mPas, as previously reported[16,17]. Measurements were done at a temperature of 298 K.

Supporting Information, References

1 Schlauersbach, J. *et al.* Bile and excipient interactions directing drug pharmacokinetics in rats. *Eur J Pharm Biopharm*, doi:10.1016/j.ejpb.2022.07.016 (2022).

2 Gargano, A. F., Lammerhofer, M., Lonn, H., Schoenmakers, P. J. & Leek, T. Mucin-based stationary phases as tool for the characterization of drug-mucus interaction. *J Chromatogr A* **1351**, 70-81, doi:10.1016/j.chroma.2014.05.031 (2014).

3 Larhed, A. W., Artursson, P., Grasjo, J. & Bjork, E. Diffusion of drugs in native and purified gastrointestinal mucus. *J Pharm Sci* **86**, 660-665, doi:10.1021/js960503w (1997).

4 Slawson, M. H. & Johnson-Davis, K. L. Quantitation of Haloperidol, Fluphenazine, Perphenazine, and Thiothixene in Serum or Plasma Using Liquid Chromatography-Tandem Mass Spectrometry (LC-MS/MS). *Methods Mol Biol* **1383**, 49-57, doi:10.1007/978-1-4939-3252-8_6 (2016).

5 Juenke, J. M., Brown, P. I., Urry, F. M., Johnson-Davis, K. L. & McMillin, G. A. Simultaneous UPLC-MS/MS assay for the detection of the traditional antipsychotics haloperidol, fluphenazine, perphenazine, and thiothixene in serum and plasma. *Clin Chim Acta* **423**, 32-34, doi:10.1016/j.cca.2013.04.014 (2013).

6 Schlauersbach, J. *et al.* Leveraging bile solubilization of poorly water-soluble drugs by rational polymer selection. *J Control Release* **330**, 36-48, doi:10.1016/j.jconrel.2020.12.016 (2021).

7 Weidemann, T. & Schwille, P. Dual-color fluorescence cross-correlation spectroscopy with continuous laser excitation in a confocal setup. *Methods Enzymol* **518**, 43-70, doi:10.1016/B978-0-12-388422-0.00003-0 (2013).

8 Endres, S. *et al.* Concentration and composition dependent aggregation of Pluronic- and Poly-(2-oxazolin)-Efavirenz formulations in biorelevant media. *J Colloid Interface Sci* **606**, 1179-1192, doi:10.1016/j.jcis.2021.08.040 (2022).

9 Prevedel, R., Diz-Munoz, A., Ruocco, G. & Antonacci, G. Brillouin microscopy: an emerging tool for mechanobiology. *Nat Methods* **16**, 969-977, doi:10.1038/s41592-019-0543-3 (2019).

10 Schlussler, R. *et al.* Mechanical Mapping of Spinal Cord Growth and Repair in Living Zebrafish Larvae by Brillouin Imaging. *Biophys J* **115**, 911-923, doi:10.1016/j.bpj.2018.07.027 (2018).

11 Allen, M. *et al.* Raincloud plots: a multi-platform tool for robust data visualization. *Wellcome Open Research* **4**, doi:10.12688/wellcomeopenres.15191.2 (2021).

12 Tomczak, M. & Tomczak, E. The need to report effect size estimates revisited. An overview of some recommended measures of effect size. **21**, 19-25 (2014).

13 Edera, P., Bergamini, D., Trappe, V., Giavazzi, F. & Cerbino, R. Differential dynamic microscopy microrheology of soft materials: A tracking-free determination of the frequency-dependent loss and storage moduli. *Physical Review Materials* **1**, 073804 (2017).

14 Gu, M., Luo, Y., He, Y., Helgeson, M. E. & Valentine, M. T. Uncertainty quantification and estimation in differential dynamic microscopy. *Phys Rev E* **104**, 034610, doi:10.1103/PhysRevE.104.034610 (2021).

15 Vial, J. & Jardy, A. Experimental comparison of the different approaches to estimate LOD and LOQ of an HPLC method. *Anal Chem* **71**, 2672-2677, doi:DOI 10.1021/ac981179n (1999).

16 Hanio, S. *et al.* Drug-Induced Dynamics of Bile Colloids. *Langmuir* **37**, 2543-2551, doi:10.1021/acs.langmuir.0c02282 (2021).

17 Koppel, D. E. Analysis of Macromolecular Polydispersity in Intensity Correlation Spectroscopy: The Method of Cumulants. *J. Chem. Phys.* **57**, 4814-4820, doi:10.1063/1.1678153 (1972).

Appendix: Biopharmaceutical characterization of poorly water-soluble drugs by NMR spectroscopy

Simon Hanio, Lena Scheller, Lorenz Meinel

Institute for Pharmacy and Food Chemistry, University of Wuerzburg, Am Hubland, DE-97074 Wuerzburg, Germany

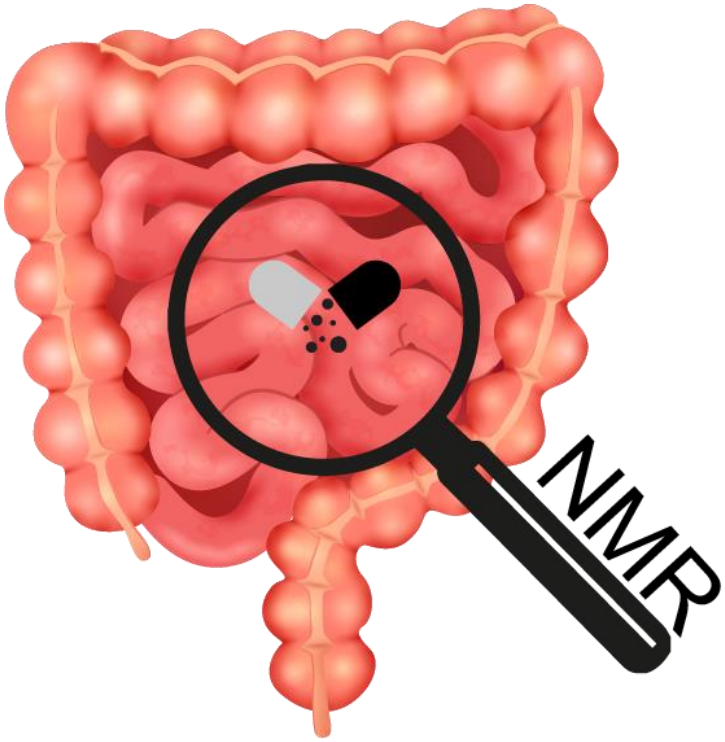

Unpublished manuscript.

Abstract

Development of poorly-water soluble drugs (PWSDs) into oral medicines is a key challenge in the pharmaceutical industry. The intestinal absorption of a PWSD is generally low and shaped by the unique gastrointestinal features, including the bile colloids and the mucus layer. Biopharmaceutical characterization is crucial for rational prioritization in the drug pipeline. To this end, we introduce a comprehensive guide for analyzing interactions between PWSD and bile/mucus by nuclear magnetic resonance (NMR) spectroscopy. Our workflow involves media preparation, mucus collection, NMR sample preparation, and NMR spectroscopic measurements, including one-dimensional and diffusion ordered experiments. Examples of interpretation of the resulting NMR data sets are given. Finally, we provide an outlook on the use of parameterized NMR datasets for the development of predictive algorithms.

Introduction

Poorly water-soluble drugs (PWSDs) are increasingly filling the industrial drug pipeline, challenging pharmaceutical scientists to develop orally bioavailable medicines[1-3]. PWSD absorption is mainly limited by the maximum achievable concentration in the intestinal lumen and the barrier resistance of the intestinal wall[4-7]. Assessing the impact of gastrointestinal features on absorption is a key part of a preclinical biopharmaceutical characterization[8].

Bile colloids are readily formed in the intestine from lecithin (L) and bile salts, including taurocholate (TC)[9,10]. Solubilization by bile is key for the systemic availability of lipophilic molecules, including fat-soluble vitamins, essential fats and many PWSD[11,12]. For years, this has been addressed in early drug development through the inclusion of TC/L in solubility and dissolution testing[13,14]. Passing of the intestinal mucosa is regulated by the selectively permeable mucus layer covering the intestinal epithelium[5,6,15]. Mucus' viscoelastic hydrogel network is formed by mucins[16,17]. Low mucus permeability of PWSD can limit the clinical success of pharmaceuticals[5,18,19]. Numerous permeability assays currently used in preclinical development lack a mucus layer[20]. There are ongoing efforts to facilitate the integration of mucus into preclinical high-throughput screening[21,22]. However, there is a need for biopharmaceutical screening that provides insights into molecular interactions and allows retrospective evaluation to be transformed into predictive evaluation.

Nuclear magnetic resonance (NMR) spectroscopy is a valuable tool in drug discovery and development[23,24]. NMR in solution can be used to assess intermolecular interactions in solution which are reflected in changes in NMR signal patterns[25-27]. Furthermore, Diffusion-Ordered NMR Spectroscopy (DOSY)-NMR enables the determination of diffusion coefficients (Ds)[28,29]. Molecular binding of PWSD to both colloidal structures, bile and mucin, was recently linked to the slowdown of PWSD diffusion[26,27,30-32].

Here, we introduce an NMR-based guide for the biopharmaceutical characterization of a PWSD. It covers media preparation and handling, including isolation and rheological testing of native porcine small intestinal mucus. The preparation of NMR samples and the setup of NMR spectroscopic measurements are described in detail. We propose a workflow to assess the interactions between bile/mucus and PWSD with and without fluorine (^{19}F). Data analysis is exemplified using actual recorded spectra. We conclude with a personal perspective on the establishment of predictive algorithms based on experimental datasets that can be collected by our or related workflows.

Data recording

The individual steps of the workflow are described in detail in separate sections below. In brief, the procedure consists of three steps:

1. Prepare media and samples.
2. Fill PWSD-containing samples and 1-fold TC/L in PBS in NMR tubes. Other reference media (i.e., without PWSD) are recommend to be dispensed for control.
3. Perform NMR spectroscopic measurements. While PWSD without ^{19}F are studied by ^{1}H-(DOSY-)-NMR, PWSD with ^{19}F are additionally probed by ^{19}F-(DOSY)-NMR. Take ^{1}H signal of DMSO-d5 signal as the reference for the ^{19}F NMR experiments.

This procedure gives different data sets for PWSD with and without ^{19}F (**Table 2**).

Table 8. Overview on nuclear magnetic resonance experiments (X = to be measured). 1-fold TC/L corresponds to a concentration of 3 mM Taurocholate and 0.75 mM Lecithin, Mucin is 0.2% (w/V) dissolved in PBS, and mucus is native porcine small intestinal mucus. PWSD concentration is 1 mM, except for mucus and 25-fold TC/L in PBS with 10 mM.

	PWSD without ^{19}F				**PWSD with ^{19}F**			
	^{1}H	^{1}H-DOSY	^{19}F	^{19}F-DOSY	^{1}H	^{1}H-DOSY	^{19}F	^{19}F-DOSY
PWSD in PBS	X	X			X	X		
PWSD in 1-fold TC/L in PBS	X				X			
1-fold TC/L in PBS	X				X			
PWSD in 5-fold TC/L in PBS	X	X			X	X		
PWSD in 25-fold TC/L in PBS							X	X
PWSD in Mucin in PBS	X	X			X	X		
PWSD in Mucus							X	X
PWSD in 25-fold TC/L in mucus							X	X

The tabulated experiments have been reduced to the minimum required to characterize the molecular interactions for a straightforward workflow and simple analysis. For a 1000 Da small molecule compound, less than 5 mg of PWSD without ^{19}F and less than 16 mg of PWSD with ^{19}F are required to perform the experiments. Once the NMR parameters have been optimized by the user, the PWSD can be automatically biopharmaceutically characterized overnight. Note that this timeline applies to our setup described below but is dependent on available spectroscopic hardware. Our workflow can be extended to additional experiments for more nuanced characterization, e.g., along concentration series of TC/L and mucin.

Data analysis

Read-out

Our workflow enables the evaluation of intermolecular interactions reflected in changes in NMR peak shift patterns and in molecular diffusion rates. When interpreting one-dimensional NMR spectra, we focus on two parameters: chemical shifts (δ in ppm) and peak shape/ width. While alterations in δ are attributed to microenvironmental changes, the peak width is related to the tumbling rate of the observed nucleus[33]. Larger structures generally show broader signals due to reduced mobilities, but multimeric species with similarly lower mobility also give broad signals[33]. In this sense, we associate signal broadening with intermolecular binding of PWSD to large colloidal structures present in the tested media. Under the assumption that only one diffusing species is present, we fit the DOSY-NMR signal attenuation to mono-exponential functions[34]. This allows a simplified comparison of PWSD diffusion coefficients in the presence of gastrointestinal components with those measured in PBS.

Bile interaction

Bile-drug interaction is reflected in changes of NMR signals of both, TC and PWSD[26,27,35]. We use the numbering of the TC signals (**Fig. 1A**), as assigned before[27,34]. Sharpening of TC-H25/26 was linked to the collapse of vesicular structures[26,27]. This morphological transition is not induced by non-interacting compounds (**Fig. 1B**) contrasting findings for interacting compounds (**Fig. 1C**). In addition, bile-interacting PWSDs shift the TC steroid scaffold signals upfield (to lower ppm values; **Fig. 1D**).

Aromatic signals are common in PWSD, absent for TC and L, and selective for PWSD in the following spectra[25,26,34,35]. Previous studies linked TC/L driven shifts in NMR aryl signals of PWSD to interaction with bile[25-27,35]. Addition of 15 mM TC and 3.75 mM L to PBS does not alter the signals of the non-interacting compounds (**Fig. 1E**) but does shift the signals of the interacting compounds (**Fig. 1F**). Using these experimental settings and a 400-MHz NMR spectrometer, a mean aryl-proton signal shift of PWSD by more than 8 Hz compared with the PBS spectrum was indicative of an interaction of PWSD with bile, as previously determined[25]. Similarly, the ^{19}F signal of a bile-interacting PWSD responds to the TC/L supplementation (**Fig. 1G**). In general, TC/L shifts bile-interacting PWSD signals to lower or higher ppm[25]. Sometimes a shift in both directions can be observed for different signals of one bile-interacting PWSD[25]. Future studies might generalize these findings and deduce underlying molecular dynamics.

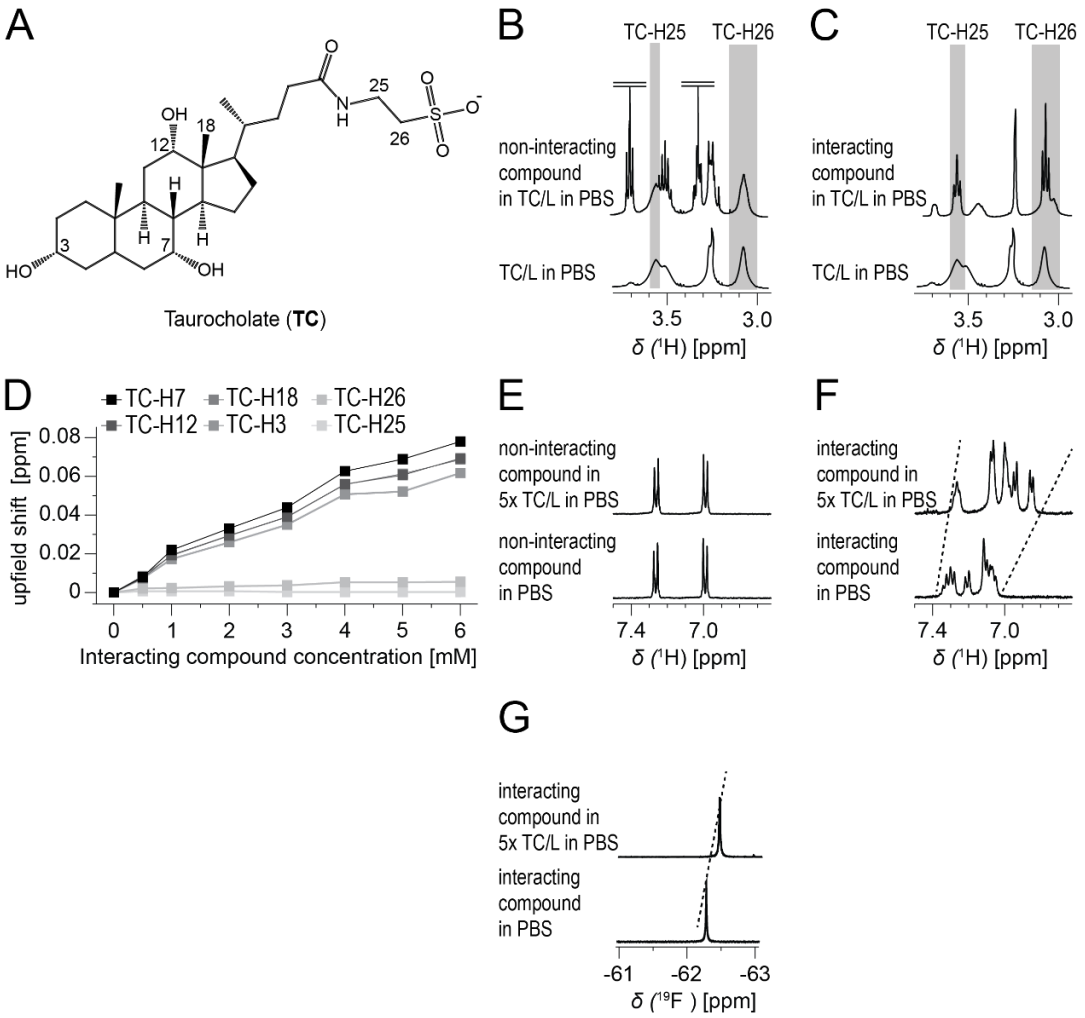

Figure 6. Analysis of interaction with bile. (A) Structure of Taurocholate (TC) with numbering scheme of the relevant atom positions. Extracts from ^{1}H-NMR spectra of a (B) non-interacting compound, Metoprolol, and a (C) interacting compound, Perphenazine, in TC/L in PBS (top, reference spectrum of TC/L in PBS is given below each, grey box highlights sharpening). (D) Upfield shift of selected TC signals as a function of concentration of an interacting compound, Perphenazine, in 1-fold TC/L in PBS. Extracts from ^{1}H-NMR spectra for a (E) non-interacting compound, Metoprolol, and a (F) interacting compound, Perphenazine, in 5x TC/L in PBS (top) and PBS (bottom, dashed line indicates shift). (G) Extracts from ^{19}F-NMR spectra of an interacting compound, Fluphenazine, in 5x TC/L in PBS (top) and PBS (bottom, dashed line indicates shift). The figure includes spectra from previous chapters, which were modified.

When dissolved in bile colloids, the average PWSD diffusion rate decreased compared to free diffusion in PBS[36]. For example, the relative decrease in diffusion rate of two interacting compounds, Fluphenazine and Naporafenib, from 5-fold TC/L in PBS to PBS was 1.8 and 2.8, respectively. This complements the one-dimensional NMR-based results for these two PWSDs, in terms of interaction with bile, and allows a more differentiated assessment. In contrast, the diffusion rate of Metoprolol, a drug that does not interact with bile, did not change by this TC/L concentration, as reported in previous chapters.

Mucin-interaction

Mucin interaction was previously assessed by HPLC elution profiles and tracer diffusion studies[37,38] [38]. Interestingly, NMR has been used sparingly in this context.

In our workflow, the evaluation of mucin-drug interaction is based on the assessment of the PWSD signals. Acetylsalicylic acid, a drug classified as non-mucin interacting[38], shows hardly any changes in its NMR signal pattern (**Fig. 2A**). While the aryl proton shifts δ of a mucin-interacting drug, Fluphenazine[38], are less affected, the signals broaden substantially (**Fig. 2B**). In addition, the fine structure of the signals is lost, which has been previously linked to the transition from monomers to aggregates[33,39].

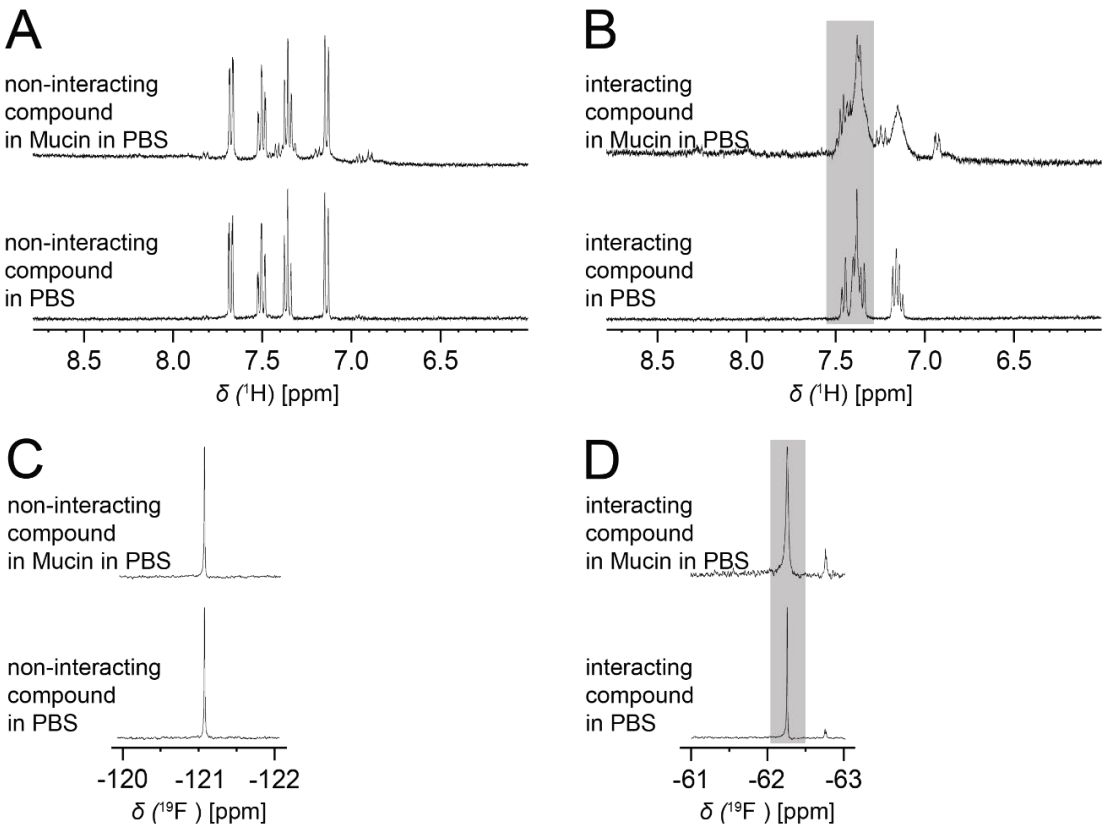

Figure 7. Analysis of interaction with mucin. Extracts from ^{1}H NMR spectra for a (A) non-interacting compound, Metoprolol, and a (B) interacting compound, Fluphenazine, in mucin in PBS (top) and PBS (bottom, grey box highlights signal broadening). Extracts from ^{19}F NMR spectra for (C) Linezolid, a non-interacting compound as reported in the previous chapter, and (D) Fluphenazine, an interacting compound as previously reported[38], in 5x TC/L in PBS (top) and PBS (bottom, grey box highlights signal broadening). The figure includes spectra from previous chapters, which were modified.

Based on pilot studies, we recommend the use of 0.2% mucin solutions in PBS, as higher mucin concentration broaden the NMR signals nonselectively (data not shown). Linezolid, non-mucin interacting as described in the previous chapter, displayed a sharp ^{19}F signal in PBS, which was not affected by mucin (**Fig. 2C**). The full width at half maximum (FWHM) of the ^{19}F signal of Linezolid was 3.82 Hz and 3.86 Hz in PBS and Mucin in PBS, respectively. In contrast, the ^{19}F signal of the interacting compound, Fluphenazine, broadened by mucin with a 2.8-fold increase in the FWHM (**Fig.2D**). Mucin-interacting substances diffuse more slowly in the presence of mucin than in free diffusion, as previously seen by non-NMR methods[31,32]. Future NMR diffusion studies could further advance these findings to integrate the diffusion coefficient as a continuous data value in the overall biopharmaceutical assessment.

Mucus-interaction

Mucus is a complex mixture that yields unspecific 1H-13C heteronuclear single quantum coherence (HSQC) spectra (Fig. 3A). From this interfering matrix, aromatic proton signals from PWSD cannot be reliably separated. However, a one-dimensional analysis is possible for PWSD with ^{19}F, as reported in the previous chapter. Signal broadening is observed for both non-interacting and interacting compounds (Fig. 3B-C). In case of the interacting compound, Fluphenazine, this coincides with a signal shift.

Drug diffusion is slowed down in mucus, but to varying degrees for interacting and non-interacting compounds. As reported in the previous chapter, Fluphenazine diffused approximately 300 times slower in mucus than in PBS, whereas non-interacting compounds diffused less than twice as slowly in mucus compared to PBS, including metoprolol, linezolid, ethanol, trifluoroacetate, trifluoroethylamine, trifluoroethanol, and water. We recommend not diluting the mucus to maximize the effects on diffusion rate and to representatively model the mucus barrier. Diffusion of ^{13}C labelled PWSD in mucus can be measured by proton-carbon heteronuclear single quantum coherence incorporated diffusion ordered spectroscopy NMR (HSQC-iDOSY NMR)[40]. This requires that the 1H-13C HSQC signal is selectively distinguishable from the mucus matrix.

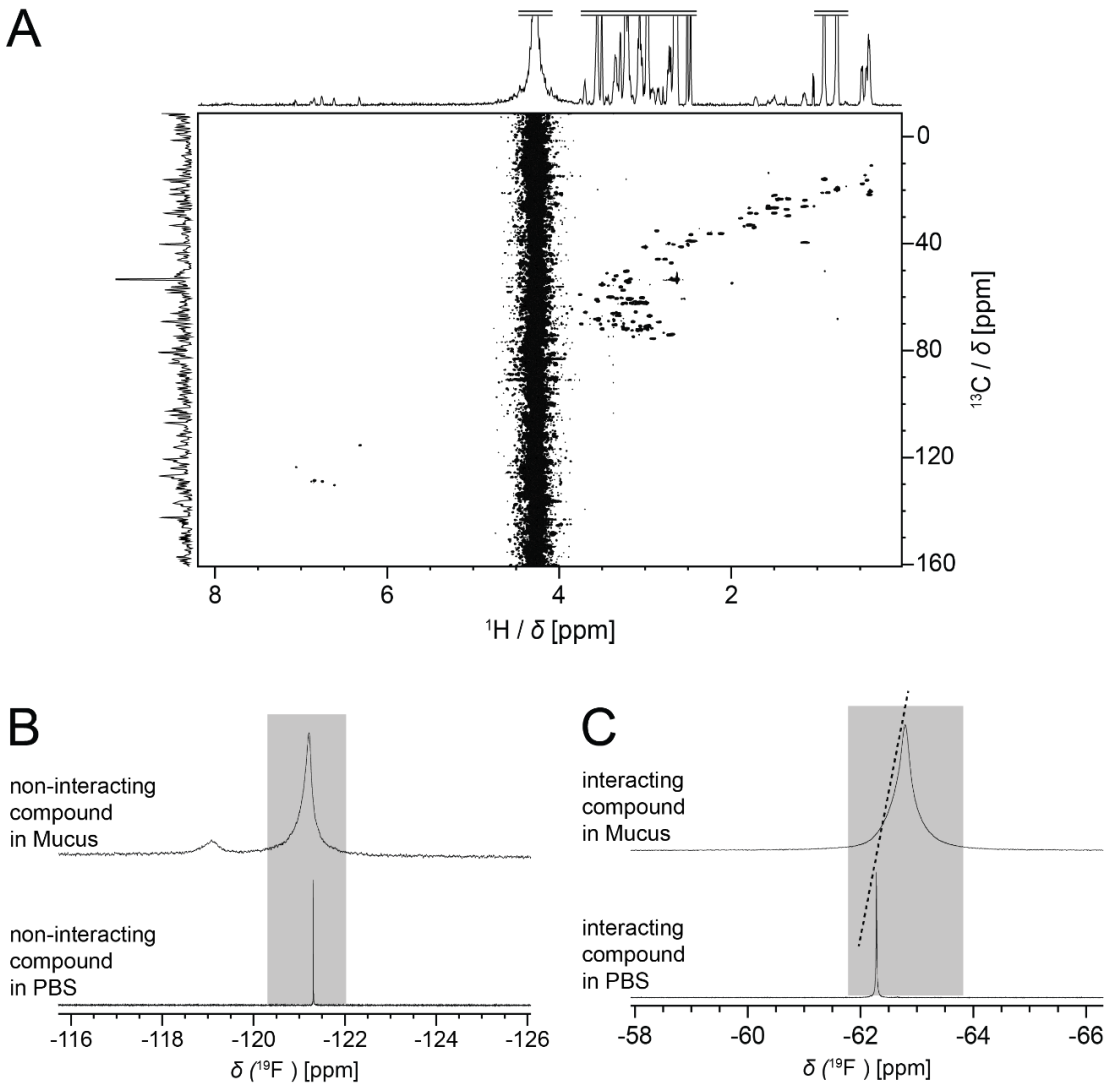

Figure 8. Analysis of interaction with mucus. (A) ^{1}H-^{13}C-HSQC spectrum of native porcine small intestinal mucus recorded with 4096 and 400 increments (td) in F2 and F1, respectively, and using the pulse sequence hsqcedetgpsisp2.2. Extracts from ^{19}F NMR spectra for (B) Linezolid, a non-interacting compound as reported in the previous chapter, and (C) Fluphenazine, an interacting compound, in mucus (top) and PBS (bottom, grey box highlights broadening, and dashed line indicates shift). The figure includes spectra from previous chapters, which were modified.

Data translation into a predictive algorithm

Previous studies have successfully translated changes in NMR patterns into quantitative structure-property relationships (QSPR)[25,41,42]. We have presented a QSPR model to predict TC/L interaction probability[25]. To make this binomial logistic regression algorithm accessible, we developed a webtool, see also SI for the script[43]. As input, the SMILES code of the compound must be entered. Besides a two-dimensional molecular structure, the logD at pH 7.4 and the CrippenMR (for the most likely protomer at pH 6.5) are computed via rdkit/scopy, from which the TC/L interaction probability is calculated[44,45]. In addition, a scatter plot is provided which relates the "CrippenMR/logD" value pair to the training/validation compounds used for model generation and testing. A data pair deviates from the model data indicate less reliable predictions. In addition, an applicability domain metric based on the sum of the tanimoto distance weighted contributions is provided allowing a quick assessment of structural similarity to the training set[46].

Similar algorithms can be developed to predict mucin-drug interactions based on NMR data collected by following our workflow. For this, the compounds from our previous study can be used, for which 2D and 3D descriptors are already available, including a manually derived subset targeting ADME properties containing about 800 of the total 2366 descriptors[25]. For exploring the experimental data space quickly, a high-capacity NMR sample robot system can increase sample throughput[47]. The resulting spectra must be parameterized to provide suitable response values for a QSPR model, e.g., the interaction-dependent signal FWHM (**Fig. 2-3**)[48]. With defined experimental endpoints at hand, resembling either continuous values (e.g., NMR shifts in ppm) or defined threshold values for a binomial classification into interacting and non-interacting compounds, depending on the dataset size, testing of different QSPR model types is conceivable, e.g., multiple linear regressions, random forests, or logistic regressions. Furthermore, (multi-)collinear descriptors could be combined into fewer latent variables[49]. After building a QSPR model, a proper validation should be performed using an external holdout set, containing about 20%[50]. The outcomes can be related to a previous study on drug retention by mucin modified HPLC columns[38]. Moreover, additional experimentally recorded retention times could be fed into the model.

The establishment of a QSPR model to predict mucin-drug interaction will be an asset for biopharmaceutical characterization in early drug development. Arguably, relationships will be established that reveal previously unknown connections paving the way for mechanistic studies. In the long term, these kinds of models can be integrated into an overarching algorithm to predict performance of drug candidates, starting from their molecular drug structure, and taking into account interactions with gastrointestinal components.

Workflow step 1: Preparing the samples

Media

Millipore water

Use deionized purified water, e.g., generate Millipore water with an in-house Millipore purification system from Merck KGaA (Darmstadt, Germany; C85358)). We refer to this as water in the following.

Phosphate-buffered saline pH 6.5

Phosphate-buffered saline pH 6.5 (PBS) is prepared following the manufactures instructions for Fasted-State Intestinal Fluid-version 1 (FaSSIF-V1) but without the addition of Taurocholate (TC) and Lecithin (L). The following substances are required for the preparation: Sodium chloride (Sigma-Aldrich; S9888), sodium hydroxide pellets (Sigma-Aldrich; 221465), monobasic sodium phosphate monohydrate (Sigma-Aldrich; S9638), and hydrochloric acid (Sigma-Aldrich; 320331). Adjust the pH value to 6.50 ± 0.05 using a pH electrode (pH/mV/°C meter, bench, pHenomenal® pH 1100 L (VWR; 662-1161)).
Use deuterium oxide (D_2O, Euroiso-top, Saarbrücken, Germany; D214H), sodium chloride, monobasic sodium phosphate monohydrate, 40% sodium deuterium oxide in deuterium oxide (Sigma-Aldrich; 176788), and 35% deuterium chloride in deuterium oxide (Sigma-Aldrich; 543047) to prepare deuterated PBS. Proceed analogously to the non-deuterated PBS but set the pD value to 6.91 ± 0.05.
PBS and other following media can be stored in Screw cap tubes (falcon tubes) with a nominal volume of 15 ml or 50 ml (Saarstedt; 62.554.502 or 62.559) or in reaction vials with a nominal volume of 1.5 or 2. mL (Saarstedt, Nümbrecht, Germany; 72.698 or 72.691).
We recommend storing PBS at 4 °C for up to one week. Allow PBS to equilibrate at room temperature for at least 30 minutes before use.

Taurocholate/Lecithin in Phosphate-buffered saline pH 6.5

Prepare FaSSIF-V1 by dissolving FaSSIF-powder (Biorelevant ltd., London, United Kingdom; FFF02) in PBS and according to manufactures instructions. Briefly, dissolve 22.4 mg FaSSIF-powder in 10 mL PBS and let the resulting colloidal solution equilibrate for 2 hours. Within the following, we refer to FaSSIF-V1 as "1-fold TC/L in PBS". 5-, 25, and 500-fold TC/L in PBS can be made analogous to TC/L in PBS but with the 5-, 25-, and 500-fold amount of FaSSIF powder, respectively. 500-fold TC/L in PBS gives a yellowish viscous colloidal solution. Store all TC/L containing solutions at room temperature and use them within 2 days.

Mucin in Phosphate-buffered saline pH 6.5

Dissolve 0.2 g mucin from porcine stomach (Sigma-Aldrich; M2378) in 100 mL PBS pH 6.5. Shake for 2 hours at 25 °C and at 300 rpm on a thermoshaker (Thermomixer F1.5 (Eppendorf, Germany). Store the suspension at room temperature and use it within 1 day. We refer to this medium as "Mucin in PBS" in the following.

Native small intestinal mucus

Fresh pig small intestines can be obtained from local slaughterhouses where pigs are slaughtered for commercial meat production. An ethical requirement is not mandatory. By law, pigs are fasted prior to slaughtering so that only small amounts of digestive residue remain in the lumen. Routinely, the entire gastrointestinal tract is provided, from which 2-3 m long section of the proximal jejunum are excised with a butcher knife. Then the intestines are tied at their ends with a cord, packed in a plastic bag, and transported on ice to the laboratory. Loosen the cords, wash the intestine with ice-cold water, and cut it into sections about 25 cm in length. The sections are opened along the mesenteric line followed by cautious (i.e., the tissue should not be damaged) mucus collection using plastic scrapers (**Fig. 4**).

Figure 9. Photo of mucus isolated with a plastic spoon from a pig small intestine opened lengthwise.

We recommend pooling 8-10 muci from different intestines aiming at reducing biological differences from batch to batch. Collect all scrapings into a large beaker on ice. Our procedure yields approximately 50-100 mL mucus. After pooling, add 1 µL of a 0.4% (w/w) sodium azide (Sigma-Aldrich; 769320) solution in PBS per 1 mL mucus and one SIGMAFAST™ Protease Inhibitor Tablet (Sigma-Aldrich; S8820) per 100 mL mucus. This prevents microbial growth and inhibits enzyme-mediated proteolysis. The pooled mucus is stirred for 24 h, at 50 rpm, at 4 °C. On the next day, the mucus is aliquoted in reaction vials and frozen at - 20 °C. We recommend storing the samples at -20 °C not longer than one year. Incubate the samples for at least 30 min at room temperature before further experimentation.

As a control, the isolated mucus should be tested with a rheometer, for instance on a Modular Compact Rheometer MCR-302 (Anton Paar, Ostfildern, Germany). Carry out the tests at 25 °C using a plate-plate geometry. Set the measuring gap to 0.3 cm. For a plate geometry with a diameter of 25 mm, 300 µL of mucus sample is sufficient to fill the gap. After transferring the mucus on top of the Peltier system, shear strain amplitude sweeps are performed with controlled strain deformation γ from 0.1% to 101% at a fixed angular frequency ω of 10 rad/s. One reads the limit of the linear viscoelastic region using a software (RheoCompassTM (Anton Paar)) and following manufactures instructions. In the linear viscoelastic region, G' must be higher than G", i.e., the mucus has a gel-like or solid/elastic structure. In addition, the flow point (G' = G") should be at a shear strain greater than 5%.

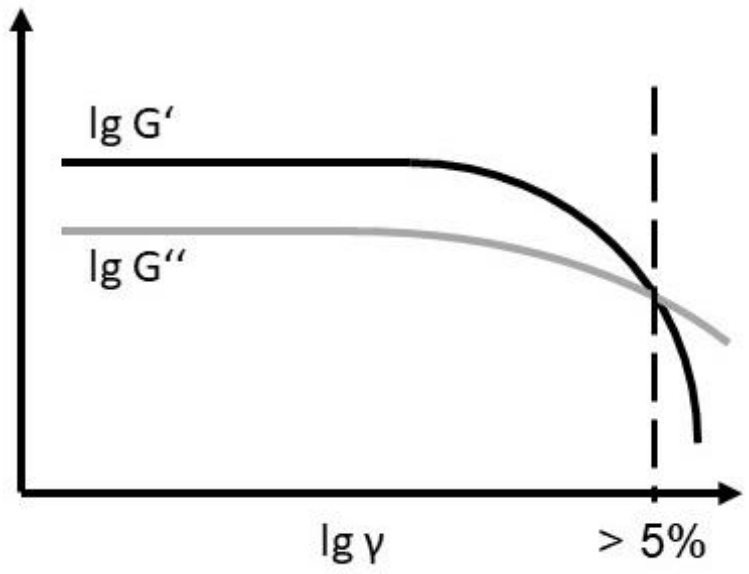

Figure 10. Schematic amplitude sweep with requirements to be fulfilled for further use of isolated mucus. The logarithmic storage modulus (G', black) and loss modulus (G'', grey) is plotted versus the logarithmic strain deformation γ. Mucus must have a gel-like structure (G' > G'' before G' leaves its plateau value) and a flow point (dashed line) of more than 5% shear strain.

If both apply, G' > G" in the linear viscoelastic region and flow point > 5% shear strain, the mucus can be further used. We refer to this rheologically verified isolate from the pig small intestine, which is further processed as described above, as "mucus" in the following.
Dispense 950 µL of the mucus into a reaction vial using a positive displacement pipette. Add 50 µL of non-deuterated 500-fold TC/L in PB. The mucus will liquefy after the addition of TC/L. Mix it (e.g., by pipetting or tapping) and allow to equilibrate/recover for at least 2 hours. The equilibrated mixture is referred to as 25x TC/L in mucus in the following.

Stock solutions

Prepare 100 µL of a 0.1 M stock solution of the compound in hexadeuterodimethyl sulfoxide (DMSO-d6, 99.9 %, Euriso-top; D010B). In the following, we refer to hexadeuterodimethyl sulfoxide as DMSO. If your compound contains fluorine-19 (^{19}F) prepare an additional 50 µL of a 1 M stock solution.
After the addition of DMSO, shake the solution for 30 s. If it is not soluble, you can use deuterated methanol (Sigma-Aldrich; 151947), deuterated ethanol (Sigma-Aldrich; 489336), deuterated PBS, or other appropriate solvents. Store the stock solution at -80 °C and for no longer than one year. Allow the stock solution to equilibrate at room temperature for at least 30 minutes before use.

Mixing

Sample preparation differs for PWSD without and with ^{19}F as follows.
PWSD without ^{19}F:
Add 10 µL 0.1 M stock solution to 990 µL of PBS, 1x TC/L in PBS, 5x TC/L in PBS, and Mucin in PBS. Vortex the samples (VTX-3000L, LMSCO. LTD., Tokyo, Japan) following by shaking for 2 hours at room temperature at 300 rpm on a mixer.
PWSD with ^{19}F:
Same as PWSD without ^{19}F, but with the following additional samples. Add 10 µL 1M stock solution to 990 µL of mucus and 25x TC/L in mucus. Note that mucus samples are not vortexed.

Workflow step 2: Preparation

Handling of nuclear magnetic resonance tubes, caps, and coaxial inserts

NMR tubes (Norell; S-5-400-7) can be reused after removing the residues of the previously measured samples. Do not use a brush for this purpose, as scratches would distort the cylindrical shape of the tube. Instead, empty the tube, fill it with 70 % v/v ethanol and place it in a sonication bath for 5 minutes. Repeat this procedure at least three times. If mucus was previously filled into the tube, repeat the procedure at least five times. The final washing step is to rinse the tube with acetone. Then place the tubes in an oven at 60 °C overnight. The next day, visually check if the tubes are clean. If so, store the clean tubes at room temperature. If not, clean them again.

The caps of the NMR tubes can be reused after cleaning, as well. To clean them, rinse them once with 70% v/v ethanol and then once with acetone. Then place the tube caps in an oven at 60 °C overnight. The next day, visually check if the tubes are clean. If so, store the clean cap tubes at room temperature. If not, clean them again.

Coaxial Inserts for NMR sample tubes (Norell, Landisville, PA, USA; NI5CCI-B) can be used for referencing and locking. This allows the study of molecular interactions and diffusion kinetics in mucus. Coaxial inserts can be reused after cleaning. For this, rinse them with 70% v/v ethanol and then with acetone. Dry the outside of tubes with a wipe. Fill the coaxial inserts with 100 µL of solvents. Fill with Hexadeuteriodimethyl sulfoxide for NMR experiments with mucus (**Fig. 5**), for all other use deuterated water (D_2O, 99.9% D) containing 0.05% 3-(trimethylsilyl)propionic-2,2,3,3-d4 sodium salt (TSP-d4, Sigma-Aldrich; 450510). Exchange the filling solution at least every 2 months.

Transfer samples to nuclear magnetic resonance tubes

Pipette 600 µL of each sample in an NMR tube. Use a plastic syringe and a standard disposable needle to transfer mucus. Avoid bubble formation in the mucus. We recommend – if appropriate custom-made equipment is available – to centrifuge the NMR tube filled with mucus for 5 s at 100 g at room temperature. Otherwise, you can hold the tube firmly in your hand and rotate your arm around your own shoulder at least ten times and as fast as possible. In this way, the mucus is pressed to the tube bottom and possible air bubbles, which would adversely affect the shim and interfere with the measurements, are pushed to the surface mucus/air (**Fig. 5**).

Coaxial inserts – use DMSO-filled for mucus samples and TSP-d4 in D_2O for all others – are lowered into the NMR tube. Clean the outside of the NMR tube with Ethanol and dry it afterwards. Insert the tube into the spinner so that the bottom of the tube reaches the bottom

of the spinner adjustment holder. Wipe the tube and spinner clean once again. The NMR samples are now ready to be measured.

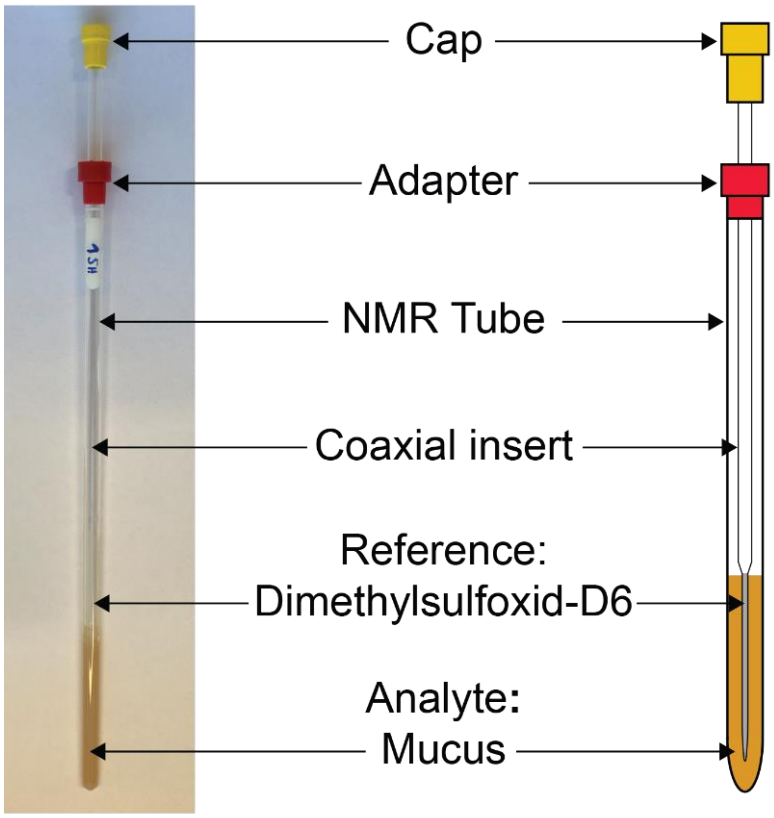

Figure 11. Photo (left) and schematic drawing (right) of the NMR tube setup for a mucus sample. A standard 5 mm NMR tube was used, mucus sample was filled in, and a coaxial insert with DMSO was lowered.

Workflow step 3: Spectra recording

Tips

We recommend using an automation software (e.g., IconNMR) to facilitate NMR data acquisition. Lock mucus samples to DMSO and all others to D_2O. In addition, we recommend optimizing NMR recording for mucus samples by pulse calibration (p1) as previously described[51].

One dimensional nuclear magnetic resonance spectroscopy

In our work, we recorded ^{1}H NMR spectra on a Bruker Avance 400 MHz spectrometer (Bruker BioSpin GmbH, Karlsruhe, Germany) operating at 400.13 MHz with a BBI BB-H 5 mm probe head. For ^{19}F NMR spectra, a Bruker Avance IV NEO 500 MHz spectrometer operating at 470.6 MHz with a Diff50 probe head was used. An overview of the acquisition parameters recommended for recording ^{1}H and ^{19}F NMR spectra is provided (**Tab.2**). When using other spectrometers, the acquisition parameters may need to be adjusted. Data processing includes a manual phase correction, automatic baseline correction, referencing to the TSP-d4 or DMSO signal and rescaling (receiver gain: 128, number of scans 128, pulse length: 0).

Table 9. Parameter for one-dimensional nuclear magnetic resonance spectroscopy experiments.

	Proton (^{1}H)	**Fluorine (^{19}F)**
Temperature [K]	300	300
Number of scans	256	256
Flip angle [°]	30	30
Spectral width [ppm]	20.55	288.62
Transmitter offset [ppm]	6.175	-110
Acquisition time [s]	3.985	0.29
Relaxation delay [s]	1.0	1.5
Spinning frequency [Hz]	20	20
Total measuring time [min]	< 30	< 30

Diffusion ordered spectroscopy nuclear magnetic resonance spectroscopy

In our work, we record ^{1}H-DOSY decay curves on a Bruker Avance III HD 600 MHz spectrometer operating at 600.4 MHz with a 5 mm BBFO probe. For ^{19}F-DOSY-NMR, a Bruker Avance IV NEO 500 MHz spectrometer operating at 470.6 MHz with a Diff50 probe head was used. The following section is a step-by-step instruction for the measurement and evaluation of a ^{1}H-DOSY and the same procedure applies to ^{19}F DOSY NMR. Set the DOSY

experiment parameters with respect to the aryl proton or ^{19}F signals of the PWSD of interest as follows.

Use the pulse sequence dstebpg3s. Do not rotate, set temperature to 300 K. Set increments to 8, number of scans to 32, diffusion time to 100 ms and the gradient duration to 1 ms.

Submit the DOSY and evaluate the decay curve according to the manufacturer's instructions (e.g., topspin instruction for Bruker devices[52]). Determine the maximum signal decay and adjust gradient duration and diffusion time to achieve a signal decay of less than 1% at highest applied gradient strength, accordingly. Your NMR department may provide you with a script, or you can calculate it using the following equation:

$$I = I_0 \times e^{-D \times \gamma^2 \times g^2 \times \delta^2 \times (\Delta - \frac{\delta}{3})}$$

where I is the observed intensity, I_0 is the reference intensity at a gradient strength of 2%, D the diffusion coefficient, and γ the gyromagnetic ratio of the observed nucleus (i.e., 4258 Hz/G for ^1H), g the gradient strength, δ the length of the gradient, and Δ the diffusion time.

Submit a DOSY using pulse sequence dstebpg3s with adjusted Δ and δ but do not exceed the maximum values limited by the NMR-hardware. Increase F1 increments to 32 and number of scans to 256.

Analyse the DOSY decay curves of both experiments and determine the diffusion coefficient. Assume the presence of one diffusing species, and consequently fit the decay to equation 1 (i.e., a mono-exponential decay).

Measure an additional DOSY experiment with the pulse sequence ledbpgp2s. Set rotation to 20 Hz. Use the same Δ, δ, and number of increments but half the number of scans to 128.

Analyze the DOSY decay curves of the experiments and determine the diffusion coefficient. D values obtained with the two different pulse sequences ledbpgp2s and dstebpg3s that differ by more than 5% suggest convection distortion. Consequently, these D values are not reliable and the DOSY must be repeated. If the difference is lower than 5%, for the evaluation of the interaction, use the D obtained by using the pulse sequence ledbpgp2s.

Supporting Information

Script

```
### Command-line python script to compute TC/L interaction probability of compound
### Version 1.0 (30.11.22): https://github.com/juppifluppi/tclint
from rdkit import Chem
from rdkit import DataStructs
from rdkit.Chem import AllChem
from rdkit.Chem.Fingerprints import FingerprintMols
from scopy.ScoPretreat import pretreat
import scopy.ScoDruglikeness
from dimorphite_dl import DimorphiteDL
import numpy as np
import sys
# load training (x,y,fil) and test set data (x2,y2,fil2)
x = [2.72, 0.15, 2.21, 2.42, 5.34, 2.15, 0.69, -2.96, 2.69, -0.82, 3.53, 0.45, 1.03, 1.49, 3.06, 2.17, 3.17,
     0.46, 1.26, 3.2, 2.95, 1.82, 2.6, 3.83, -0.62, 2.07, 1.11, 2.34, 3.14, 2.87, 2.51, 1.31, 2.04, 0.02, 1.75,
     4.57, 1.82, 2.0, 1.48, 1.81, 1.63, 0.41, 3.75, -3.43, 0.05, 1.93, 1.38, 2.63, 0.11, 1.76, 1.78, 2.41, 1.13,
     0.52, 0.32, 4.62, 5.61, 0.53, 4.19, 1.25, 2.78, 3.39, 3.22, 2.55, 2.69, 1.78, 1.29, -0.64, -3.46, 1.35,
     1.2, 0.82, -1.55, 3.18, 1.3, 0.79, -1.06, 3.17, 1.2, -1.74, -1.48, 2.03, 1.41, 3.45, 1.58, 4.01, 1.76,
     1.03, 2.71, 1.8, 2.07, -0.16, 1.03, -1.24, -0.17, -0.88, 3.83, 0.68, 0.39, 1.79, 1.35, -2.1, -0.19, 0.52,
     2.71, 1.67, 0.06, 2.82]
y = [129.53, 34.51, 106.23, 80.15, 142.54, 89.67, 103.07, 85.89, 110.48, 42.08, 194.1, 72.77, 79.08,
     46.81, 100.68, 107.17, 83.72, 105.02, 119.38, 114.12, 73.53, 46.66, 90.11, 152.95, 101.82, 94.15,
     72.57, 93.95, 91.32, 91.39, 116.46, 58.1, 83.77, 51.2, 94.14, 96.35, 99.94, 80.49, 74.9, 113.62,
     118.58, 122.69, 97.26, 106.64, 73.19, 127.35, 127.12, 100.11, 61.64, 95.14, 145.14, 89.59, 93.12,
     36.11, 56.66, 188.18, 227.4, 69.74, 152.91, 71.46, 106.07, 119.01, 127.22, 86.69, 81.14, 48.86,
     73.94, 76.86, 33.83, 81.66, 75.45, 40.7, 111.87, 79.18, 87.19, 53.42, 36.85, 97.2, 42.41, 34.75,
     84.09, 111.85, 55.75, 82.72, 70.56, 187.31, 104.6, 68.05, 86.29, 77.38, 69.74, 61.9, 106.78, 107.08,
     81.1, 32.44, 112.21, 63.22, 81.36, 68.39, 77.8, 103.41, 46.58, 70.95, 148.76, 79.76, 38.31, 130.78]
x2 = [-0.14, -1.53, 2.07, 2.77, 1.96, 1.91, -2.01, -0.46, 0.56, 1.97, 1.1, 4.34, 1.5, 1.79, 0.08, 0.33, 0.39,
     1.57]
y2 = [45.59, 51.88, 94.15, 92.01, 78.36, 86.59, 103.64, 57.3, 58.41, 136.25, 85.39, 140.98, 93.02, 51.91,
     82.93, 42.48, 65.53, 73.8]
fil = ['Clc1c(F)ccc(Nc2ncnc3c2cc(NC(=O)C=CC[NH+](C)C)c(OC2COCC2)c3)c1',
     'O=C1NC=Nc2[nH]ncc12', 'FC(F)(F)C(C)(C)c1nccc(-
     c2c(C)nc(NC(=O)N3C(C(=O)N)CCC3)s2)c1',
     'Brc1c(N)c(C[NH2+]C2CCC(O)CC2)cc(Br)c1',
     'Ic1c(OCC[NH+](CC)CC)c(I)cc(C(=O)c2c(CCCC)oc3c2cccc3)c1',
```

'[NH+](CCC=C1c2c(cccc2)CCc2c1cccc2)(C)C',
'Clc1c(C2C(C(=O)OCC)=C(COCC[NH3+])NC(C)=C2C(=O)OC)cccc1',
'O=C(NC1C(=O)N2C(C(=O)[O-])C(C)(C)SC12)C([NH3+])c1ccc(O)cc1',
'ClC(F)(F)Oc1ccc(NC(=O)c2cc(c(N3CC(O)CC3)nc2)-c2[nH]ncc2)cc1',
'O=C(Oc1c(C(=O)[O-])cccc1)C',
'O=C(OC)NC(C(=O)NN(CC(O)C(NC(=O)C(NC(=O)OC)C(C)(C)C)Cc1ccccc1)Cc1ccc(-c2ncccc2)cc1)C(C)(C)C', 'O=C(N)Cc1ccc(OCC(O)C[NH2+]C(C)C)cc1',
'O=C(OC1CC2[NH+](C)C(C1)CC2)C(CO)c1ccccc1', 'O=C(OCC)c1ccc(N)cc1',
'O=C(Oc1ccc(C(c2ncccc2)c2ccc(OC(=O)C)cc2)cc1)C',
'O=C(NC)c1nccc(Oc2cc3sc(NC4C(O)CCCC4)nc3cc2)c1',
'Brc1c(N)c(C[NH+](C)C2CCCCC2)cc(Br)c1',
'O=C1N(CCCC[NH+]2CCN(c3ncccn3)CC2)C(=O)CC2(C1)CCCC2', 'O=C([O-])c1c2n(Cc3ccc(-c4c(-c5nnn[n-]5)cccc4)cc3)c(OCC)nc2ccc1',
'Fc1c(C(=O)NC)ccc(C2=Nn3c(Cc4cc5c(nccc5)cc4)cnc3N=C2)c1',
'O=C(N)N1c2c(cccc2)C=Cc2c1cccc2', 'S=C1N(C(=O)OCC)C=CN1C', 'S(=O)(=O)(N)c1ccc(-n2c(-c3ccc(C)cc3)cc(C(F)(F)F)n2)cc1',
'Clc1c(Nc2c(S(=O)(=O)C(C)C)cccc2)nc(Nc2c(OC(C)C)cc(c(C)c2)C2CC[NH2+]CC2)nc1',
'Clc1ccc(C(N2CC[NH+](CCOCC(=O)[O-])CC2)c2ccccc2)cc1',
'O(C)c1cc2c(C(O)C3[NH+]4CC(C=C)C(C3)CC4)ccnc2cc1',
'ClC(Cl)C(=O)NC(C(O)c1ccc([N+](=O)[O-])cc1)CO',
'Clc1cc2[nH+]ccc(NC(CCC[NH+](CC)CC)C)c2cc1',
'Clc1cc2N(CCC[NH+](C)C)c3c(Sc2cc1)cccc3',
'Clc1cc2C(=CCC[NH+](C)C)c3c(Sc2cc1)cccc3',
'C(=Cc1ccccc1)C[NH+]1CCN(C(c2ccccc2)c2ccccc2)CC1',
'Clc1c([NH+]=C2NCCN2)c(Cl)ccc1', 'Clc1c(C(C(=O)OC)N2Cc3c(scc3)CC2)cccc1',
'O=C1N(C)C(=O)c2n(C)cnc2N1C',
'O=C(CO)C1(O)C2(C)CC(C3C(C(=O)C2)C2(C)C(=CC(=O)CC2)CC3)CC1',
'OC1(C#C)C2(C)CC(C3C(C4(C)CC(=Cc5oncc5C4)CC3)CC2)CC1',
'FC12C3(C)C(=CC(=O)C=C3)CCC1C1C(C)(C(O)(C(=O)CO)C(C)C1)CC2O',
'O(C)c1cc2c(cc1)CC1[NH+](C)CCC32C1CCCC3', 'Clc1c(Nc2c(CC(=O)[O-])cccc2)c(Cl)ccc1', 'O=C(OC1C(=O)N(CC[NH+](C)C)c2c(SC1c1ccc(OC)cc1)cccc2)C',
'Clc1cc2NC(=O)N(C3CC[NH+](CCCN4C(=O)Nc5c4cccc5)CC3)c2cc1', 'O=C([O-])c1cc(-c2c(O)c(N=NC3C(=O)N(c4cc(C)c(C)cc4)N=C3C)ccc2)ccc1',
'Clc1ccc(C(=O)c2ccc(OC(C(=O)OC(C)C)(C)C)cc2)cc1', 'O=C([O-])C(NC(=O)c1ccc(NCc2nc3C(=O)N=C(N)Nc3nc2)cc1)CCC(=O)[O-]',
'Clc1c(S(=O)(=O)N)cc(C(=O)[O-])c(NCc2occc2)c1', 'Clc1cc(C(=O)NCCc2ccc(S(=O)([O-])=NC(=O)NC3CCCCC3)cc2)c(OC)cc1',
'S(=O)(=O)(NC(=O)NC1CCC(C)CC1)c1ccc(CCC(=O)NN2C(=O)C(CC)=C(C)C2)cc1',
'Clc1ccc(C2(O)CC[NH+](CCCC(=O)c3ccc(F)cc3)CC2)cc1',

'Clc1c(S(=O)(=O)N)cc2S(=O)(=O)NCNc2c1',
'O=C(CO)C1(O)C2(C)C(C3C(C4(C)C(=CC(=O)CC4)CC3)C(O)C2)CC1',
'O=C(Nc1cc(Nc2nc(-c3cnccc3)ccn2)c(C)cc1)c1ccc(CN2CC[NH+](C)CC2)cc1',
'[NH+](CCCN1c2c(cccc2)CCc2c1cccc2)(C)C', 'Clc1ccc(C(=O)n2c(C)c(CC(=O)[O-
])c3c2ccc(OC)c3)cc1', 'O=C(NN)c1ccncc1', 'OC(C[NH2+]C(C)C)c1cc(O)c(O)cc1',
'Clc1c(C2(Cn3ncnc3)OC(COc3ccc(N4CCN(c5ccc(N6C(=O)N(C(CC)C)N=C6)cc5)CC4)cc3)
CO2)ccc(Cl)c1',
'O=C1OC2CC3(OC(C(CC)C)C(C)CC3)OC(CC=C(C)C(OC3OC(C)C(OC4OC(C)C(O)C(O
C)C4)C(OC)C3)C(C)C=CC=C3C4(O)C(C(O)C(C)=CC14)OC3)C2', 'O=C([O-
])C(C)c1cc(C(=O)c2ccccc2)ccc1', 'Clc1c(OCc2cc(F)ccc2)ccc(Nc2ncnc3c2cc(-
c2oc(C[NH2+]CCS(=O)(=O)C)cc2)cc3)c1', 'O=C(Nc1c(C)cccc1C)C[NH+](CC)CC',
'Clc1cc2c(C(=C3CCN(C(=O)OCC)CC3)c3ncccc3CC2)cc1', 'FC(F)(C)c1c(-
c2c(Oc3ccc(C=CC(=O)[O-])cc3)c3c(s2)cc(O)cc3)ccc(F)c1',
'FC(F)(F)c1nccc(C(=O)Nc2cc(c(C)cc2)-c2cc(OCCO)nc(N3CCOCC3)c2)c1',
'[NH2+](CCCC12c3c(cccc3)C(c3c1cccc3)CC2)C',
'FC(F)(F)c1nc2c(C(F)(F)F)cccc2c(C(O)C2[NH2+]CCCC2)c1',
'O=C1C(C)=CC(=O)c2c1cccc2', 'O=C(Nc1c(C)cccc1C)C1[NH+](C)CCCC1', 'S(=O)(=O)([O-
])CN(C)C=1C(=O)N(N(C)C=1C)c1ccccc1', '[NH2+]=C(N=C(N)N)N(C)C',
'Clc1c(N)cc(OC)c(C(=O)NCC[NH+](CC)CC)c1',
'O(CCc1ccc(OCC(O)C[NH2+]C(C)C)cc1)C', 'O=[N+]([O-])c1n(CCO)c(C)nc1',
'O=C(N)C=1C(=O)C2(O)C(O)=C3C(=O)c4c(O)ccc(N(C)C)c4CC3CC2C([NH+](C)C)C=1[
O-]', 'Clc1c([N-]C(=O)c2c(O)ccc(Cl)c2)ccc([N+](=O)[O-])c1', 'O=[N+]([O-
])c1c(C2C(C(=O)OC)=C(C)NC(C)=C2C(=O)OC)cccc1', 'O=[N+]([O-
])c1oc(C=NN2C(=O)NC(=O)C2)cc1', 'O=C([O-])c1c(O)cc(N)cc1',
'O(C)c1c(OC)ccc(Cc2[nH+]ccc3c2cc(OC)c(OC)c3)c1', 'O=C(Nc1ccc(O)cc1)C',
'SC(C([NH3+])C(=O)[O-])(C)C', 'O=C(NC1C(=O)N2C(C(=O)[O-
])C(C)(C)SC12)COc1ccccc1', 'Clc1cc2N(CCC[NH+]3CCN(CCO)CC3)c3c(Sc2cc1)cccc3',
'O=C1N(N(C)C(C)=C1)c1ccccc1', 'O=C1C(C(CC)c2ccccc2)=C([O-])c2c(O1)cccc2',
'O=C1C(c2ccccc2)(c2ccccc2)NC(=O)N1',
'Fc1c(C2(Cn3ncnc3)OCC(COc3ccc(N4CCN(c5ccc(N6C(=O)N(C(C(O)C)CC)N=C6)cc5)CC
4)cc3)C2)ccc(F)c1',
'O=C(OCC(=O)C1(O)C2(C)C(C3C(C4(C)C(=CC(=O)C=C4)CC3)C(O)C2)CC1)C',
'O=C(OCC[NH+](CC)CC)c1ccc(N)cc1', '[NH+](C(CN1c2c(Sc3c1cccc3)cccc2)C)(C)C',
'O(CC(O)C[NH2+]C(C)C)c1c2c(ccc1)cccc2', 'O=C1N(N(C)C(C)=C1CCC)c1ccccc1',
'O=C1N(C)C(=O)c2n(CC(O)C)cnc2N1C',
'O(CCO)CCN1CCN(C2=[NH+]c3c(Sc4c2cccc4)cccc3)CC1',
'O=C(OCC)C(NC(C(=O)N1C(C(=O)[O-])CC2C1CCC2)C)CCc1ccccc1',
'S(CCNC(NC)=C[N+](=O)[O-])Cc1oc(C[NH+](C)C)cc1', 'O=C([O-])c1c(O)cccc1',
'S(C(=O)C)C1C2C3C(C)(C4(OC(=O)CC4)CC3)CCC2C2(C)C(=CC(=O)CC2)C1',

```
        'S(=O)([O-])(=Nc1noc(C)c1)c1ccc(N)cc1',
        'S(=O)(=O)(NC)Cc1cc2c(CC[NH+](C)C)c[nH]c2cc1', 'Brc1c(N)nc(-n2nccc2)nc1-n1nccc1',
        'O=C(OCC[NH+](C)C)c1ccc(NCCCC)cc1',
        'O=C(N)C=1C(=O)C2(O)C(O)=C3C(=O)c4c(O)cccc4C(O)(C)C3CC2C([NH+](C)C)C=1[O-
        ]', 'O=C1N(C)C(=O)c2nc[nH]c2N1C', 'S(=O)([O-])(=NC(=O)NCCCC)c1ccc(C)cc1',
        'Ic1cc(F)c(NC=2N(C)C(=O)C(C)=C3N(c4cc(NC(=O)C)ccc4)C(=O)N(C(=O)C=23)C2CC2)c
        c1', 'O(C)c1c(OC)cc(Cc2c(N)nc(N)[nH+]c2)cc1OC', 'O=C([O-])C(CCC)CCC',
        'O(C)c1c(OC)ccc(C(C#N)(C(C)C)CCC[NH+](CCc2cc(OC)c(OC)cc2)C)c1']
fil2 = ['S(=O)(=O)(N)c1sc(NC(=O)C)nn1', 'SCC(C(=O)N1C(C(=O)[O-])CCC1)C',
        'O(C)c1cc2c(C(O)C3[NH+]4CC(C=C)C(C3)CC4)ccnc2cc1',
        '[NH+](CCC1=C(C(C)c2ncccc2)c2c(cccc2)C1)(C)C',
        'O(C(c1ccccc1)c1ccccc1)CC[NH+](C)C', '[NH+](CCC=C1c2c(OCc3c1cccc3)cccc2)(C)C',
        'O=C(N)C=1C(=O)C2(O)C(O)=C3C(=O)c4c(O)cccc4C(C)C3C(O)C2C([NH+](C)C)C=1[O-
        ]', 'O=C1N(C)C(=O)c2n(CCO)cnc2N1C', 'O=C([O-])C(C)c1ccc(CC(C)C)cc1',
        'Clc1ccc(C2(O)CC[NH+](CCC(C(=O)N(C)C)(c3ccccc3)c3ccccc3)CC2)cc1',
        'O=C(Oc1c(C)c(C)c(OCC(O)C[NH2+]C(C)C)cc1C)C', 'FC(F)(F)c1cc(NC(=O)c2cc(Nc3nc(-
        c4cnccc4)ccn3)c(C)cc2)cc(-n2cc(C)nc2)c1',
        '[SH0](=O)(Cc1c(C)c(OC)c(C)cn1)c1[nH]c2c(n1)cc(OC)cc2', 'O=C(Nc1ccc(OCC)cc1)C',
        'O=C(Nc1ncccc1)C=1N(C)S(=O)(=O)c2c(C=1[O-])cccc2', 'OCc1c(O)c(C)ncc1CO',
        'OC(C[NH2+]C(C)(C)C)c1cc(CO)c(O)cc1', 'Nc1c(-c2ccccc2)nc2c(N)nc(N)nc2n1']
# convert to rdkit mols (o,ox)
o=[]
for lines in fil:
   o.append(Chem.MolFromSmiles(lines))
ox=[]
for lines in fil2:
   ox.append(Chem.MolFromSmiles(lines))
# if datafile (*.dat) is given as input: compute properties for each line
if sys.argv[1].split(".")[-1] == "dat":
   try:
      with open("results.dat","a") as f:
         f.write("SMILES" + "\t" + "logD" + "\t" + "CrippenMR" + "\t" + "Probability" + "\n")
      with open(sys.argv[1],"r") as smx:
         for lines in smx:
               SMI = str(lines)
               dimorphite_dl = DimorphiteDL(
                  min_ph = 6.4,
                  max_ph = 6.6,
                  max_variants = 1,
```

```
                label_states = False,
                pka_precision = 0.1)
            SMI = str(dimorphite_dl.protonate(SMI)[0])
            mol = Chem.MolFromSmiles(SMI)
            sdm = pretreat.StandardizeMol()
            mol = sdm.disconnect_metals(mol)
            logd = scopy.ScoDruglikeness.molproperty.CalculateLogD(mol)
            mr = scopy.ScoDruglikeness.molproperty.CalculateMolMR(mol)
            tcl1 = ( ( logd - 1.510648) / 1.708574 ) * 1.706694
            tcl2 = ( ( mr - 90.62889 ) / 35.36033 ) * 2.4925333
            tcl3 = 1 / ( 1 + ( 2.718281828459045 ** ( -1 * ( 0.9872289 + tcl1 + tcl2 ) ) ) )
            with open("results.dat","a") as f:
                f.write(str(SMI) + "\t" + str(round(logd,2)) + "\t" + str(round(mr,2)) + "\t" +
    str(int(round(tcl3*100,0))) + "\n")
    except:
        print("Something is wrong with your SMILES codes.")
    sys.exit()
# if SMILES codes are given as input: protonate and pretreat given SMILES, compute descriptors
     via rdkit/scopy, calculate probability
try:
    SMI = str(sys.argv[1])

    dimorphite_dl = DimorphiteDL(
        min_ph = 6.4,
        max_ph = 6.6,
        max_variants = 1,
        label_states = False,
        pka_precision = 0.1
    )
    SMI = str(dimorphite_dl.protonate(SMI)[0])
    mol = Chem.MolFromSmiles(SMI)
    sdm = pretreat.StandardizeMol()
    mol = sdm.disconnect_metals(mol)
    logd = scopy.ScoDruglikeness.molproperty.CalculateLogD(mol)
    mr = scopy.ScoDruglikeness.molproperty.CalculateMolMR(mol)
    tcl1 = ( ( logd - 1.510648) / 1.708574 ) * 1.706694
    tcl2 = ( ( mr - 90.62889 ) / 35.36033 ) * 2.4925333
    tcl3 = 1 / ( 1 + ( 2.718281828459045 ** ( -1 * ( 0.9872289 + tcl1 + tcl2 ) ) ) )
    print("TC/L interaction probability model")
```

```
    print("--------------------------------")
    print("Compound properties:")
    print("logD: " + str(round(logd,2)))
    print("CrippenMR: " + str(round(mr,2)))
    print("TC/L interaction probability: " + str(int(round(tcl3*100,0))) + " %")
    print("--------------------------------")
except:
    print("Something is wrong with your SMILES code.")
    sys.exit()
# copmute tanimoto ecfp_4 fingerprints to calculate SDC metrics
fp1 = AllChem.GetMorganFingerprint(mol, 2)
g=[]
for molx in o:
    fp2 = AllChem.GetMorganFingerprint(molx, 2)
    Tan = DataStructs.TanimotoSimilarity(fp1,fp2)
    try:
        scd = 2.718281828459045 ** ((-3 * Tan)/(1 - Tan))
        g.append(scd)
    except:
        pass
li=[]

for k in ox:
    lkx=[]
    fp1 = AllChem.GetMorganFingerprint(k, 2)
    for molx in o:
        fp2 = AllChem.GetMorganFingerprint(molx, 2)
        Tan = DataStructs.TanimotoSimilarity(fp1,fp2)
        try:
            scd = 2.718281828459045 ** ((-3 * Tan)/(1 - Tan))
            lkx.append(scd)
        except:
            pass
    li.append(np.sum(lkx))
lit=[]
for k in o:
    lkx=[]
    fp1 = AllChem.GetMorganFingerprint(k, 2)
    for molx in o:
```

```
        fp2 = AllChem.GetMorganFingerprint(molx, 2)
        Tan = DataStructs.TanimotoSimilarity(fp1,fp2)
        try:
            scd = 2.718281828459045 ** ((-3 * Tan)/(1 - Tan))
            lkx.append(scd)
        except:
            pass
    lit.append(np.sum(lkx))
# output values
print("Modeling sets:")
print("Training set logD: "+str(round(np.min(x),2))+" - "+str(round(np.max(x),2))+" (Mean:
      "+str(round(np.mean(x),2))+"; SD: "+str(round(np.std(x),2))+")")
print("Training set CrippenMR: "+str(round(np.min(y),2))+" - "+str(round(np.max(y),2))+"
      (Mean: "+str(round(np.mean(y),2))+"; SD: "+str(round(np.std(y),2))+")")
print("Validation set logD: "+str(round(np.min(x2),2))+" - "+str(round(np.max(x2),2))+" (Mean:
      "+str(round(np.mean(x2),2))+"; SD: "+str(round(np.std(x2),2))+")")
print("Validation set CrippenMR: "+str(round(np.min(y2),2))+" - "+str(round(np.max(y2),2))+"
      (Mean: "+str(round(np.mean(y2),2))+"; SD: "+str(round(np.std(y2),2))+")")
print("---------------------------------")
print("SDC applicability domain metrics:")
print("Training set: "+str(round(np.min(lit),2))+" - "+str(round(np.max(lit),2))+" (Mean:
      "+str(round(np.mean(lit),2))+"; SD: "+str(round(np.std(lit),2))+")")
print("Compound: "+str(round(np.sum(g),2)))
print("---------------------------------")

print("Version: 1.0 (30.11.22)")
print("Web version: https://tclint.streamlit.app/")
print("More info can be found on: https://github.com/juppifluppi/tclint")
sys.exit()
```

Acknowledgement

We acknowledge the financial support by BASF SE for SH. We acknowledge proofreading by Theresa Zorn and Dr. Jonas Schlauersbach. We appreciate coding support by Joseph Kehrein.

References

1 Williams III, R. O., Watts, A. B. & Miller, D. A. *Formulating poorly water soluble drugs*. Vol. 3 (Springer, 2012).

2 Fahr, A. & Liu, X. Drug delivery strategies for poorly water-soluble drugs. *Expert Opin Drug Deliv* **4**, 403-416, doi:10.1517/17425247.4.4.403 (2007).

3 Boyd, B. J. *et al.* Successful oral delivery of poorly water-soluble drugs both depends on the intraluminal behavior of drugs and of appropriate advanced drug delivery systems. *Eur J Pharm Sci* **137**, 104967, doi:10.1016/j.ejps.2019.104967 (2019).

4 Buckley, S. T., Frank, K. J., Fricker, G. & Brandl, M. Biopharmaceutical classification of poorly soluble drugs with respect to "enabling formulations". *Eur J Pharm Sci* **50**, 8-16, doi:10.1016/j.ejps.2013.04.002 (2013).

5 Sigurdsson, H. H., Kirch, J. & Lehr, C. M. Mucus as a barrier to lipophilic drugs. *Int J Pharm* **453**, 56-64, doi:10.1016/j.ijpharm.2013.05.040 (2013).

6 Boegh, M. & Nielsen, H. M. Mucus as a barrier to drug delivery - understanding and mimicking the barrier properties. *Basic Clin Pharmacol Toxicol* **116**, 179-186, doi:10.1111/bcpt.12342 (2015).

7 Savjani, K. T., Gajjar, A. K. & Savjani, J. K. Drug solubility: importance and enhancement techniques. *ISRN Pharm* **2012**, 195727, doi:10.5402/2012/195727 (2012).

8 Panchagnula, R. & Thomas, N. S. Biopharmaceutics and pharmacokinetics in drug research. *Int J Pharm* **201**, 131-150, doi:10.1016/s0378-5173(00)00344-6 (2000).

9 Boyer, J. L. Bile formation and secretion. *Compr Physiol* **3**, 1035-1078, doi:10.1002/cphy.c120027 (2013).

10 Perez de la Cruz Moreno, M. *et al.* Characterization of fasted-state human intestinal fluids collected from duodenum and jejunum. *J Pharm Pharmacol* **58**, 1079-1089, doi:10.1211/jpp.58.8.0009 (2006).

11 Hofmann, A. F. The continuing importance of bile acids in liver and intestinal disease. *Arch Intern Med* **159**, 2647-2658, doi:10.1001/archinte.159.22.2647 (1999).

12 Pavlovic, N. *et al.* Bile Acids and Their Derivatives as Potential Modifiers of Drug Release and Pharmacokinetic Profiles. *Front Pharmacol* **9**, 1283, doi:10.3389/fphar.2018.01283 (2018).

13 Klein, S. The use of biorelevant dissolution media to forecast the in vivo performance of a drug. *AAPS J* **12**, 397-406, doi:10.1208/s12248-010-9203-3 (2010).

14 Fagerberg, J. H. *et al.* Dissolution rate and apparent solubility of poorly soluble drugs in biorelevant dissolution media. *Mol Pharm* **7**, 1419-1430, doi:10.1021/mp100049m (2010).

15 Cornick, S., Tawiah, A. & Chadee, K. Roles and regulation of the mucus barrier in the gut. *Tissue Barriers* **3**, e982426, doi:10.4161/21688370.2014.982426 (2015).

16 Celli, J. *et al.* Viscoelastic properties and dynamics of porcine gastric mucin. *Biomacromolecules* **6**, 1329-1333, doi:10.1021/bm0493990 (2005).

17 Bansil, R. & Turner, B. S. The biology of mucus: Composition, synthesis and organization. *Adv Drug Deliv Rev* **124**, 3-15, doi:10.1016/j.addr.2017.09.023 (2018).

18 Bhat, P. The limiting role of mucus in drug absorption: Drug permeation through mucus solution. *International Journal of Pharmaceutics* **126**, 179-187, doi:10.1016/0378-5173(95)04120-6 (1995).

19 Srinivasan, S. S. *et al.* RoboCap: Robotic mucus-clearing capsule for enhanced drug delivery in the gastrointestinal tract. *Sci Robot* **7**, eabp9066, doi:10.1126/scirobotics.abp9066 (2022).

20 Berben, P. *et al.* Drug permeability profiling using cell-free permeation tools: Overview and applications. *Eur J Pharm Sci* **119**, 219-233, doi:10.1016/j.ejps.2018.04.016 (2018).

21 Wright, L., Barnes, T. J., Joyce, P. & Prestidge, C. A. Optimisation of a High-Throughput Model for Mucus Permeation and Nanoparticle Discrimination Using Biosimilar Mucus. *Pharmaceutics* **14**, doi:10.3390/pharmaceutics14122659 (2022).

22 Falavigna, M. *et al.* Mucus-PVPA (mucus Phospholipid Vesicle-based Permeation Assay): An artificial permeability tool for drug screening and formulation development. *Int J Pharm* **537**, 213-222, doi:10.1016/j.ijpharm.2017.12.038 (2018).

23 Holzgrabe, U. *NMR spectroscopy in pharmaceutical analysis*. (Elsevier, 2017).

24 Pellecchia, M., Sem, D. S. & Wuthrich, K. NMR in drug discovery. *Nat Rev Drug Discov* **1**, 211-219, doi:10.1038/nrd748 (2002).

25 Schlauersbach, J. *et al.* Predicting Bile and Lipid Interaction for Drug Substances. *Mol Pharm* **19**, 2868-2876, doi:10.1021/acs.molpharmaceut.2c00227 (2022).

26 Hanio, S. *et al.* Drug-Induced Dynamics of Bile Colloids. *Langmuir* **37**, 2543-2551, doi:10.1021/acs.langmuir.0c02282 (2021).

27 Wiest, J. *et al.* Geometrical and Structural Dynamics of Imatinib within Biorelevant Colloids. *Mol Pharm* **15**, 4470-4480, doi:10.1021/acs.molpharmaceut.8b00469 (2018).

28 Pages, G., Gilard, V., Martino, R. & Malet-Martino, M. Pulsed-field gradient nuclear magnetic resonance measurements (PFG NMR) for diffusion ordered spectroscopy (DOSY) mapping. *Analyst* **142**, 3771-3796, doi:10.1039/c7an01031a (2017).

29 James, T. L. & McDonald, G. G. Measurement of the self-diffusion coefficient of each component in a complex system using pulsed-gradient fourier transform NMR. *Journal of Magnetic Resonance (1969)* **11**, 58-61, doi:10.1016/0022-2364(73)90081-4 (1973).

30 Vogtherr, M., Marx, A., Mieden, A. C. & Saal, C. Investigation of solubilising effects of bile salts on an active pharmaceutical ingredient with unusual pH dependent solubility by NMR spectroscopy. *Eur J Pharm Biopharm* **92**, 32-41, doi:10.1016/j.ejpb.2015.02.016 (2015).

31 Falavigna, M., Stein, P. C., Flaten, G. E. & di Cagno, M. P. Impact of Mucin on Drug Diffusion: Development of a Straightforward in Vitro Method for the Determination of Drug Diffusivity in the Presence of Mucin. *Pharmaceutics* **12**, doi:10.3390/pharmaceutics12020168 (2020).

32 Larhed, A. W., Artursson, P. & Bjork, E. The influence of intestinal mucus components on the diffusion of drugs. *Pharm Res* **15**, 66-71, doi:10.1023/a:1011948703571 (1998).

33 LaPlante, S. R. *et al.* Compound aggregation in drug discovery: implementing a practical NMR assay for medicinal chemists. *J Med Chem* **56**, 5142-5150, doi:10.1021/jm400535b (2013).

34 Endres, S. *et al.* Concentration and composition dependent aggregation of Pluronic- and Poly-(2-oxazolin)-Efavirenz formulations in biorelevant media. *J Colloid Interface Sci* **606**, 1179-1192, doi:10.1016/j.jcis.2021.08.040 (2022).

35 Schlauersbach, J. *et al.* Leveraging bile solubilization of poorly water-soluble drugs by rational polymer selection. *J Control Release* **330**, 36-48, doi:10.1016/j.jconrel.2020.12.016 (2021).

36 Wiest, J. *et al.* Geometrical and Structural Dynamics of Imatinib within Biorelevant Colloids. *Mol. Pharmaceutics* **15**, 4470-4480, doi:10.1021/acs.molpharmaceut.8b00469 (2018).

37 Larhed, A. W., Artursson, P., Grasjo, J. & Bjork, E. Diffusion of drugs in native and purified gastrointestinal mucus. *J Pharm Sci* **86**, 660-665, doi:10.1021/js960503w (1997).

38 Gargano, A. F., Lammerhofer, M., Lonn, H., Schoenmakers, P. J. & Leek, T. Mucin-based stationary phases as tool for the characterization of drug-mucus interaction. *J Chromatogr A* **1351**, 70-81, doi:10.1016/j.chroma.2014.05.031 (2014).

39 Murugesan, J. R. *et al.* Revealing dye and dye-drug aggregation into nano-entities using NMR. *Dyes and Pigments* **153**, 300-306, doi:10.1016/j.dyepig.2018.02.026 (2018).

40 McLachlan, A. S., Richards, J. J., Bilia, A. R. & Morris, G. A. Constant time gradient HSQC-iDOSY: practical aspects. *Magn Reson Chem* **47**, 1081-1085, doi:10.1002/mrc.2518 (2009).

41 Willighagen, E. L., Denissen, H. M., Wehrens, R. & Buydens, L. M. On the use of 1H and 13C 1D NMR spectra as QSPR descriptors. *J Chem Inf Model* **46**, 487-494, doi:10.1021/ci050282s (2006).

42 Verma, R. P. & Hansch, C. Use of 13C NMR chemical shift as QSAR/QSPR descriptor. *Chem Rev* **111**, 2865-2899, doi:10.1021/cr100125d (2011).

43 Kehrein, J. & Hanio, S. *TC/L interaction probability model*, <https://tclint.streamlit.app> (2022).

44 Wildman, S. A. & Crippen, G. M. Prediction of Physicochemical Parameters by Atomic Contributions. *Journal of Chemical Information and Computer Sciences* **39**, 868-873, doi:10.1021/ci990307l (1999).

45 Yang, Z. Y., Yang, Z. J., Lu, A. P., Hou, T. J. & Cao, D. S. Scopy: an integrated negative design python library for desirable HTS/VS database design. *Brief Bioinform* **22**, doi:10.1093/bib/bbaa194 (2021).

46 Liu, R. & Wallqvist, A. Molecular Similarity-Based Domain Applicability Metric Efficiently Identifies Out-of-Domain Compounds. *J Chem Inf Model* **59**, 181-189, doi:10.1021/acs.jcim.8b00597 (2019).

47 Soininen, P. *et al.* High-throughput serum NMR metabonomics for cost-effective holistic studies on systemic metabolism. *Analyst* **134**, 1781-1785, doi:10.1039/b910205a (2009).

48 Willcott, M. R. MestRe Nova. *Journal of the American Chemical Society* **131**, 13180-13180, doi:10.1021/ja906709t (2009).

49 Kiralj, R. & Ferreira, M. M. C. Is your QSAR/QSPR descriptor real or trash? *Journal of Chemometrics* **24**, 681-693, doi:10.1002/cem.1331 (2010).

50 Cherkasov, A. *et al.* QSAR modeling: where have you been? Where are you going to? *J Med Chem* **57**, 4977-5010, doi:10.1021/jm4004285 (2014).

51 Wu, P. S. & Otting, G. Rapid pulse length determination in high-resolution NMR. *J Magn Reson* **176**, 115-119, doi:10.1016/j.jmr.2005.05.018 (2005).

52 Rainer Kerssebaum, N. A. L., Bruker BioSpin GmbH, Rheinstetten, Germany. *DOSY and Diffusion by NMR*, <http://sopnmr.ucsd.edu/assets/pdf/DOSY_and_Diffusion.pdf> (2006).

Conclusion and outlook

Formulation scientists seek solutions to improve the oral bioavailability of poorly-water soluble drugs. Most strategies are pharmaceutical-galenic and aim to maximize the apparent solubility of a drug, either by altering the physical state of a drug (e.g., salt design, size-particle reduction) or by excipient-based approaches (e.g., solubilizers, lipid-based delivery systems, amorphous solid dispersions). In addition, biopharmaceutical optimization can be pursued to boost oral drug product performance. For example, bile is key to efficient solubilization of poorly-water soluble drugs in the intestine. To date, however, there is a lack of molecular understanding of the dynamics of bile colloids in response to stimuli during gastrointestinal-based drug delivery. Possible drivers of dynamics range from exogenous trigger such as drug substance and excipients to endogenous key player in the intestine such as the mucus layer covering the intestinal epithelium. In this vein, this thesis explores the molecular dynamics between gastrointestinal components and oral drug products.

Bile colloids were found to be adaptable in solubilizing drug substances while providing a constant bioavailable drug fraction in the intestine. In addition, pharmaceutical polymers were identified that alter the arrangement and geometry of the bile colloid and thus affect the solubilization of drugs by bile. This suggests a practical optimization parameter that directs formulations towards efficient solubilization by bile through rational polymer selection. Lastly, bile temporarily stiffened mucus isolated from pigs and selectively facilitated transport of drugs through mucus. This culminated in a blueprint to evaluate the importance of bile on drug permeability through mucus based on molecular properties.

Overall, the biopharmaceutical perspectives outlined in this thesis has the potential to substantially improve the pharmaceutical development outcome and to unleash innovative formulation strategies. Generalizing the findings of this thesis by expanding the chemical space using high-throughput screening datasets might allow to establish overarching algorithms predictive for the mucus/bile/drug interplay and aiming to optimize drug presentation to the intestinal epithelium. In addition, this work can stimulate further research in the field of mucus, addressing the following pressing questions, among others. How can the pharmaceutical treatment of patients after cholecystectomy be optimized? Was there an evolutionary pressure related to the permeability of mucus to essential molecules that favored pulsatile release of the gallbladder in humans over continuous emptying from the liver? Is there a connection between a positive food effect and the benefit from bile-facilitated lifting across mucus?

Abbreviations

This section contains a table listing the abbreviations and their meaning used in this thesis. Unless noted, the abbreviation is the same across all chapters.

Abbreviation	Meaning	Chapter
^{1}H NMR	^{1}H Nuclear Magnetic Resonance	
γflow	Flow point	
γLVR	Limit of the linear viscoelastic region	
δ	Chemical shift	
η0	Zero-shear rate viscosity	
τy	Yield stress	
ACN	Acetonitrile	
Alexa	Alexa Fluor 647	
ASD	Amorphous solid dispersions	
ANOVA	Analysis of variance	
AUC	Analytical ultracentrifugation	1
AUC	Area Under Curve	2-3
BSM	Bile salt micelles	
CG	Coarse-grained	
cmax	Maximum of plasma concentration	
COSY	Correlated spectroscopy	
D	Diffusion coefficient	
D_2O	Deuterated water	
DCl	Deuterium chloride	
Dextran-Alexa	Alexa Fluor 647 coupled to a 10-kDa dextran	
DFG	Deutsche Forschungsgemeinschaft	
DLS	Dynamic light scattering	
DMM	Differential dynamic microscopy	
DMSO	Dimethyl sulfoxide	
DMSO-d6	Hexadeuteriodimethyl sulfoxide	
DOSY	Diffusion-ordered spectroscopy	
EFRE	Europäischer Fonds für regionale Entwicklung	
FaSSIF-V1	Fasted State Simulated Intestinal Fluid-Version 1	
FCS	Fluorescence correlation spectroscopy	
GIT	Gastrointestinal tract	
HIRI	Helmholtz Institute for RNA-based Infection Biology	
HPLC	High performance liquid chromatography	1

continued next page

Abbreviation	Meaning	Chapter
HPLC	High pressure liquid chromatography	2-3, Annex
HPMC-AS	Hydroxypropyl methylcellulose acetate succinate	
HSQC	Heteronuclear single quantum coherence	
ILL	Institut Laue – Langevin	
ITC	Isothermal titration calorimetry	
J0	Instantaneous compliance	
Jm	Viscoelastic compliance	
JCSM	Jena Center for Soft Matter	
K	Flow consistency index	
L	Lecithin	
LC-MS/MS	Liquid chromatography-tandem mass spectrometry	
MD	Molecular dynamics	
MIM	Mixed micelles	
MSD	Mean-squared-displacement	
N	Flow behaviour index	
NaOD	Sodium deuteroxide	
NMR	Nuclear Magnetic Resonance	
NOESY	Nuclear Overhauser enhancement spectroscopy	
OD	Optical density	
P	Perphenazine	
PBS	Phosphate buffered saline	
PDI	Polydispersity Index	
PK	Pharmacokinetic	
PIPC	1-Palmitoyl-2-linoleoylphosphatidylcholine	
PWSD	Poorly water-soluble drugs	
QSPR	Quantitative structure-property relationships	
RP	Reversed phase	
Rxy	Correlation coefficient	
SANS	Small-angle neutron scattering	
SFB	Sonderforschungsbereich	
SD	Standard deviation	
TAB	Thüringer Aufbaubank	
TC	Taurocholate	
TC/L MIM	Taurocholate and lecithin mixed micelles	
TFA	Trifluoroacetic acid	
TM	Mean retardation times	
tmax	Time to peak drug concentration	
TFE	Trifluoroethanol	
TSP-d4	3-(Trimethylsilyl)propionic-2,2,3,3-d4	

continued next page

Abbreviation	Meaning	Chapter
UHPLC	Ultra-high performance liquid chromatography	
Vitamin E TPGS	D-α-Tocopherol polyethylene glycol 1000 succinate	

Curriculum Vitae

List of publications

First authorship

Hanio, S.; Schlauersbach, J.; Lenz, B.; Spiegel, F.; Bockmann, R. A.; Schweins, R.; Nischang, I.; Schubert, U. S.; Endres, S.; Poppler, A. C.; Brandl, F. P.; Smit, T. M.; Kolter, K.; Meinel, L., Drug-Induced Dynamics of Bile Colloids. *Langmuir* **2021**.

Schlauersbach, J.; Hanio, S.; Lenz, B.; Vemulapalli, S. P. B.; Griesinger, C.; Poppler, A. C.; Harlacher, C.; Galli, B.; Meinel, L., Leveraging bile solubilization of poorly water-soluble drugs by rational polymer selection. *J Control Release* **2021**, *330*, 36-48.

Co-authorship

Scheller, L.; Bachmann, S.; Zorn, T.; Hanio, S; Gbureck, U.; Fatouros, D; Poppler, A. C.; Meinel, L., Solid microemulsion preconcentrates on pH responsive metal-organic framework for tableting. *Eur J Pharm Biopharm* **2023**, 186, 105-111

Spangardt, C.; Kessler, C.; Dobrzewski, R.; Tepler, A.; Hanio, S.; Klaubert, B.; Meinel, L., Leveraging Dissolution by Autoinjector Designs. *Pharmaceutics* **2022**, 14 (11).

Schlauersbach, J.; Hanio, S.; Raschig, M.; Lenz, B.; Scherf-Clavel, O.; Meinel, L., Bile and excipient interactions directing drug pharmacokinetics in rats. *Eur J Pharm Biopharm* **2022**, 178, 65-68

Schlauersbach, J.; Kehrein, J.; Hanio, S.; Galli, B.; Harlacher, C.; Heidenreich, C.; Lenz, B.; Sotriffer, C.; Meinel, L., Predicting Bile and Lipid Interaction for Drug Substances. *Mol Pharm* **2022**, 19 (8), 2868-2876.

Endres, S.; Karaev, E.; Hanio, S.; Schlauersbach, J.; Kraft, C.; Rasmussen, T.; Luxenhofer, R.; Bottcher, B.; Meinel, L.; Poppler, A. C., Concentration and composition dependent aggregation of Pluronic- and Poly-(2-oxazolin)-Efavirenz formulations in biorelevant media. *J Colloid Interface Sci* **2022**, 606 (Pt 2), 1179-1192.

Guntzel, P.; Schilling, K.; Hanio, S.; Schlauersbach, J.; Schollmayer, C.; Meinel, L.; Holzgrabe, U., Bioinspired Ion Pairs Transforming Papaverine into a Protic Ionic Liquid and Salts. *ACS Omega* **2020**, *5* (30), 19202-19209.

Posters

Hanio, S. et al. The impact of bile on drug diffusivity in mucus. Poster Pitch Abstracts, Controlled Release Society Local Chapters Meeting Germany and BeNeLux & France, Aachen, Germany, **2022**, p. 98

Hanio, S. et al. Drug-induced dynamics of bile colloids. Poster Abstracts, BioBarrier 2021, Virtual, **2021**, p. 85

Hanio, S. et al. Drug-induced dynamics of bile colloids. Flash Talk & Poster Abstracts, Controlled Release Society Local Chapters Meeting Germany and BeNeLux & France, Virtual, **2021**, p. 60

Hanio, S. et al. Drug concentration dependent geometrical and structural dynamics of biorelevant colloids. Poster Presentation, Controlled Release Society German Chapter Annual Meeting, Munich, Germany, **2020**, p. 38

Acknowledgments

First, I would like to sincerely thank Prof. Dr. Dr. Lorenz Meinel for giving me the opportunity to work in his research group on poorly water-soluble drugs. I am appreciative that he has paved the way for numerous exciting collaborations with academic and industrial partners during my PhD journey. For his guidance, scientifically helpful advice, and innovative ideas, I am deeply grateful. Our joint stimulating discussions over the past four years have greatly helped me to develop into an independent scientist.

I would like to thank BASF SE for the financial funding. It was great to have you on board for my projects, Dr. Felicitas Guth and Dr. Karl Kolter as well as Dr. Sung Min-Pyo, Dr. Ferdinand-Paul Brandl, and Dr. Theo Smit. In addition, I would like to thank all partners, colleagues, and friends for their scientific contributions to this work. These include in especially Prof. Dr. Ann-Christin Pöppler, Prof. Dr. Katrin Heinze, Prof. Dr. Jochen Guck, Prof. Dr. Ulrich S. Schubert, Prof. Dr. Rainer A. Böckmann, Prof. Dr. Christian Griesinger, Prof. Dr. Oliver Scherf-Clavel, Dr. Stephanie Möllmert, Dr. Ivo Nischang, Dr. Ralf Schweins, Dr. Peter Bellstedt, Dr. Susbohan Choudhury, Dr. Sahithya P. B. Vemulapalli, Dr. Cornelius Harlacher, Dr. Bruno Galli, Theresa Zorn, Franziska Spiegel, Conrad Möckel, Sebastian Endres, Andreas Inho Höpfel, and Christoph Keßler.

Special thanks go to all members of the Meinel group for their support, primarily Lena Scheller, Bettina Lenz, and Dr. Jonas Schlauersbach. Working together with you has always been a lot of fun.

I would like to thank my entire family for their constant and tireless support. I could not have undertaken this journey without Viktoria, on whose love this work is founded.

Documentation of Authorship

This section contains a list of the individual contribution for each author given in percentage to the publications reprinted in this thesis. The column listing Simon Hanio's contribution is highlighted in grey. Unpublished manuscripts are handled, accordingly.

Chapter 1

Hanio S, Schlauersbach J, Lenz B, Spiegel F, Böckmann R A, Schweins R, Nischang I, Schubert U S, Endres S, Pöppler A-C, Brandl F P, Smit T M, Kolter K, Meinel L (2021)
"**Drug induced dynamics of bile colloids**"
Langmuir, vol. 37, issue 8, pp. 2543-2551, 2021;
DOI: 10.1021/acs.langmuir.0c02282

Author	1	2	3	4	5	6	7	8	9	10	11	12	13	14	Sum
^{1}H nuclear magnetic resonance spectroscopy	5%	5%													10%
1D selective Nuclear Overhauser enhancement spectroscopy	3%	3%							2%						8%
Zeta potential, dynamic light scattering	1%	2%	1%												4%
Molecular dynamics				5%	3%										8%
Equilibrium solubility determination	2%	2%													4%
Analytical ultracentrifugation	3%						5%								8%
UV-Vis measurements	2%	2%													4%
Small-angle neutron scattering	3%					5%									8%
Isothermal titration calorimetry	6%														6%
Publication writing	9%	6%					2%							8%	25%
Coordination					1%	1%	1%	1%		0.5%	0.5%	0.5%	0.5%	9%	15%
Total	34%	20%	1%	5%	4%	6%	8%	1%	2%	0.5%	0.5%	0.5%	0.5%	17%	100%

Chapter 2

Schlauersbach J, Hanio S, Lenz B, Vemulapalli S, Griesinger C, Pöppler A, Harlacher C, Galli B, Meinel L (2021)
"Leveraging bile solubilization of poorly water-soluble drugs by rational polymer selection"
Journal of controlled release, vol. 330, pp. 36-48, 2021;
DOI: 10.1016/j.jconrel.2020.12.016

Author	1	2	3	4	5	6	7	8	9	Sum
Dynamic light scattering (DLS)	4%		1%							5%
^{1}H nuclear magnetic resonance (NMR) spectroscopy	8%	8%				2%				18%
^{1}H diffusion-ordered spectroscopy (DOSY)	2%	2%		4%						8%
Flux	8%	17%								25%
HPLC Analysis	3%	2%	1%							6%
Publication writing	10%	3%		1.5%		1.5%			9%	25%
Coordination				0.5%	2%		1%	1%	8.5%	13%
Total	35%	32%	2%	6%	2%	3.5%	1%	1%	17.5%	100%

Chapter 3

Hanio S, Möllmert S, Möckel C, Choudhury S, Höpfel A I, Zorn T, Endres S, Schlauersbach J, Scheller L, Keßler C, Scherf-Clavel O, Bellstedt P, Schubert U S, Pöppler A-C, Heinze K G, Guck J, Meinel L (2023)
"**Impact of bile on the intestinal mucus**"
Submitted manuscript.

Author	SH	SM	CM	SC	AH	TZ	SE	JS	LS	CK	OSC	PB	US	ACP	KGH	JG	LM	Sum
Mucus collection and sample preparation	2%																	2%
Fluorescence correlation spectroscopy				4%	4%													8%
Bulk rheology	5%																	5%
Nuclear-magnetic resonance spectroscopy	5%					4%	2%					1%						12%
Confocal Brillouin microscopy	1.5%	5.5%	0.5%							0.5%								8%
Differential dynamic microscopy	1%		5%															6%
Flux studies	7%								1%									8%
Pharmacokinetic study in rats	1%							2%			1%							4%
Publication writing	13%	2%		1%							1%			2%	1%	1%	8%	29%
Coordination												1%	2%	2%	2%	3%	8%	18%
Total	35.5%	7.5%	5.5%	5%	4%	4%	2%	2%	1%	0.5%	2%	2%	2%	4%	3%	4%	16%	100%

Appendix

Hanio S, Scheller L, Meinel L (2023)
"Biopharmaceutical characterization of poorly-water soluble drugs by nuclear magnetic resonance spectroscopy"
Unpublished manuscript.

Author	SH	LS	LM	Sum
Literature analysis, interpretation	20%			20%
Publication writing	40%	5	10%	55%
Coordination		5	20%	25%
Total	60%	10%	30%	100%

Erklärung zu den Eigenanteilen des Doktoranden sowie der weiteren Doktoranden als Koautoren an Publikationen und Zweitpublikationsrechten bei einer kumulativen Dissertation.

Für alle in dieser kumulativen Dissertation verwendeten Manuskripte liegen die notwendigen Genehmigungen der Verlage (‚reprint permission') für die Zweitpublikation vor, außer das betreffende Kapitel ist noch gar nicht publiziert. Dieser Umstand wird einerseits durch die genaue Angabe der Literaturstelle der Erstpublikation auf der ersten Seite des betreffenden Kapitels deutlich gemacht oder die bisherige Nichtveröffentlichung durch den Vermerk „unpublished" oder „nicht veröffentlicht" gekennzeichnet.
Die Mitautoren der in dieser kumulativen Dissertation verwendeten Manuskripte sind sowohl über die Nutzung als auch über die oben angegebenen Eigenanteile informiert.
Die Anteile der Mitautoren an den Publikationen sind in den vorausgehenden Tabellen aufgeführt.

Prof. Dr. Dr. Lorenz Meinel Unterschrift

Simon Hanio Unterschrift